The Dynamics of Equatorial Mass-Flow Adjustment

by
Pedro Leite Silva Dias
Wayne H. Schubert

Department of Atmospheric Science
Colorado State University
Fort Collins, Colorado

Colorado State University

Department of Atmospheric Science

Paper No. 312

THE DYNAMICS OF EQUATORIAL MASS-FLOW ADJUSTMENT

by

Pedro Leite Silva Dias

Wayne H. Schubert

The research reported here has been supported by the Global Atmospheric Research Program, Climate Dynamics Research Section, National Science Foundation, Grants ATM76-09370 and ATM78-08125.

Department of Atmospheric Science
Colorado State University
Fort Collins, Colorado

June 1979

Atmospheric Science Paper No. 312

ABSTRACT

The problem of the adjustment of the mass and wind fields in a divergent barotropic model is solved on the equatorial β-plane. Contrary to the traditional f-plane analysis, the motion does not tend to a perfect geostrophic balance on a short time scale. However, the β-plane approximation allows for the presence of Rossby waves and since these waves are quasi-geostrophic, they may be regarded as the adjusted state. It is also shown that the concept of an adjusted state on the β-plane is dependent on the dispersive properties and energetics of Rossby and gravity waves.

Two basic experiments are shown: the first is a perturbation in the geopotential field, and the second is a perturbation in the rotational part of the wind field. When perturbing the mass field on a small scale compared to the equatorial Rossby radius of deformation, most of the initial energy is dispersed by gravity waves; but altering the vorticity field is a very efficient way to localize the energy input. The adjusted state shows asymmetries that cannot be obtained on an f-plane analysis. The circulation patterns produced by steady mass and momentum sources and sinks are also shown. Possible consequences of the results for tropical dynamics are discussed in terms of the effect of clouds on the environment.

ACKNOWLEDGEMENTS

The authors wish to express their appreciation to Drs. Akira Kasahara, Bernhard Haurwitz, Stephen Cox, Duane Stevens, William Gray, Howard Frisinger, John McBride, Maria Silva Dias, Messrs. James Hack, Scott Fulton, and Ms. Alison Bridger for advice and assistance.

This research was done while one of us (PSD) was on leave from the Departamento de Meteorologia of the Instituto Astronômico e Geofisico of the Universidade de São Paulo, Brazil, and under a scholarship from the Conselho Nacional de Desenvolvimento Cientifico e Tecnologico - CNPq.

Many thanks go to Odilia Panella who typed the manuscript and to Mark Howes who drafted the figures.

Acknowledgement is made to the National Center for Atmospheric Research, which is sponsored by the National Science Foundation, for computing time in this research.

This research was supported by the National Science Foundation under Grants ATM76-09370 and ATM78-08125.

TABLE OF CONTENTS

TABLE OF CONTENTS continued

LIST OF TABLES

LIST OF FIGURES

LIST OF FIGURES continued

LIST OF FIGURES continued

1.0 INTRODUCTION

The nature of tropical motion has excited the imagination of researchers for a long time not only because of its presumed importance for mid-latitude phenomena but also for the challenge of understanding the unique role of latent heat release in driving large-scale circulations. A considerable amount of effort has been devoted to the development of theories on how small-scale convective motions interact with large-scale motions. However, when one examines the literature, only a few references to the problem of the adjustment of the mass and wind fields at low latitudes can be found. The objective of this research is to study the dynamical adjustment of the mass and wind fields at low latitudes. This is a relatively simple problem that can be studied without having to resort to complicated scale interactions. When one studies the problem of the adjustment of the mass and wind fields, the large-scale dynamics of the atmosphere are isolated and possible effects of small-scale convection are taken as a known forcing. Thus, this research may be regarded as a study of the basic dynamics of the tropical region.

The process of the adjustment of the mass and wind fields is closely related to the problem of energy dispersion in the atmosphere. This theory was developed by Rossby (1945) and Yeh (1949) but with the advent of the baroclinic instability theory by Charney (1947), which consists of energy conversion rather than propagation, the theory lacked further development. Only recently has the problem of energy dispersion been revisited by Hoskins, et al. (1977), who studied the

linear barotropic vorticity equation on the sphere. In the following sections, we briefly discuss the current theories of tropical motions from an energetics point of view and discuss the reasons why we believe that the process of adjustment might be important.

1.1 Energetics of Tropical Motion

The current theories of tropical motions can be easily understood in terms of energy generation and conversion. Some researchers (Nitta and Yanai, 1969; Burpee, 1972) have suggested that the kinetic energy of wave disturbances in the trades is supplied through barotropic instability, which involves a conversion of zonal kinetic energy (ZKE) to eddy kinetic energy (EKE). Another possible source of EKE has to do with boundary terms through the divergence of wave energy flux. This possibility was suggested by Mak (1969) who showed that in a two-layer model large-scale tropical waves can be forced laterally by pressure interaction with middle latitude disturbances. The next possible mechanism for increase of EKE is the conversion from eddy available potential energy (EAPE). With the advance of numerical models incorporating moist convection it was suggested that eddy available potential energy in the tropics is maintained chiefly by the release of latent heat and is converted to eddy kinetic energy (Manabe and Samagorinsky, 1967).

Observational studies of the energetics of the tropics have given a somewhat inconsistent picture concerning the maintenance of easterly waves. In the classical baroclinic and barotropic instability processes in middle latitudes it is clear that the basic state flow must give up potential or kinetic energy to the perturbation. However, Nitta (1972)

showed that the generation of EAPE over the Marshall Islands due to condensational heating and the conversion from EAPE to EKE plays the most important role in the energy balance of the disturbances. Reed et al. (1977) and Norquist et al. (1977) found that baroclinic and barotropic conversions contributed almost equally to the maintenance of the kinetic energy of the African waves.

Theoretical studies (Rennick, 1976; Pedgley and Krishnamurti, 1976; Simmons, 1977) indicate that the wavelength of the African disturbances can be explained by barotropic instability of the basic flow because the barotropic conversion term is about one order of magnitude larger than the baroclinic conversion term. However, other characteristics of the model results, such as horizontal and vertical structure and growth rates, are not as well reproduced and one could argue that the effect of latent heat is not properly handled.

Thus, it seems that the mechanisms responsible for the maintenance of tropical waves are dependent on the basic state on which the disturbances are superimposed. The dynamics of tropical waves in the Pacific region seem to be related to internal energy conversions in which the so-called CISK mechanism (Conditional Instability of the Second Kind) is the primary cause. The CISK mechanism proposed by Charney and Eliassen (1964) and Ooyama (1964) involves an internal convective feedback which enhances the vertical motion.

The energy equations imply a continuous generation, conversion, and dissipation of energy, but nothing is implied with respect to the scale of the atmospheric response to forcing.

1.2 Scale and Organization

An interesting example of the problem of scale and organization of tropical motions is the CISK mechanism. The concept of CISK as initially visualized by Ooyama (1964) and Charney and Eliassen (1964) involved a cooperative behavior between the small-scale latent heat release and the large-scale dynamical field in such a way that the condensational heating drives the low level convergence (through boundary layer processes) which in turn supplies moisture to the clouds. In the wave-CISK hypothesis (Yamasaki, 1969; Lindzen, 1974; Stevens et al., 1977; and many others) the convergence is produced by the wave dynamics. It has been suggested by Gray and Jacobson (1977) and McBride and Gray (1979) that the cluster-scale feedback through latent heat release and radiative gradients is a powerful forcing mechanism which ultimately controls the disturbance.

The critical point in the development of the tropical depression through the CISK mechanism is the need to lower the surface pressure by the heating of a hydrostatic atmospheric column. Increasing the intensity of the low pressure requires small dispersion of the heating perturbation. In other words, if a heating perturbation at the center of the depression is quickly wiped away, and the associated energy dispersed to a large area, the intensification of the system will be hindered. Thus, we are interested in the processes which occur after a heating perturbation, not only in terms of the ability of the atmosphere to retain the initial signal, but also the type of circulation generated by such forcing.

Observational studies of the tropical region have indicated that the local warming is approximately zero although the implied heating

by the release of latent heat in the column (inferred from precipitation reaching the surface) is on the order of several degrees per day (Reed and Recker, 1971; Gray, 1973; Yanai et al., 1973). Thus, there is observational evidence that the dispersion of thermal energy (or equivalently the dispersion of the geopotential perturbation) is important in the real atmosphere.

In the momentum field we know that dissipation acts on a longer time scale (on the order of several days) but there is considerable evidence from cloud modelling that kinetic energy may be generated by clouds under appropriate conditions of wind shear (Moncrieff and Miller, 1976; Moncrieff, 1978). A recent observational study on tropical cyclone formation (McBride, 1979) suggests that the cloud influence on cyclone genesis is not only through the latent heat release but also through the generation of momentum by clouds, a process that ultimately inhibits the energy dispersion as we will see later.

Thus, it seems that one of the basic questions that we have to answer in order to grasp the dynamics of tropical motions concerns the ability of the atmosphere to adjust to imbalances between pressure and wind.

In any of the mentioned theories of tropical motions (boundary effects, conversion of ZKE to EKE, or generation of EAPE and conversion of EAPE to EKE) an adjustment of the mass and wind fields is implied. However, the nature of the resulting motion such as its scale and organization are not explained by the energy transformation equations. The growth of a tropical depression through the CISK mechanism is an example of the importance of the organization of the mass and wind fields.

The task of explaining the nature and scale of motions generated by such imbalances in the pressure and wind fields in a generally stratified atmosphere is certainly difficult. However, in certain simplified physical systems the process of dynamical adjustment of the pressure and wind fields has been studied with success. An example is the so-called geostrophic adjustment problem first discussed by Rossby (1938) and Obukhov (1949).

1.3 The mass-wind adjustment problem

In general, the geostrophic adjustment problem has been studied with the so-called shallow water equations on an f-plane since this is the simplest context in which the problem arises. Rossby's work (1938) considers only the relationship between the initial unbalanced state and the final geostrophically balanced state. The linear transient adjustment was studied for the one dimensional case by Cahn (1945) and for the two dimensional case by Obukhov (1949). The effect of horizontal shear of the basic flow (Blumen and Washington, 1969) and the effect of non-linear terms (Blumen, 1967) have also been considered. Blumen (1972) has extensively reviewed studies of the geostrophic adjustment problem.

For the type of mass-wind adjustment that occurs in the equatorial region the traditional f-plane analysis seems inappropriate in view of the small Coriolis parameter. On the other hand, the β-effect is maximum at the equator suggesting that its inclusion in the problem of equatorial mass-wind adjustment might be important. In fact, the β-effect has been considered in the traditional geostrophic

adjustment problem by Matsumoto (1960), Dobrischman (1964), Geisler and Dickinson (1972) and others, but none of these works treat the equatorial case explicitly.

A variable Coriolis parameter introduces a turning point into the differential equation for single frequency waves (Longuet-Higgins, 1965). As a consequence the wave character of the solution is confined to a certain domain determined by the turning points; outside this domain the solution is exponentially decaying. As shown by Longuet-Higgins (1965) there are in general two turning latitudes when spherical geometry is considered. The usual mid-latitude β-plane approximation (Lindzen, 1967) implies no turning points, i.e., the solution is wave-like over the whole domain and therefore energy is allowed to disperse to infinity as in Matsumoto's and Dobrischman's work. On the equatorial β-plane there are two turning latitudes located symmetrically with respect to the Equator and therefore the energy is trapped (Matsuno, 1966; Bretherton, 1964). Since the energy is trapped, we do not expect a steady geostrophic current to be established on the equatorial β-plane because the energy in ageostrophic motion (or gravity waves) is not allowed to disperse to infinity. Geisler and Dickinson (1972) use a linear approximation for f^2 and only one turning point is situated north of the reference latitude. Thus, there can be dispersion of gravity waves towards the south.

It should be remarked at this point that the introduction of the β-plane approximation into the shallow water equations implies that the steady geostrophic solution must be zonally directed (Dobrischman 1964; Blumen, 1972). The more accurate solution on a rotating sphere

also gives the same result for steady geostrophic flow. However, the β-plane approximation allows for the presence of Rossby waves and since these waves are quasi-geostrophic, they may be regarded as the adjusted state (Matsumoto, 1960).

Thus, our main concern will be to study the characteristics of the motion that is left after the energy in ageostrophic motion (gravity waves) is dispersed.

The use of the shallow water equations to study the mass-wind adjustment problem is not overly restrictive because the governing equations for a stratified fluid, linearized about a basic state at rest, can be separated into horizontal structure equations and a vertical structure equation; the horizontal structure equations are the shallow water equations and the separation constant H is the depth of the homogeneous ocean (Taylor, 1936; Eckart, 1960).

A considerable amount of work has been done in oceanography on the response of the tropical ocean to atmospheric forcing. (Yoshida, 1959; Lighthill, 1969; Moore and Philander, 1976; Anderson and Rowlands, 1976; Cane and Sarachick, 1976). The emphasis is however, on the effect of wind stress in generating ocean currents and although the equations and method of solution are akin to our problem the objectives are different.

1.4 Outline

In this study we shall solve an initial value problem governed by the linearized shallow water equations on an equatorial β-plane (Matsuno, 1966; Lindzen, 1967). The basic state is assumed to be at

rest although some considerations on how the inclusion of a horizontally sheared basic state might modify the results are discussed in Chapter 7. The normal mode technique is employed to solve the initial value problem since the free wave solutions of the governing equations form a complete set (Matsuno, 1966).

In Chapter 2, we review the governing equations and discuss the method of solution including a generalization to the three dimensional case (stratified atmosphere).

The equatorial β-plane is known to be a valid approximation for internal modes having small H (the so-called equivalent depth). For the external mode of an isothermal atmosphere, H is approximately 10 km (Lindzen, 1967) and the inclusion of the full effects of the geometry of the earth are necessary. In Chapter 2, we also show that the linearized initial value problem on the sphere is a simple generalization of the equatorial β-plane solution. The generalization is accomplished by replacing the β-plane free wave solutions with the spherical free wave solutions, which are called Hough functions (Kasahara, 1976). In Chapter 3, we discuss the process of dispersion of energy on the equatorial β-plane and on the sphere (for the external mode) under the assumption of zonal periodicity.

The initial value problem with an initial condition in the geopotential field and no wind is discussed in Chapter 4. The opposite case, i.e. no geopotential perturbation but wind perturbation initially is treated in Chapter 5. The initial value problems discussed in Chapter 4 and 5 can also be interpreted as an impulsive forcing in the geopotential and momentum fields respectively. In Chapter 6 the

adjustment of the mass and wind fields in the presence of a steady mass sink/source is studied.

It turns out that the internal mode of a two level baroclinic model with typical parameters of the tropical atmosphere can be well represented by the equatorial β-plane shallow water equations (Chapter 2) provided we interpret the geopotential as thickness (or temperature) and the momentum field as the wind shear between the upper and lower levels.

Finally, in Chapter 7, we analyze the results of Chapters 4, 5, and 6 in a unified way, discuss the implications of this work, and suggest future research in this area.

2.0 GOVERNING EQUATIONS

In this chapter we discuss the solution of the linearized primitive equations on the equatorial β-plane for a basic state of no motion. These equations are separable into horizontally and vertically dependent parts (section 2.1). The vertical structure is discussed in section 2.2 and the horizontal structure which is given by the so-called shallow water equations is treated in section 2.3. The free wave solutions so constructed form a complete and orthogonal set. Therefore, an initial condition can be represented by a superposition of such free waves and the solution for the initial value problem can be easily obtained as shown in section 2.4. The inclusion of Rayleigh damping terms and thermal forcing can also be easily accomplished as shown in section 2.4.

The generalization of the solution of the initial value problem to the sphere can be done using Hough functions computed by the method of Kasahara (1976). In section 2.5, we show how this can be done.

2.1 Perturbation Equations

The perturbation equations on an equatorial β-plane for a basic state of no motion are

$$\frac{\partial u}{\partial t} - \beta y v + \frac{\partial \phi}{\partial x} = 0 \,, \qquad (2.1.a)$$

$$\frac{\partial v}{\partial t} + \beta y u + \frac{\partial \phi}{\partial y} = 0 \,, \qquad (2.1.b)$$

$$\frac{\partial u}{\partial x} + \frac{\partial v}{\partial y} + \frac{\partial \omega}{\partial p} = 0 \,, \qquad (2.1.c)$$

$$\frac{\partial}{\partial t}\left(-\frac{\partial \phi}{\partial p}\right) - \bar{\sigma}\,\omega = 0 \quad , \qquad (2.1.d)$$

where (u,v) are the eastward and northward velocity components and $\omega = \frac{dp}{dt}$ is the vertical velocity in the p-coordinate; ϕ is the geopotential, f is the Coriolis parameter ($f = 2\Omega \sin\varphi$) where φ is the latitude, and $\bar{\sigma} = \left(-\frac{\bar{\alpha}}{\bar{\theta}}\frac{\partial \bar{\theta}}{\partial p}\right)$ is the static stability parameter of the basic state atmosphere. For a statically stable atmosphere $\bar{\sigma}$ is a positive parameter.

Equations (2.1.c) and (2.1.d) can be combined to eliminate ω resulting in

$$\frac{\partial}{\partial t}\left[-\frac{\partial}{\partial p}\left(\frac{1}{\bar{\sigma}}\frac{\partial \phi}{\partial p}\right)\right] + \nabla \cdot \mathbb{V} = 0 \quad , \qquad (2.2)$$

where $\mathbb{V} = (u,v)$. Equations (2.1.a), (2.1.b) and (2.2) constitute a system of three equations for the three unknowns u, v and ϕ. The next step to solve (2.1.a), (2.1.b) and (2.2) is to assume

$$\frac{\partial}{\partial p}\left(\frac{1}{\bar{\sigma}}\frac{\partial \phi}{\partial p}\right) = -\frac{1}{c^2}\phi \quad , \qquad (2.3)$$

where c^{-2} is a constant of proportionality. Equation (2.3) is formally equivalent to assuming that the solution of (2.1) is separable into horizontal and vertical dependent equations as is usually done (e.g. Lindzen, 1967). Given suitable vertical boundary conditions, the constant c^2 can be determined as an eigenvalue of (2.3). The constant c has the dimension of speed and therefore we can write $c^2 = gH$ where H has dimension of height. Equations (2.1.a), (2.1.b) and (2.2) reduce to a system of equations independent of pressure, namely

$$\frac{\partial u}{\partial t} - \beta y v + \frac{\partial \phi}{\partial x} = 0 \quad , \tag{2.4.a}$$

$$\frac{\partial v}{\partial t} - \beta y v + \frac{\partial \phi}{\partial y} = 0 \quad , \tag{2.4.b}$$

$$\frac{\partial \phi}{\partial t} + gH \nabla \cdot \mathbf{V} = 0 \quad , \tag{2.4.c}$$

for each eigenvalue H of (2.3).

The system (2.4) is the so-called divergent barotropic model, i.e. the governing equations for a layer of incompressible and homogeneous fluid with a free surface in hydrostatic balance. Equations (2.4) are also known as the shallow water equations. The coefficient H in (2.4.c) is known as the equivalent depth after Taylor (1936). For the sake of completeness, we discuss the free wave solutions of (2.4) in section 2.3; these solutions were originally discussed by Matsuno (1966).

Alternatively, (2.4) can be interpreted as the system of equations governing a two level baroclinic model in p-coordinate, as shown by Matsuno (1966). Let us first divide the atmosphere into two discrete layers as shown in Figure 2.1. The u and v components of the wind and the geopotential are defined at the odd levels; the vertical p-velocity ω is defined at the even levels. The boundary conditions are $\omega_0 = \omega_4 = 0$. The linearized governing equations about a basic state at rest are

$$\frac{\partial u_1}{\partial t} - \beta y v_1 + \frac{\partial \phi_1}{\partial x} = 0 \quad , \tag{2.5.a}$$

$$\frac{\partial u_3}{\partial t} - \beta y v_3 + \frac{\partial \phi_3}{\partial x} = 0 \quad , \tag{2.5.b}$$

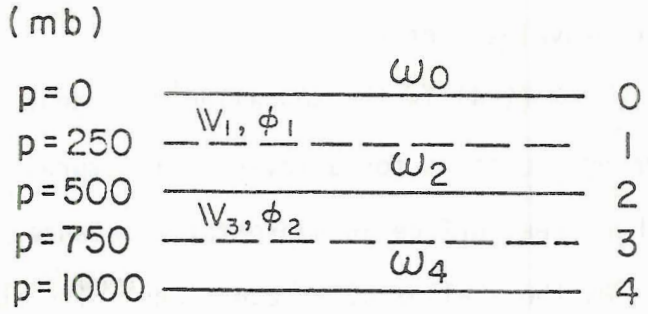

Figure 2.1 Vertical staggering of variables in a two-level baroclinic model.

$$\frac{\partial v_1}{\partial t} + \beta y u_1 + \frac{\partial \phi_1}{\partial y} = 0 \ , \qquad (2.5.c)$$

$$\frac{\partial v_3}{\partial t} + \beta y u_3 + \frac{\partial \phi_3}{\partial y} = 0 \ , \qquad (2.5.d)$$

$$\frac{\partial u_1}{\partial x} + \frac{\partial v_1}{\partial y} + \frac{\omega_2}{\Delta p} = 0 \ , \qquad (2.5.e)$$

$$\frac{\partial u_3}{\partial x} + \frac{\partial v_3}{\partial y} - \frac{\omega_2}{\Delta p} = 0 \ , \qquad (2.5.f)$$

$$\frac{\partial}{\partial t}\left(\frac{\phi_3 - \phi_1}{\Delta p}\right) + \bar{\sigma}_2 \omega_2 = 0 \ , \qquad (2.5.g)$$

where $\bar{\sigma}_2 = \left(-\frac{\bar{\alpha}}{\bar{\theta}} \frac{\partial \bar{\theta}}{\partial p}\right)_2$. Subtracting (2.5.b) and (2.5.d) from (2.5.a) and (2.5.c) respectively and defining

$$u_d = u_1 - u_3 \ , \qquad (2.6)$$

$$v_d = v_1 - v_3 \ , \qquad (2.7)$$

$$\phi_d = \phi_1 - \phi_3 \ , \qquad (2.8)$$

we get

$$\frac{\partial u_d}{\partial t} - \beta y v_d + \frac{\partial \phi_d}{\partial x} = 0 \ , \qquad (2.9.a)$$

$$\frac{\partial v_d}{\partial t} + \beta y u_d + \frac{\partial \phi_d}{\partial y} = 0 \ . \qquad (2.9.b)$$

The objective now is to reduce (2.5.e), (2.5.f) and (2.5.g) to one single equation in u_d, v_d and ϕ_d similar to (2.4.c). This can be achieved by subtracting (2.5.e) from (2.5.f) and substituting the result in the thermodynamic equation (2.5.g). The final equation is

$$\frac{\partial \phi_d}{\partial t} + \frac{\bar{\sigma}^2 \nabla^2 p}{2} \nabla \cdot \mathbf{W}_d = 0 \ , \qquad (2.9.c)$$

where $\mathbf{W}_d = (u_d, v_d)$. Comparing (2.9) with (2.4) we see that the equivalence is perfect provided we interpret u and v in (2.4) as the wind shear and ϕ as the thickness (or temperature). The speed of pure gravity waves on the fluid of depth H in (2.4) is now

$$c = \sqrt{gH} = \Delta p \sqrt{\frac{\bar{\sigma}^2}{2}} \ , \qquad (2.10)$$

and represents the phase speed of an internal gravity wave in the two level baroclinic model.

Although the main concern of this research is the horizontal structure of (2.1) for a specified vertical mode H, it is useful to consider some particular solutions of (2.3). This is the objective of the next section.

2.2 Vertical structure

Let us first consider the solution of (2.3) under the boundary conditions

$$\omega = 0 \quad \text{at} \quad p = 0 \quad \text{and} \quad p = p_o \ . \qquad (2.11)$$

The boundary conditions (2.11) can be easily seen to be equivalent to

$$\frac{\partial \phi}{\partial p} = 0 \quad \text{at} \quad p = 0 \quad \text{and} \quad p = p_o \ . \qquad (2.12)$$

If we further assume that the static stability is constant with pressure the solutions of (2.3) are given by

$$\phi_j = A_j \cos \sqrt{\frac{\bar{\sigma}}{c_j}}\, p \ , \qquad (2.13)$$

where the A_j are arbitrary constants and the eigenvalues c_j are such that

$$c_j = \frac{p_o \sqrt{\bar{\sigma}}}{\pi j}, \quad j = 0, \pm 1, \ldots \quad . \tag{2.14}$$

The horizontal divergence has this same vertical structure according to (2.4.c) since we can also assume a separable solution in time. The $j = 0$ mode has constant divergence with height and corresponds to the barotropic non-divergent mode because of the boundary conditions (2.11). The equivalent depth of the $j = 0$ mode is infinity according to (2.14) since $gH_j = c_j^2$.

The $j = 1$ mode has one level of zero divergence at $p = 500$ mb while the $j = 2$ mode has two and so on. The barotropic divergent mode (or the so-called external mode) has been eliminated from this analysis because of the boundary condition (2.11). Had we assumed $gw = \frac{d\phi}{dt} = 0$ as the boundary condition, (2.12) at $p = p_o$ would be replaced by

$$\frac{\partial \phi}{\partial t} + \bar{\sigma} \rho_o \phi = 0 \quad \text{at} \quad p = p_o \, , \tag{2.15}$$

where ρ_o is the air density at $p = p_o$. The usual approximation of applying the lower boundary condition at a pressure surface $p = p_o =$ const. has been applied in (2.15). In this case the functional form of the vertical structure of ϕ is still given by (2.13) but the eigenvalues c_j are defined by the transcendental equation

$$\tan\left(\frac{\sqrt{\bar{\sigma}}}{c_j} p_o\right) = \frac{\bar{\sigma} \rho_o p_o}{\left(\frac{\sqrt{\bar{\sigma}}}{c_j} p_o\right)} \, . \tag{2.16}$$

Table 2.1 contains a summary of the results for the first five values of the eigenvalue c_j with the boundary condition (2.11) at $p = 0$ and with (2.15) applied at the lower boundary $p = p_o$. The numerical values of p_o, $\bar{\sigma}$ and ρ_o are respectively 1000 mb, $1.6 \times 10^{6} m^4 s^{-2} kg^{-2}$ and 1.2 kgm^{-3}. It is clearly seen that the effect of having $\omega = 0$ at $p = p_o$ is simply to eliminate the barotropic divergent solutions of (2.1) while the internal modes are practically unchanged.

	$c(ms^{-1})$	
j	$\omega = 0$ at $p = 0$ and $p = p_o$	$\omega = 0$ at $p = 0$ $w = 0$ at $p = p_o$
0	∞	322.5
1	40.5	39.9
2	20.2	20.2
3	13.5	13.5
4	10.1	10.1

Table 2.1. Eigenvalues c_j of (2.16) with $\omega = 0$ at $p = 0$ and $p = p_o$ and with $\omega = 0$ at $p = 0$ and $w = 0$ at $p = p_o$. The value of $\bar{\sigma}$ is $1.6 \times 10^{-6} m^4 s^2 kg^{-2}$.

The results obtained above are dependent on the assumption of constant static stability $\bar{\sigma}$ with pressure. Jacobs and Wiin-Nielsen (1966) have shown that (2.3) with the boundary conditions (2.11) can be solved in terms of Bessel functions if $\bar{\sigma}$ is evaluated for a basic state characterized by constant lapse rate. Wiin-Nielsen (1971 generalized their solution to the more realistic lower boundary condition (2.15). In both cases the spectrum is discrete. For an isothermal basic state the spectrum consists of a discrete part given by the barotropic mode and a continuous part. However, for the

purposes of this research the assumption of constant $\overline{\sigma}$ is sufficient and therefore there is no need to enter into the details of the more realistic basic state discussed by Wiin-Nielsen (1971).

Our main concern for this research is that (2.3) with the boundary condition (2.11) or (2.15) at $p = p_o$ form a Sturm-Liouville type boundary value problem (Morse and Feshback, 1953). Thus, the corresponding solutions ϕ_j are orthogonal in the sense that

$$\int_o^{p_o} \phi_i \, \phi_j \, dp = \delta_{i,j} \quad , \tag{2.17}$$

(where $\delta_{i,j}$ is the Kronecher delta function) and form a complete set in the interval $[o, p_o]$. Consequently, any function of p can be represented by a series of eigenfunctions ϕ_j in the interval $[o, p_o]$ as

$$G(p) = \sum_{j=0}^{\infty} a_j \, \phi_j \, (p) \, , \tag{2.18}$$

where G(p) is the arbitrary function of p and

$$a_j = \int_o^{p_o} G(p)\phi_j(p) \, d \, p \, . \tag{2.19}$$

In (2.18) we have assumed that the ϕ_j are normalized such that

$$\int_o^{p_o} \phi_j^2 \, (p) \, dp = 1 \, . \tag{2.20}$$

As a consequence of the completeness and orthonormality of ϕ_j, any initial condition which is separable in vertical and horizontal structure can be projected onto the vertical modes given by (2.13) with c_j

given either by (2.14) or (2.16). We now proceed to solve (2.4), which gives the horizontal structure of any solution of (2.1).

2.3 Horizontal structure

The horizontal structure of the solution of (2.1) is given by the shallow water equations (2.4). These equations on the equatorial β-plane were first successfully solved by Matsuno (1966). His method of solution is employed in this section and an extention to the zonally symmetric case is performed in section 2.3.3.

It is convenient to transform the shallow water equations (2.4) to non-dimensional form. The natural scaling for system (2.4) is

$$[L] = \left(\frac{c}{\beta}\right)^{\frac{1}{2}} , \quad [T] = \left(\frac{1}{c\beta}\right)^{\frac{1}{2}}, \tag{2.21}$$

where c is an eigenvalue of (2.3) corresponding to the wave speed of pure gravity waves on a fluid of depth H ($c = \sqrt{gH}$). The length scale [L] can be interpreted as the usual Rossby radius of deformation $\lambda = \frac{c}{f}$ evaluated at latitude [L] i.e.,

$$[L] = \lambda([L]) = \frac{c}{f([L])} = \frac{c}{\beta[L]} , \tag{2.22}$$

and [T] is the inverse of the Coriolis parameter at the latitude [L] (Cane and Sarachik, 1976). Figure 2.2 shows the number of non-dimensional time units per day (left scale) or the time scale [T] (right scale) in days as a function of the eigenvalue $c = \sqrt{gH}$. The number of non-dimensional length units per 1000 km as a function of c is displayed in Figure 2.3 (left scale). The length scale [L] is shown on the right scale of Figure 2.2.

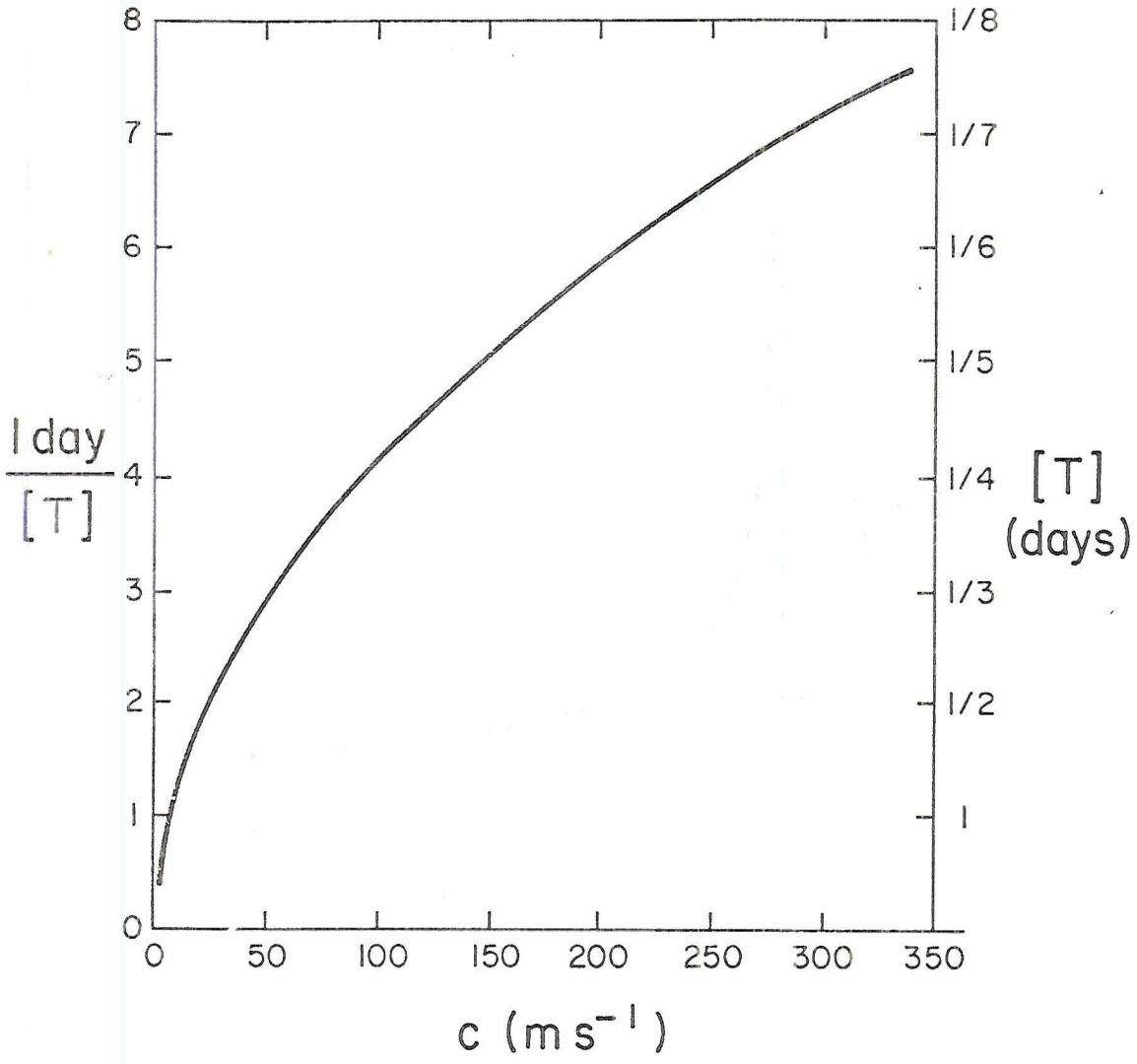

Figure 2.2 Number of non-dimensional time units per day (left scale) or time scale [T] in days (right scale) as a function of $c = \sqrt{gH}$.

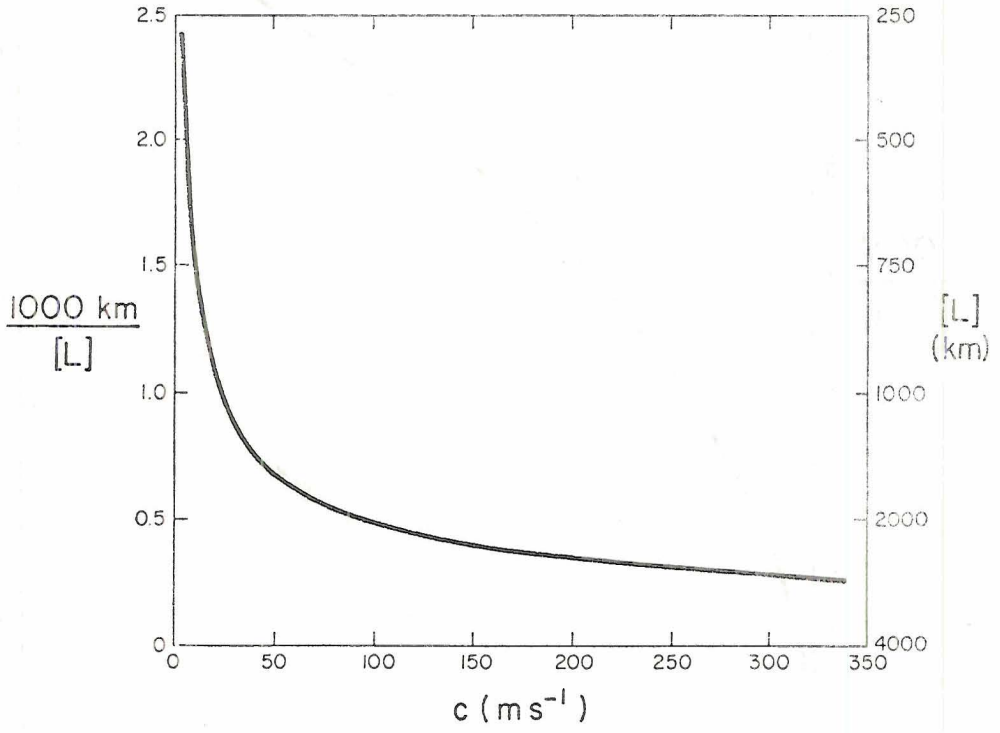

Figure 2.3 Number of non-dimensional length units per 1000 km (left scale) or length scale [L] in kilometers (right scale) as a function of $c = \sqrt{gH}$.

Taking gH as the scaling for ϕ in (2.4), the non-dimensional forms of the shallow water equations become

$$\frac{\partial \hat{u}}{\partial \hat{t}} - \hat{y}\hat{v} + \frac{\partial \hat{\phi}}{\partial \hat{x}} = 0 \ , \tag{2.23.a}$$

$$\frac{\partial \hat{v}}{\partial \hat{t}} - \hat{y}\hat{u} + \frac{\partial \hat{\phi}}{\partial \hat{y}} = 0 \ , \tag{2.23.b}$$

$$\frac{\partial \hat{\phi}}{\partial t} + \frac{\partial \hat{u}}{\partial x} + \frac{\partial \hat{v}}{\partial y} = 0 \ , \tag{2.23.c}$$

where the symbol (^) refers to non-dimensional quantities. After dropping the symbol (^) for simplicity, we write (2.23) in vector form as

$$\frac{\partial \xi}{\partial t} + \Omega \xi = 0, \tag{2.24}$$

where

$$\xi(x,y,t) = \begin{bmatrix} u(x,y,t) \\ v(x,y,t) \\ \phi(x,y,t) \end{bmatrix} \ , \tag{2.25}$$

and the linear operator Ω is defined by

$$\Omega = \begin{bmatrix} 0 & y & \frac{\partial}{\partial x} \\ -y & 0 & \frac{\partial}{\partial y} \\ \frac{\partial}{\partial x} & \frac{\partial}{\partial y} & 0 \end{bmatrix} \ . \tag{2.26}$$

We shall first assume that $\xi(x,y,t)$ is cyclic in the zonal direction with zonal period L_x. Thus, $\xi(x,y,t)$ can be represented as a series in the zonal direction as

$$\xi(x,y,t) = \sum_k \xi_k(y,t)\, e^{ikx} \quad , \tag{2.27}$$

where k is confined to multiple values of $\frac{2\pi}{L_x}$ since we have imposed zonal periodicity of length L_x, i.e.,

$$k = \frac{2\pi m}{L_x} \quad , \quad m = 0, \pm 1, \pm 2, \ldots \ . \tag{2.28}$$

The boundary condition in the meridional direction is

$$\xi_k(y,t) \to 0 \quad \text{as} \quad y \to \pm\infty \quad , \tag{2.29}$$

compatible with the infinite equatorial β-plane.

We now seek solutions of (2.24) proportional to $e^{i\omega_k t}$, where the ω_k are the eigenfrequencies associated with the zonal wavenumber k. The system of equations to be solved takes the form

$$i\omega_k u_k - y v_k + ik\phi_k = 0 \ , \tag{2.30.a}$$

$$i\omega_k v_k + y u_k + \frac{d\phi_k}{dy} = 0 \ , \tag{2.30.b}$$

$$i\omega_k \phi_k + iku_k + \frac{dv_k}{dy} = 0 \ , \tag{2.30.c}$$

or in vector form

$$i\omega_k \xi_k + \Omega_k \xi_k = 0 \ , \tag{2.31}$$

where Ω_k is defined as in (2.26) except that $\frac{\partial}{\partial x} \to ik$. Solving (2.31) subject to the boundary condition (2.29) poses an eigenvalue problem which can be easily solved as shown in section 2.3.1. The eigenfunctions of (2.31) form a complete and orthogonal set (Matsuno, 1966; Cane and Sarachik, 1976) and therefore, any mathematically "well behaved" initial condition $\xi(x,y,o)$ can be represented by a series of the

eigenfunctions. For the objectives of this research, it is sufficient to consider a square integrable function in the interval $(-\infty, +\infty)$ as a "well behaved" function.

In section 2.4, we use the completeness and orthogonality of the eigenfunctions of the linearized shallow water equations about a basic state at rest to formulate the initial value problem.

2.3.1 Eigenfrequencies

The vector equation (2.31) can be reduced to the single ordinary differential equation in the meridional velocity v

$$\frac{d^2 v_k}{dy^2} + (\omega_k - k^2 + \frac{k}{\omega_k} - y^2)\, v_k = 0 , \tag{2.32}$$

with the boundary condition derived from (2.29)

$$v \to 0 \quad \text{as} \quad y \to \pm\infty . \tag{2.33}$$

The original system of three equations and three unknowns has been reduced to an equation of the Sturm-Liouville type known as the Schrödinger equation. The customary way to solve that equation is to factor out the behavior of the solutions at infinity by setting

$$v_k(y) = e^{-\frac{y^2}{2}}\, \psi(y)$$

which reduces (2.32) to a Hermite differential equation. The final solution is

$$v_k(y) = e^{-\frac{y^2}{2}}\, H_n(y) \tag{2.34}$$

and

$$\omega_k^2 - k^2 + \frac{k}{\omega_k} = 2n + 1, \quad n = 0, 1, 2, \ldots, \quad (2.35)$$

where $H_n(y)$ is the Hermite polynomial of order n. The definition of Hermite polynomials and some of their properties are shown in Appendix A. (2.35) is a third order polynomial in ω_k provided the longitudinal wavenumber k and the index n are specified. For each n, we have a definite meridional structure which is called mode n. Two of the roots of (2.35) correspond to inertia-gravity waves: one which propagates to the west ($\omega > 0$) and the other to the east ($\omega < 0$). The third root corresponds to a westward propagating Rossby wave ($\omega > 0$). Therefore, the eigenfrequencies of (2.32) are perfectly characterized by three indices k, n, and r where k is the zonal wavenumber, n is the meridional mode, and r is 0, 1 or 2, i.e.

$\omega_{k,n,0}$ → Rossby wave

$\omega_{k,n,1}$ → Westward propagating gravity wave

$\omega_{k,n,2}$ → Eastward propagating gravity wave.

An approximation for the three roots of (2.35) can be easily obtained using the following relationships

$$\omega_{k,n,0} + \omega_{k,n,1} + \omega_{k,n,2} = 0,$$

$$\omega_{k,n,0}\omega_{k,n,1} + \omega_{k,n,0}\omega_{k,n,2} + \omega_{k,n,1}\omega_{k,n,2} = -(k^2+2n+1),$$

$$\omega_{k,n,0}\omega_{k,n,1}\omega_{k,n,2} = -k,$$

and assuming that $\omega_{k,n,1} \approx -\omega_{k,n,2}$. The results are

$$\omega_{k,n,1(2)} = \pm \sqrt{k^2 + 2n + 1} \quad , \tag{2.36}$$

$$\omega_{k,n,o} = \frac{k}{k^2 + 2n + 1} \quad . \tag{2.37}$$

The plus sign in (2.36) gives the frequency of the westward propagating inertia-gravity wave and the negative sign corresponds to the eastward moving inertia-gravity wave. The third root given by (2.37) is the westward moving Rossby wave. Note that the frequency of the Rossby wave is zero if the wavenumber k is zero. For Rossby modes the zero frequency exhibits degeneracy since there is more than one eigenfunction corresponding to it as we will see later.

The three roots of (2.35) for $n = 0$ are

$$\omega_{k,o} = k \quad , \tag{2.38}$$

$$\omega_{k,o} = -\frac{k}{2} + \sqrt{\frac{k^2}{4} + 1} \quad , \tag{2.39}$$

$$\omega_{k,o} = -\frac{k}{2} - \sqrt{\frac{k^2}{4} + 1} \quad . \tag{2.40}$$

The classification of the roots is based on their behavior as a function of n assuming that n is a continuous parameter, i.e.

$$\omega_{k,0} = \lim_{n \to 0} \omega_{k,n} \quad . \tag{2.41}$$

Thus,

$$\omega_{k,0,0} = \begin{cases} k & \text{for } k < \frac{1}{\sqrt{2}} \\ \sqrt{(\frac{k}{2})^2 + 1} - \frac{k}{2} & \text{for } k \geq \frac{1}{\sqrt{2}} \end{cases} \tag{2.42}$$

$$\omega_{k,0,1} = \begin{cases} \sqrt{(\frac{k}{2})^2 + 1} - \frac{k}{2} & \text{for } k < \frac{1}{\sqrt{2}} \\ k & \text{for } k \geq \frac{1}{\sqrt{2}} \end{cases} \tag{2.43}$$

$$\omega_{k,0,2} = -\sqrt{(\frac{k}{2})^2 + 1} - \frac{k}{2} \quad \text{for all } k \tag{2.44}$$

where $\omega_{k,0,0}$ corresponds to the Rossby wave, $\omega_{k,0,1}$ to the westward propagating gravity wave and $\omega_{k,0,2}$ to the eastward propagating gravity wave. The peculiar behavior of the n = 0 mode led Matsuno to inspect more carefully the character of the associated eigenfunctions. He showed that the ϕ-eigenfunction associated with the root $\omega_{k,0} = k$ does not satisfy the boundary condition $\phi \to 0$ as $y \to \pm\infty$ and therefore has to be neglected. Blandford (1966), in a similar study, failed to recognize the peculiar behavior of the n = 0 mode and considered the $\omega = k$ solution as being valid.

In view of the peculiar behavior of the n = 0 mode, we see that $\omega_{k,0,0}$ does not exist for $k < 2^{-\frac{1}{2}}$ and $\omega_{k,0,1}$ does not exist for $k \geq 2^{-\frac{1}{2}}$ and that $\omega_{k,0,1}$ merges continuously to $\omega_{k,0,0}$ at $k = 2^{-\frac{1}{2}}$. Thus, for small k the westward moving solution of the n = 0 mode oscillates with higher frequency (in the gravity wave regime) while for large k the frequency is low (Rossby wave regime). This is the so-called mixed Rossby-gravity wave.

Matsuno (1966) also points out the existence of another possible solution not included in (2.35). Putting $v \equiv 0$ in the system of governing equations (2.30), we get

$$i\omega_k u_k + ik\phi_k = 0 \ , \tag{2.45.a}$$

$$yu_k + \frac{d\phi_k}{dy} = 0 \ , \tag{2.45.b}$$

$$i\omega_k \phi_k + iku_k = 0 \ . \tag{2.45.c}$$

The first and third equations form a system of two algebraic equations which has a non-trivial solution only if

$$(\omega_k - k)\ (\omega_k + k) = 0 \ ,$$

and therefore

$$u = -\phi \quad \text{if} \quad \omega_k = k$$

or

$$u = \phi \quad \text{if} \quad \omega_k = -k \ .$$

Equation (2.45) can now be written as

$$\frac{d\phi_k}{dy} \pm y\phi_k = 0$$

and the solutions are

$$\phi_k = u_k = a\, e^{-\frac{1}{2}y^2} \quad \text{for } \omega_k = -k \ , \tag{2.46}$$

$$\phi_k = -u_k = a\, e^{\frac{1}{2}y^2} \quad \text{for } \omega_k = k \ , \tag{2.47}$$

where a is an arbitrary constant. However, the solution corresponding to $\omega_k = k$ is not bounded as $y \to \pm\infty$ and it has to be rejected. Matsuno points out that the solution $\omega_k = -k$ can be obtained from the frequency equation (2.35) if we set $n = -1$. This particular solution is called the $n = -1$ mode and can be considered an eastward propagating wave with $v \equiv 0$, which is also called the Kelvin mode. The eigenfrequency as associated with the Kelvin wave is labelled $\omega_{k,-1,2}$ since it is an eastward propagating wave.

2.3.2 Eigenfunctions for $k \neq 0$

Multiplying (2.30.a) by $i\omega_k$ and (2.30.c) by $-ik$ and adding the results, we get

$$u_k = \frac{1}{i(\omega_k^2 - k^2)} \left(\omega_k y v_k + k \frac{dv_k}{dy}\right), \tag{2.48}$$

provided $\omega_k \neq \pm k$. If $\omega_k = -k$ the associated eigenfunction has already been found (2.46). Analogously,

$$\phi_k = -\frac{1}{i(\omega_k^2 - k^2)} \left(k y v_k + \omega_k \frac{dv_k}{dy}\right). \tag{2.49}$$

The next step is to substitute v_k into (2.48) and (2.49) by the already known solution given in terms of Hermite polynomials (2.34). The result is

$$u_k = \frac{1}{i(\omega_k^2 - k^2)} \left[\omega_k y H_n(y) - k y H_n(y) + k \frac{dH_n(y)}{dy}\right] e^{-\frac{1}{2}y^2} \tag{2.50}$$

and

$$\phi_k = -\frac{1}{i(\omega_k^2 - k^2)} \left[k y H_n(y) + \omega_k y H_n(y) + \omega_k \frac{dH_n(y)}{dy}\right] e^{-\frac{1}{2}y^2}. \tag{2.51}$$

Making use of the recurrence formula and the differentiation formula for Hermite polynomials, we obtain

$$u_k = \frac{1}{i(\omega_k^2 - k^2)} \left[\tfrac{1}{2}(\omega_k - k) H_{n+1}(y) + n(\omega_k + k) H_{n-1}(y) \right] e^{-\frac{1}{2}y^2}, \quad (2.52)$$

$$\phi_k = \frac{1}{i(\omega_k^2 - k^2)} \left[\tfrac{1}{2}(\omega_k - k) H_{n+1}(y) - n(\omega_k + k) H_{n-1}(y) \right] e^{-\frac{1}{2}y^2}. \quad (2.53)$$

In vector form, the eigensolution $\xi_{k,n,r}$ is

$$\xi_{k,n,r}(y) = \begin{bmatrix} \tfrac{1}{2}(\omega_{k,n,r} - k) H_{n+1}(y) + n(\omega_{k,n,r} + k) H_{n-1}(y) \\ i\,(\omega_{k,n,r}^2 - k^2) H_n(y) \\ \tfrac{1}{2}(\omega_{k,n,r} - k) H_{n+1}(y) - n(\omega_{k,n,r} + k) H_{n-1}(y) \end{bmatrix} e^{-\frac{1}{2}y^2}, \quad (2.54)$$

where the indices k and n refer, respectively, to a particular zonal wavenumber and meridional mode, and r = 0, 1 or 2 depending on whether we are considering the Rossby mode, westward or eastward propagating gravity wave, respectively.

The parity of the eigensolutions $\xi_{k,n,r}(y)$ follows from the parity of Hermite polynomials because $H_n(y)$ is even or odd if n is even or odd respectively. When n is odd the u and ϕ fields are symmetric relative to the equator and the v-field is antisymmetric. This case is called symmetric after Longuet-Higgins (1968). The v_k field is even if n is even and the associated u_k and ϕ_k fields are odd; this is called the antisymmetric mode.

Equation (2.54) is valid for n = 0 but the index r takes the value 1 and 2 if $k < 2^{-\frac{1}{2}}$ or 0 and 2 if $k \geq 2^{-\frac{1}{2}}$ as described earlier. The eigensolution associated with the Kelvin mode (n = -1) can be written as

$$\xi_{k,-1,2}(y) = \begin{bmatrix} H_o(y) \\ 0 \\ H_o(y) \end{bmatrix} e^{-\frac{1}{2}y^2} \tag{2.55}$$

since $H_o(y)$ is a constant according to A.3.

The magnitude of the eigenfunctions $\xi_{k,n,r}$ are arbitrary so far. In order to normalize the eigenfunctions, we require that the total energy integrated over the y-domain $(-\infty, +\infty)$ is invariant for each mode corresponding to each eigenfrequency. The integrated total energy $E_{k,n,r}$ is easily obtained by the kinetic energy equation (multiplying (2.30.a) and (2.30.b) by u_k and v_k, respectively), adding the result to the available potential energy equation (multiplying (2.30.c) by ϕ) and integrating over the whole domain $(-\infty, +\infty)$ using the boundary conditions (2.29). The result is

$$E_{k,n,r} = \| \xi_{k,n,r}(y) \|^2 = \langle \xi_{k,n,r}(y) \cdot \xi_{k,n,r}(y) \rangle , \tag{2.56}$$

where the symbol $\langle\ \rangle$ indicates the inner product

$$\langle \xi_{k,n,r} \cdot \xi_{k,n,r} \rangle = \int_{-\infty}^{+\infty} (u_{k,n,r} \cdot u^*_{k,n,r} + v_{k,n,r} \cdot v^*_{k,n,r} + \phi_{k,n,r} \cdot \phi^*_{k,n,r})\, dy . \tag{2.57}$$

In (2.57) the symbol (*) denotes the complex conjugate. Thus, the magnitude of the normalized eigenvectors can be easily obtained by dividing the previously obtained $\xi_{k,n,r}$ by its norm defined by (2.56). The norm of $\xi_{k,n,r}$ is

$$E_{k,n,r} = 2^n n!\, \pi^{\frac{1}{2}} \left[(\omega_{k,n,r}-k)^2 (n+1) + n\, (\omega_{k,n,r}+k)^2 + (\omega_{k,n,r}^2 - k^2)^2 \right] . \tag{2.58}$$

From now on, when we refer to the eigenfunction $\xi_{k,n,r}$ we should interpret it as the normalized eigenfunction

$$\xi_{k,n,r}(y) = \begin{bmatrix} \frac{1}{2}(\omega_{k,n,r}-k)\, H_n(y) + n\, (\omega_{k,n,r}+k)\, H_{n-1}(y) \\ i\, (\omega_{k,n,r}^2 - k^2)\, H_n(y) \\ \frac{1}{2}(\omega_{k,n,r}-k)\, H_n(y) - n\, (\omega_{k,n,r}+k)\, H_{n-1}(y) \end{bmatrix} \frac{e^{-\frac{1}{2}y^2}}{\sqrt{E_{k,n,r}}} . \tag{2.59}$$

2.3.3 Eigenfunction of the zonally symmetric case ($k = 0$)

As we have already discussed, the zonally symmetric case ($k = 0$) presents a degenerate behavior since the eigenfrequencies of the Rossby mode are all zero. Also, the distinction of eastward and westward moving waves looses meaning when $k = 0$; the eigenfrequencies of gravity modes appear in pairs of positive and negative values for the same meridional number n.

The objective of this section is to construct a set of orthonormal eigenvectors associated with the zonally symmetric degenerate mode. Remembering that $\omega = 0$ when $k = 0$ for the Rossby mode, (2.30) is reduced to

$$y u_o + \frac{d\phi_o}{dy} = 0 , \tag{2.60.a}$$

$$v_o \equiv 0 , \tag{2.60.b}$$

which is the governing equation for a zonal geostrophic current. The Rossby mode for $k = 0$ is called the geostrophic mode after Kasahara (1978) since the same governing equation is obtained with spherical

geometry except for the curvature terms in (2.60.a). Kasahara's approach for constructing the normal modes of (2.60) is to assume polynomial functions of various degrees for u_0 and calculate ϕ_0 or vice versa. The geostrophic modes so obtained are not orthogonal but a simple vector orthogonalization routine based on the Gram-Schmidt process can be applied. Tribbia (1978) retained the normal mode expansion for the zonally symmetric case considering that any geostrophic u and ϕ are eigenfunctions of (2.60). The resulting eigenvectors can also be orthogonalized.

Although Kasahara's or Tribbia's approach could be applied to our problem, a close look at the normalized eigenfunctions defined by (2.59) suggests an alternative procedure.

The eigenfunctions $\xi_{k,n,r}(y)$ form a complete and orthonormal set if $k \neq 0$ (Matsuno, 1966; Cane and Sarachik, 1976). The orthogonality proof however, fails if degeneracy occurs. This is exactly the case for Rossby modes if $k = 0$. But we might speculate on the nature of the eigenfunctions $\xi_{k,n,0}(y)$ as k tends to zero. First, we shall prove that such a limit exists and then that it satisfies the governing equations for zonal geostrophic current. Secondly, we consider the orthogonality and completeness of the limiting set of eigenfunctions.

The frequencies of Rossby type waves have the following asymptotic behavior for small zonal wavenumber k,

$$\omega_{k,n,0} = \frac{k}{2n + 1} \quad . \tag{2.61}$$

In order to obtain (2.61) we use the fact that inertia-gravity waves for $k = 0$ have frequency

$$\omega_{0,n,1(2)} = \pm \sqrt{(2n+1}} \tag{2.62}$$

and the relation

$$\omega_{k,n,0} \ \omega_{k,n,1} \ \omega_{k,n,2} = k \ . \tag{2.63}$$

The normalized zonal wind component of the eigensolutions $\xi_{k,n,0}(y)$ is

$$u_{k,n,0} = \frac{\left[\tfrac{1}{2}(\omega_{k,n,0}-k)\ H_{n+1}(y) + n\ (\omega_{k,n,0}+k)\ H_{n-1}(y)\right] e^{-\frac{1}{2}y^2}}{(2^n n!\pi^{\frac{1}{2}})^{\frac{1}{2}} \left[(\omega_{k,n,0}-k)^2 (n+1) + n\ (\omega_{k,n,0}+k)^2 + (\omega_{k,n,0}{}^2 - k^2)^2\right]^{\frac{1}{2}}} . \tag{2.64}$$

Let us consider now the asymptotic behavior of $u_{k,n,0}$ as $k \to 0$. Substituting $\omega_{k,n,0}$ from (2.61) in (2.64), taking the limit as $k \to 0$ and applying L'Hopital's rule we find that

$$\lim_{k \to 0} u_{k,n,0}(y) = \frac{[n(n+1)]^{\frac{1}{2}} \left[2(n+1)\ H_{n+1}(y) - H_{n-1}(y)\right] e^{-\frac{1}{2}y^2}}{\left[2^n (2n+1)\ n!\ \pi^{\frac{1}{2}}\right]^{\frac{1}{2}}} . \tag{2.65.a}$$

Analogously, we obtain

$$\lim_{k \to 0} v_{k,n,0}(y) = 0 \ , \tag{2.65.b}$$

and

$$\lim_{k \to 0} \phi_{k,n,0}(y) = \frac{[n(n+1)]^{\frac{1}{2}} \left[2(n+1)\ H_{n+1}(y) + H_{n-1}(y)\right] e^{-\frac{1}{2}y^2}}{\left[2^n (2n+1)\ n!\ \pi^{\frac{1}{2}}\right]^{\frac{1}{2}}} . \tag{2.65.c}$$

Thus, as $k \to 0$ the eigenfunction associated with the n'th meridional mode of the Rossby wave tends to a function which is a combination of Hermite functions of order (n-1) and (n+1). It is an easy task to

prove that (2.65) satisfy the zonal geostrophic equation (2.60) if we use the recurrence relation (A.4) and the differentiation formula for Hermite polynomials (A.5). The orthonormality is also easily proved using (A.1). The completeness follows from the completeness of Hermite functions. We can now write

$$\xi_{0,n,0}(y) = \begin{bmatrix} \lim\limits_{k\to 0} u_{k,n,0}(y) \\ \lim\limits_{k\to 0} v_{k,n,0}(y) \\ \lim\limits_{k\to 0} \phi_{k,n,0}(y) \end{bmatrix} =$$

$$\begin{bmatrix} \dfrac{[n(n+1)]^{\frac{1}{2}} \left[2(n+1)\, H_{n+1}(y) + H_{n-1}(y)\right]}{\left[2^n (2n+1)\, n!\, \pi^{\frac{1}{2}}\right]^{\frac{1}{2}}} \\ 0 \\ \dfrac{[n(n+1)]^{\frac{1}{2}} \left[2(n+1)\, H_{n+1}(y) - H_{n-1}(y)\right]}{\left[2^n (2n+1)\, n!\, \pi^{\frac{1}{2}}\right]^{\frac{1}{2}}} \end{bmatrix} e^{-\frac{1}{2} y^2}, \qquad (2.66)$$

and $\xi_{k,n,r}(y)$ form an orthonormal and complete set of eigenfunctions over the whole range of k.

The completeness of the eigenfunctions $\xi_{k,n,r}(y)$ in the interval $(-\infty, +\infty)$ and the completeness of e^{ikx} in the interval $(-L_x, L_x)$ with k given by (2.28) allows to expand an arbitrary function G(x,y) in the series

$$G(x,y) = \sum_{k=-\infty}^{+\infty} \sum_{n=-1}^{\infty} \sum_{r=0}^{2} a_{k,n,r}\, \xi_{k,n,r}(y)\, e^{ikx} \qquad (2.67)$$

with

$$a_{k,n,r} = \langle G_k(y) \cdot \xi_{k,n,r}(y) \rangle \ , \tag{2.68}$$

where

$$G_k(y) = \frac{1}{2L} \int_{-L}^{L} G(x,y)\, e^{-ikx}\, dx \ . \tag{2.69}$$

The dimensional form of the eigenfunction $\xi_{k,n,r}(y)$ is clearly seen to be dependent on c_j and therefore it can be written as

$$\xi_{j,k,n,r}(y) = \begin{bmatrix} c_j & 0 & 0 \\ 0 & c_j & 0 \\ 0 & 0 & c_j^2 \end{bmatrix} \hat{\xi}_{k,n,r}\left([L]\hat{y}\right) \ , \tag{2.70}$$

where the symbol (^) has been replaced over the non-dimensional variables.

2.4 Initial Value Problem - Equatorial β-plane

Let us consider now the solution of system (2.1) with a specified distribution of diabatic heating $\dot{Q}$ and momentum forcing (F_x, F_y). More precisely, we propose to solve

$$\frac{\partial u}{\partial t} - \beta y v + \frac{\partial \phi}{\partial x} = -\kappa u + F_x \ , \tag{2.71.a}$$

$$\frac{\partial v}{\partial t} + \beta y v + \frac{\partial \phi}{\partial y} = -\kappa u + F_y \ , \tag{2.71.b}$$

$$\frac{\partial}{\partial t}\left[-\frac{\partial}{\partial p}\left(\frac{1}{\bar{\sigma}}\frac{\partial \phi}{\partial p}\right)\right] + \nabla \cdot \mathbf{W} = \frac{1}{cp}\frac{\partial}{\partial p}\left(\frac{\dot{Q}}{\bar{\sigma}}\right) - \kappa \frac{\partial}{\partial p}\left(-\frac{1}{\bar{\sigma}}\frac{\partial \phi}{\partial p}\right), \tag{2.71.c}$$

where κ is a Rayleigh drag coefficient in (2.71.a) and (2.71.b), and the rate coefficient for Newtonian cooling in (2.71.c). These linear terms are not necessary for the method of solution here described

but they correspond to the simplest form of restoring forces that might arise as the system is disturbed from rest.

We will make use of the completeness of the eigensolutions of the vertical structure equation (2.3) and the eigensolutions of the linearized shallow water equations to solve (2.4). We first expand $u(x,y,p,t)$, $v(x,y,p,t)$, $\phi(x,y,p,t)$ and the term on the right hand side of (2.71.c) into a series of the eigensolutions $\phi_j(p)$ of the vertical structure equation as in (2.18) obtaining

$$u \approx \sum_{j=0}^{J} u_j(x,y,t)\,\phi_j(p)\,, \qquad v \approx \sum_{j=0}^{J} v_j(x,y,t)\,\phi_j(p)\,,$$

$$\phi \approx \sum_{j=0}^{J} \Phi_j(x,y,t)\,\phi_j(p)\,, \qquad \frac{\partial}{\partial p}\left(\frac{\dot{Q}}{\sigma}\right) \approx \sum_{j=0}^{J} q_j(x,y,t)\,\phi_j(p)\,,$$

$$F_x \approx \sum_{j=0}^{J} F_{x,j}(x,y,t)\,\phi_j(p)\,, \qquad F_y \approx \sum_{j=0}^{J} F_{y,j}(x,y,t)\,\phi_j(p)\,, \tag{2.72}$$

where u_j, v_j, Φ_j, q_j, $F_{x,j}$ and $F_{y,j}$ are the expansion coefficients, generally functions of x,y and t defined by (2.19) and J is the truncation limit of the vertical modes. In order to write (2.72) we have assumed that the eigenvalues of the vertical structure equation form a discrete set. However, if the spectrum of the vertical structure equation is continuous as in an unbounded atmosphere (Eckart, 1960), the sum in (2.72) is replaced by an integral. If the spectrum is part discrete and part continuous, (2.72) should be rewritten as combination of sum and integral respectively.

The series expansion (2.72) is assured by the completeness of ϕ_j as discussed in section 2.2. Substituting (2.72) into (2.71), multiplying (2.71.a), (2.71.b) and (2.71.c) by $\phi_i(p)$, integrating over the interval $[o,p_o]$ and using the orthogonality of $\phi_j(p)$ we obtain

$$\frac{\partial u_j}{\partial t} - \beta_y v_j + \frac{\partial \Phi_j}{\partial x} = -\kappa u_j + F_{x,j} , \qquad (2.73.a)$$

$$\frac{\partial v_j}{\partial t} - \beta_y u_j + \frac{\partial \Phi_j}{\partial y} = -\kappa v_j + F_{y,j} , \qquad (2.73.b)$$

$$\frac{\partial \Phi_j}{\partial t} + c_j^2 \nabla \cdot \mathbb{V}_j = c_j^2 (q_j - \kappa \Phi_j) , \qquad (2.73.c)$$

where (2.3) has also been applied.

We now see that after projecting the solution (u,v,ϕ) onto the vertical modes, we get a system of equations for the expansion coefficients which is simply the linearized shallow water equations discussed in section 2.3 with non-homogeneous terms in representing the external forcing and the linear damping terms.

It is convenient to work with the non-dimensional form of (2.73) using the time and length scales shown in section 2.3 and write it in vector form as

$$\frac{\partial \xi}{\partial t} + \Omega \xi = \mathbb{F}_j - \kappa_j \xi , \qquad (2.74)$$

where ξ and Ω are defined by (2.25) and (2.26), respectively, and

$$\mathbb{F}_j = \begin{bmatrix} F_{x,j} \\ F_{y,j} \\ q_j \end{bmatrix} (c_j^5 \beta)^{-\frac{1}{2}} , \qquad (2.75)$$

$$\kappa_j = (c_j^5 \beta)^{-\frac{1}{2}} \kappa \quad . \tag{2.76}$$

In the two-level baroclinic model discussed in section 2.1, the inclusion of linear damping terms and a specified external forcing yields the vector equation (2.75) with

$$\mathrm{IF}_j(x,y,t) = \begin{bmatrix} F_x \\ F_y \\ \dot{R(Q)}_2 \end{bmatrix} (c^5 \beta)^{-\frac{1}{2}} \quad . \tag{2.77}$$

The main concern of this research is the solution of (2.71) for a specified equivalent depth; we thus drop the index 'j' on the right hand side of (2.74) for simplicity. It should be remembered that the solution of (2.74) can either be interpreted as one particular internal mode or as the wind shear and thickness of the two-level baroclinic model of section 2.1.

We can clearly assume that the solution $\xi(x,y,t)$ and the forcing $\mathrm{IF}_j(x,y,t)$ can be represented by a series of the eigenfunctions $\xi_{k,n,r}(y)\, e^{ikx}$ as discussed at the end of section 2.3. According to (2.67) we have

$$\xi(x,y,t) \approx \sum_{k=-K}^{K} \sum_{n=-1}^{N} \sum_{r=0}^{2} c_{k,n,r}(t)\, \xi_{k,n,r}(y)\, e^{ikx} \tag{2.78}$$

and

$$\mathrm{IF}(x,y,t) \approx \sum_{k=-K}^{K} \sum_{n=-1}^{N} \sum_{r=0}^{2} f_{k,n,r}(t)\, \xi_{k,n,r}(y)\, e^{ikx} , \tag{2.79}$$

where K and N are the truncation limits of the Fourier series in the zonal direction and of meridional modes, respectively. Substituting (2.78) and (2.79) into (2.74), multiplying the result by $\xi^*_{k,\ell,m}(y)$, integrating over the whole domain S ($S = \{(x,y) / x\varepsilon[-L,L],\ y\varepsilon(-\infty,+\infty)\}$) and applying the boundary condition (2.29) we obtain

$$\frac{d}{dt}\, c_{k,n,r}(t) - (i\omega_{k,n,r} - \kappa)\, c_{k,n,r}(t) = f_{k,n,r}(t) \qquad (2.80)$$

for each k, n and r in (2.78). The above equation is familiar from the theory of the linear harmonic oscillator problem. The general solution of (2.80) is

$$c_{k,n,r}(t) = c_{k,n,r,}(0)\, \exp\,[(i\omega_{k,n,r} - \kappa)\, t\,] + \int_0^t f_{k,n,r}(s)$$

$$\exp\,[-(i\omega_{k,n,r} - \kappa)\,(s-t)]\, ds\ . \qquad (2.81)$$

This is the solution presented by Cane and Sarachik (1976) except for the damping term κ.

Let us consider now some particular solutions of (2.81). If there is no external forcing and there are no damping terms in (2.74) the solution of (2.80) reduces to

$$c_{k,n,r}(t) = c_{k,n,r}(0)\, \exp\,(i\omega_{k,n,r}\, t)\ , \qquad (2.82)$$

where $c_{k,n,r}(0)$ is determined from the initial conditions $\xi(x,y,0)$ as

$$c_{k,n,r}(0) = \langle \xi_k(y,0) \cdot \xi_{k,n,r}(y) \rangle\ , \qquad (2.83)$$

where

$$\xi_k(y,0) = \frac{1}{2L_x} \int_{-L_x}^{L_x} \xi(x,y,0)\, e^{-ikx}\, dx\ . \qquad (2.84)$$

Thus, the solution of (2.74) reduces to a superposition of the free wave solutions, each oscillating at its own frequency.

If the initial condition is $\xi(x,y,0) \equiv 0$ and the forcing is at a single frequency ν such that

$$IF(x,y,t) = IF(x,y)\, e^{-i\nu t} \quad , \tag{2.85}$$

the solution of (2.80) is simplified to

$$c_{k,n,r}(t) = \frac{f_{k,n,r}}{[i(\omega_{k,n,r}-\nu)-\kappa]} \left[e^{-i\nu t} - e^{-(i\omega_{k,n,r}+\kappa)t}\right], \tag{2.86}$$

where

$$f_{k,n,r} = \langle IF_k(y) \cdot \xi_{k,n,r}(y)\rangle, \tag{2.87}$$

and

$$IF_k(y) = \frac{1}{2L_x} \int_{-L_x}^{L_x} IF(x,y)\ e^{-ikx}\, dx \ , \tag{2.88}$$

is the Fourier component of the forcing IF at wavenumber k. The second term within brackets in the numerator of (2.86) is the transient solution; if $\kappa > 0$ the asymptotic behavior of (2.86) is

$$c_{k,n,r}(t) = \frac{f_{k,n,r}\ e^{-i\nu t}}{i(\omega_{k,n,r} - \nu) - \kappa} \quad , \tag{2.89}$$

for a steady forcing we have

$$c_{k,n,r} = \frac{f_{k,n,r}}{i\omega_{k,n,r} - \kappa} \quad . \tag{2.90}$$

If there is no damping, (2.90) is singular for geostrophic modes. However, for a steady forcing we have

$$c_{0,n,0}(t) = \lim_{\omega_{k,n,0} \to 0} \frac{t_{k,n,0}(1 - e^{-i\omega_{k,n,0}t})}{i\omega_{k,n,0}} = t f_{0,n,0} . \qquad (2.91)$$

Thus, at resonance we have the algebraic or secular growth represented by (2.91). We clearly see that the closer the frequency of the forcing is to the natural frequencies of the system, the larger is the response.

Our main concern in this research is the horizontal structure of the solution of (2.71) for particular values of j. The equatorial β-plane is known to be a good approximation for the internal modes of small equivalent depth (Lindzen, 1967). For the external mode (or large equivalent depth H) the meridional structure of the eigensolutions $\xi_{k,n,\ell}(y)$ is not trapped near the Equator except for low n and therefore a more accurate geometry and Coriolis term in (2.71) is necessary. In the next section, we show that the solution on the sphere is formally the same as on the equatorial β-plane except that the eigensolutions of the horizontal structure equation are now given by Hough functions (Longuet-Higgins, 1968).

2.5 Initial value problem-sphere

The perturbation equations on the sphere using the same basic state as in (2.1) are

$$\frac{\partial u}{\partial t} - fv + \frac{\partial \phi}{a \cos\varphi \, \partial \lambda} = 0 , \qquad (2.92.a)$$

$$\frac{\partial v}{\partial t} + fu + \frac{\partial \phi}{a \, \partial \varphi} = 0 , \qquad (2.92.b)$$

$$\nabla \cdot \mathbf{V} + \frac{\partial \omega}{\partial p} = 0 , \qquad (2.92.c)$$

$$\frac{\partial}{\partial t}\left(-\frac{\partial \phi}{\partial p}\right) - \bar{\sigma}\omega = 0 , \qquad (2.92.d)$$

where the notation is the same as in (2.1) except that λ is the longitude, φ is the latitude, a is the radius of the earth, f is $2\Omega \sin\varphi$ and

$$\nabla \cdot \mathbf{V} = \frac{1}{a \cos\varphi}\left(\frac{\partial u}{\partial \lambda} + \frac{\partial v \cos\varphi}{\partial \varphi}\right). \qquad (2.93)$$

Combining (2.92.c) with (2.92.d) we obtain (2.2) except that the divergence is now defined by (2.93). The condition for separability into horizontal and vertical structure equations is seen to be the same as before and therefore the vertical structure equation is given by (2.3) where $c_j^2 = gH_j$ is the separation constant. The horizontal structure is now given by the linearized shallow water equations over a sphere i.e.,

$$\frac{\partial u_j}{\partial t} - 2\Omega \sin\varphi\, v_j + \frac{1}{a \cos\varphi}\frac{\partial \phi_j}{\partial \lambda} \qquad (2.94.a)$$

$$\frac{\partial v_j}{\partial t} - 2\Omega \sin\varphi\, u_j + \frac{\partial \phi_j}{a\,\partial \varphi} = 0 , \qquad (2.94.b)$$

$$\frac{\partial \phi_j}{\partial t} + gH_j \nabla \cdot \mathbf{V}_j = 0 , \qquad (2.94.c)$$

where $\nabla \cdot V_j$ is given by (2.93). We can scale (2.94) by

$$\hat{u}_j = u_j c_j^{-1} , \qquad \hat{v}_j = v_j c_j^{-1} ,$$

$$\hat{\phi}_j = \phi_j c_j^{-2} , \qquad \hat{t} = t\,2\Omega , \qquad (2.96)$$

where $c_j = \sqrt{gH_j}$ is the j-th eigenvalue of the vertical structure equation (2.3) and H_j is the equivalent depth. As in the equatorial

β-plane case, we write (2.94) in vector form as

$$\frac{\partial x_j}{\partial t}(\lambda,\varphi,t) + \Omega_j\, x_j(\lambda,\varphi,t) = 0 \,, \tag{2.96}$$

where the symbol (^) has been dropped for simplicity. In (2.96) we have

$$x_j(\lambda,\varphi,t) = \begin{bmatrix} u_j(\lambda,\varphi,t) \\ v_j(\lambda,\varphi,t) \\ \phi_j(\lambda,\varphi,t) \end{bmatrix} \tag{2.97}$$

and

$$\Omega_j = \begin{bmatrix} 0 & \sin\varphi & \dfrac{\varepsilon_j^{-\frac{1}{2}}}{\cos\varphi}\dfrac{\partial}{\partial\lambda} \\ \sin\varphi & 0 & \varepsilon_j^{-\frac{1}{2}}\dfrac{\partial}{\partial\varphi} \\ \dfrac{\varepsilon_j^{-\frac{1}{2}}}{\cos\varphi}\dfrac{\partial}{\partial\lambda} & \dfrac{\varepsilon_j^{-\frac{1}{2}}}{\cos\varphi}\dfrac{\partial}{\partial\varphi}[(\,)\cos\varphi] & 0 \end{bmatrix} \tag{2.98}$$

with

$$\varepsilon_j = \frac{4\Omega^2 a^2}{c_j^2} \,. \tag{2.99}$$

Equation (2.96) is usually termed Laplace's tidal equations and the solutions have been discussed in great detail by Longuet-Higgins (1968) and more recently by Kasahara (1976). The solution x_j of (2.96) dropping the subscript j, is expressed by

$$x(\lambda,\varphi,t) = H_{s,\ell}(\lambda,\varphi)\exp(i\,\sigma_{s,\ell}\,t) \,, \tag{2.100}$$

where $H_{s,\ell}(\lambda,\varphi)$ represents the horizontal structure of normal modes with s denoting the wavenumber in the zonal direction ($s = 0,1,2,\ldots$),

ℓ the meridional index and $\sigma_{s,\ell}$ the dimensionless frequency of the normal modes. The longitudinal dependence of $H_{s,\ell}(\lambda,\varphi)$ is given by

$$H_{s,\ell}(\lambda,\varphi) = \Theta_{s,\ell}(\varphi) \exp(i s \lambda), \tag{2.101}$$

where $\Theta_{s,\ell}$ is called the Hough vector that has three components, namely

$$\Theta_{s,\ell}(\varphi) = \begin{bmatrix} u_{s,\ell}(\varphi) \\ v_{s,\ell}(\varphi) \\ \phi_{s,\ell}(\varphi) \end{bmatrix} . \tag{2.102}$$

The eigenfrequencies $\sigma_{s,\ell}$ are divided in two different categories: eastward and westward gravity waves and westward propagating Rossby waves, the so-called waves of the first kind and waves of the second kind, respectively.

Clearly the analogy between the shallow water equations on the equatorial β-plane and on the sphere is perfect. Thus, the method of solution shown in section 2.4 for the initial value problem can be easily extended to the sphere provided we notice the following correspondence

$$s \leftrightarrow k$$
$$\ell \leftrightarrow n$$
$$\sigma \leftrightarrow \omega$$
$$\Theta \leftrightarrow \xi \quad .$$

One important difference between the linear operator Ω_j on the sphere and Ω_j on the equatorial β-plane is the inclusion of Lamb's parameter ε_j on the sphere. On the equatorial β-plane the non-dimensional form of the shallow water equation does not depend on c_j explicitly, and

therefore the dimensional form of ξ is simply obtained by a matrix multiplication as in (2.70). On the sphere, however, we have to solve for $\sigma_{s,\ell}$ and $\Theta_{s,\ell}$ for each vertical mode j and then make a matrix multiplication analogous to (2.70) to obtain the dimensional form since ε_j appears in the linear differential operator Ω_j (2.98). It should be remarked that the fortuitous happening on the equatorial β-plane is a consequence of the boundary condition at infinity; had we chosen a finite β-plane the determination of the eigenfunction and eigensolutions would be dependent on the particular vertical mode through the horizontal scaling.

Thus, the computer program to solve (2.74) can be easily organized in such a way to accept different sets of eigenvalues and eigenfunctions with minor modifications. Provided the eigenvalues and eigenfunctions of the shallow water equations are given, the only part of the program that depends on the particular version being used is the integration routine in the meridional direction to compute the inner product. On the infinite equatorial β-plane the integral in y is from $-\infty$ to $+\infty$ and an appropriate weighting function (e^{-y^2}) in the Gauss-Hermite quadrature method can be used (Abramowitz and Stegun, 1970). Thus, the non-dimensional eigenfunctions $\xi_{k,n}(y)$ are computed at the Gaussian latitudes given by the zeroes of Hermite polynomials. Because of the Gaussian quadrature points are unevenly spaced, it is convenient to recompute the eigenfunctions $\xi_{k,n,r}(y)$ at equally spaced latitudes after the expansion coefficients $c_{k,n,r}$ are determined. On the sphere, we use the regular Gaussian quadrature with the abcissas and weights given by Abramowitz and Stegun (1970). In this case, the Gaussian

latitudes are almost equally spaced and therefore there is no need to recompute the Hough functions at equally spaced latitudes for display purposes.

3.0 FREE WAVE SOLUTIONS OF THE SHALLOW WATER EQUATIONS

The objective of this chapter is to present the horizontal structure and dispersive characteristics for the free wave solutions of the shallow water equations. This is important because the method of solution of the initial value problem is based on the method of eigenfunction expansion, and the basis functions are the free waves of the shallow water equations. Knowing the structure and dispersive characteristics of the basis functions helps us in understanding the behavior of the solution in space and time.

The eigenfrequencies are discussed in section 3.1 and the process of dispersion of energy is treated in section 3.2. Section 3.3 deals with the eigenfunctions and the energetics of the free modes. We also compare some of the results obtained on the equatorial β-plane with the sphere for $\varepsilon = 10$ and $\varepsilon = 500$. The $\varepsilon = 10$ case closely corresponds to the external mode (also called the divergent barotropic mode) of an isothermal atmosphere and the $\varepsilon = 500$ corresponds to the equivalent depth of the first internal mode of the two-level baroclinic model discussed in section 2.1.

Lindzen (1967) has discussed the validity of the equatorial β-plane with emphasis on planetary scale waves. For ε sufficiently large and n sufficiently small the equatorial β-plane provides us with a good approximation for the eigenfrequencies of free waves on the sphere. This statement is based on the behavior of the governing equation for the meridional velocity (2.32) as a function of y; if $y < y_T$, where

$$y_T = \sqrt{\omega_k^2 - k + \frac{k}{\omega_k}} = \sqrt{2n+1}\ , \qquad (3.1)$$

the coefficient of v_k in (2.32) is positive and the solution is wave-like. If $y > y_T$ the solution of (2.32) is exponentially damping in order to satisfy the boundary condition. In dimensional form (3.1) can be written as

$$y_T = a\,\varepsilon^{-1/4}\sqrt{2n+1}\ , \qquad (3.2)$$

since the length scale [L] (2.21) can be written as

$$[L] = a\,\varepsilon^{-1/4}\ , \qquad (3.3)$$

where a is the radius of the earth and ε is Lamb's parameter defined by (2.99).

When the turning latitude y_T is such that $y_T < y_p$ (where y_p is the latitude of the pole) we expect (2.32) to be a reasonable approximation. Figure 3.1 shows y_T as a function of ε and it is clear that for $\varepsilon = 10$ (external mode) the equatorial β-plane gives valid approximations only for $n \leq 2$. For an internal mode of equivalent depth H = 180 m, we have $\varepsilon = 500$ and the condition $y_T < y_p$ is satisfied up to n = 25. In this chapter we shall also discuss the relative error of the β-plane for $\varepsilon = 10$ and $\varepsilon = 500$ in view of the condition $y_T < y_p$.

3.1 Eigenfrequencies - equatorial β-plane and sphere

Figure 3.2 taken from Matsuno (1966) shows the eigenfrequencies of the free wave solutions of the shallow water equations on the equatorial β-plane as a function of the wavenumber k. The mixed Rossby gravity wave links the low frequency Rossby regime to the higher frequency westward propagating gravity waves. The difference

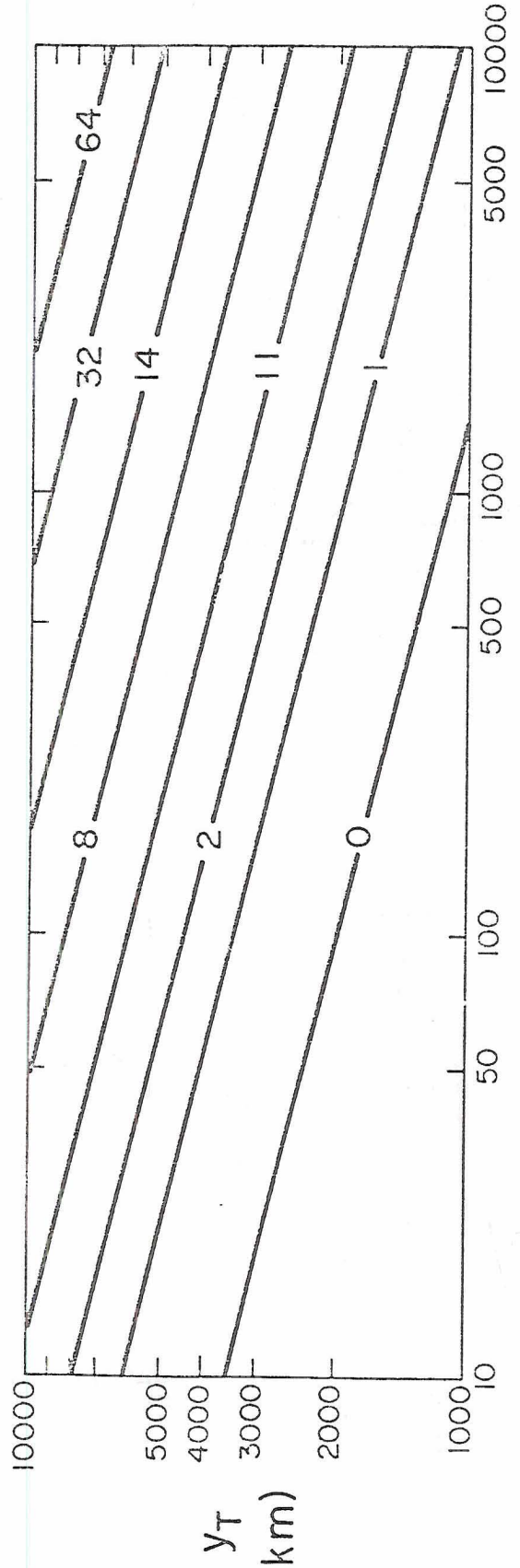

Figure 3.1 Turning latitude y_T in kilometers as a function of Lamb's parameter ϵ for various meridional modes n as labeled.

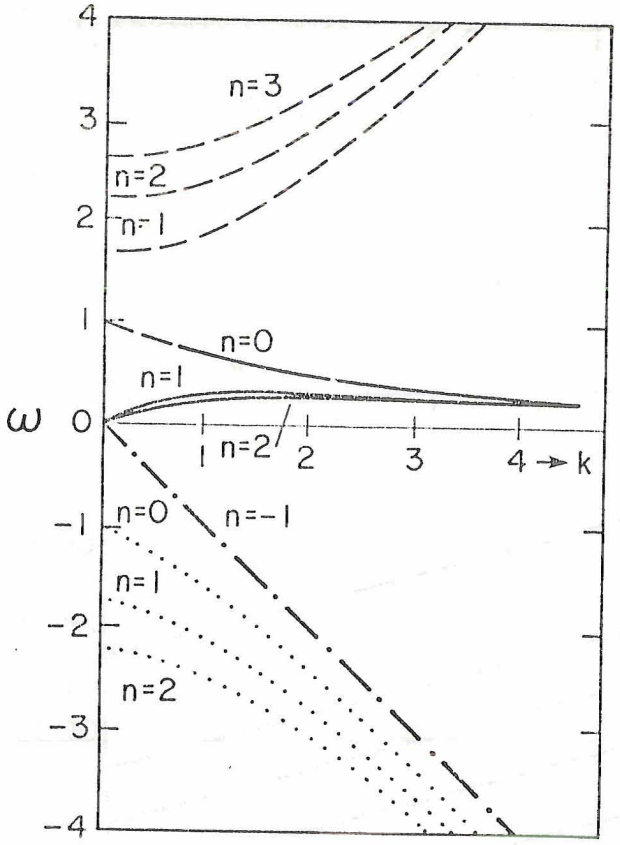

Figure 3.2 Frequencies as a function of wavenumber k for different meridional modes n as labeled. Dashed line: westward gravity wave. Solid line: Rossby wave. Dotted line: eastward gravity wave. Dash-dotted line: Kelvin wave. (From Matsuno, 1966.)

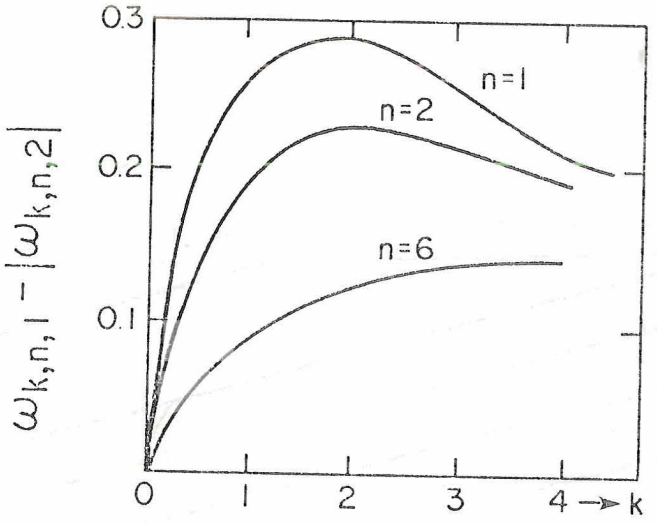

Figure 3.3 Difference between the absolute value of the frequency of the westward and eastward gravity waves as a function of wavenumber k and n as labeled.

between the modulus of the frequency of eastward and westward propagating gravity waves is shown in Figure 3.3. The frequency of the westward propagating wave is larger than that of the eastward wave. The maximum difference occurs for the low order meridional modes between the non-dimensional zonal wavenumbers 2 and 3. The maximum difference is approximately 15% for the $n = 1$ meridional mode and consequently the phase speed of the westward propagating gravity wave is about 15% faster than the companion eastward wave. The effect of the rotation of the earth on gravity waves decreases as the wavelength decreases and therefore the eastward and westward waves tend to the same frequency in absolute value.

The effect of spherical geometry on the frequency of free waves of the divergent barotropic model is shown in Figures 3.4 and 3.5 for $\varepsilon = 10$ and $\varepsilon = 500$, respectively. The ordinate of Figures 3.4 and 3.5 is the percent error of the β-plane eigenfrequency relative to the sphere eigenfrequency and the abcissa is the wavenumber s on the sphere ($s = 0, 1, 2, \ldots$). In order to compare the eigenfrequencies on the sphere to those obtained on the equatorial β-plane, we have two problems: (a) the relationship between the non-dimensional wavenumber k on which the β-plane eigenfrequencies are dependent (Figure 3.2) and the wavenumbers allowed on the sphere, and (b) the equivalence between the meridional indices n (on the equatorial β-plane) and ℓ (on the sphere) as defined in Chapter 2.

The non-dimensional wavenumber k in the β-plane analysis is related to the wavenumber s on the sphere by

$$k = \varepsilon^{-\frac{1}{4}} s \qquad s = 0, 1, 2, \ldots \quad . \tag{3.4}$$

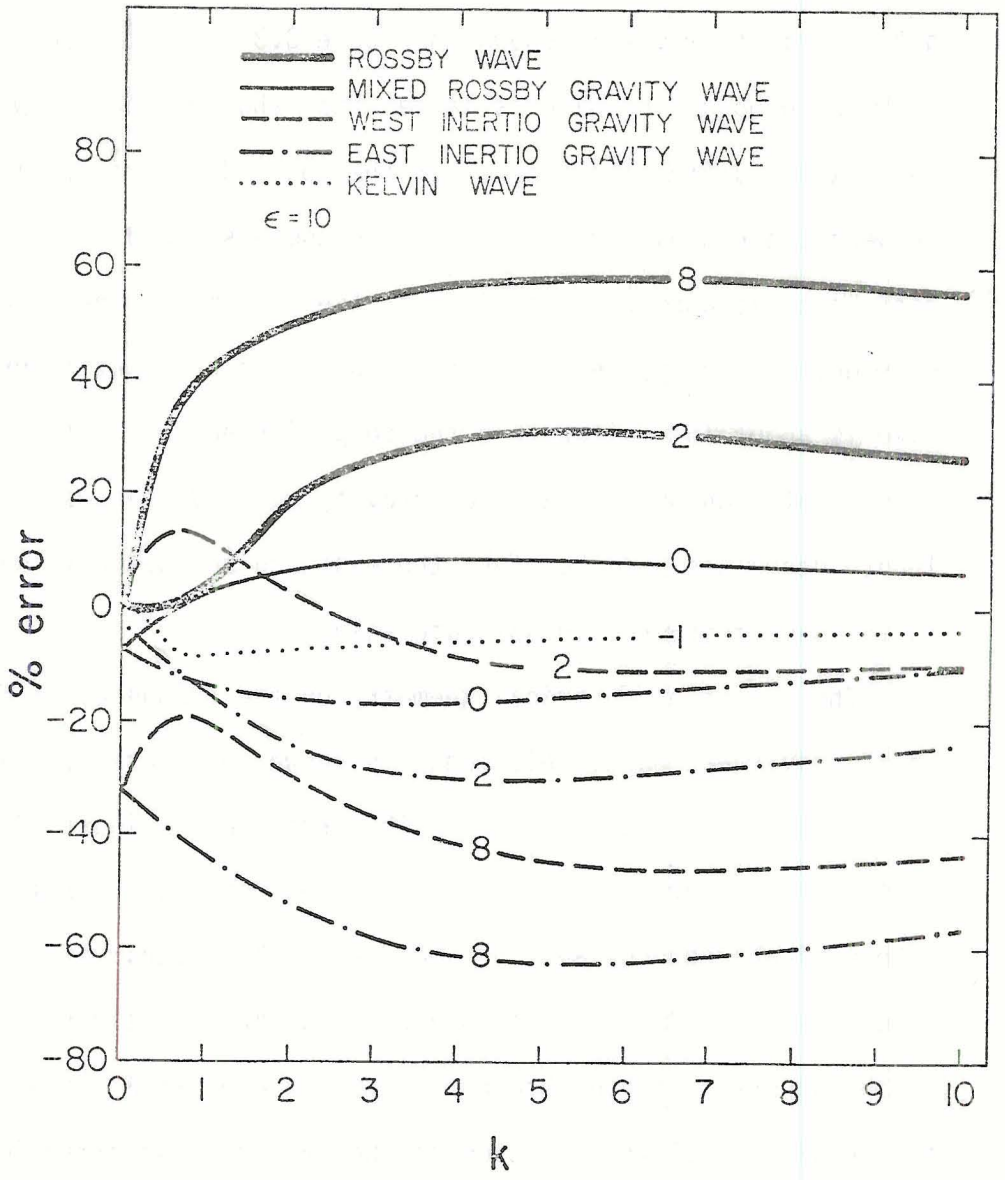

Figure 3.4 Percent error of the equatorial β-plane eigenfrequency relative to the corresponding eigenfrequency on the sphere as a function of the zonal wavenumber s (on the sphere) for all types of waves and various meridional modes n as labeled. The equatorial β-plane values were made dimensional assuming ε=10.

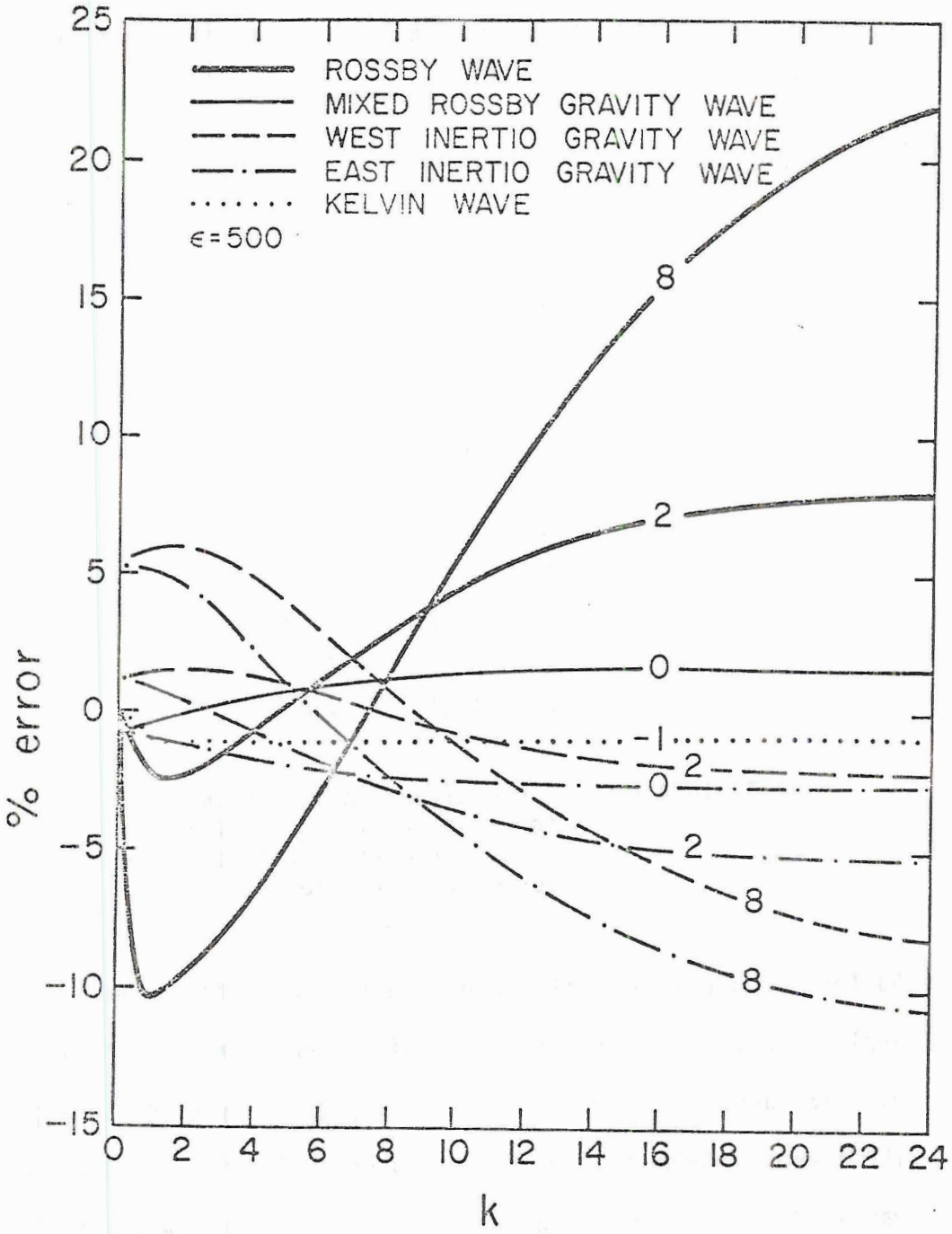

Figure 3.5 Same as Figure 3.4 but for ε=500.

Thus, the zonal periodicity imposed in the zonal direction of length $2\pi a$ on the equatorial β-plane implies that k takes the values shown in Table 3.1.

s	k	
	$\varepsilon = 10$	$\varepsilon = 500$
0	0	0
1	0.56	0.21
2	1.12	0.42
3	1.69	0.63
4	2.25	0.85
5	2.81	1.06
6	3.37	1.27
7	3.94	1.48
8	4.50	1.69

Table 3.1 The non-dimensional wavenumber k for zonal periodicity of length $2\pi a$ as a function of ε; s is the wavenumber on the sphere.

As for the matching of the sphere meridional index ℓ and the equatorial β-plane meridional index n, we consider the asymptotic form of the eigenfrequencies on the sphere for $\varepsilon \to \infty$ given by Longuet-Higgins (1968). The correspondence between Rossby waves (RW), mixed Rossby gravity waves (MRGW), westward gravity waves (WGW), Kelvin waves (KW) and eastward gravity waves (EGW) on the β-plane (index n) and on the sphere (index ℓ) is shown in Table 3.2.

wave type	n	ℓ
KW	$n = -1$	$\ell = 0$
EGW	$n \geq 0$	$\ell \geq 1$, $\ell = n+1$
MRGW	$n = 0$	$\ell = 0$
RW	$n \geq 1$	$\ell \geq 1$, $\ell = n$
WGW	$n \geq 1$	$\ell \geq 0$, $\ell = n-1$

Table 3.2. Correspondence between the β-plane index n and the sphere index ℓ for a Kelvin wave (KW), eastward gravity wave (EGW), mixed Rossby gravity wave (MRGW), Rossby wave (RW) and westward gravity wave (WGW).

Table 3.2 shows the $n \geq 1$ Rossby modes on the β-plane are identified with the rotational waves with the same meridional index on the sphere. The Kelvin wave is identified with the lowest eastward propagating mode ($\ell = 0$) of the first class as defined by Longuet-Higgins (1968); the eastward propagating gravity waves for $n \geq 0$ merge into the $\ell = n+1$ eastward modes of the first class. The mixed Rossby gravity wave ($n = 0$) corresponds to the $\ell = 0$ rotational mode of the second class and the westward gravity waves for $n \geq 1$ are identified with $\ell = n-1$ westward modes of the first class.

Returning now to Figure 3.4 (for $\varepsilon = 10$) we see that the eigenfrequencies of the $n = 2$ rotational waves are determined by the β-plane to within 20% only for $s = 1, 2$. The error for larger values of s remains approximately constant at 30% up to $s = 7$, decreasing for $s > 7$. Although the turning latitude for $n = 2$ and $\varepsilon = 10$ is less than the latitude of the pole in the equatorial β-plane (Figure 3.1), the phase speed of the rotational mode is overestimated by as much as 30%. The mixed Rossby-gravity wave ($n = 0$) is well estimated since the errors are within 10%. The frequency of westward propagating gravity waves

up to $n = 2$ is estimated to within 15% by the equatorial β-plane but the error is positive for long waves and negative for short waves, thus affecting the process of dispersion of energy as we shall see later. The eastward gravity waves seem to be more sensitive to the β-plane approximation than their westward companions. The phase speed of Kelvin waves is underestimated by less than 10% for long waves, decreasing towards higher s.

For the $\varepsilon = 500$ case (Figure 3.5) we have extended the wavenumber domain on the sphere up to $s = 24$ in order to cover approximately the same range in the non-dimensional wavenumber k domain as in the $\varepsilon = 10$ case (Table 3.1). According to Figure 3.1, the turning latitude of the $n = 8$ mode is approximately 5600 km and therefore we expect the $n = 8$ frequencies to be well estimated. However, the frequency associated with rotational modes is not as well estimated as that of gravity modes; the β-plane frequency is underestimated for $s = 1$ (-10%) and overestimated for large s (over 25% for $s = 20$). At $s = 24$ the relative error curves are leveling off except for the $n = 8$ Rossby mode. In section 3.2 we discuss the effect of the larger error for the rotational frequencies on the process of dispersion of energy.

The β-plane estimate for $\varepsilon = 500$ (Figure 3.5) has a tendency to overestimate (underestimate) the magnitude of the phase speed of longer (shorter) gravity waves but the magnitude of the relative error is smaller than for rotational waves. Although the errors for $\varepsilon = 500$ are acceptable, we have to consider the dispersion of energy which is related to the slope of the frequency curves with respect to zonal wavenumber. This is the objective of the next section.

3.1.1 Dispersion of energy

The key concept for understanding the process of dispersion of energy is the group velocity. In a dispersive system the speed of propagation of energy is different from the phase speed of waves; the energy is propagated with the group velocity (Lamb, 1952; Rossby, 1945; Longuet-Higgins, 1964).

The east-west group velocity on the equatorial β-plane can be written as

$$c_g = \frac{\partial \omega_k}{\partial k} = \frac{\left(k - \frac{k}{2\omega_k}\right)}{\left(\omega_k - \frac{k}{2\omega_k^2}\right)} \qquad (3.5)$$

which, together with the dispersion relation (2.35) gives Figure 3.6 for Rossby waves, gravity waves, mixed Rossby gravity waves and non-dispersive Kelvin wave as a function of zonal wavenumber k (abcissa) and n as labelled.

Figure 3.6 shows that as k increases the group velocity of gravity waves and Rossby waves tends to 1.0 and 0.0, respectively. For $k < 1$, the magnitude of the group velocity of Rossby and gravity waves is comparable. Long Rossby waves disperse towards the west ($c_g < 0$) and short Rossby waves have a small but positive group velocity (eastward dispersion). The westward propagating gravity wave also shows this peculiar behavior but the spectral region of eastward group velocity is very small and near the origin (ultra-long waves). The qualitative behavior of the $n = 0$ mode is similar to the $n \geq 1$ gravity waves but the whole pattern is shifted towards positive group velocity. Thus, the mixed Rossby gravity wave behaves like a gravity wave for small k and as a Rossby wave for larger k from an energy dispersion point of view.

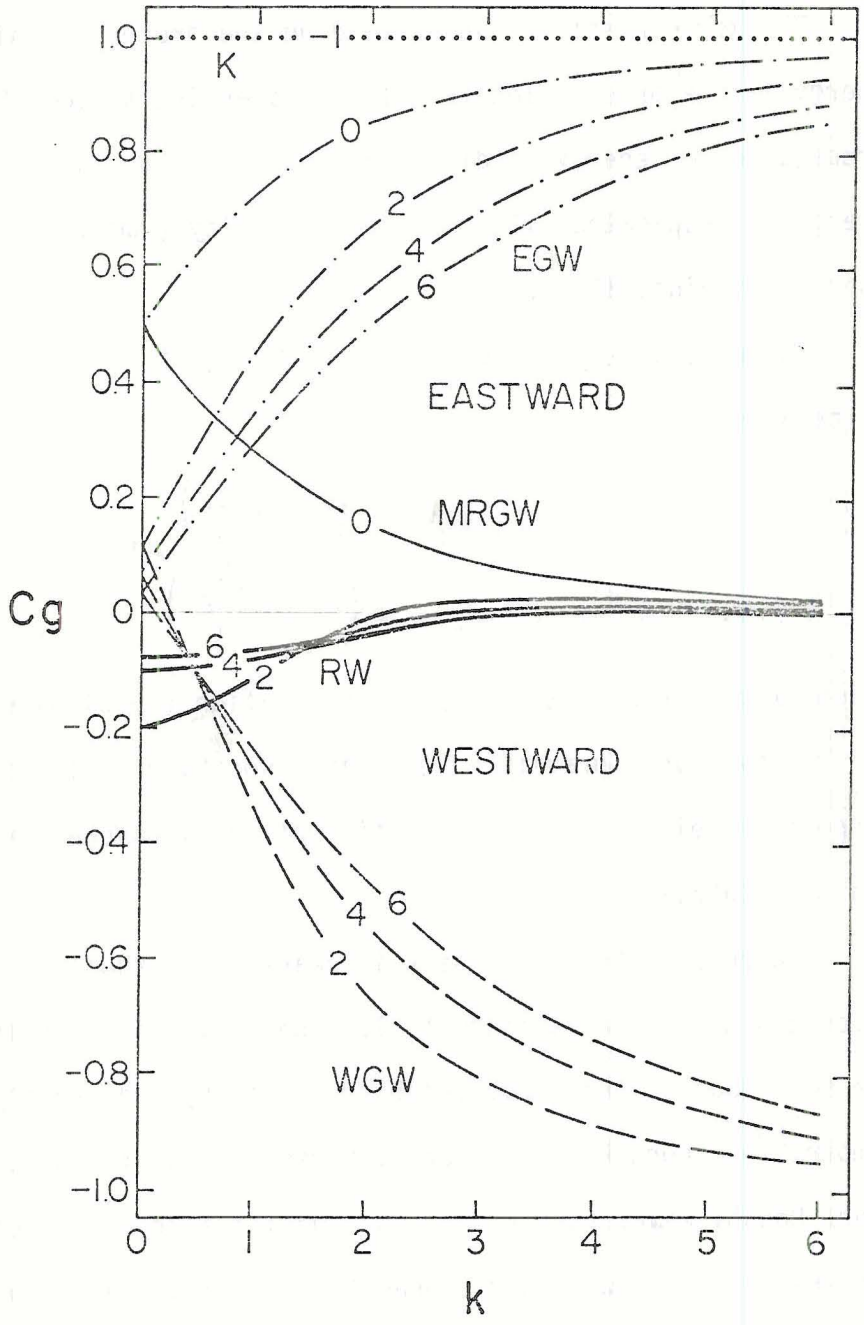

Figure 3.6 Group velocity c_g on the equatorial β-plane as a function of the zonal wavenumber k (abcissa) and meridional mode n (as labeled) for various types of waves as indicated.

So far we have discussed the group velocity of the free wave solutions of (2.4) assuming an infinite domain in the x-direction. Let us consider now the concept of group velocity when the allowed zonal wavenumbers are quantized by the imposed zonal periodicity, following the work done by Hoskins et al. (1977).

Let us consider two waves of the form $e^{i(k_1 x+\omega_1 t)}$ and $e^{i(k_2 x+\omega_2 t)}$ called waves I and II, respectively. If we set the phase difference between waves I and II equal to $2\pi j$ ($j = 0, \pm 1, \pm 2, \ldots$) we can write the following equation relating x to t:

$$x = \frac{2\pi j - (\omega_1 - \omega_2)t}{k_1 - k_2} \qquad j = 0, \pm 1, \pm 2, \ldots \quad . \tag{3.6}$$

The above equation defines the solid lines in the (x,t) plane shown in Figure 3.7. At a point (x_1, t_1) on these lines, waves I and II have the same phase except for a 2π factor. Without loss of generality, we may assume that at $t = 0$ there is a crest of wave I at $x = 0$ so that crests are located at $x_m = \frac{2\pi m}{k}$ ($m = 0, \pm 1, \pm 2, \ldots$) initially. Crests of wave I move in time with the phase speed $c_1 = -\frac{k_1}{\omega_1}$ defining the family of straight lines

$$x = \frac{2\pi m - \omega_1 t}{k_1} \qquad m = 0, \pm 1, \pm 2, \ldots \quad . \tag{3.7}$$

These lines define the position of crests in the (x,t) plane as shown in Figure 3.7 (dashed lines). The interception between the straight lines defined by (3.6) and (3.7) define points in the (x,t) plane where both waves reinforce each other i.e., the phase difference between wave I and II is zero (except for a factor 2π) and both waves

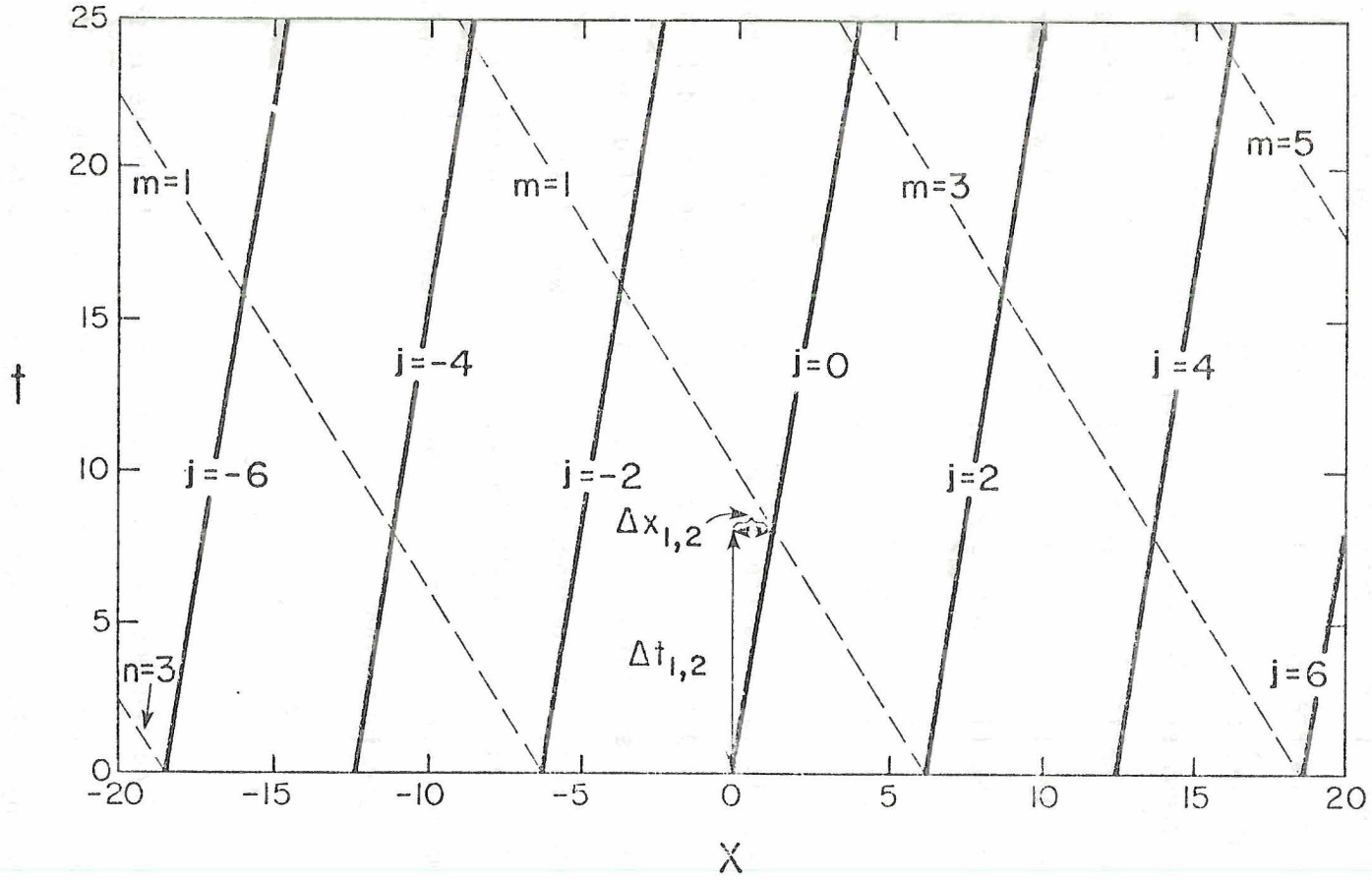

Figure 3.7 Solid lines: constant phase difference in the x-t plane between wave I and II for various j as labeled. Dashed lines: position of crests in the x-t plane as defined (3.7) for wave I and for various m as labeled. Waves I and II are the β-plane mixed Rossby-gravity waves at k=1 and k=3, respectively. See text for explanation.

show a crest at the interception point. If we take $j = 0$ and $m = 1$ we reproduce Hoskins et al. (1977) formulas for the distances and times between trough reinforcements. The interception points for arbitrary j and m have coordinates

$$x_{1,2}(j,m) = 2\pi \frac{\omega_1(j-m) + m\,\omega_2}{k_1\omega_2 - k_2\omega_1} \tag{3.8}$$

$$t_{1,2}(j,m) = 2\pi \frac{k_1(m-j) - m\,k_2}{k_1\omega_2 - k_2\omega_1} \tag{3.9}$$

with $j = 0, \pm1, \pm2, \ldots$ and $m = 0, \pm1, \pm2, \ldots$.

We can now interpret Figure 3.7 more carefully. The phase difference lines are labelled $j = 0, \pm2, \ldots$ according to (3.5) and the slope $\frac{\omega_2-\omega_1}{k_2-k_2}$ is that of the β-plane mixed Rossby gravity wave at $k_1 = 1$ (wave I) and $k_2 = 3$ (wave II). The lines labelled $m = \pm1, \pm3, \ldots$ are defined by (3.7) and the slope c_1 is that of the mixed Rossby gravity wave for wavenumber $k_1 = 1$. The train of reinforcement points appears to move along the constant phase difference line (solid line) with speed c_g given by

$$c_g = \frac{\omega_2 - \omega_1}{k_1 - k_2} \,. \tag{3.10}$$

In the limit when $k_2 \to k_1$, we have the standard definition of group velocity $c_g = \frac{\partial\omega}{\partial k}$ (3.1). However, when periodicity is implied in the zonal direction (3.10) is the appropriate definition of the speed of propagation of the energy associated with waves I and II (Hoskins et al., 1977).

Figure 3.7 shows that at $t = 0$ we have reinforcement points situated at $x = \frac{2\pi j}{k_1-k_2}$ $(j = 0, \pm2, \pm4)$. If we follow this train in

time along constant phase difference lines, reinforcement will occur at the time interval $\Delta t_{1,2}$ given by

$$\Delta t_{1,2} = 2\pi \left| \frac{k_2 - k_1}{k_1\omega_2 - k_2\omega_1} \right| \tag{3.11}$$

and the successive distance between the reinforcement points of the same train will be

$$\Delta x_{1,2} = 2\pi \left| \frac{\omega_1 - \omega_2}{k_1\omega_2 - k_2\omega_1} \right| \tag{3.12}$$

as indicated in Figure 3.7.

The direction of propagation of the reinforcement train depends on the slope of constant phase difference lines defined by (3.10). For the two mixed Rossby gravity waves shown in Figure 3.7 the train of reinforcement points moves towards the east at $c_g = 0.16$ (in dimensional units $c_g = 0.16\sqrt{gH}$) since the slope is positive. A negative c_g implies westward propagation of energy.

The distance between reinforcement points ($\Delta x_{1,2}$ in degrees of latitude), time interval in which they occur ($\Delta t_{1,2}$ in days) and implied group velocity ($c_{1,2}$ degrees per day), based on the Hough function frequencies for $\varepsilon = 10$, are shown in Table 3.3 for the mixed Rossby gravity wave ($\ell = 0$) and for the $\ell = 1$, 2 and 8 meridional modes of Rossby waves. The number in parentheses is the percent of the β-plane estimate relative to the sphere.

The reinforcement train associated with low meridional number Rossby waves propagates towards the west in the longwave part of the spectrum and towards the east for shorter waves. For higher meridional

$\varepsilon = 10$

	s_1	s_2 = 3	5	7	9	3	5	7	9	3	5	7	9
MRGW (ℓ=0)	1	1.0 (-1)	1.0 (-2)	1.1 (-3)	1.1 (-3)	62 (-7)	47 (-3)	37 (-2)	31 (-1)	62 (-6)	45 (-1)	34 (1)	28 (2)
	3		1.4 (-9)	1.5 (-9)	1.6 (-9)		38 (0)	31 (1)	27 (1)		27 (10)	20 (11)	17 (11)
	5			1.9 (-10)	2.1 (-10)			27 (2)	23 (3)			14 (13)	11 (13)
	7				2.4 (-9)				21 (3)				9 (13)
RW (ℓ=1)	1	6.6 (23)	5.5 (8)	5.3 (3)	5.2 (1)	88 (125)	19 (183)	0 (-1000)	6 (-76)	-13 (83)	-3 (163)	-0 (>1000)	1 (-76)
	3		3.1 (-17)	3.1 (-19)	3.2 (-20)		21 (-16)	21 (-2)	19 (2)		7 (2)	7 (21)	6 (27)
	5			3.1 (-27)	3.2 (-24)			21 (6)	19 (7)			7 (42)	6 (41)
	7				3.4 (-24)				18 (9)				5 (42)
RW (ℓ=2)	1	11.8 (48)	9.8 (17)	9.1 (7)	8.8 (3)	132 (194)	47 (175)	19 (192)	7 (275)	-11 (99)	-5 (135)	-2 (173)	-1 (266)
	3		5.2 (-20)	5.0 (-25)	5.0 (-26)		8 (-75)	12 (-24)	13 (-4)		2 (-68)	2 (0)	3 (30)
	5			4.6 (-32)	4.6 (-33)			15 (9)	15 (13)			3 (51)	3 (58)
	7				4.7 (-34)				15 (16)				3 (76)
RW (ℓ=8)	1	104.1 (37)	77.7 (-8)	66.8 (-25)	61.0 (-33)	424 (257)	226 (158)	144 (108)	101 (77)	-4 (160)	-3 (179)	-2 (176)	-2 (163)
	3		34.3 (-40)	29.6 (-48)	27.2 (-52)		60 (94)	36 (57)	23 (29)		-2 (223)	-1 (233)	-1 (168)
	5			22.6 (-57)	20.8 (-60)			15 (7)	8 (40)			-1 (151)	-0 (48)
	7				18.3 (-62)				2 (36)				-0 (262)
		$\Delta t_{1,2}$ (days)				$\Delta x_{1,2}$ (° latitude)				$c_{1,2}$ (° day^{-1})			

Table 3.3 Distance between reinforcement points $\Delta x_{1,2}$ (degrees of latitude), time interval in which they occur $\Delta t_{1,2}$ (days) and implied group velocity (degrees per day) for the mixed Rossby-gravity wave ($\ell = 0$) and some Rossby waves ($\ell = 1$, 2 and 8) on the sphere for $\varepsilon = 10$.

modes the spectral interval of westward energy propagation is much broader but the group velocity is smaller. The energy associated with the shorter waves tends to move as a whole pattern since the frequencies lie on almost straight lines (Figure 3.2).

If the initial disturbance has most of the energy in the $\ell = 1$, $1 \leq s \leq 3$ Rossby modes the reinforcement points will occur about 90° westwards after about 6.5 days. Given an initial disturbance with maximum energy in the short wave part of the spectrum of the $\ell = 1$ mode, Table 3.3 shows that reinforcement occurs approximately 20° towards the east after 3.2 days.

The time between reinforcements associated with higher order meridional modes is generally so large for long waves (see the $\ell = 8$ mode in Table 3.3) that it is of little or no meteorological significance. For short waves the time between reinforcements is of the order of 20 days for the $\ell = 8$ rotational mode and the implies group velocity is almost zero, reflecting the stationary nature of the disturbance.

The characteristic positions and times of reinforcements ($\Delta x_{1,2}$ and $\Delta t_{1,2}$ respectively) and the implied group velocity for energy initially in long waves ($1 \leq s \leq 3$) or in shorter waves ($7 \leq s \leq 9$) for $\ell = 0$, 1, 2 and 8 and for $\varepsilon = 500$ are given in Table 3.4. The time between reinforcements $\Delta t_{1,2}$ is very large even for the low order meridional modes except for the mixed Rossby gravity wave. The implied group velocity is towards the west for $n \geq 1$ and towards the east for the mixed Rossby gravity wave.

	ε = 500							
	MRGW (ℓ = 0)		RW (ℓ = 1)		RW (ℓ = 2)		RW (ℓ = 8)	
	$1 \leq s \leq 3$	$5 \leq s \leq 7$	$1 \leq s \leq 3$	$5 \leq s \leq 7$	$1 \leq s \leq 3$	$5 \leq s \leq 7$	$1 \leq s \leq 3$	$5 \leq s \leq 7$
$\Delta t_{1,2}$ (days)	2.4 (1)	2.8 (-0)	216 (7)	12 (4)	500 (15)	24 (10)	2720 (112)	116 (80)
$\Delta x_{1,2}$ (degrees)	31 (-2)	21 (-1)	133 (7)	23 (20)	3 (14)	53 (25)	281 (98)	143 (106)
$c_{1,2}$ (°/day)	13 (-2)	8 (-0)	-9 (1)	-2 (15)	-6 (-0)	-2 (13)	-2 (-7)	-1 (15)

Table 3.4 Same as Table 3.3 but for $\varepsilon = 500$.

There are two basic differences between the dispersive characteristics of internal and external rotational modes: (a) the internal modes disperse the energy towards the west even for shorter zonal scales ($s \geq 5$); and (b) although the group velocity of internal long zonal scales ($s \leq 3$) is not much smaller than the external group velocity, the time between reinforcements is much larger thus implying that the two waves go around the earth many times before reinforcing each other (approximately 6 times for the $s = 1$, $\ell = 1$ rotational mode on the sphere).

The dispersion of energy due to gravity waves on the sphere is summarized in Table 3.5 for initial energy in the regions $1 \leq s \leq 3$ and $5 \leq s \leq 7$ and for $\varepsilon = 10$ and $\varepsilon = 500$. As in Tables 3.3 and 3.4, the parameters $\Delta t_{1,2}$, $\Delta x_{1,2}$ and $c_{1,2}$ are shown in units of days, degrees, and degrees per day, respectively. The numbers in parentheses are the errors of the β-plane estimated relative to the sphere.

The group velocity for gravity waves (Table 3.5) is on the order of 140° day^{-1} to 220° day^{-1} in absolute value for the $\varepsilon = 10$ modes compared to -13° day^{-1} to 7° day^{-1} for the rotational modes given in Table 3.3. The upper limit of $c_{1,2}$ for gravity waves is reached for the reinforcement between shorter waves, and more important, $\Delta t_{1,2}$, $\Delta x_{1,2}$ and $c_{1,2}$ are almost independent of s_1 and s_2. Therefore, the pattern moves as a whole at about 220° day^{-1} or 283 ms^{-1} with very little dispersion, at approximately the phase speed of pure gravity waves ($c = 290$ ms^{-1} or 226° day^{-1}) on a fluid of depth $H = 8400$ m ($\varepsilon \approx 10$). Higher meridional modes for $\varepsilon = 10$ are almost non-dispersive including the long waves as shown in Table 3.5 for $n = 8$ (both eastward and

		WGW(ℓ=0)		WGW(ℓ=1)		WGW(ℓ=7)		EGW(ℓ=1)		EGW(ℓ=3)		EGW(ℓ=9)	
		$1 \le s \le 3$	$5 \le s \le 7$	$1 \le s \le 3$	$5 \le s \le 7$	$1 \le s \le 3$	$5 \le s \le 7$	$1 \le s \le 3$	$5 \le s \le 7$	$1 \le s \le 3$	$5 \le s \le 7$	$1 \le s \le 3$	$5 \le s \le 7$
ε=10	$\Delta t_{1,2}$	0.7 (-17)	1.5 (-2)	0.6 (-23)	0.8 (5)	0.2 (10)	0.2 (38)	0.9 (10)	1.1 (59)	0.4 (7)	0.4 (49)	0.2 (36)	0.2 (67)
	$\Delta x_{1,2}$	102 (-37)	324 (-6)	96 (-60)	166 (-7)	45 (-73)	45 (-11)	182 (-10)	242 (50)	80 (-41)	95 (25)	36 (-60)	36 (8)
	$c_{1,2}$	-140 (-24)	-215 (-4)	-169 (-48)	-215 (-11)	-220 (-76)	-222 (-36)	204 (-18)	224 (-6)	201 (-45)	221 (-16)	219 (-71)	222 (-35)
ε=500	$\Delta t_{1,2}$	1.4 (-1)	1.9 (-3)	1.1 (-1)	1.3 (-3)	0.6 (-6)	0.7 (-9)	2.4 (0)	2.8 (-0)	1.1 (-1)	1.2 (-3)	0.6 (-6)	0.7 (-8)
	$\Delta x_{1,2}$	3 (11)	34 (-5)	3 (2)	20 (-11)	2 (-39)	9 (-45)	48 (-3)	71 (-3)	11 (-17)	24 (-15)	5 (-56)	11 (-47)
	$c_{1,2}$	-2 (12)	-18 (-3)	-3 (3)	-16 (-7)	-4 (-35)	-14 (-39)	20 (-3)	25 (-3)	10 (-16)	19 (-13)	9 (-54)	18 (-43)

Table 3.5 Distance between reinforcement points $\Delta x_{1,2}$ (degrees of latitude), time interval in which they occur $\Delta t_{1,2}$ (days) and implied group velocity (degrees per day) for westward gravity waves (ℓ = 0, 1 and 7) and eastward gravity waves (ℓ = 1, 3 and 9) for ε = 10 and ε = 500.

westward modes). Reinforcement for gravity waves typically occurs in less than a day except for the lowest meridional mode and towards the west (east) for westward (eastward) propagating modes. If the initial condition contains high energy in these modes the dispersion due to rotational modes may be obscured by the fast dispersive character of gravity waves since they go around the globe in a time-scale shorter than the typical reinforcement time of Rossby waves.

A different picture emerges when considering the dispersion associated with the internal modes shown in Table 3.5 ($\varepsilon = 500$). The group velocities of the westward gravitational modes and of the internal rotational waves shown in Table 3.4 are comparable at least in the long wave part of the spectrum. However, the time and distance between reinforcements are much shorter ($\Delta t_{1,2}$ in the order of a few days compared to 12 to 2720 days for the rotational modes in Table 3.4). Although the upper limit on the absolute value of the group velocity for $\varepsilon = 500$ is 32° day^{-1}, Table 3.5 shows the $c_{1,2}$ is well below this limit for the spectral regions under consideration. However, $|c_{1,2}|$ tends toward the upper limit as s_1 and s_2 increase.

Another point that should be raised concerns the east-west asymetry produced by the different dispersive characteristics of westward and eastward gravity modes in agreement with Figure 3.3. Except for large ℓ, $\Delta t_{1,2}$, $\Delta x_{1,2}$ and $c_{1,2}$ may differ significantly, and for initial energy in small ℓ the asymmetry of the gravity wave front can be quite marked as shown in Chapter 4.

The distortion of the process of energy dispersion by the equatorial β-plane approximation is shown in percent error relative to the

sphere in Tables 3.3, 3.4 and 3.5 (number in parenthesis). For the external modes the errors are consistently small (less than 15%) only for the mixed Rossby gravity wave. If the initial energy is in certain zonal wavenumbers of the $\ell = 1$ and 2 Rossby modes, the β-plane estimates of $\Delta t_{1,2}$ or $\Delta x_{1,2}$ may be within 20% of the correct result on the sphere as seen in Table 3.3. However, the error distribution as a function of wavenumber is such that we cannot have both $\Delta t_{1,2}$ and $\Delta x_{1,2}$ within 20% in the same spectral region.

Errors in estimating $\Delta x_{1,2}$ for Rossby modes are likely to be very large if the zonal wavenumbers s_1 and s_2 are on each side of the hump of the frequency curve. The group velocity becomes negligible and the reinforcement points remain almost stationary, occurring at the time interval given by $\Delta t_{1,2}$. The spectral region for which the group velocity changes sign is a function of ℓ as shown in Figure 3.2. Thus, if the initial energy is in high order meridional modes the stationary disturbance will only appear if the maximum energy is in higher zonal wavenumbers.

An interesting aspect of the dispersion of energy for $\varepsilon = 500$ is related to relatively large errors for $\Delta t_{1,2}$ and $\Delta x_{1,2}$ in view of the small error for individual frequencies (Figure 3.5). The β-plane frequencies are within 10% or less of the solutions on the sphere for $1 \leq s \leq 9$ and $\ell \leq 8$ but $\Delta t_{1,2}$ and $\Delta x_{1,2}$ can be overestimated by more than 80%. Even for the $\ell = 2$ Rossby mode, the relative errors of $\Delta x_{1,2}$ and $\Delta t_{1,2}$ are larger than for individual frequencies. This is a consequence of the slope of the relative error curve for Rossby modes discussed in section 3.1.

The β-plane yields better results for the dispersion by gravity modes than by rotational modes. Figures 3.3 and 3.4 show that the error is estimating individual frequencies of eastward gravity modes is larger than for the westward gravity modes. As a consequence the β-plane timing and positioning of eastward bound reinforcement points is not as well estimated as the westward bound reinforcement points.

The non-divergent barotropic model studied by Hoskins et al. (1977) performs very well with respect to the energy dispersion between short waves ($s \geq 7$). However, for long waves and specifically for $s \leq 3$ the dispersion is drastically affected by the non-divergence assumption. In the non-divergent model the group velocity between ultralong waves of the $\ell = 1$ mode is positive (Table 1 of Hoskins et al., 1977) whereas in the divergent model, the reinforcement train moves towards the east ($c_{1,2} = -13°$ day^{-1} for $\ell = 1$, $1 \leq m \leq 3$). For waves such that $3 < s < 7$ the group velocity towards the east implied by the divergent model is about 30% slower than the non-divergent model prediction.

The excessive westward wave speed of rotational ultralong waves is discussed by Phillips (1963). For ultralong waves the magnitude of horizontal divergence is not negligible compared to the vertical component of the vorticity (Burger, 1958) and therefore any model built upon the assumption of small or zero divergence is not appropriate to describe the characteristics of such ultralong waves.

3.2 Eigensolutions - equatorial β-plane and sphere

The eigensolutions of the linearized shallow water equations on the equatorial β-plane have been previously discussed by Matsuno (1966). For the sake of completeness we discuss some of the characteristics

of the eigensolutions that are relevant for the interpretation of the results presented in Chapters 4 through 6. We shall first discuss the normalized zonal kinetic energy K_u, the normalized meridional kinetic energy K_v and the normalized available potential energy P as functions of non-dimensional wavenumber k and meridional mode n. Secondly, the horizontal structure of the eigensolutions will be reviewed. Although Matsuno (1966) compared the eigensolutions for different values of n but the same zonal wavenumber k, he did not compare waves of the same meridional number n but different zonal wavenumbers. In this section, we shall discuss this case since it is important for the interpretation of the results presented later. We also compare the energetics and structure of the free wave solutions on the equatorial β-plane with the results obtained on the sphere.

3.2.1 The energetics of the eigensolutions

The normalized zonal kinetic energy K_u, the normalized meridional kinetic energy K_v and the normalized available potential energy P are defined by

$$K_u = \tfrac{1}{2} \int_{-\infty}^{+\infty} u_{k,n}^2 (y)\, dy \,, \tag{3.13}$$

$$K_v = \tfrac{1}{2} \int_{-\infty}^{+\infty} v_{k,n}^2 (y)\, dy \,, \tag{3.14}$$

$$P = \tfrac{1}{2} \int_{-\infty}^{+\infty} \phi_{k,n}^2 (y)\, dy \,. \tag{3.15}$$

The normalization condition (2.59) implies that

$$K_u + K_v + P = \tfrac{1}{2} \,. \tag{3.16}$$

Substituting the definition for $\phi_{k,n,r}(y)$ given by (2.59) into (3.15), we obtain

$$P = \int_{-\infty}^{+\infty} \frac{[\tfrac{1}{4}(\omega_{k,n,r}^2 - k^2) H_{n+1}(y) + n^2(\omega_{k,n,r}^2 + k^2) H_{n-1}(y) - (\omega_{k,n,r} - k) n (\omega_{k,n,r} + k) H_{n+1}(y) H_{n-1}(y)] e^{-\frac{1}{2}y^2}}{2^n n! \pi^{\frac{1}{2}} [(\omega_{k,n,r}^2 - k^2)(n+1) + n(\omega_{k,n,r}^2 + k^2) + (\omega_{k,n,r}^2 - k^2)]} dy \tag{3.17}$$

for $n \geq 1$. The third term in the integrand vanishes because of the orthogonality of Hermite polynomials (A.1). The terms involving the square of Hermite polynomials are easily evaluated using (A.2). The final result is

$$P = \frac{1}{2\left[1 + \dfrac{(\omega_{k,n,r}^2 - k^2)^2}{(\omega_{k,n,r} - k)^2 (n+1) + n(\omega_{k,n,r} + k)^2}\right]} \tag{3.18}$$

for $n \geq 1$. A close look at the expression for $u_{k,n,r}(y)$ in (2.59) reveals that

$$K_u = P , \qquad n \geq 1 \tag{3.19}$$

because the only difference between K_u and P is the sign of the third term in the integrand of (3.17) which vanishes as discussed above. Using (3.16) and (3.19) we finally have

$$K_v = \tfrac{1}{2} - 2P , \qquad n \geq 1 . \tag{3.20}$$

The available potential energy of the $n = 0$ mode can be obtained in a similar way and the result is

$$P = K_u = \frac{1}{2[1 + (\omega+k)^2]} , \tag{3.21}$$

$$K_v = \tfrac{1}{2} - 2P , \qquad n = 0 .$$

The eigensolution corresponding to the Kelvin wave ($n = -1$) is independent of the wavenumber k according to (2.55) and therefore

$$K_u = P = \tfrac{1}{4} , \quad K_v = 0 \quad \text{for} \quad n = -1 . \tag{3.22}$$

From section 2.3.3 , we know that for the geostrophic modes $\omega \to 0$ as $k \to 0$, and therefore by taking the limit of (3.18) as $k \to 0$ we obtain

$$K_u = P = \tfrac{1}{2} \quad \text{for geostrophic modes} . \tag{3.23}$$

Figure 3.8 shows the magnitude of K_u or P (a) and K_v (b) for the eastward gravity waves (dashed line) and westward gravity modes (solid line) as a function of the non-dimensional wavelength k (abcissa) and n as labelled. The magnitude of K_u (or P) increases with increasing k and decreasing n for the gravity waves and accordingly, the magnitude of K_v decreases as k increases and n decreases. The Kelvin wave (dash-dotted line in Figure 3.8) has no meridional kinetic energy since $v \equiv 0$ on the equatorial β-plane. Only minor differences are found between the eastward and the westward gravity modes; K_u of the eastward mode is larger than K_u of the westward mode, the difference being larger for small k and n. As k increases the kinetic energy of the n'th eastward mode merges into the (n+1)'th westward mode. For $k = 0$ both modes have exactly the same K_u (or P). As for K_v , the same behavior is found i.e., the merging of the n'th eastward gravity mode into the (n+1)'th westward gravity modes as k increases. At $k = 0$, all gravity modes share the same meridional kinetic energy ($K_v = 0.25$).

Figure 3.9 is the same as Figure 3.8 but for Rossby waves. The mixed Rossby gravity wave has been included on this diagram although it should have been displayed as a westward gravity wave for $k < 2^{-\frac{1}{2}}$

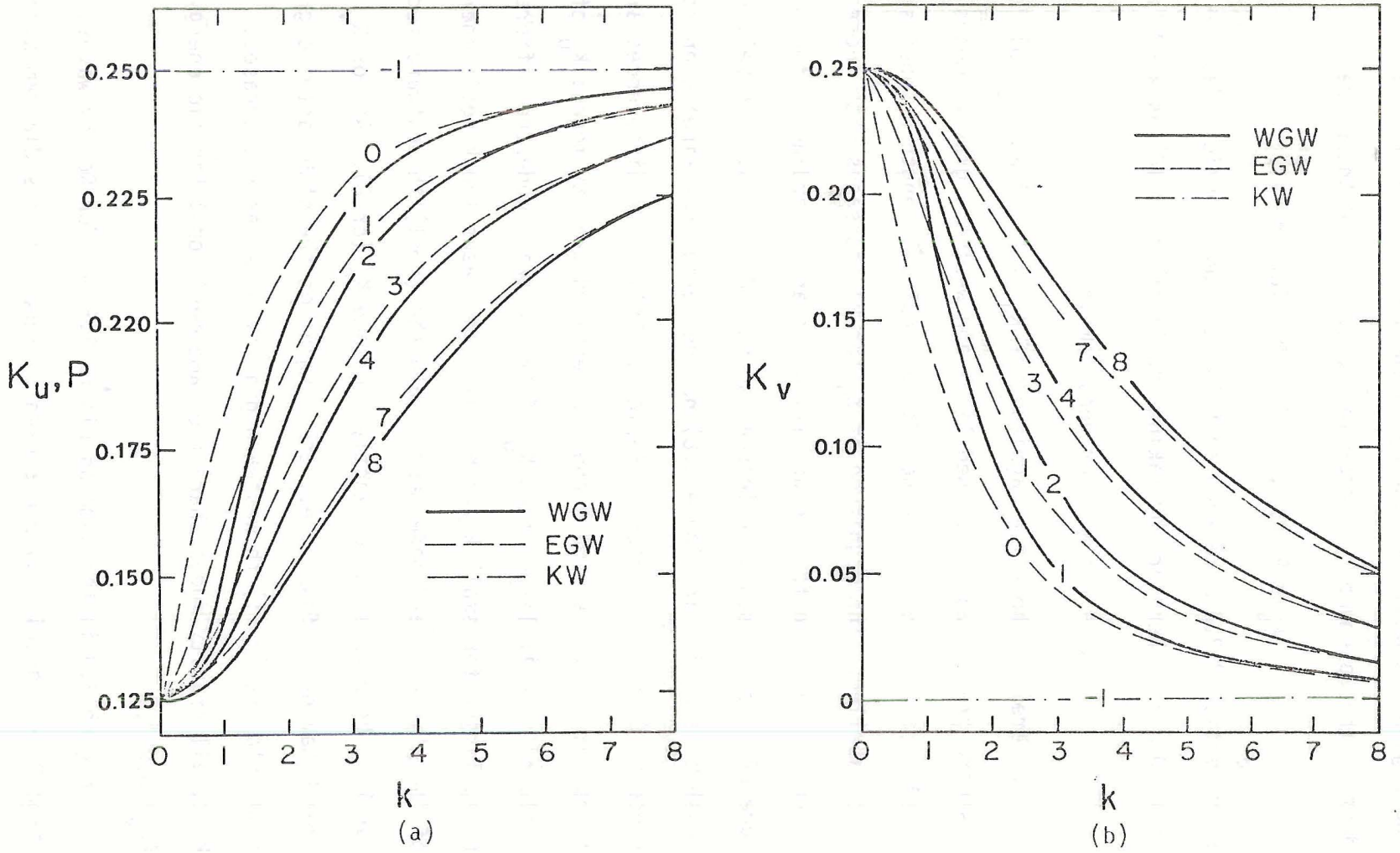

Figure 3.8 Normalized kinetic energy in the u-field K_u (a) and in the v-field K_v (b) for gravity waves as a function of k (abcissa) and n as labeled. In the equatorial β-plane K_u=P where P is the available potential energy.

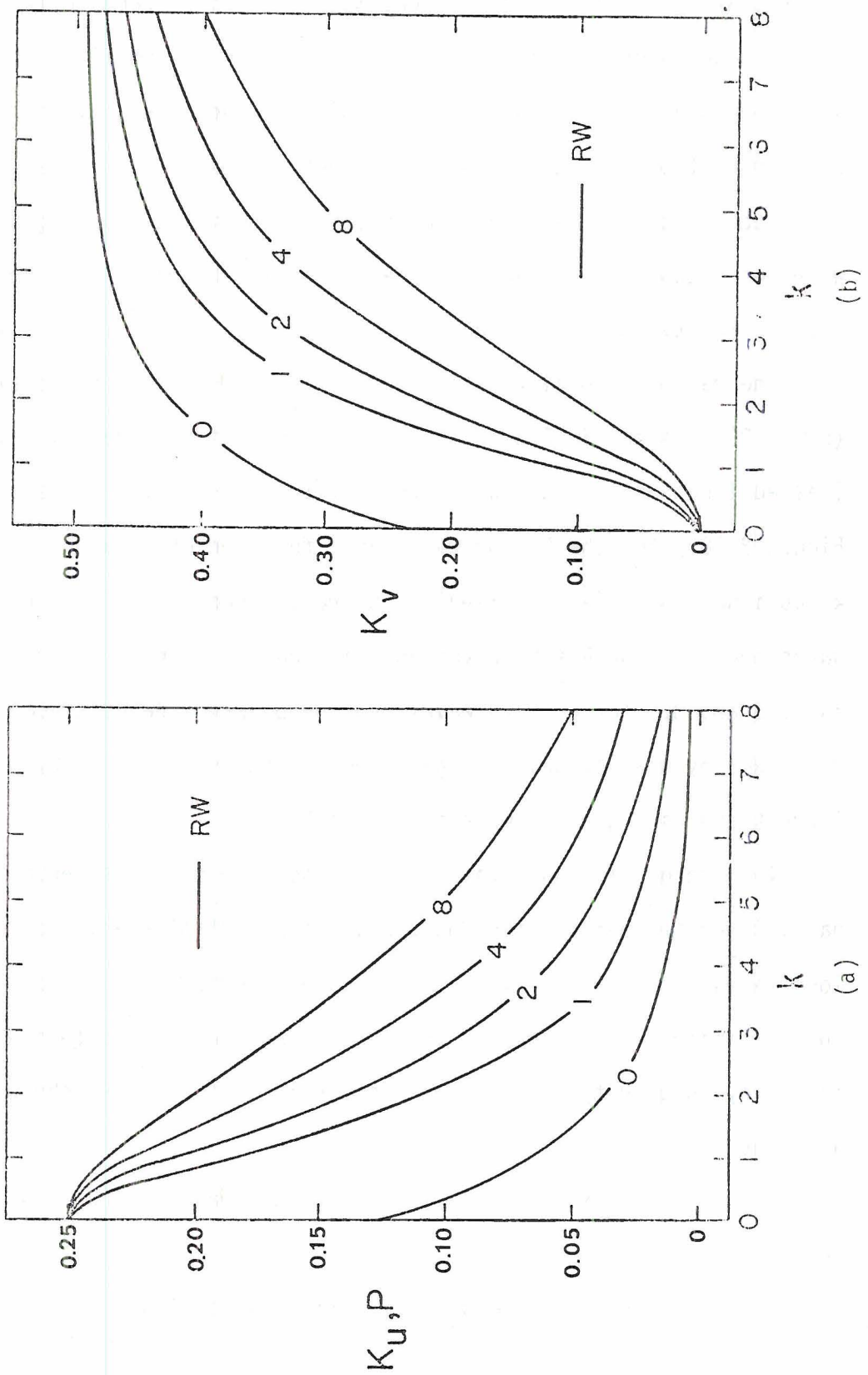

Figure 3.9 Same as Figure 3.8 but for Rossby waves.

as discussed in section 2.3.1. As a first approximation Figure 3.9 shows that K_u is larger than K_v provided $k < n$, i.e. zonal motion predominates over meridional motion for large n and small k. For ultralong waves ($k < 1$) however, most of the kinetic energy is in the zonal direction. At $k = 0$ (the geostrophic modes) K_v vanishes since $v \equiv 0$ according to (2.66). The energetics of the mixed Rossby gravity wave tends towards the typical behavior of Rossby modes for large k and to gravity modes as k decreases to zero.

The ratio of total kinetic energy ($K = K_u + K_v$) to the total energy ($E = K + P$) is shown in Figure 3.10.a for the eastward gravity waves (dashed lines) and for the westward gravity waves (solid lines) and in Figure 3.10.b for the Rossby waves as a function of zonal wavenumber k (abcissa) and n (as labelled). The ratio tends to 0.5 for gravity waves and to 1 for Rossby waves as k increases. For $k = 0$, the ratio is 0.75 and 0.5 for gravity waves and Rossby waves respectively. The mixed Rossby gravity wave is again seen to behave as a Rossby wave for large k and as a gravity wave for small k.

The energy of Rossby waves is thus seen to be almost equally partitioned between kinetic and available potential energy for ultralong waves while most of the energy is in kinetic form in short waves. The partition of total energy in kinetic and available potential forms of energy in gravity waves is not as sensitive to k as Rossby waves are since

$$0.5 \leq K / (K+P) \leq 1 \quad \text{for Rossby waves}$$

and

$$0.5 \leq K / (K+P) \leq 0.75 \quad \text{for gravity waves .}$$

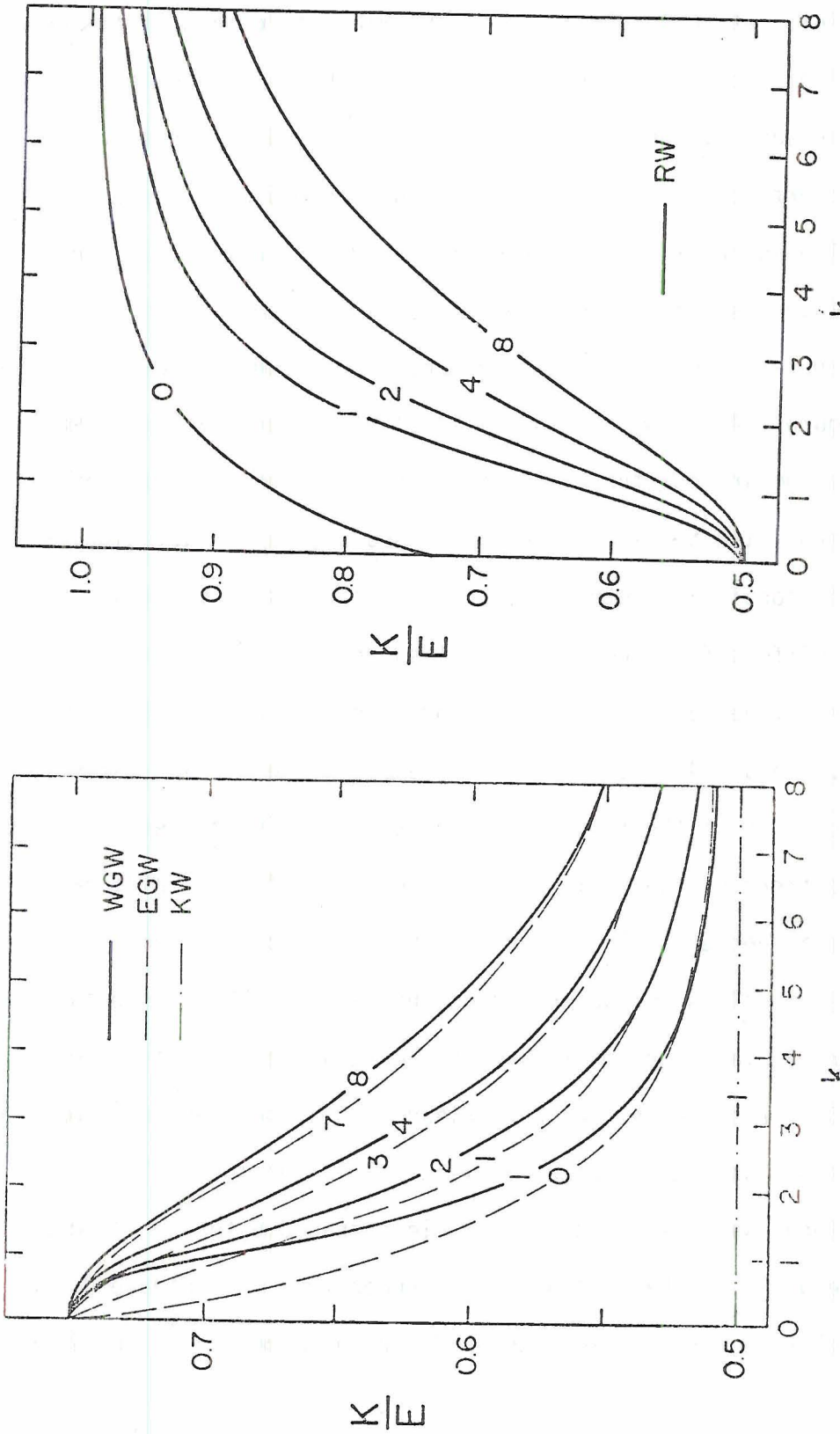

Figure 3.10 Ratio K/E of total kinetic energy (K_u+K_v) to total energy (E) for gravity waves (a) and Rossby waves (b) as a function of k (abcissa) and n as labeled.

Another important conclusion that can be drawn from Figure 3.10 is that more information is contained in the wind field than in the geopotential field for short Rossby waves since the ratio K/E tends to 1 as k increases. In gravitational modes both wind and pressure fields are important since the ratio K/E tends to 0.5 as k increases.

The asymptotic behavior of K_u (or P), K_v and K/E of the β-plane free waves as k tends to zero (not shown) agree with the $\varepsilon \to \infty$ case on the sphere. The results on the sphere as a function of ε are shown in Figures 14 (s = 0) and 15 (s = 1, 2) of Longuet-Higgins (1968). Let us compare now the ε = 500 equatorial β-plane estimate of partition of energy with the sphere results discussed by Longuet-Higgins (1968). For the zonally symmetric case, the β-plane estimate of K/E for gravity waves differs from the sphere by less than 2% up to $\ell = 5$. The geostrophic modes are not discussed by Longuet-Higgins. For s = 1 and 2 (k = 0.21 and 0.42 according to Table 3.1), the β-plane fails to reproduce some of the features on the sphere. The difference appears in the trend of the ratio K/E as a function of the meridional index. The ratio decreases as a function of the meridional index on the sphere for class two waves and on the β-plane the reverse is true (figure 3.8.a). The magnitude of the relative error is however, less than 3% for the modes shown in Figure 3.8.a and therefore comparable to the β-plane errors already discussed in sections 3.1 and 3.2. For rotational waves the ratio K/E is less than 0.5 for s = 1 and 2 on the sphere while on the β-plane it is larger than 0.5 (Figure 3.8.b), but the relative error is less than 5% for the modes shown in Figure 3.10.

The β-plane seems to perform slightly better for gravity waves ($\varepsilon = 500$) as far as the ratio of kinetic energy to total energy is concerned. The energetics of Kelvin waves and mixed Rossby gravity waves are also well reproduced by the β-plane.

The ratio of kinetic energy to total energy K/E for the external mode as a function of s (ordinate) and meridional index ℓ (as labelled) for gravity waves and rotational waves are shown in Figure 3.11 (taken from Kasahara, 1976). Although the general trend as a function of s is the same as in the equatorial β-plane case (Figure 3.10) the trend as a function of ℓ is opposite (refer to Table 3.2 for the relationship between ℓ and n). The conclusions drawn from the β-plane case concerning the relative importance of the geopotential and wind fields are still valid provided that the dependence on ℓ (or n) is reversed.

3.2.2 The two-dimensional structure

The horizontal structure of the normal modes of the shallow water equations on the equatorial β-plane can be conveniently displayed independently of Lamb's parameter ε. Figures 3.12 - 3.17 show the two dimensional distribution of the wind and geopotential fields for $k = 0.5$ (a) and $k = 6.5$ (b). In all figures one wave length is shown in the x-direction and the ordinate is the non-dimensional y. Figure 2.3 allows us to readily estimate horizontal distance in Figures 3.12 - 3.18 in dimensional units provided ε is given, e.g., for $\varepsilon = 10$ one non-dimensional length unit is approximately 3600 km. The relationship between the non-dimensional wavenumber k and the wavenumber s on the sphere is given by (3.4). Thus, $k = 0.5$ corresponds to $s \approx 1$ and $k = 6.5$ to $s \approx 12$ for $\varepsilon = 10$. For $\varepsilon = 500$ the nearest integer wavenumbers on the sphere are $s = 3$ and $s = 32$ for $k = 0.5$ and $k = 6.5$ respectively.

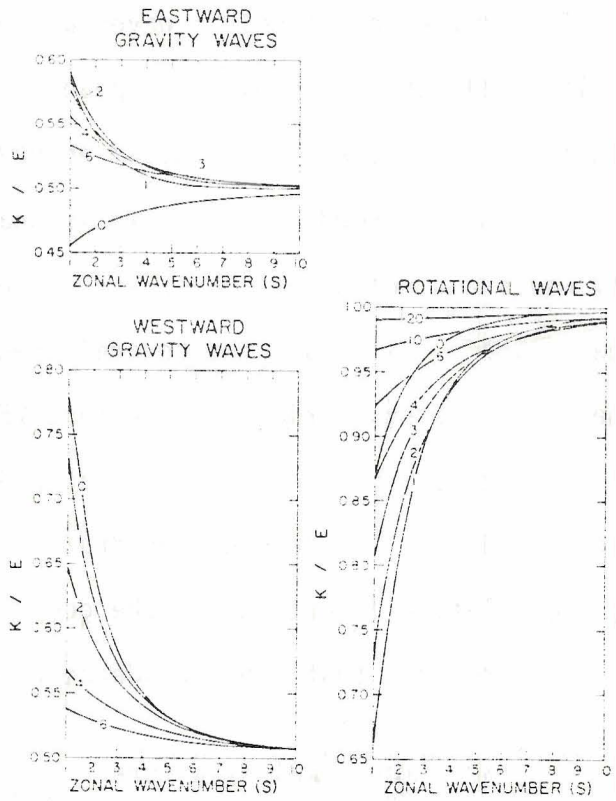

Figure 3.11 Ratio of kinetic energy K ($K=K_u+K_v$) to the total energy E (E=K+P) for gravity waves and rotational waves as a function of the zonal wavenumber s and meridional index ℓ,as labeled on each line.
(after Kasahara,1976)

Rossby modes are shown in Figure 3.12 for n = 1 and in Figure 3.13 for n = 6. The balance of the pressure and wind fields is such that v is approximately in geostrophic balance with ϕ for long waves and u with ϕ for short waves. Consequently, $\frac{\partial u}{\partial t}$ ($\frac{\partial v}{\partial t}$) is large (small) for long (short) waves. The relationship between the kinetic energy and available potential energy discussed in the previous section is evident when comparing Figures 3.12.a and 3.12.b, namely, the small geopotential deviations for larger k (the geopotential field is scaled by 1000 in Figure 3.12.b) implying that most of the energy is in kinetic form (mostly in meridional motion) as shown by Figures 3.9 and 3.10.b. Figures 3.12 and 3.13 indicate the following about the latitudinal distribution of P and K: for large n (Figure 3.13) pressure gradients are small in the equatorial regions contrary to the low n case (Figure 3.12). On the other hand, the wind intensity is high in the equatorial region in both cases. It can be argued that the tendency for geostrophy in equatorial areas makes u (or v) large since the Coriolis parameter is small. The maximum amplitude of the geopotential field shifts northwards as n increases as shown in Figures 3.12 and 3.13. The latitudes of wind maxima are, however, related to the meridional number n and do not have a definite latitudinal preference.

Figures 3.14 and 3.15 display the n = 1 and n = 6 westward gravity waves respectively. The n = 1 is a peculiar wave since for larger k it looks like a Kelvin wave (Figure 3.17) moving towards the west (notice the convergence at x = 0 which tends to build the high pressure). However, the pressure and wind fields are π out of phase with respect to the Kelvin wave. The smallness of the meridional wind component could have been anticipated by the spectral distribution of kinetic

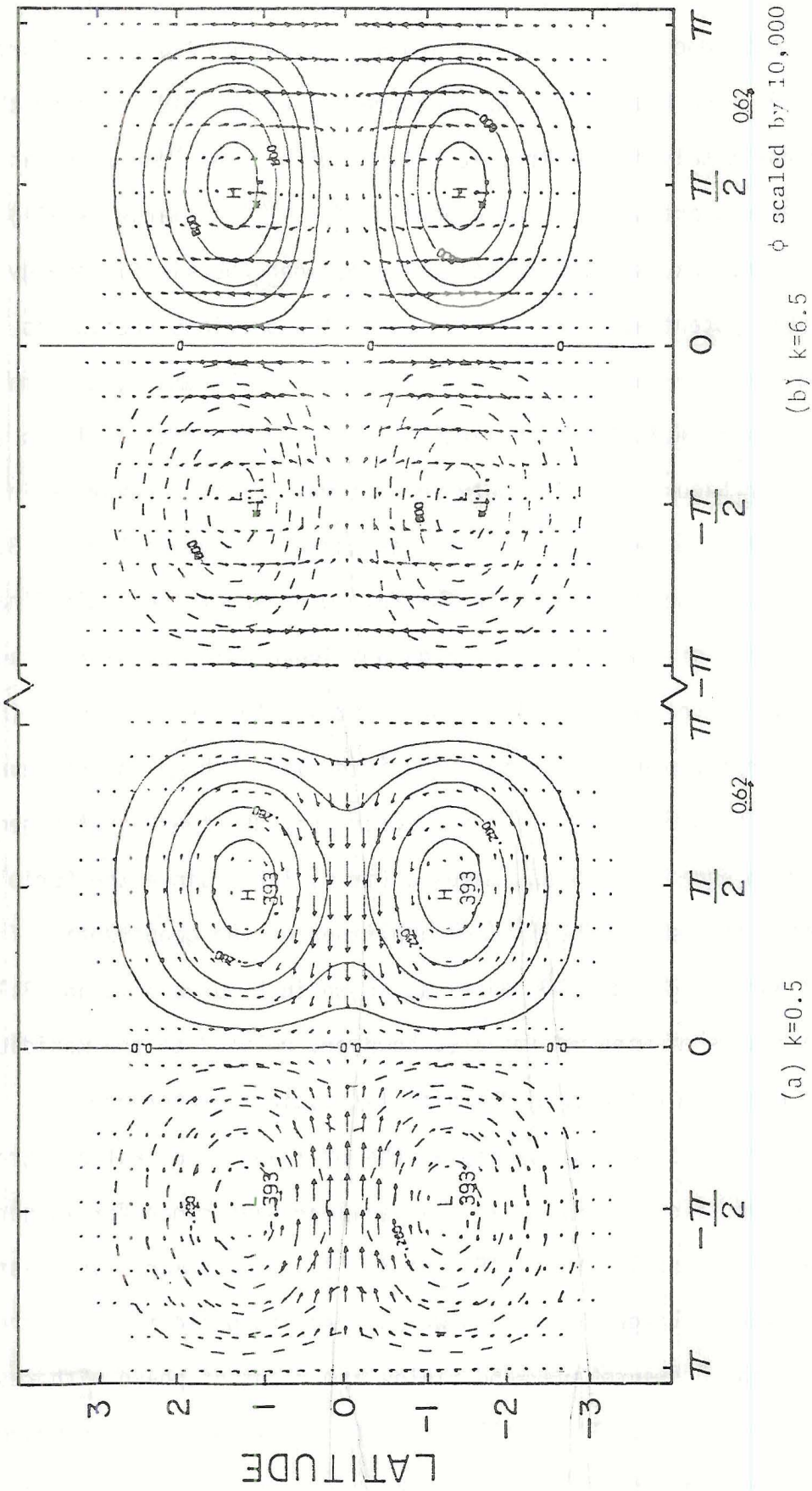

Figure 3.12 The n=1 Rossby wave on the equatorial β-plane in non-dimensional units. The wind and geopotential are normalized such that the total energy is 0.5 (according to (3.16)). The abcissa is kx and the ordinate is the non-dimensional latitude y.

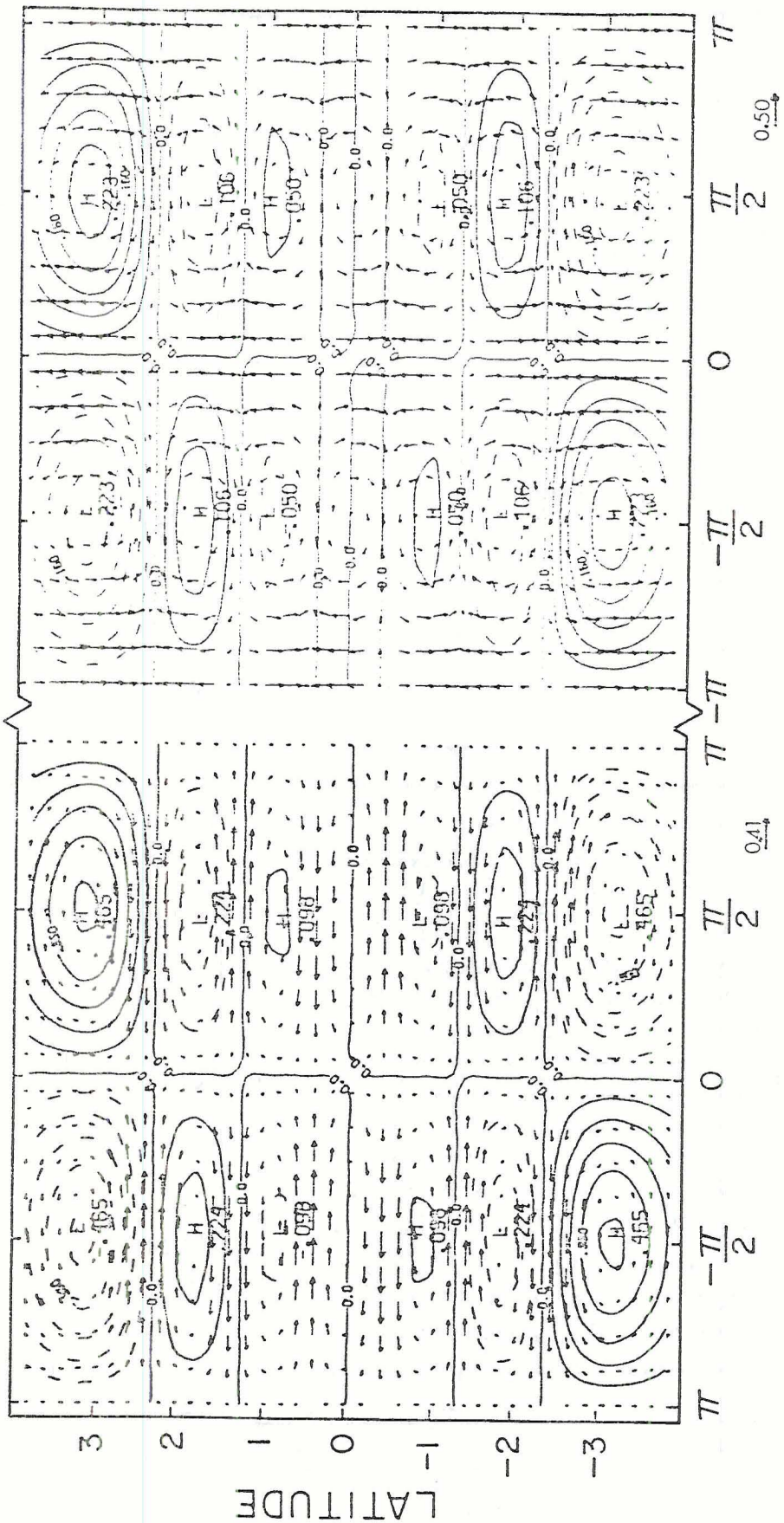

Figure 3.13 Same as Figure 3.12 but for the n=6 Rossby wave.

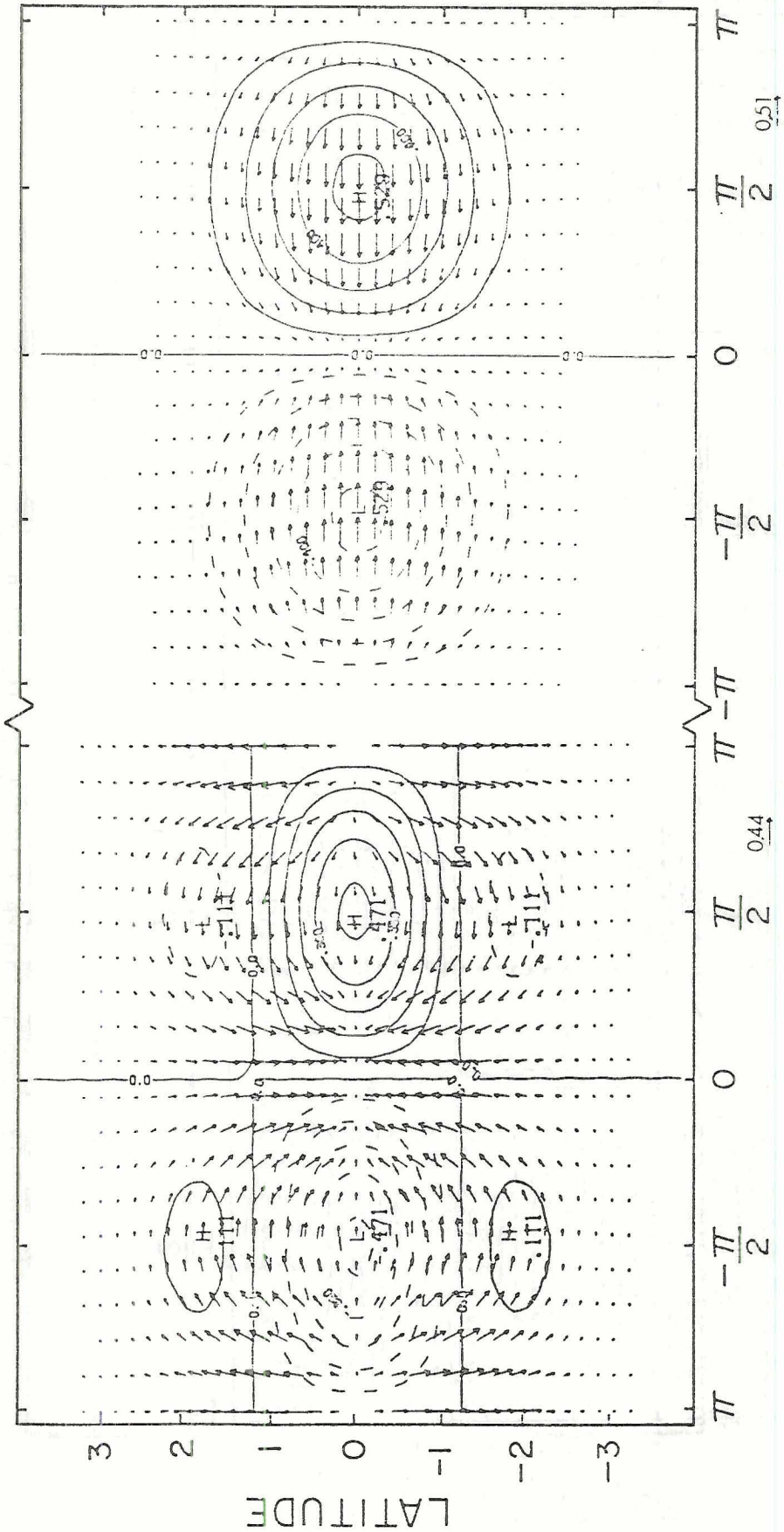

(a) k=0.5 (b) k=6.5

Figure 3.14 Same as Figure 3.12 but for the n=1 westward gravity wave.

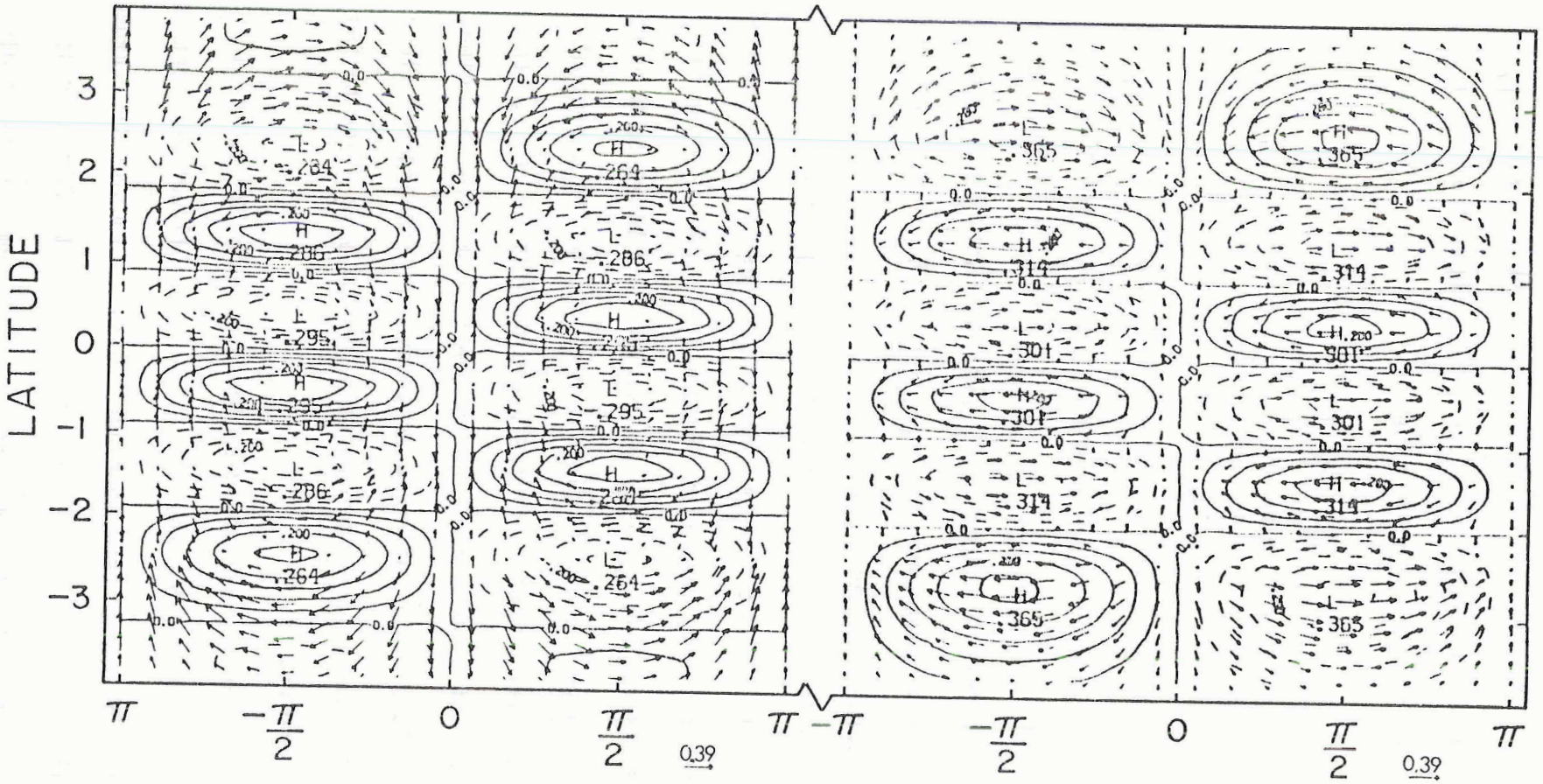

Figure 3.15 Same as Figure 3.12 but for the n=6 westward gravity wave.

energy shown in Figure 3.8. As k increases the frequency $\omega_{k,1,1}$ tends towards k (Figure 3.2) and therefore (2.59) shows that the eigenfunction $\xi_{k,1,1}(y)$ is approximately given by

$$\xi_{k,1,1}(y) = \begin{bmatrix} 2k \\ 0 \\ -2k \end{bmatrix} \frac{e^{-\frac{1}{2}y^2}}{\sqrt{E_{k,1,1}}} \qquad (3.24)$$

which only differs from the Kelvin wave eigenfunction $\xi_{k,-1,2}(y)$ (2.55) by the k factor. Also of some interest is the behavior of the number of zeros of $u_{k,n,1}$ and $\phi_{k,n.1}$ as a function of latitude as k increases; the term dependent on $H_{n+1}(y)$ in (2.59) looses its importance since it is multiplied by $(\omega_{k,1,1}-k)$. This effect is clearly shown in Figures 3.14 and 3.15.

The zonality of the wind field for short gravity waves is also pronounced for the n = 6 mode but not as much as for n = 1, as predicted by the kinetic energy partition (Figure 3.8). No tendency for geostrophy is observed for gravity waves; the wind blows towards high pressure and when the air is flowing parallel to the geopotential isolines it usually does so in the wrong direction. Thus, local accelerations of u and v are high in order to satisfy the momentum equations. As a result of the ageostrophy, the divergence field is large and the direction of propagation is easily verified by inspecting the local tendency of ϕ.

The mixed Rossby gravity wave for k = 0.5 and k = 6.5 is shown in Figures 3.16.a and 3.16.b respectively. Two well defined vortices are centered at the Equator and in Figure 3.16.b we notice the predominance of meridional motion. The magnitude of the perturbation pressure field is also very small for the shorter wave (the geopotential field in Figure 3.16.b is scaled by 10,000).

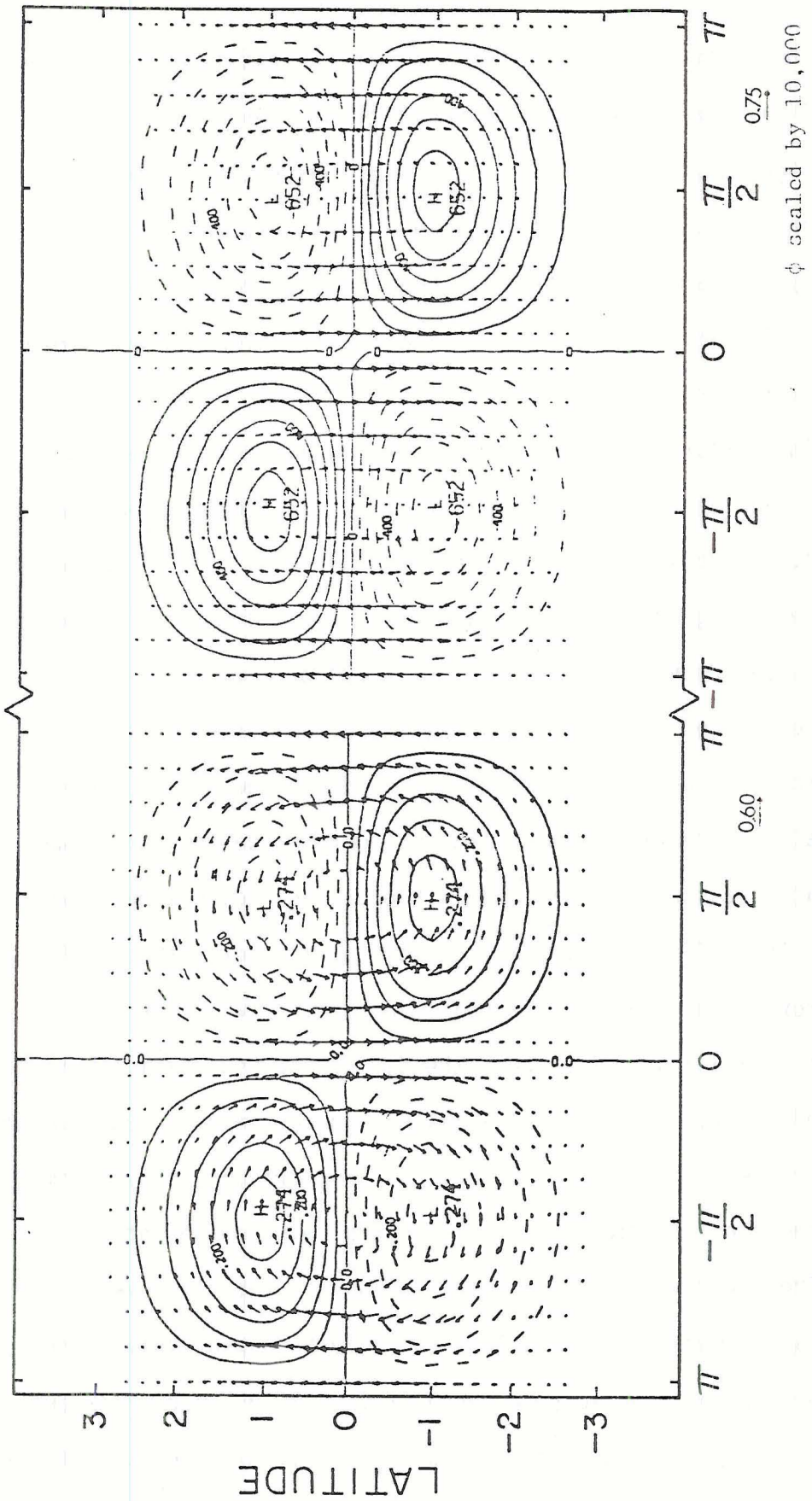

(a) k=0.5 (b) k=6.5

Figure 3.16 Same as Figure 3.12 but for the mixed Rossby-gravity wave.

The vortex centered at the Equator for the mixed Rossby gravity wave is a characteristic of modes of even order because v is symmetric about the Equator and u and ϕ are antisymmetric as discussed in section 2.3.2. Contrary to pure gravity waves, the mixed Rossby gravity wave shows a marked tendency for geostrophy at higher latitudes. For shorter waves, the v-component is very large, another characteristic of Rossby waves.

The perturbation geopotential and zonal wind of the β-plane Kelvin wave are independent of the zonal wavenumber k as shown by (2.55). The balance between the zonal velocity and the meridional geopotential gradient is clearly observed in Figure 3.17 which shows the β-plane Kelvin wave for an arbitrary zonal wavenumber.

Let us consider now the vorticity and divergence fields associated with the free wave solutions of the divergent barotropic model. We have already mentioned the effect of convergence in gravity waves in generating a strong geopotential rise thus building a high pressure area. This effect can perhaps be most easily identified in Figure 3.14 for the $n = 1$ westward propagating gravity wave for $k = 0.5$. Figure 3.18.a and 3.18.b shows the divergence and vorticity fields for this particular wave. The maximum convergence is centered at the Equator where there is no vorticity. The vorticity comes primarily from the zonal gradient of the meridional wind component ($\frac{\partial v}{\partial x}$).

The divergence and vorticity fields of a Rossby wave ($k = 0.5$ and $n = 1$) are shown in Figure 3.19.a and 3.19.b respectively. The cyclonic and anticyclonic vortices centered at $y = 0.8$ in Figure 3.12 are clearly shown in the vorticity field (Figure 3.19.b). The regions of maximum and minimum convergence are located at $y = 1.2$ but $\frac{\pi}{2}$ out of phase.

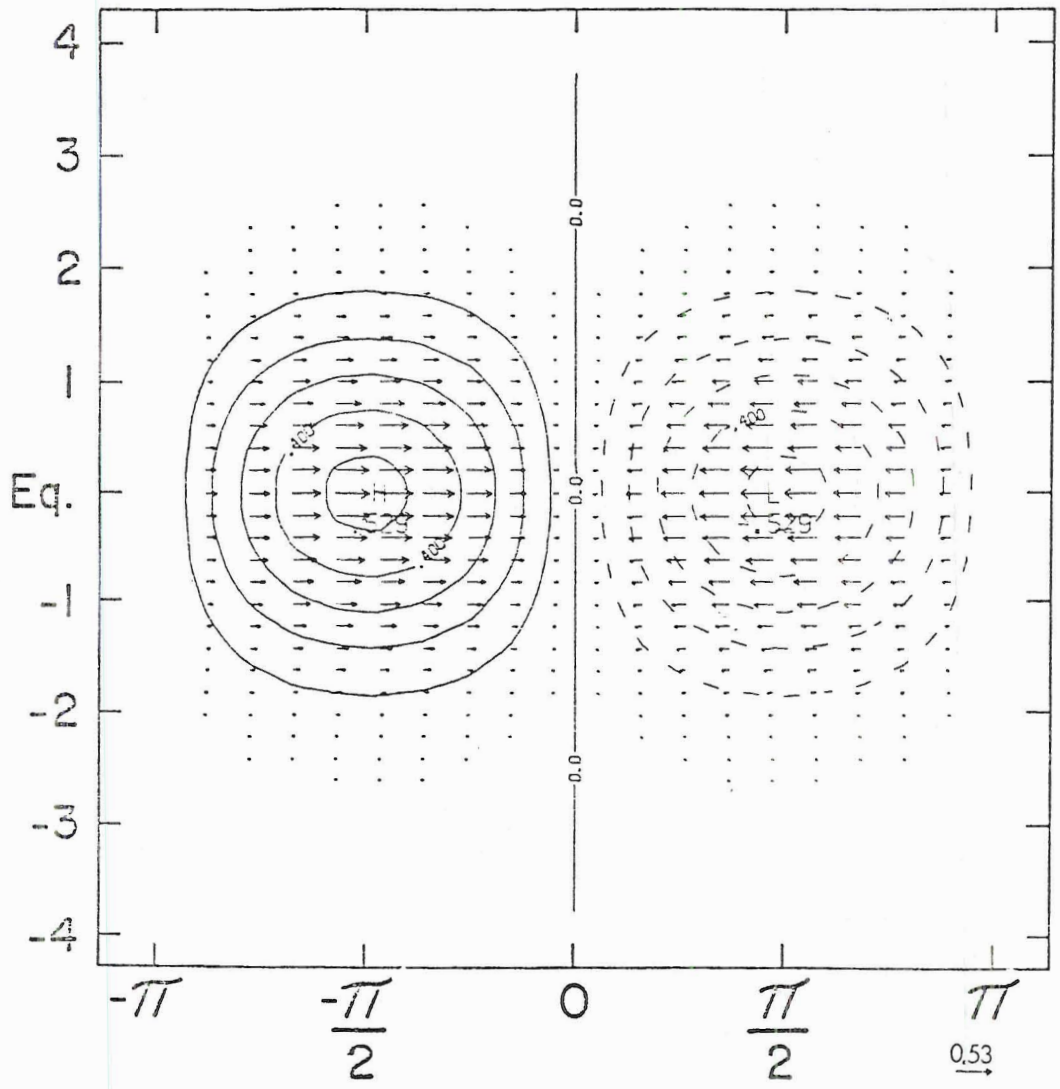

Figure 3.17 Non-dimensional geopotential and wind fields of an equatorial β-plane Kelvin wave. The geopotential and wind fields are normalized such that the total energy is 0.5 (according to (3.16)). The abcissa is kx and the ordinate is the non-dimensional latitude y.

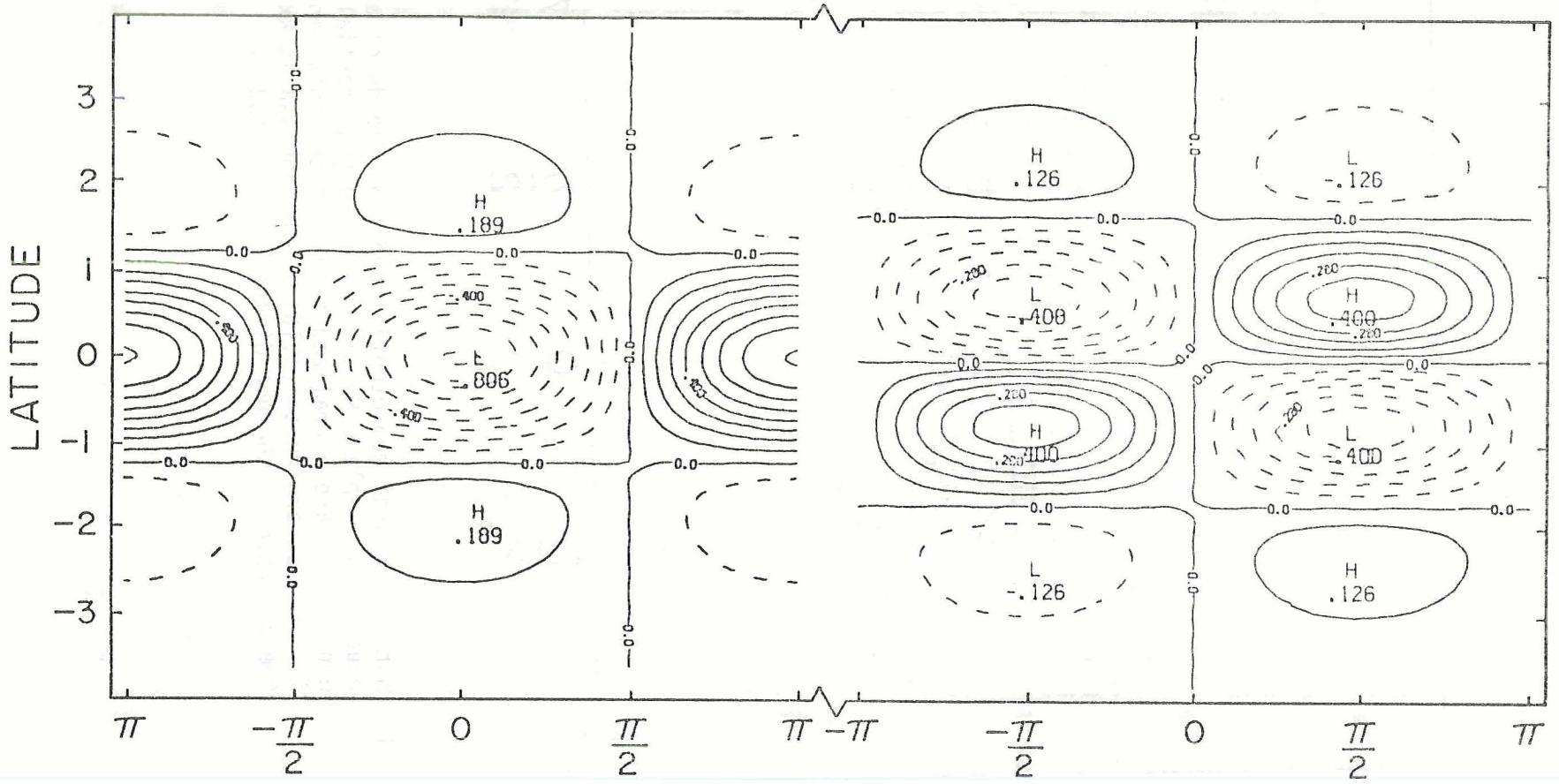

(a) divergence (b) relative vorticity

Figure 3.18 Non-dimensional divergence (a) and relative vorticity (b) fields associated with the n=1 westward gravity wave shown in Figure 3.14.a (k=0.5). The abcissa is kx and the ordinate is the non-dimensional latitude y.

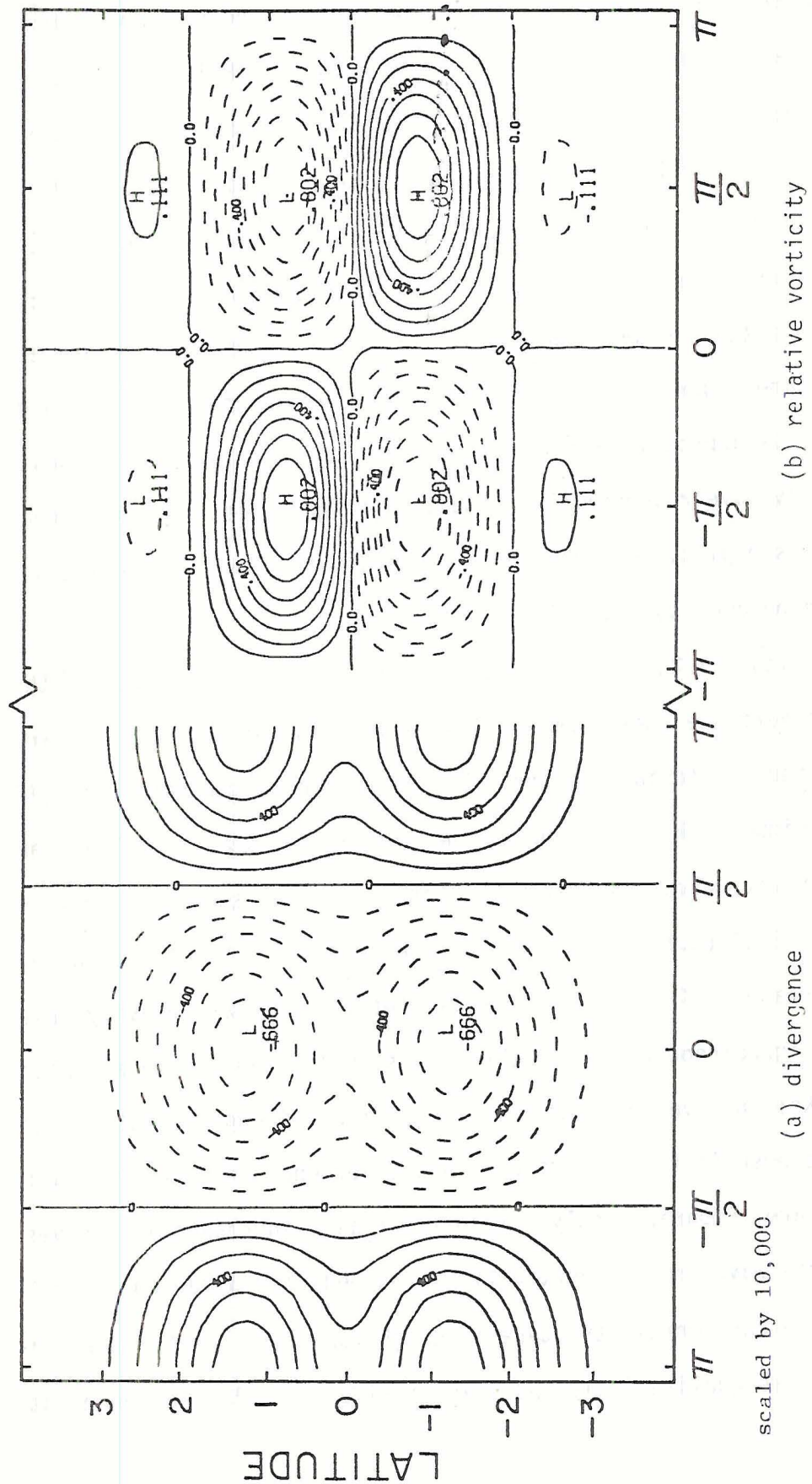

Figure 3.19 Same as Figure 3.18 but for the n=1 Rossby wave shown in Figure 3.12.a (k=0.5).

However, the striking difference between the Rossby wave shown in Figure 3.19 and the gravity wave in Figure 3.18 is the ratio between the vorticity and divergence maxima; for the Rossby wave the ratio is approximately 12 and for the gravity wave it is approximately 0.5. Thus, for the long Rossby wave shown in Figure 3.19 the vorticity is about one order of magnitude larger than the divergence, and for the $n = 1$ westward gravity wave the vorticity and divergence are about the same order. At $k = 6.5$ and $n = 1$ the ratio of vorticity to divergence is approximately 300 and 0.1 for the Rossby wave and westward gravity wave respectively. Thus, as k increases, the divergence becomes negligible compared to vorticity in Rossby waves and divergence becomes dominant in gravity waves.

Figure 3.20 shows the ratio of the maximum vorticity to the maximum divergence ($\max|\zeta|/\max|\delta|$) as a function of the zonal wavenumber k on the equatorial β-plane. For Rossby waves the ratio $\max|\zeta|/\max|\delta|$ is minimum at $k \approx 0.85$, increasing rapidly for $k \gtrsim 0.85$. This same ratio for gravity waves is fairly constant over the range of k shown in Figure 3.20 ($0.1 \leq k \leq 7$) being of the order of 0.5 but decreasing as k increases. The peculiar behavior of the eastward gravity wave in the neighborhood of $k = 1.5$ does not seem to have a simple explanation. Long Kelvin waves have more vorticity than divergence but for $k > 0.6$ the reverse is true. Vorticity and divergence in mixed Rossby gravity waves are comparable only for small k; as k increases it behaves like a Rossby wave and the vorticity far exceeds the divergence for $k > 2$.

The horizontal structure of Hough functions on the sphere for $\varepsilon = 500$ are qualitatively and quantitatively similar to the equatorial

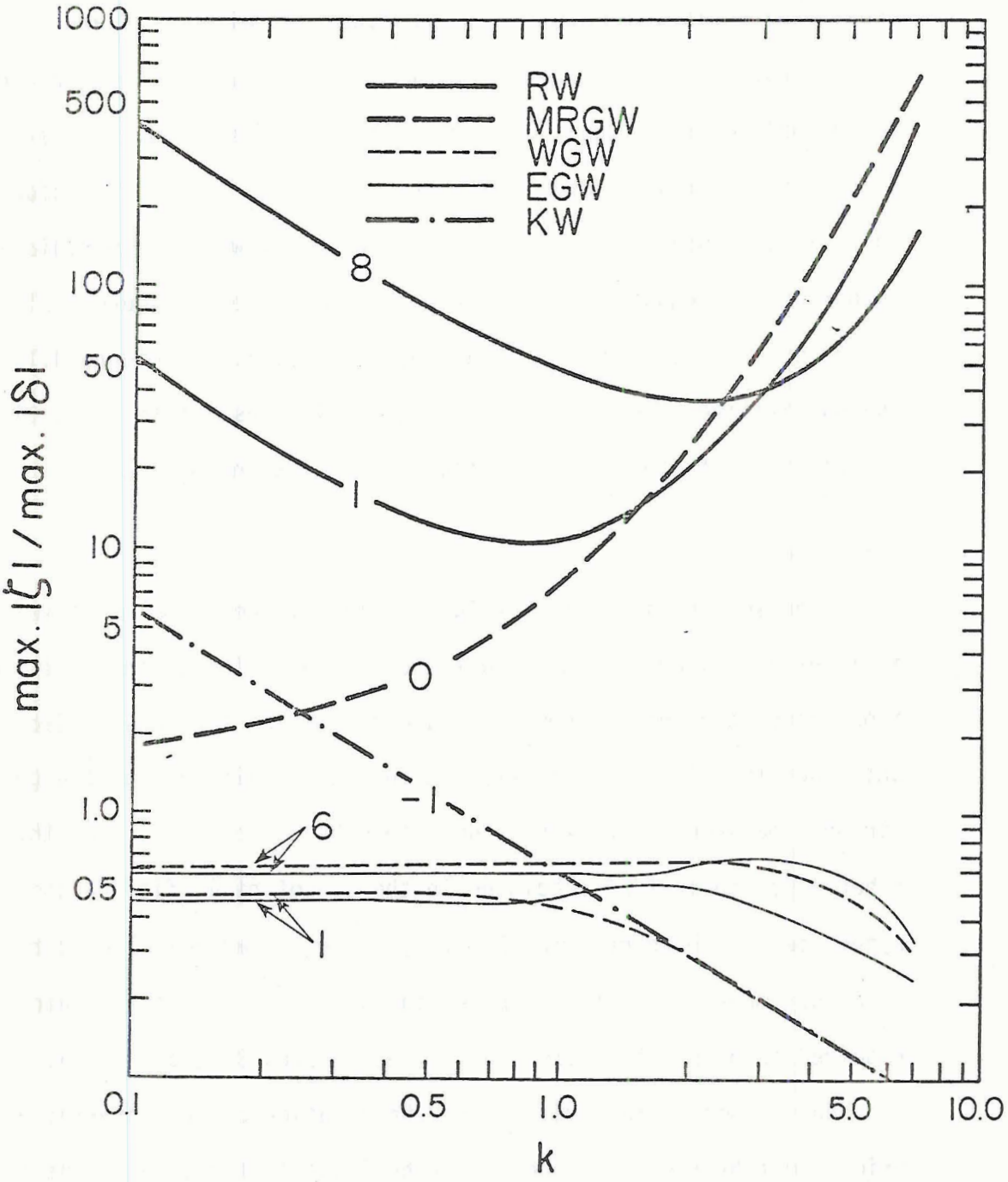

Figure 3.20 Ratio of maximum vorticity to maximum divergence as a function of the non-dimensional wavenumber k on the equatorial β-plane for all types of waves and for various meridional modes n as labeled.

β-plane free waves discussed so far and need not be shown here. The equatorial β-plane estimate of Hough functions with $\varepsilon = 10$ are qualitatively good in the neighborhood of the equator even for higher order meridional modes. Figure 3.21 shows the $\ell = 6$ Rossby wave (a) and the $\ell = 5$ westward gravity wave on the sphere ($\varepsilon = 10$) for $s = 1$. According to Table 3.2, which gives the correspondence between the meridional numbers on the equatorial β-plane and on the sphere, Figure 3.21.a can be compared to Figure 3.13.a and Figure 3.21.b to Figure 3.15.a . The qualitative agreement is fairly good with respect to latitudinal distribution of highs and lows and wind maxima and minima.

3.3 Discussion

When solving an initial value problem by the normal mode technique it is extremely helpful to know the characteristics of the basis functions since the initial condition and/or forcing term are projected onto such functions. Obviously, an initial condition near the geostrophic balance can be mostly described by Rossby modes. On the other hand, an initial condition in the geopotential field alone (e.g. a geopotential bump near the Equator) cannot be accurately described by Rossby modes since the geopotential gradients near the Equator are required to be small by geostrophy (see Figures 3.12 and 3.13).

Thus, some characteristics of the solution can be inferred a priori just by the knowledge of the horizontal structure of the basis functions. On the other hand, knowledge of the frequency and dispersive characteristics of the free waves also help us in understanding the time behavior of the solution. If the initial condition is projected mostly onto gravity modes we expect the initial configuration

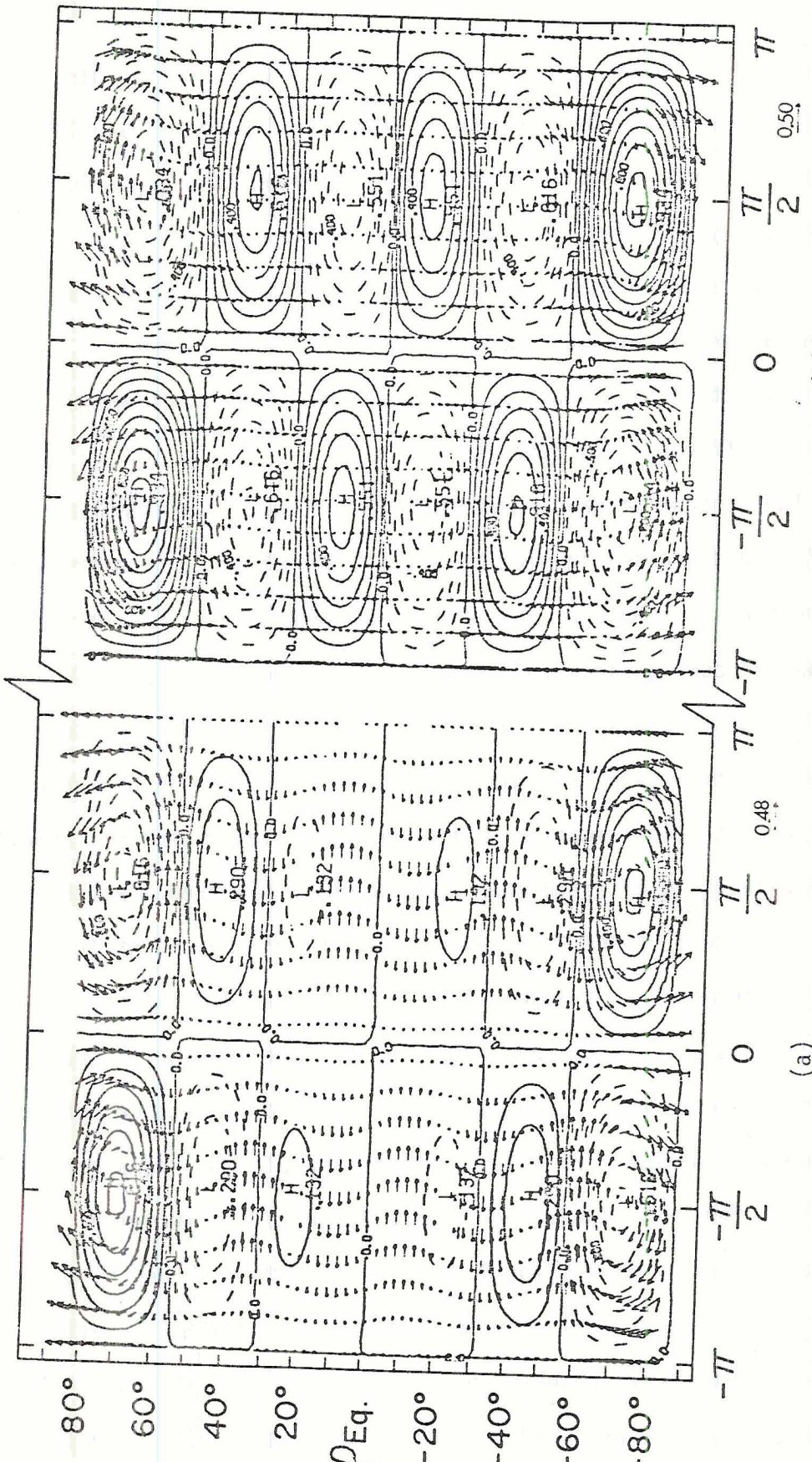

Figure 3.21 The ℓ=6, s=1 Rossby wave (a) and the ℓ=5, s=1 westward gravity wave on the sphere for ε=10. The wind and geopotential fields are normalized such that the total energy is 0.5. The abcissa is $k\lambda$ and the ordinate is the latitude φ in degrees.

to be rapidly dispersed, especially if it contains more energy in the short wave part of the spectrum as shown in Figure 3.6 and Table 3.5. Along this same line, the Rossby wave contribution to the initial condition can yield dispersion of energy to the east and west: the westward dispersion is mainly of long waves and the eastward dispersion is characterized by short waves (Figure 3.6 and Table 3.3). Depending on the spectral distribution of energy in the zonal direction we may observe different time behaviors.

The concept of wave reinforcement introduced by Hoskins et al. (1977) and discussed in section 3.1.1, although based on a frequency argument, also depends on the meridional structure of the wave. Suppose we are considering two waves: wave I (short) and wave II (long). Reinforcement occurs when the two ridges (or troughs) come together, but if the two waves have maxima, minima and zeroes at different latitudes it is not meaningful to consider reinforcements. However, for a wide range of meridional modes we have observed that the meridional structure of the free waves is not highly dependent on the zonal wavenumber (Figures 3.12 to 3.16 are an example).

In this chapter we have also compared the equatorial β-plane eigenfrequencies and dispersive characteristics (distance and time between reinforcement of waves) with the results on the sphere. As expected, for small equivalent depth (large ε) the agreement is fairly good as discussed in section 3.1. In Chapters 4, 5 and 6 we present solutions of the initial value problem on the equatorial β-plane and on the sphere and we observe that the β-plane estimate for $\varepsilon = 10$ is qualitatively good provided the initial conditon and/or forcing is located near the Equator and is of small dimension compared to the

equatorial Rossby radius of deformation. Another constraint is related to the period of time over which we observe the solution: the characteristic time scale of wave reinforcement for Rossby modes is of the order of a few days as shown in Table 3.3 and therefore the evolution of the initial condition over a period of a few hours is expected to be qualitatively similar on the sphere and on the equatorial β-plane.

4. INITIAL CONDITION IN THE GEOPOTENTIAL FIELD

The problem of adjustment of the mass and wind fields when an initial perturbation is given solely in the geopotential field is treated in this chapter. According to section 2.1 such an initial condition can be interpreted as an instantaneous mass source or sink, and the results can be interpreted as internal modes, or as wind shear and thickness in a two level baroclinic model.

In section 4.1, we discuss the general form of the initial condition on the equatorial β-plane. The partition of energy between Rossby modes and gravity modes for a symmetrical ϕ-perturbation as a function of size and latitude is shown in section 4.2. In section 4.2, we also discuss the effect of the partition of energy on the future behavior of the solution. In section 4.4, we discuss the solution on the sphere for the external mode (ε=10). A summary of the results can be found in section 4.5.

4.1 Initial Condition

Let us consider now the initial value problem on the equatorial β-plane with the initial condition given by

$$\xi(x,y,o) = \left[\exp \left\{ - \frac{\left[x^2 + (y-y_o)^2 \right]}{r_e^2} \right\} \right]_o^o \qquad (4.1)$$

The above expression depends on the two parameters r_e and y_o: the first is the e-folding half width of the bell shaped initial condition and the second is the latitude of its center.

The initial condition (4.1) can either be interpreted as a geopotential perturbation in the homogeneous fluid due to accumulation of mass or interpreted as a temperature perturbation in the stratified fluid as discussed in Chapter 2. In particular, for the two-level baroclinic model, the initial condition (4.1) corresponds to a bell-shaped thickness perturbation with maximum unit value at $x = 0$ and $y = y_o$. Taking $\Delta p = 500$ mb and a lapse rate of 2.2° C km^{-1} we easily compute c to be approximately 41 ms^{-1} and therefore $\varepsilon \simeq 500$. The above lapse rate is typical of the conditionally unstable tropical atmosphere. Accordingly, for a unit non-dimensional thickness perturbation we have

$$\hat{\phi} = 1 \rightarrow \phi_{\varepsilon=500} \simeq 1716^2 S^{-2} \rightarrow \Delta T = 6°C \tag{4.2}$$

where ΔT is the temperature difference in the 500 mb layer between levels 1 and 3 in Figure 2.1.

The first step to solve the initial value problem governed by linearized shallow water equations (2.4) with the initial condition (4.1) is to find the Fourier components $\xi_k(y,o)$ of (4.1) according to (2.69). The result is

$$\xi_k(y,o) = \left[\pi^{1/2} \frac{r_e^2}{2} L_x^{-1} \operatorname{erf}\left(\frac{L_x}{r_e}\right) \exp\left\{ -\left[\frac{(y-y_o)^2}{r_e^2} + \frac{r_e^2 k^2}{4} \right] \right\} \right] \tag{4.3}$$

where k is given by (2.28). The e-folding half width of the Fourier spectrum of (4.1) is

$$k_e = \frac{2}{r_e} \tag{4.4}$$

Thus, (4.4) shows that a narrow initial condition in ϕ is projected onto a broad band of zonal waves and vice-versa with maximum $\xi_k(y,o)$ always at k=0. The localization of maxima and shape of the Fourier spectrum of the initial condition is of great importance for the process of dispersion of energy as discussed in Chapter 3.

In most situations to be considered in this chapter, L_x (the zonal periodicity) and r_e are such that the approximation

$$\text{erf}\ (\frac{L_x}{r_e}) \approx 1 \tag{4.5}$$

can be safely applied to (4.3). The next step is to find the projection of $\xi_k(y,o)$ onto the normal modes $\xi_{k,n,r}(y)$ in order to define the expansion coefficient $c_{k,n,r}$ as in (2.83). Once the coefficients $c_{k,n,r}$ are determined, the series expansion for the solution at any arbitrary point (x,y) and time t can be performed (Equation 2.78), and the solution is known within the desired truncation in the zonal wavenumber k and meridional index n.

4.2 Partition of energy

Parseval's theorem allows us to estimate the partition of energy between Rossby and gravity modes given the initial condition (4.1). A measure of the partition is given by the parameter R defined by

$$R = \frac{TE_{RW}}{TE} = \frac{\sum_{\text{all } k,n} c_{k,n,o}^2}{\sum_{\text{all } k,n,r} c_{k,n,r}^2} \tag{4.6}$$

R is the ratio of the total energy in Rossby waves (TE_{RW}) to the total energy in the initial condition (TE). The value of R is important in understanding the dynamical characteristics of the motion evolving

from the initial condition (4.1). Most of the initial energy goes into Rossby modes if R is near unity and the time behavior of the solution is slow (i.e., in approximate geostrophic balance). If R is small, most of the initial energy is in gravity modes which have a fast time character and tend to rapidly propagate outward with little dispersion in the short wave part of the zonal spectrum (Figure 3.6).

Figure 4.1 shows the ratio of total energy in Rossby waves to the total initial energy as defined by (4.6) as a function of the e-folding half-width r_e at y_0=0 and y_0=1.2 as labeled. The scale at the top of Figure 4.1 is in dimensional units for ε=500; in this case the disturbance at y_0=1.2 is centered at approximately 14°N. The ratio increases as r_e increases and it is larger for y_0=1.2 implying that more energy goes into Rossby waves for large disturbances and those centered at higher latitudes. The two curves tend to merge for very large disturbances simply reflecting the fact that the initial condition at y_0=0 and y_0=1.2 are not clearly distinguishable if $r_e >> y_0$.

The smallness of R and its larger value for large-scale geopotential disturbances away from the Equator can be easily explained by the structure and energetics of Rossby waves as discussed in Chapter 3. Most of the total energy in Rossby waves is in kinetic energy form (Figure 3.10) and the geopotential gradients are small near the Equator as required by geostrophy (Figure 3.12-3.13). A small perturbation at the Equator requires a broad spectrum in the zonal wavenumber k according to (4.4) and as k increases the total energy in Rossby waves is almost all in kinetic form (Figure 3.10), i.e. there is more information in the wind field for large k (small zonal wavelength). This explains why less energy goes into rotational modes

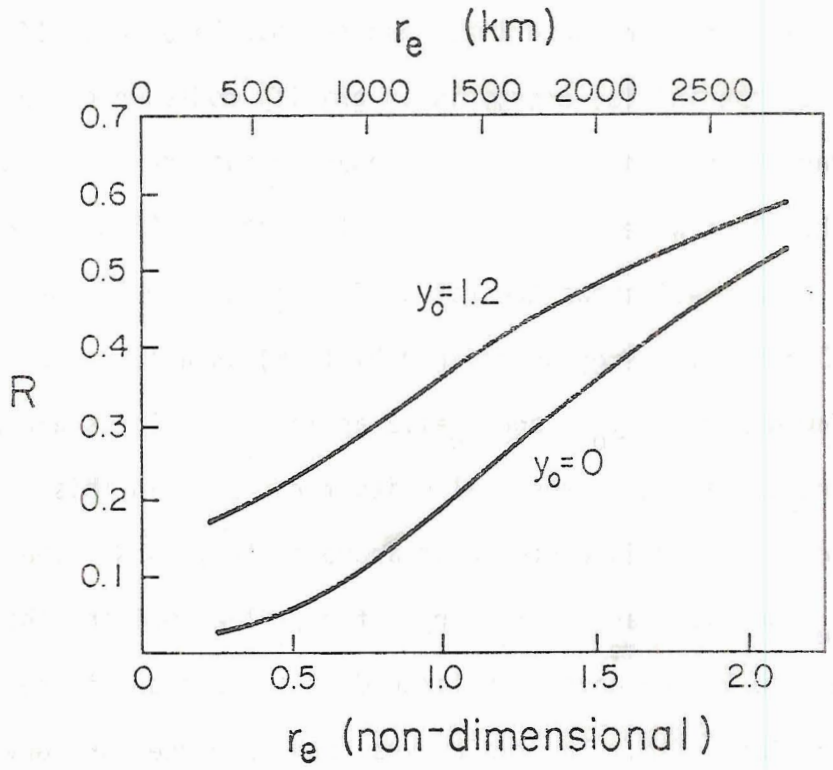

Figure 4.1 Ratio R of the total energy in Rossby modes to the total initial energy as a function of the half width r_e for the initial condition given by (4.1) centered at the Equator (y_0=0) and at y_0=1.2 (14°N for ε=500). The scale at the top is dimensional based on ε=500.

for small-scale geopotential disturbances. Shifting the geopotential perturbation away from the Equator makes it possible for higher order meridional modes to contribute to the representation of the initial condition since large n Rossby modes have maximum geopotential perturbation away from the Equator (Figure 3.13). Figure 3.10 shows that for a fixed zonal wavenumber, the ratio K/E decreases for higher meridional index n Rossby modes and therefore we would expect a larger fraction of the disturbance centered at y_o=1.2 to be represented by Rossby waves.

For a geopotential perturbation with the parameter r_e larger than the equatorial Rossby radius of deformation a more significant percentage of the initial energy goes into Rossby waves. In particular, if the non-dimensional half-width is twice the equatorial Rossby radius (r_e=2) we have an equal partition of energy between Rossby waves and gravity waves.

Knowing the ratio R of the initial condition and the energetics of Rossby waves we can anticipate gross features of the time evolution of the initial value problem. Let us consider for example the development of the broad initial geopotential perturbation r_e=2. In this case the Fourier components (4.4) show that the energy is concentrated near k=0 with a sharp cut-off near the origin. In other words, most of the energy is concentrated in the long wave part of the spectrum. Figure 4.1 shows that 50% of the energy is in Rossby modes and Figure 3.9 shows that in long Rossby waves P=K_u is nearly zero. The initial geopotential perturbation tends to remain at the initial position being slowly dispersed westward (Figure 3.6). Thus, we can say that if the disturbance is large compared to the equatorial Rossby radius of deformation the wind field tends to adjust to the mass field.

On the other hand, a small initial geopotential perturbation has a broad spectrum in the zonal direction according to (4.4) and little energy goes into the slow dispersive Rossby modes according to Figure 4.1. Moreover, Rossby modes of shorter wavelength have more energy in the wind field (Figure 3.10) and therefore the initial geopotential perturbation is drastically reduced. The small energy and slow dispersive motion left after the gravity waves disperse most of the initial energy is primarily in the wind field. Thus, we can say that the mass field has adjusted to the wind field since there was no motion initially.

On the f-plane, the classical geostrophic adjustment problem also predicts a wind adjustment for large disturbances and mass adjustment for small disturbances. However, in this case the comparison is made with the local Rossby deformation radius $\frac{c}{f}$, which tends to infinity as the Equator is approached. When the β-effect is included the relevant parameter is the equatorial Rossby radius of deformation defined by (2.22). We should also bear in mind that the adjusted state is not the same on the f-plane and on the equatorial β-plane as discussed in section 1.3.

4.3 Equatorial β-plane example

In Figures 4.2 to 4.6, we show the evolution in time of the initial condition in the geopotential field given by (4.1) for $r_e=0.35$ ($r_e \simeq 480$ km for $\varepsilon=500$) and $y_o=1.2$ ($y_o \simeq 14°$ N for $\varepsilon=500$). Figure 4.1 shows that for such an initial condition about 20% of the initial energy is described by Rossby modes. The results of such an experiment are therefore representative of relatively small perturbations. If we interpret the results as being produced by the 2-level

baroclinic model with ε=500 we are describing a perturbation of a scale slightly larger than a tropical cloud cluster (Williams and Gray, 1973). Truly localized disturbances require a prohibitive number of eigenfunctions to be accurately reproduced by the series representation given by (2.79) but Figure 4.1 shows that, from an energy partition point of view, the results would not be qualitatively different had we chosen $0.2<r_e<0.5$.

In most of the experiments performed on the equatorial β-plane, we have looked at the solution up to t=8 (t≃3 days for ε=500). We have chosen the period in the zonal direction L_x and a displaying area such that the influence of the periodicity is not felt within the time frame of the experiment. This can be easily computed remembering that the maximum group velocity allowed in the governing equations is the phase speed of pure gravity waves c or, in non-dimensional units, one unit of length per unit time. Thus, if we limit the horizontal area to 3 units in the zonal and meridional direction we can use L_x=12 non-dimensional length units. The value of k is dependent on L_x as shown by (2.28) and the dispersive characteristics of the system are affected by the choice of L_x. However, within the time frame of the experiments this effect is negligible.

Figure 4.2 is an x-t cross section at y=1.2 of the geopotential field for the geopotential disturbance centered at y_o=1.2 with e-folding half-width r_e=0.35. Figure 4.2.a is the complete solution and Figure 4.2.b (scaled by 1000) is the quasi-geostrophic solution, i.e., the gravity modes were eliminated from the series solution (2.78). Figure 4.2.a shows that at t=0 the geopotential perturbation is concentrated around the origin x=0 and that it is rapidly dispersed by

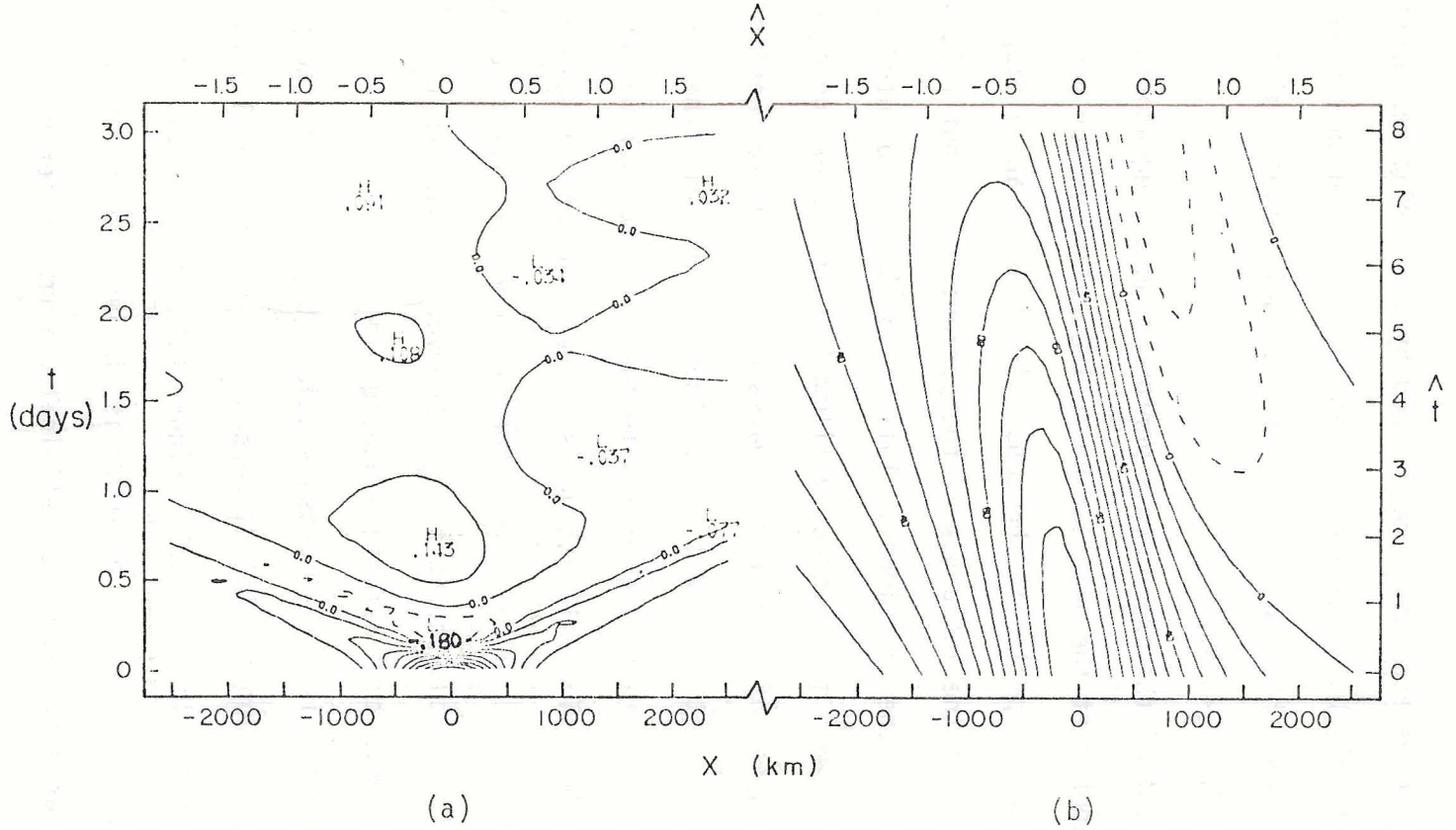

Figure 4.2 x-t cross section of the non-dimensional geopotential field at $y=1.2$ for an initial condition in the ϕ-field defined by (4.1) with $y_0=1.2$ and $r_e=0.35$. Part (a) is the solution including all types of waves and part (b) is the Rossby mode solution. The scales on top and right are non-dimensional and the bottom and left scales are dimensional assuming $\varepsilon=500$. The geopotential field in (b) is scaled by 10,000.

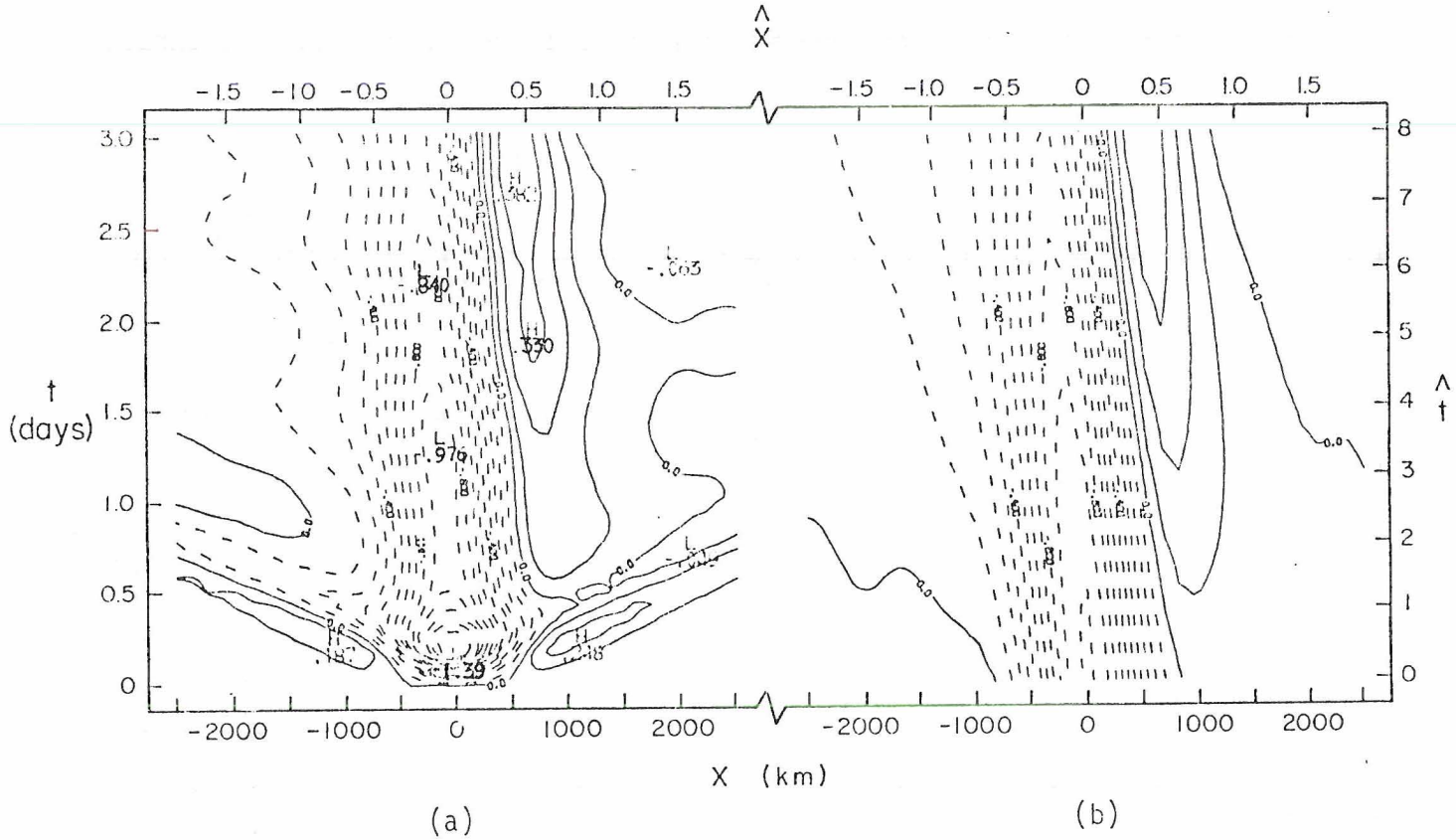

Figure 4.3 Same as Figure 4.2 but for the non-dimensional vorticity field (not scaled).

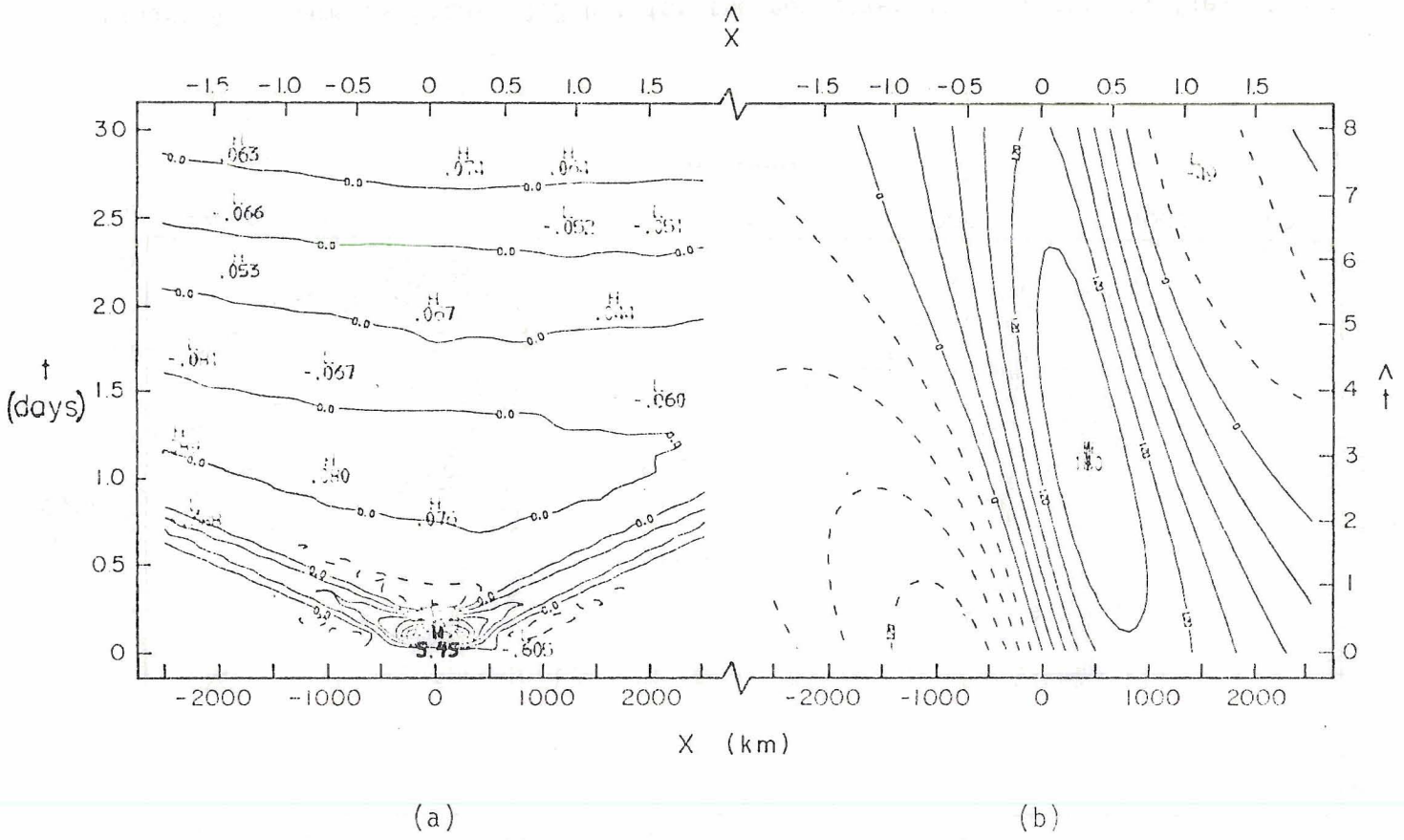

Figure 4.4 Same as Figure 4.2 but for the non-dimensional divergence field. Part (b) is scaled by 10,000.

the gravity modes in the form of fast moving gravity fronts, one propagating towards the west and the other towards the east. The gravity front travels at almost the maximum group velocity allowed in the system (c_g = 1 non-dimensional unit), in agreement with the results on dispersion of gravity waves discussed in Chapter 3.

The amplitude of the ϕ-perturbation is reduced to less than 15% of the initial value after $t \approx 2$ in agreement with the expected behavior based on energy partition (Figure 4.1). Comparing Figures 4.2.a with 4.2.b we clearly see that the geopotential field after t=1 is primarily due to the Rossby mode contribution. The region of positive geopotential perturbation drifts towards the west and at the same time it is spread over a larger area showing the slow dispersive character of Rossby waves. A small negative geopotential perturbation appears to the east of the initial perturbation in Figure 4.2.a and we can trace it to the Rossby mode contribution in Figure 4.2.b. This negative geopotential area is a reflection of the eastward dispersion of shorter Rossby waves (Figure 3.6).

Figure 4.3 and 4.4 show the x-t cross section of the vorticity and divergence fields respectively, at y=1.2. As in Figure 4.2, the complete solution is shown in Figures 4.3.a and 4.4.a while the Rossby mode contribution to the total solution is shown in Figures 4.3.b and 4.4.b. The divergence field in Figure 4.4.b is scaled by 10,000. Figures 4.3 and 4.4 clearly show that the motion left after the passage of the gravity front is primarily due to Rossby waves, with divergence at least one order of magnitude smaller than the vorticity. This result could have been anticipated based on Figure 3.20 which shows that the ratio of vorticity to divergence in Rossby waves is very large. The

vorticity associated with the slow dispersive gravity waves is a small perturbation on the vorticity field of the quasi-geostrophic part of the solution as inferred from Figure 4.3.a and 4.3.b.

The divergence field in Figure 4.4.a progressively becomes more zonal as time increases. This is due to the slow dispersion of long gravity waves as shown in Figure 3.6. Positive and negative zonal bands of divergence alternate in time with a period of approximately 2.5 non-dimensional time units implying a frequency typical of long gravity waves as shown in Figure 3.2. The divergence associated with Rossby modes (Figure 4.4.b) has a negligible contribution to the total divergence field (Figure 4.4.a).

Although the geopotential and vorticity (Figure 4.2.b and 4.3.b respectively) of the Rossby mode contribution to the initial condition at t=0 is symmetrical about the origin x=0, the divergence field (Figure 4.4.b) is antisymmetrical. As a result, the initial development is such that the whole geopotential configuration drifts toward the west; the positive divergence lowers the geopotential perturbation to the east of the initial geopotential maxima, eventually to negative values. Towards the west a slow increase in the geopotential values is observed reflecting the initial convergence shown in Figure 4.4.b.

The non-dimensional divergence field in Figure 4.4 can be made dimensional by the factor $(T)^{-1}$. From (2.21) with $\varepsilon=500$, we have

$$[T]^{-1}_{\varepsilon=500} \simeq 3.1 \times 10^{-5} S^{-1} \tag{4.7}$$

The vertical motion at the middle level of the 2-level baroclinic model can be obtained from the divergence field through the continuity equation as in (2.5.e). In dimensional units (mb day^{-1}) and for

ε = 500 we have

$$\omega_2 = 1.3 \times 10^3 \, (\nabla \cdot V) \text{ mb day}^{-1} \qquad (4.8)$$

Figure 4.4.a shows that the vertical motion oscillates between $\pm$ 16 mb day^{-1} (using (4.2) and (4.8)) for an initial positive temperature deviation of 1° C in the 500 mb layer between levels 1 and 3 of the 2-level baroclinic model (Figure 2.1). The maximum vertical motion associated with the Rossby modes in the x-t cross section shown in Figure 4.4.b is approximately 4 mb day^{-1} at t=3. However, the initial imbalance generates a violent response in the divergence field in a very short time as shown in Figure 4.4.a. The associated maximum upward vertical motion for the 1° C instantaneous heating at the 500 mb level is approximately 750 mb day^{-1}.

From Figure 4.2, 4.3, and 4.4 we conclude that the low frequency Rossby type of motion is dominant in the neighborhood of the initial ϕ-perturbation after approximately one non-dimensional time unit. Figure 2.2 allows us to convert this adjustment time to dimensional units; for c > 5 ms^{-1} we see that one non-dimensional unit is less than one day. In particular, for ε=500 (c=41 ms^{-1}) the quasi-geostrophic motion is dominant after less than half a day (scale on left of Figures 4.2, 4.3 and 4.4). In section 4.5 we further discuss the adjustment time which in our case has to do with the time required for the Rossby mode solution to become dominant. In the classical geostrophic adjustment problem the adjustment time is defined as the time required for the geostrophic solution to become dominant (Cahn, 1945; Obukhov, 1949).

In view of the character of the solution after the fast moving gravity waves leave the area of the initial disturbance, let us consider the two dimensional wind and geopotential fields at particular times. Figure 4.5.a, b, c, and d shows the two-dimensional wind and geopotential fields at t=0, t=2.7, t=5.3 and t=8 for the same experiment discussed so far. In Figure 4.5 the lower and left scales are in dimensional units for ε=500 and the upper and right scales are non-dimensional. As for dimensional time we have: t=0, 1, 2, and 3 days for Figures 4.5.a, b, c, and d respectively. The geopotential field in Figure 4.5 is scaled by 10,000 and the arrows are proportional to the wind speed. At t=2.7 (Figure 4.5.b) we can still see the gravity wave front at the corners of the figure with its characteristic ageostrophic motion. Comparing Figures 4.5.a, b, c, and d, we see that the initial ϕ-perturbation has dropped to less than 10% of the initial value and has moved westward and slightly northward 0.7 non-dimensional length units (900 km for ε=500).

Another interesting detail in the development of the initial condition (4.1) is the appearance of the low ϕ cell to the east of the initial perturbation. This can also be seen in Figure 4.2 and it is basically a Rossby motion feature since it is also shown in Figure 4.2.b. Associated with this low pressure center we observe cyclonic vorticity as shown in the x-t vorticity cross section (Figure 4.3). The intensity of this low pressure center becomes comparable to the remnant of the initial ϕ-perturbation after 3 days (ε=500) at about 5% of the initial value. The vortex generated in geostrophic response to the initial ϕ-perturbation is highly asymetrical and the central pattern is stretched in the zonal direction reflecting

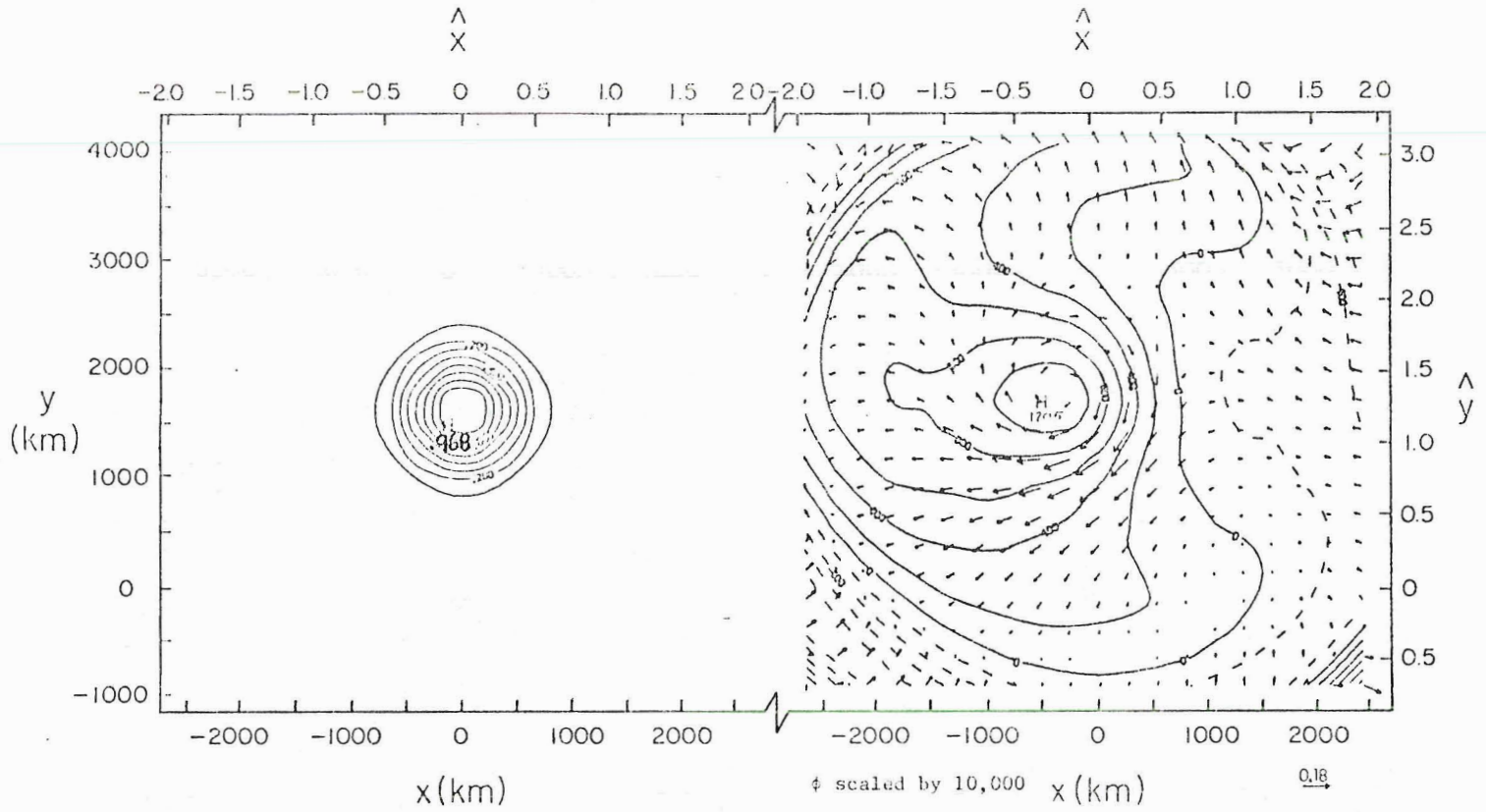

(a) t=0 (b) t=2.7

Figure 4.5 Two-dimensional wind and geopotential fields in non-dimensional units for the initial condition of Figure 4.2 at t=0 (a), t=2.7 (b), t=5.3 (c) and t=8.0 (d). The scales on the top and right are non-dimensional and the bottom and left scales are dimensional for ε=500. For ε=500 the solution is displayed at t=1 day (b), t=2 days (c) and t=3 days (d).

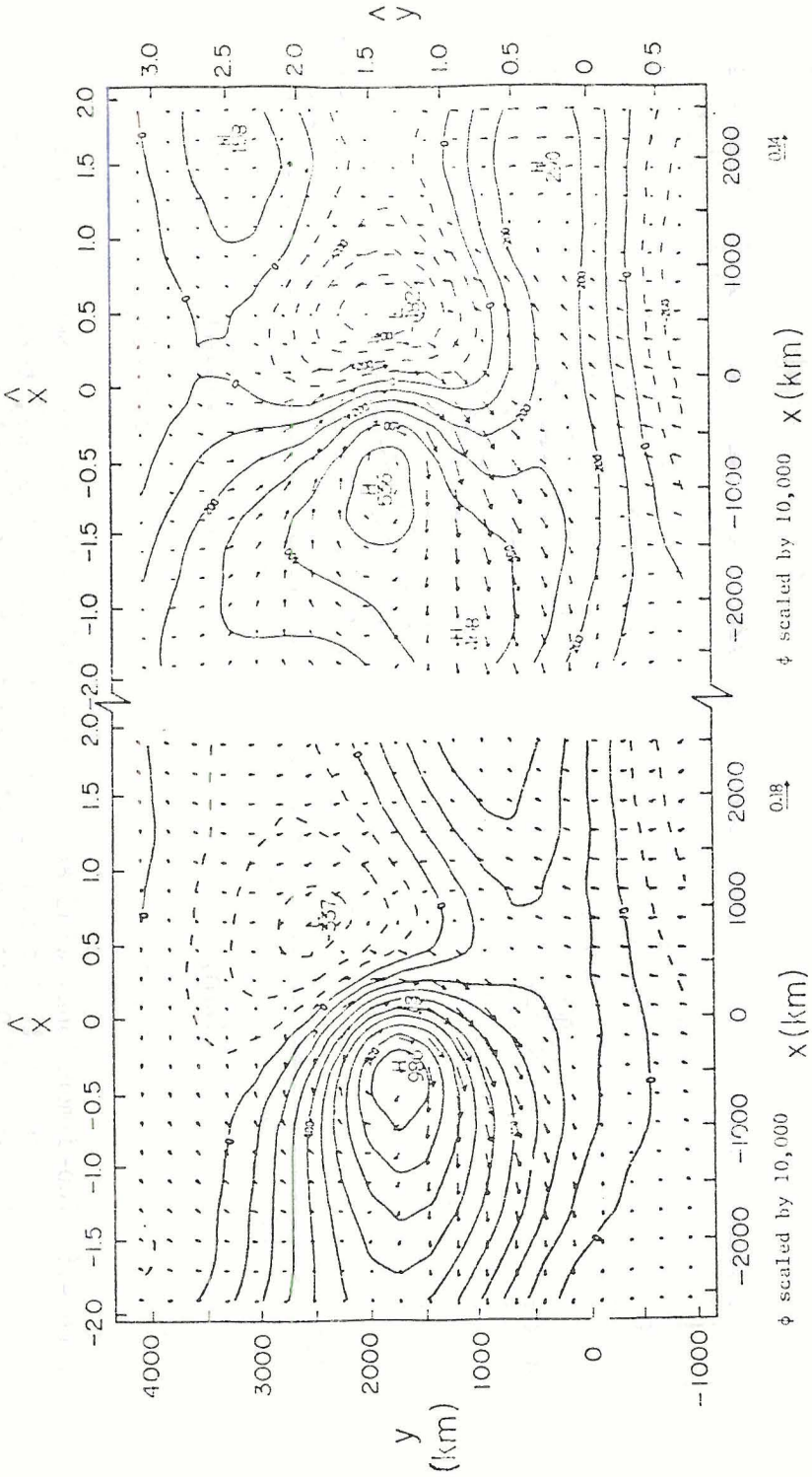
(c) t=5.3
(d) t=8.0
Figure 4.5 (continued)
y (km)
x (km)
φ scaled by 10,000
0.18
0.04

a westward dispersion of the energy in long Rossby waves. The wind maximum in the neighborhood of the initial ϕ-perturbation lies to the SE of the high ϕ center at t=2.7 and 5.3 (Figure 4.5.b and 4.5.c respectively). At t=8.0 the maximum wind is still located to the SE but the whole pattern is not so well characterized by the Rossby wave type motion because, as the energy in Rossby waves gets dispersed, the local effect of slow dispersive gravity waves becomes comparable as shown in Figure 4.5.b.

The two-dimensional vorticity field associated with the wind field of Figures 4.5.b and 4.5.d is shown in Figures 4.6.a (t=2.7) and Figure 4.6.b (t=8.0). The label of the contour lines in Figure 4.6 are non-dimensional; they can be made dimensional by the factor $[T]^{-1}$ which for ε=500 takes the value given in (4.7). At t=2.7 (t=1 day for ε=500) the vorticity field (Figure 4.6.a) is dominated by a fairly symmetrical area of cyclonic relative vorticity and a region of anticyclonic relative vorticity. The anticyclonic region develops to the east of the cyclonic region with maximum intensity towards the southeast. At t=8.0 (t=3 days for ε=500) the intensity of the anti-cyclonic region has decreased while the cyclonic one has increased. At this same time the development of another cyclonic center can be observed near the Equator stretching northward suggesting a cross equatorial transfer of energy in Rossby modes. This new anticyclonic center is not a gravity wave feature since it also appears in the Rossby mode solution (not shown).

In Figure 4.5.d we can identify the anticyclonic vorticity field near the equator as a vortex with little geopotential perturbation. This is because the short Rossby waves, which have positive group

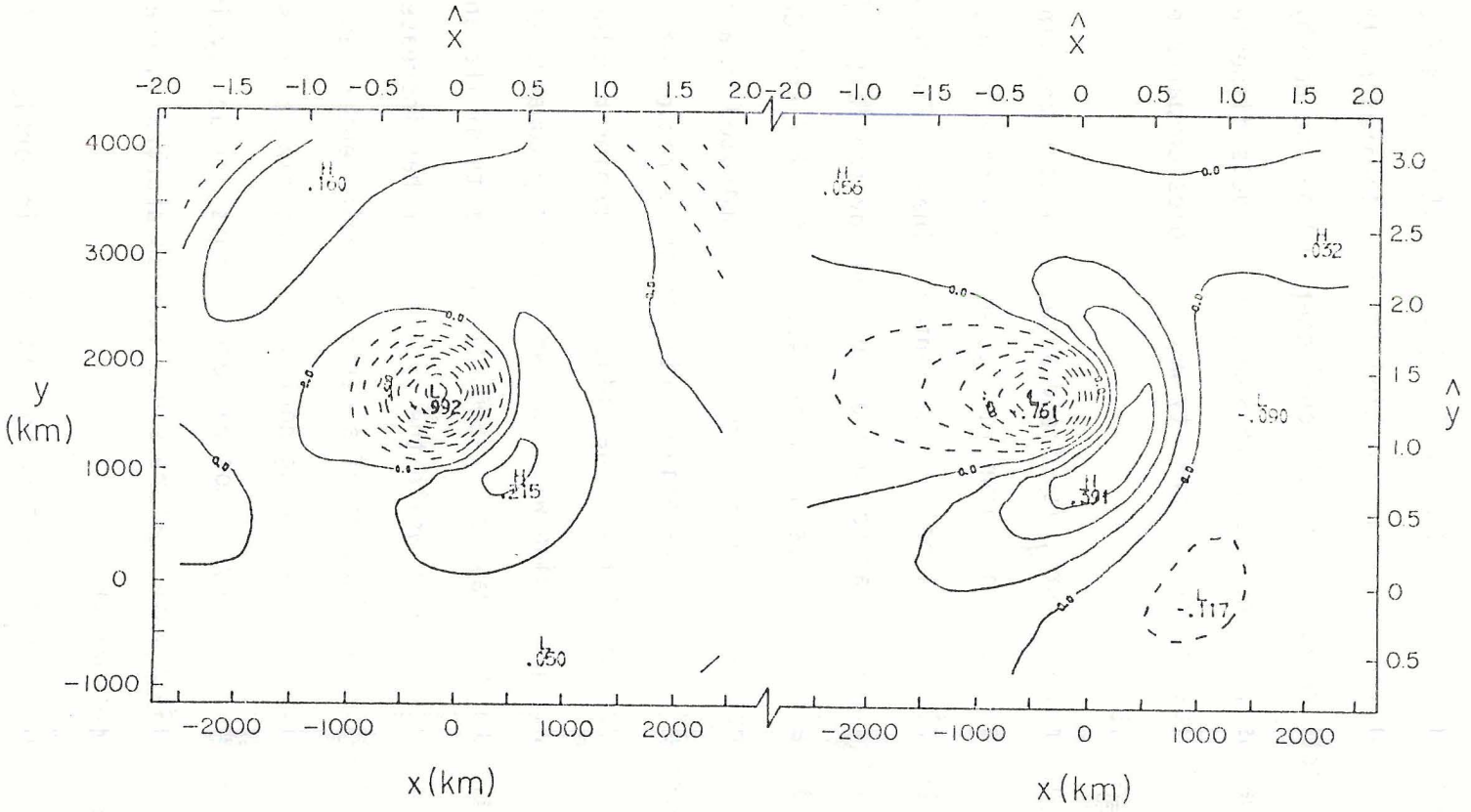

Figure 4.6 The two-dimensional relative vorticity field in non-dimensional units for the wind field shown in Figure 4.5.b and Figure 4.5.d (t=2.7 and t=8.0 or, in dimensional units, t=1 day and t=3 days for ε=500). The scales on top and right are non-dimensional and the bottom and left scales are dimensional for ε=500.

velocity, have small geopotential amplitude near the Equator. The bulk of the geopotential field near the Equator is a manifestation of the long gravity waves which have small group velocity.

The tendency for a SW-NE tilt in the relative vorticity field produced by an initial vorticity source has been noted by Hoskins (1977). Although an asymmetry of the same sort is obtained on the sphere with variable β-parameter, our solution shows that this can also be produced on a β-plane provided the initial disturbance is put away from the reference latitude (the Equator in our case).

The wind and geopotential fields at t=0, 2.7, 5.3, and 8.0 for the bell shaped initial condition discussed so far but centered at the Equator (y_0=0) is shown in Figure 4.7. As in Figure 4.5, the arrows are proportional to the wind speed and the geopotential field is scaled by 10,000.

As predicted in section 4.2, based on the partition of energy (Figure 4.1), the solution now shows much more variation in time. At t=2.7 (Figure 4.7.b) the geopotential field has split into two cells symmetric about the Equator and the maximum perturbation is less than 4% of the initial value. At t=5.3 (Figure 4.7c) and t=8.0 (Figure 4.7.d) the long wave character of the slow dispersive gravity wave is dominant in the geopotential field. However, there are some common features among Figures 4.7a, b, c, and d such as the strong zonal current at the Equator which is characteristic of symmetric Rossby waves (odd meridional number) as shown in Figure 3.12.

Figure 4.8 shows the vorticity field associated with the wind field at t=2.7 (Figure 4.8.a) and t=8.0 (Figure 4.8.b). The vorticity field is antisymmetric with respect to the Equator, implying anti-cyclonic relative vorticity in both hemispheres, and changes little

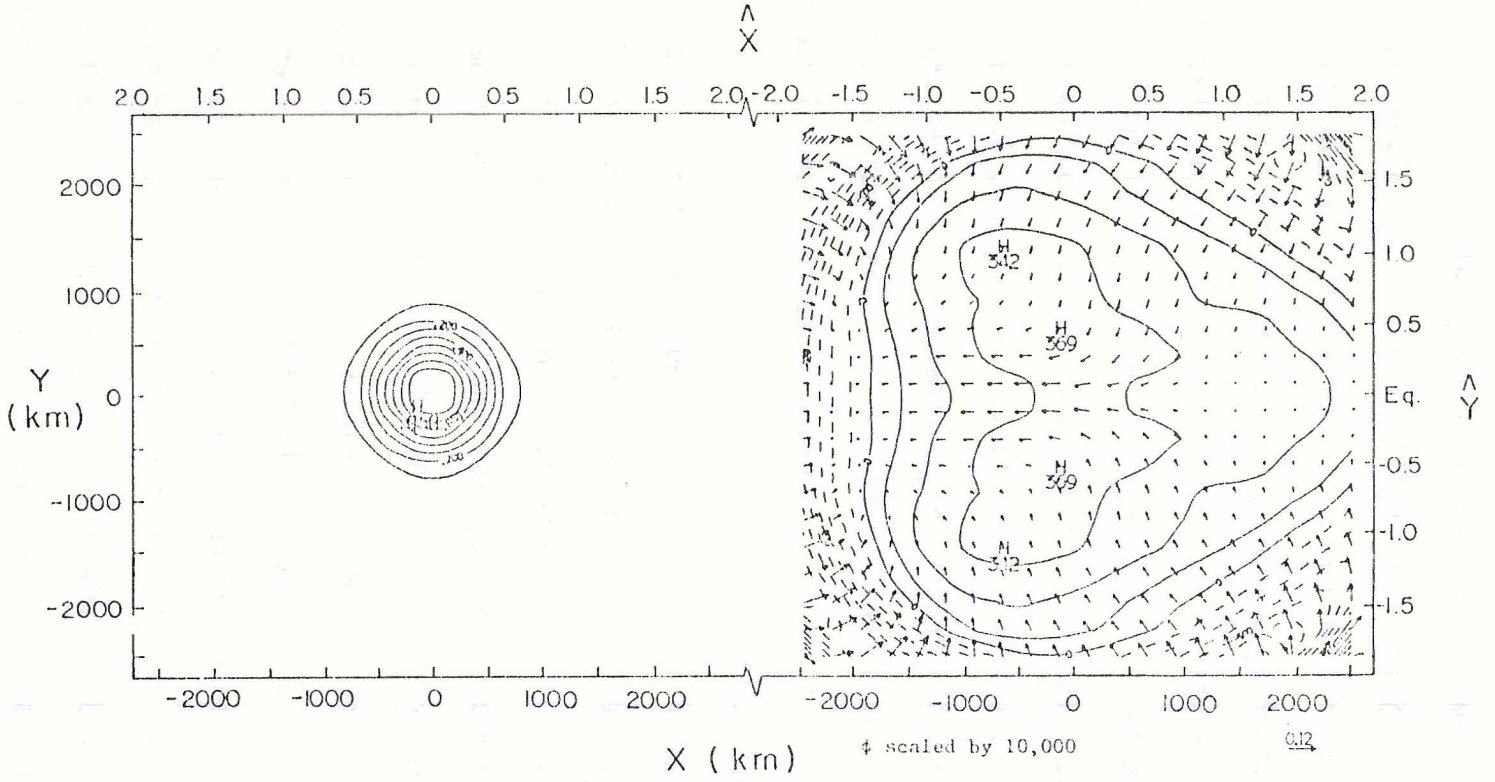

(a) t=0 (b) t=2.7

Figure 4.7 Same as Figure 4.5 but for the bell-shaped ϕ-perturbation given by (4.1) centered at the Equator (y_0=0).

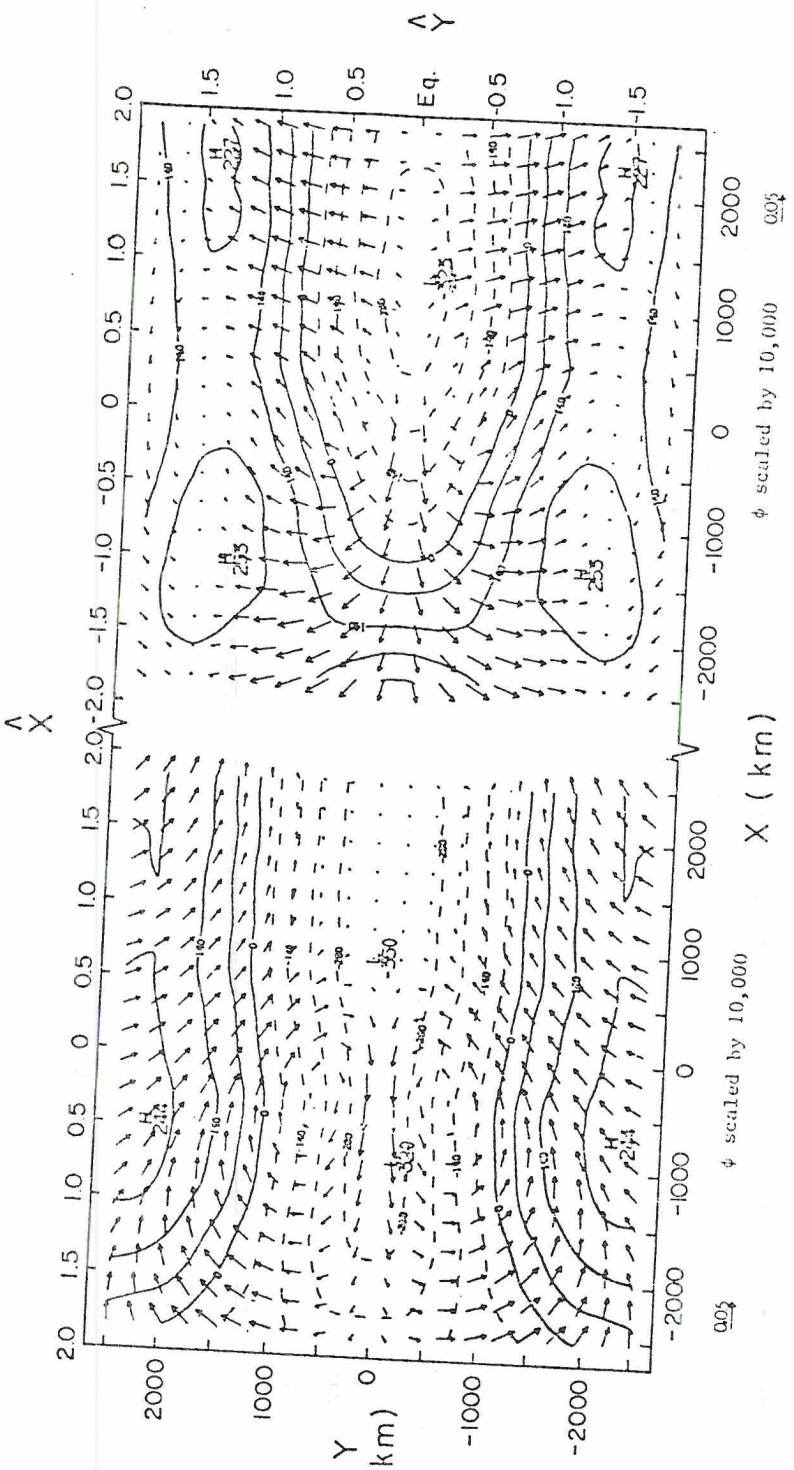

(c) t=5.3

(d) t=8.0

Figure 4.7 (continued)

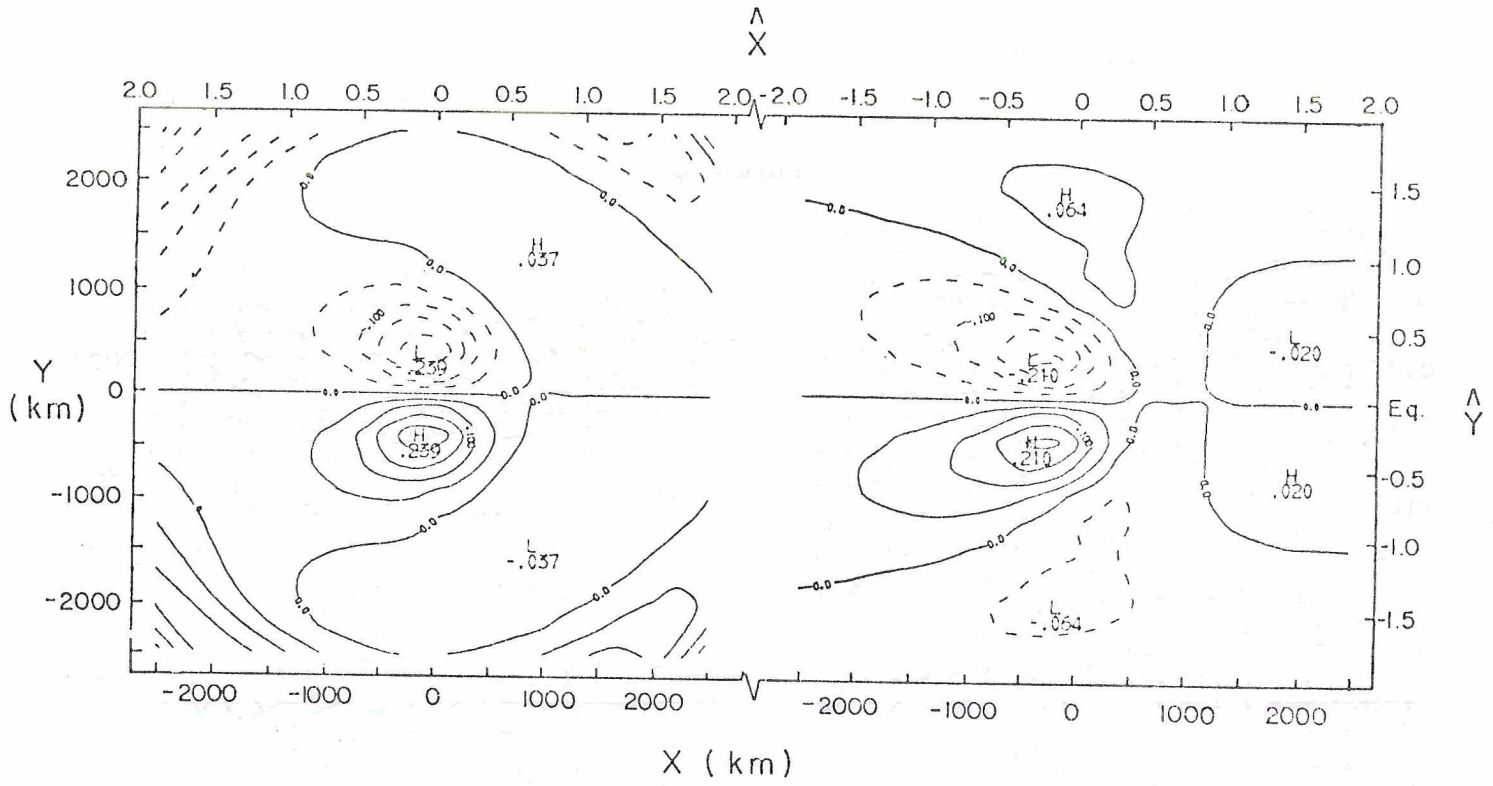

(a) t=2.7 (b) t=8.0

Figure 4.8 Non-dimensional vorticity field corresponding to Figure 4.7.b and Figure 4.7.d (t=2.7 and t=8.0 respectively).

between t=2.7 (t=1 day for ε=500) and t=8.0 (t=3 days for ε=500). The vorticity field in Figure 4.8 is a Rossby mode feature although only 4% of the initial energy goes into Rossby modes. For a 1° C initial perturbation, in the middle level of the 2-level baroclinic model, the maximum absolute relative vorticity is about $1.2 \times 10^{-6} s^{-1}$ at t=1 day compared to 5.1×10^{-6} for the $y_0 = 1.2$ case at the same time (Figure 4.6.a).

The example shown in Figures 4.7 and 4.8 representing the initial evolution of a small bell shaped geopotential perturbation at the Equator shows that the initial condition leaves an impression in the wind field as vorticity. Although the initial geopotential perturbation is quickly wiped away, the wind field remains with a strong eastward zonal current in the neighborhood of the initial perturbation.

Although the initial condition centered at $y_0 = 1.2$ (Figure 4.5) and $y_0 = 0$ (Figure 4.7) differ only by the latitude where they are located, the time behavior of the solution is quite different as predicted in section 4.2 from an energy partition point of view. Besides the fact that only a small part of the initial energy goes into Rossby modes, the peculiar behavior of planetary waves near the Equator, where f is zero, contributes to the distinctive behavior of the ϕ-perturbation centered at the Equator.

4.4 Sphere (ε=10) example

In view of the results obtained in Chapter 3, we solve the problem of adjustment of the mass and wind field on the sphere for the external mode (ε=10). The technique is the same as on the equatorial β-plane except that the basis functions are Hough functions as discussed in section 2.5. It should be remembered that the initial condition

(4.1) has to be corrected for the convergence of meridians in order to be reproduced on the sphere. This effect is small in equatorial regions since it depends on the cosine of latitude but becomes large at higher latitudes.

Figure 4.9 shows the ratio between the energy in Rossby modes and the total initial energy (potential energy in this case) for the external mode on the sphere as a function of the dimensional half width r_e (top scale) for various latitudes as labeled. The lower scale in Figure 4.9 is the half width of the initial geopotential perturbation in non-dimensional units to facilitate comparison with the equatorial β-plane results shown in Figure 4.1.

The partition of energy on the equatorial β-plane for the bell shaped geopotential initial perturbation (Figure 4.1) can be extrapolated to the external mode (ε=10). The equatorial β-plane case centered at y_o = 1.2 closely corresponds to the φ-perturbation on the sphere at 40° N (Figure 4.9). Comparing Figures 4.1 and 4.9 we see that for small perturbations, say $r_e < 0.5$ (or $r_e < 1800$ km for ε=10), the equatorial β-plane and the sphere agree fairly well, mainly for the disturbance centered at the Equator.

In general, more energy goes into Rossby modes on the sphere than on the equatorial β-plane as the size of the initial φ-perturbation increases. The results shown in Figure 4.9 are however, qualitatively in agreement with Figure 4.1 and the discussion in section 4.2 on the partition of energy and the behavior of solution in time are still valid.

Figure 4.10.a, b, c, and d show the wind and geopotential fields at t=0, 6, 12, and 24 hour respectively for the initial condition in the geopotential field centered at λ=-90° and ϕ =25°. The half width

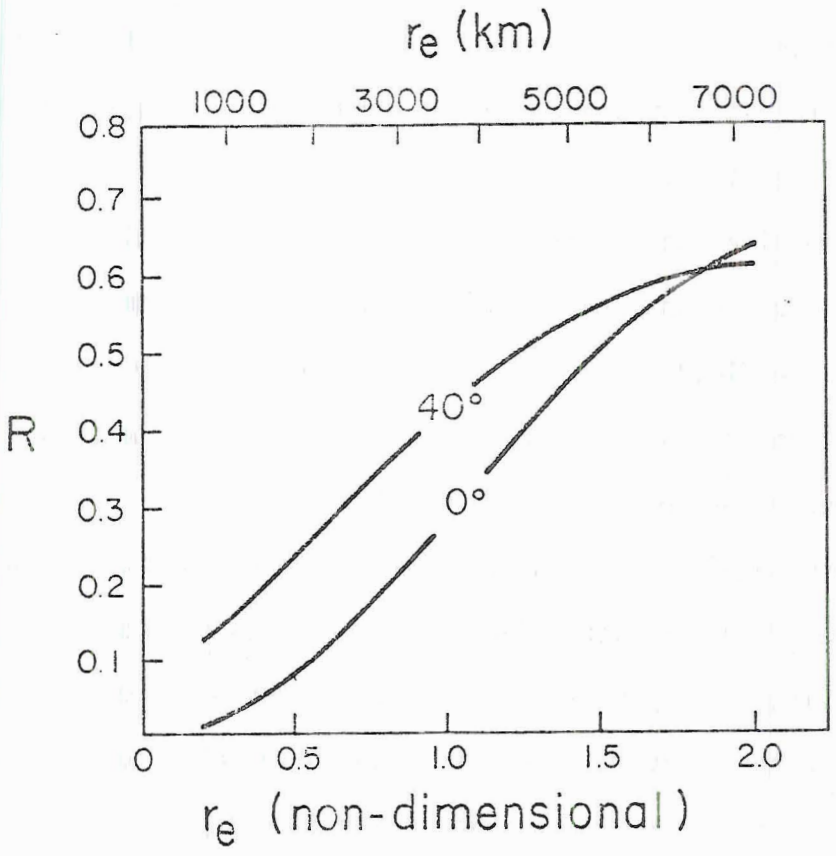

Figure 4.9 Ratio R between the energy in Rossby modes to the total initial energy for a bell shaped initial condition in the ϕ-field given by (4.1) on the sphere (ε=10), centered at different latitudes as labeled.

is approximately 1300 km. At t=0 (Figure 4.10.a) we have a negative geopotential perturbation, i.e. low pressure, and at t=6 hours (Figure 4.10.b) the pressure has increased at the center of the initial perturbation and moved north-northeast. The quasi-geostrophic nature of the flow at the center of the perturbation is already clearly seen as well as the gravity wave front. The initial bell shaped low pressure propagates outwards drawing fluid from the undisturbed region. As the fluid converges towards the ring of low pressure, the pressure builds up behind. However, this is not a symmetrical effect as can clearly be seen after 6 hours (Figure 4.10.b). The high pressure is more intense on the western side of the disturbance and this is due to the different dispersive characteristics of westward and eastward moving gravity waves. The westward moving waves are less dispersive than the eastward waves as shown in Table 3.5 and therefore the western part of the gravity front is sharper.

At t = 12 hours (Figure 4.10.c), a high pressure region to the east of the remnant of the initial low pressure is developing; at t = 24 hours (Figure 4.10.d) it is well defined and the wind field is strongest between the high and the low in geostrophic response to the strong pressure gradient. In Figure 4.10.c the gravity wave front has not yet reached the antipodean point and the bulk of the energy in gravity modes is concentrated in the neighborhood of the gravity front. At t = 24 hours the dispersion of gravity waves can be noticed since the gravity wave type of motion is spread over a much larger area. This is a consequence of the small difference in group velocity of gravity waves as a function of zonal wavenumber and meridional number. Thus, the gravity wave front breaks up and looses

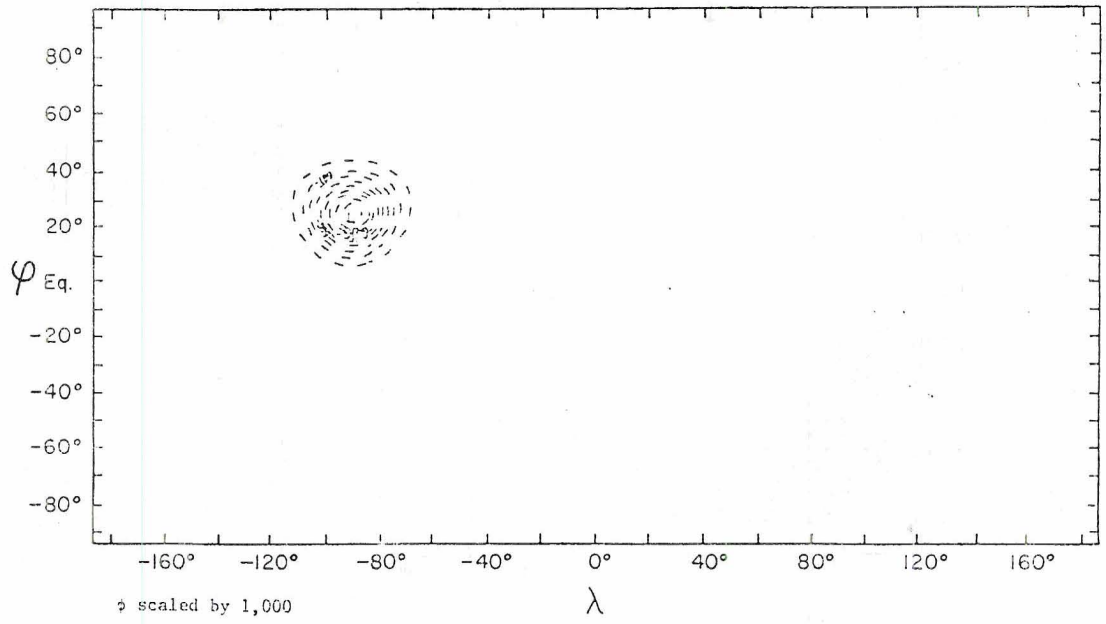

(a) t=0

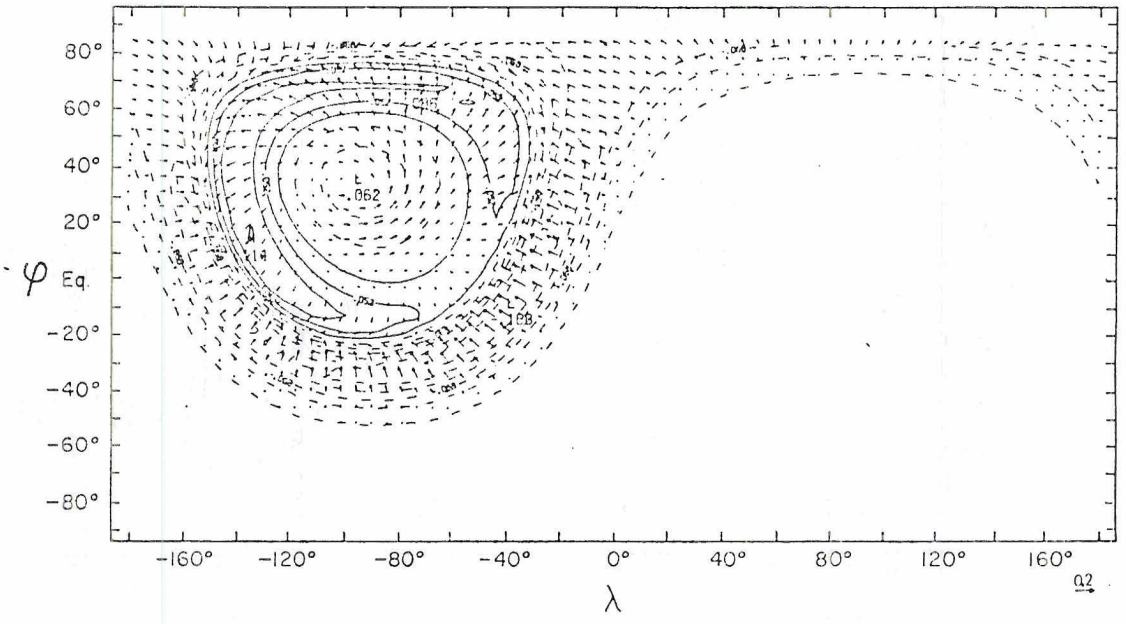

(b) t=6 hours

Figure 4.10 Initial value problem on the sphere for the external mode (ε =10). The initial condition, given by (4.1) and shown in (a), is a ϕ-perturbation centered at $\varphi_c=25^0$ $\lambda=-90^0$. The solution at t=6 hours, t=12 hours and t=24 hours is displayed in (b),(c) and (d), respectively.

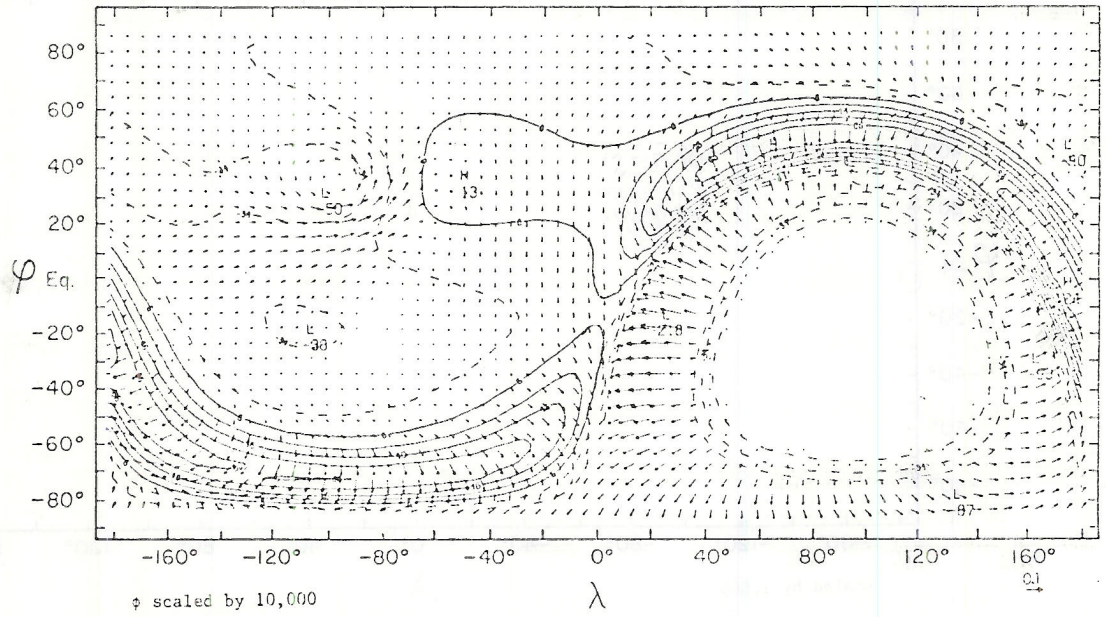

(c) t=12 hours

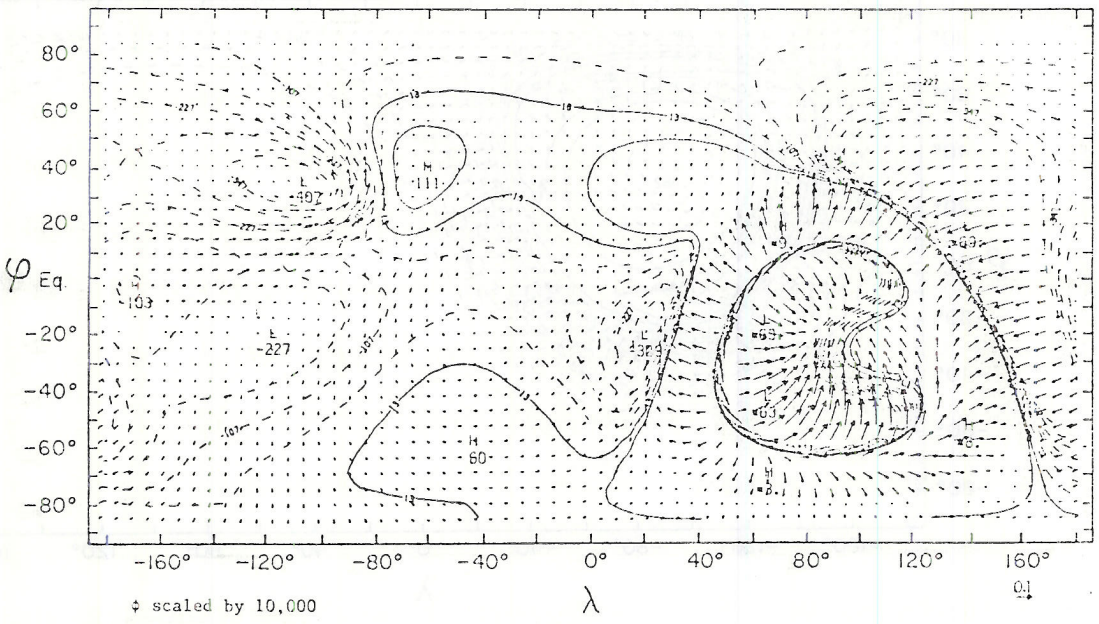

(d) t=24 hours

Figure 4.10 (continued)

its identity after a certain time and eventually there is ageostrophic motion spread over the whole globe with no clear organization since the narrow initial condition contains energy over a wide spectrum.

Most of the characteristics of the Rossby mode contribution to the solution on the sphere are present on the equatorial β-plane solution. As suggested by Figure 4.9, the equatorial β-plane partition of energy assuming ε=10 closely approximates the result on the sphere provided the disturbance is small and located near the Equator. On the other hand, Table 3.3 shows that the equatorial β-plane prediction of group velocity as defined by (3.7) can be large, on the order of 100% for long Rossby waves. However, the time between reinforcement for long waves and low order meridional modes is on the order of 10 days and the group velocity is on the order of 10°-15° day^{-1}. If we look at the solution up to t = 1 day we clearly see that the β-plane solution for ε=10 can reproduce, at least qualitatively, the exact solution on the sphere.

4.5 Summary and Discussion

In this chapter we have presented the solution of the initial value problem governed by the linearized shallow water equations about a basic state at rest subjected to an initial condition in the geopotential field. The analytical expression for the initial ϕ-perturbation is given by (4.1), which is a bell shaped bump centered at latitude y_o with half width r_e. The Fourier components of the initial condition are given by (4.3); the spectrum in the zonal direction is such that a wide initial condition is projected onto a narrow spectral band according to (4.4), which gives the e-folding half width of the Fourier spectrum.

A certain fraction of the ϕ-perturbation initial condition goes into Rossby modes as shown in section 4.1; for such an initial condition most of the energy goes into gravity modes unless the initial disturbance is large compared to the equatorial Rossby radius of deformation (Figure 4.1). For small scale disturbances we conclude in section 4.1 that the mass field adjusts to the wind since very little energy goes into Rossby modes and therefore there is practically no quasi-geostrophic motion left after the gravity waves disperse the bulk of the initial energy.

An example is shown on the equatorial β-plane in section 4.2 for a ϕ-disturbance centered at $y_o = 1.2$ and $r_e = 0.35$. For such initial condition, approximately 20% of the initial energy goes into Rossby modes; this experiment is shown in Figures 4.2 through 4.6. In the two-level baroclinic model discussed in section 2.7 with Lamb's parameter ε=500, the experiment can be interpreted as a sudden heating with maximum heating at 500 mb. Thus, at t=0 we perturb the thickness field without any effect on the wind field. During the time interval between t=0 to t=3 days we notice the fast dispersion of the heating by gravity waves and the development of a cold area to the east of the initial disturbance. At t=3 days the cold and warm areas have comparable intensity and the wind is close to thermal balance since the solution at this time is mostly made up of slow dispersive Rossby modes. Approximately 10% of the input heating is not dispersed by gravity modes. As for possible consequences of these results to the real atmosphere we postpone the discussion to Chapter 7.

In the experiment shown in Figures 4.2 to 4.5 we have noted the fast adjustment time i.e., the time required to observe the Rossby modes contribution to the solution. The time for adjustment T_a can be defined as

$$T_a = \frac{r_e}{c_g} \tag{4.9}$$

where c_g is the characteristic group velocity of gravity waves. Thus, if the initial condition is projected onto the short wave part of the zonal spectrum, the adjustment is fast since in this situation c_g in (4.9) is close to the maximum value allowed in the system (c_g=1), as shown in Figure 3.6. For the bell shaped initial condition considered here, the energy is concentrated near the origin with e-folding half width of the spectrum given by (4.4). Figure 3.6 shows that the group velocity of long gravity waves can be small and therefore the adjustment time is slow; the wider the initial bell shaped ϕ-perturbation, the slower is the dispersion of the gravity modes although more energy goes into Rossby modes in this case. Figure 4.11 is an example of such behavior. It shows an x-t cross section of the divergence field at $y = 1.2$ for an initial ϕ-perturbation defined by (4.1) centered at $y_o = 1.2$ and of half width $r_e = 2$. As in Figure 4.2-4.4, the lower and left scales are in dimensional units assuming ε=500 and the top and right scales are non-dimensional. The non-dimensional contour lines in Figure 4.11 can be made dimensional by (4.7) assuming ε=500.

The divergence field is representative of gravity modes according to Figure 3.20 since Rossby waves are primarily rotational. Figure 4.11 shows that the divergence field is indeed being slowly dispersed

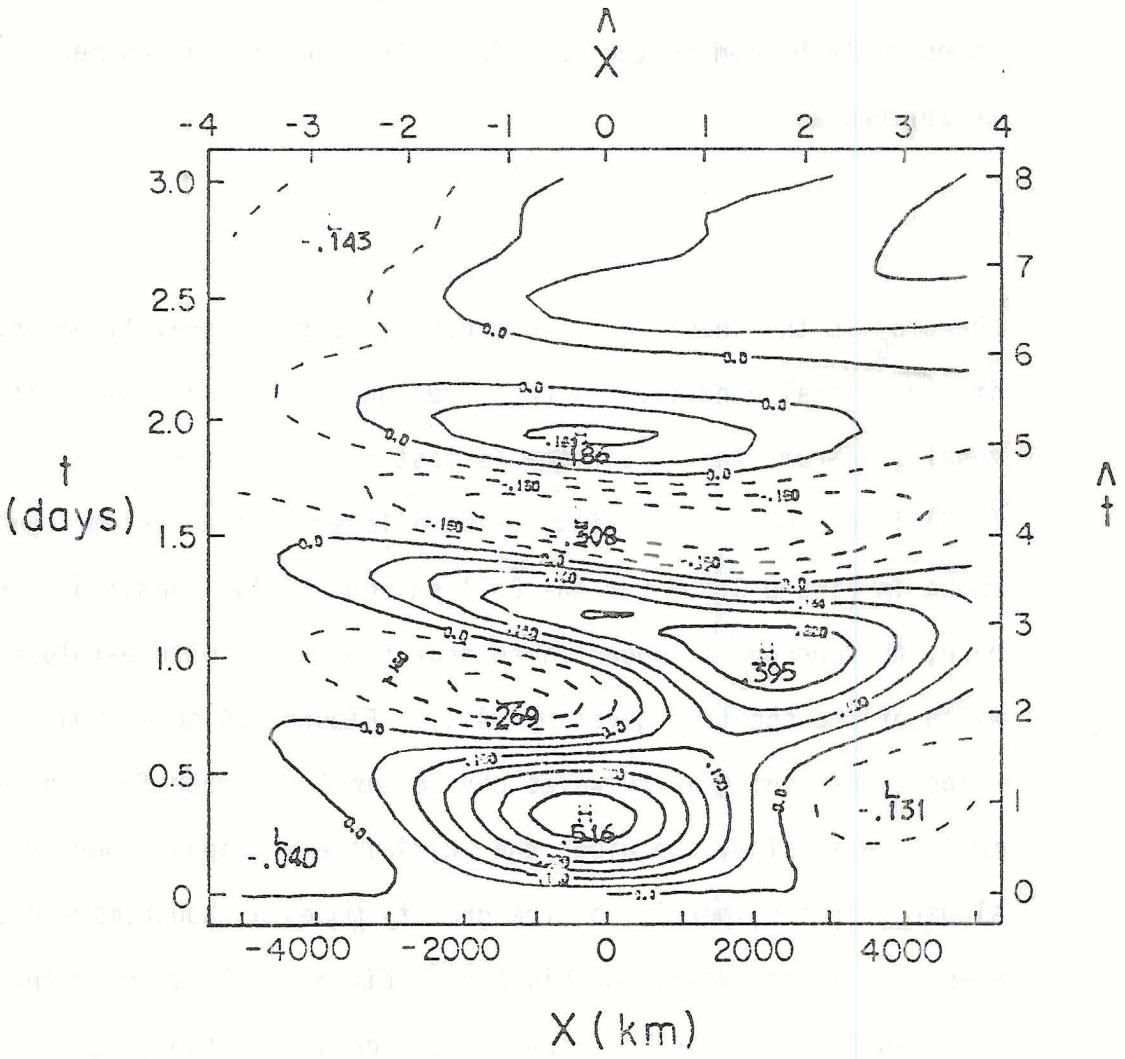

Figure 4.11 x-t cross section of the non-dimensional divergence field at y=1.2 for an initial condition in the geopotential field given by (4.1) with r_e=2.0 and y_0=1.2. The scales on the top and right are non-dimensional and the bottom and left scales are dimensional for ε=500.

since the maximum absolute value decreases with time but not nearly as fast as in Figure 4.3, where the small scale geopotential initial condition is treated.

In section 4.4 we have discussed the barotropic case on the sphere with Lamb's parameter ε=10. From the energy partition point of view, the results are qualitatively similar to the equatorial β-plane if the initial condition is small and near the Equator. Figure 4.10 shows the initial condition and the wind and geopotential fields at t=6 hour, 12 hour and 24 hour for a disturbance centered at 25° of latitude north with e-folding half width of 1300 km. This is a global experiment and therefore it shows unique features of the process of adjustment in a bounded domain. Unless there is selective damping for the gravity wave type of motion, the Rossby wave solution soon becomes overshadowed by the gravity wave activity.

5. INITIAL CONDITION IN THE WIND FIELD

The problem of adjustment of the mass and wind fields for an initial condition in the rotational part of the wind field is discussed in this chapter. It can be interpreted as an instantaneous addition of momentum with no counterpart in the pressure field. As in Chapter 4, the results can either be interpreted as internal modes or as wind shear and thickness of the two-level baroclinic model discussed in section 2.1.

The functional form of a vortex like initial condition is shown in section 5.1 and the partition of energy between Rossby modes and gravity modes is discussed in section 5.2. Examples of the solution of the initial value problem are shown in sections 5.3 and 5.4 (equatorial β-plane and sphere respectively). The results are summarized in section 5.5.

5.1 Vortex initial condition

The initial condition to be considered now has the following functional form on the equatorial β-plane

$$\xi(x,y,o) = \begin{bmatrix} (y-y_o)\exp\left\{-\dfrac{[x^2+(y-y_o)^2]}{r_e^2}\right\} \\ -x\exp\left\{-\dfrac{[x^2+(y-y_o)^2]}{r_e^2}\right\} \\ o \end{bmatrix} \frac{(2e)^{1/2}}{r_e} \qquad (5.1)$$

The radius of maximum wind speed of the initial anticyclonic vortex (5.1) is

$$r_{max} = \frac{r_e}{\sqrt{2}} \tag{5.2}$$

where $r = \sqrt{x^2 + (y-y_o)^2}$. The anticyclonic vortex defined by (5.1) depends on the two parameters r_e and y_o: r_e is the e-folding width of the exponential factor in (5.1) and therefore a measure in the size of the vortex and y_o is the latitude of the center of the vortex. The initial condition (5.1) is normalized by the factor $(2e)^{1/2}\ r_e^{-1}$ such that the maximum wind is one non-dimensional unit for any r_e.

The relative vorticity associated with the initial vortex (5.1) is

$$\zeta = 2\left[\frac{[x^2 + (y-y_o)^2]}{r_e^2} - 1\right] \exp\left\{-\frac{[x^2 + (y-y_o)^2]}{r_e^2}\right\} \frac{(2e)^{1/2}}{r_e} \tag{5.3}$$

and the divergence is zero. Thus, there is anticyclonic vorticity inwards from the radius r_{max} and cyclonic vorticity outwards.

The Fourier coefficients of (5.1) are

$$\xi_k(y,o) = \begin{bmatrix} (y-y_o)L_x^{-1}\ \frac{r_e}{2}\ (\frac{\pi}{2})^{1/2}\ \text{erf}\ (\frac{L_x}{r_e})\ \exp\left\{-\left[\frac{(y-y_o)^2}{r_e^2} + \frac{r_e^2k^2}{4}\right]\right\} \\ i\ \frac{r_e^{-3}}{4}\ L_x^{-1}\ \pi^{1/2}\ \text{erf}\ (\frac{L_x}{r_e})k\ \exp\left\{-\left[\frac{(y-y_o)^2}{r_e^2} + \frac{r_e^2k^2}{4}\right]\right\} \\ o \end{bmatrix} \frac{(2e)^{1/2}}{r_e} \tag{5.4}$$

Thus, the Fourier spectrum of the zonal component of the wind is of the form $\exp(-0.25\ r_e^{-2}\ k^2)$ and the meridional component is proportional to $k \exp(-0.25\ r_e^{-2}\ k^2)$. The Fourier coefficient of the meridional wind of (5.1) is such that the energy peak is located at

$$k_{max} = \frac{2}{r_e} \quad . \tag{5.5}$$

Thus, a wide vortex (r_e large) is projected onto a narrow spectral band and vice-versa. Changing the width of the initial vortex we are able to shift the region of maximum energy in the spectral domain. In the next section we study the partition of energy between Rossby modes and gravity modes as well as the distribution of energy as a function of zonal wavenumber k and meridional index n.

5.2 Partition of energy

We now proceed to discuss the partition of energy in Rossby waves and gravity waves as was done with the initial condition in the ϕ-field in Chapter 4. The initial condition has a flat geopotential field and therefore it has no potential energy; all the initial energy is in kinetic form, and the initial wind field is non-divergent. Rossby waves are primarily rational (Fig 3.20) and short Rossby waves have much more information in the wind field than in the geopotential field since the ratio K/E is large (Figure 3.10). Thus, a small vortex like initial condition of the form (5.1) is expected to be projected mostly onto shorter Rossby waves. In particular, the vortex centered at the Equator has a structure similar to mixed Rossby gravity waves (Figure 3.16), i.e. the equatorial vortex is projected mostly onto the n=0 meridional mode.

As in Chapter 4, Parseval's theorem is applied and the results are summarized in Figure 5.1 where the ratio R (4.6) of total energy in Rossby modes to total energy in the initial condition is shown as a function of r_e for disturbances centered at $y_o = 0$ and $y_o = 1.2$. The

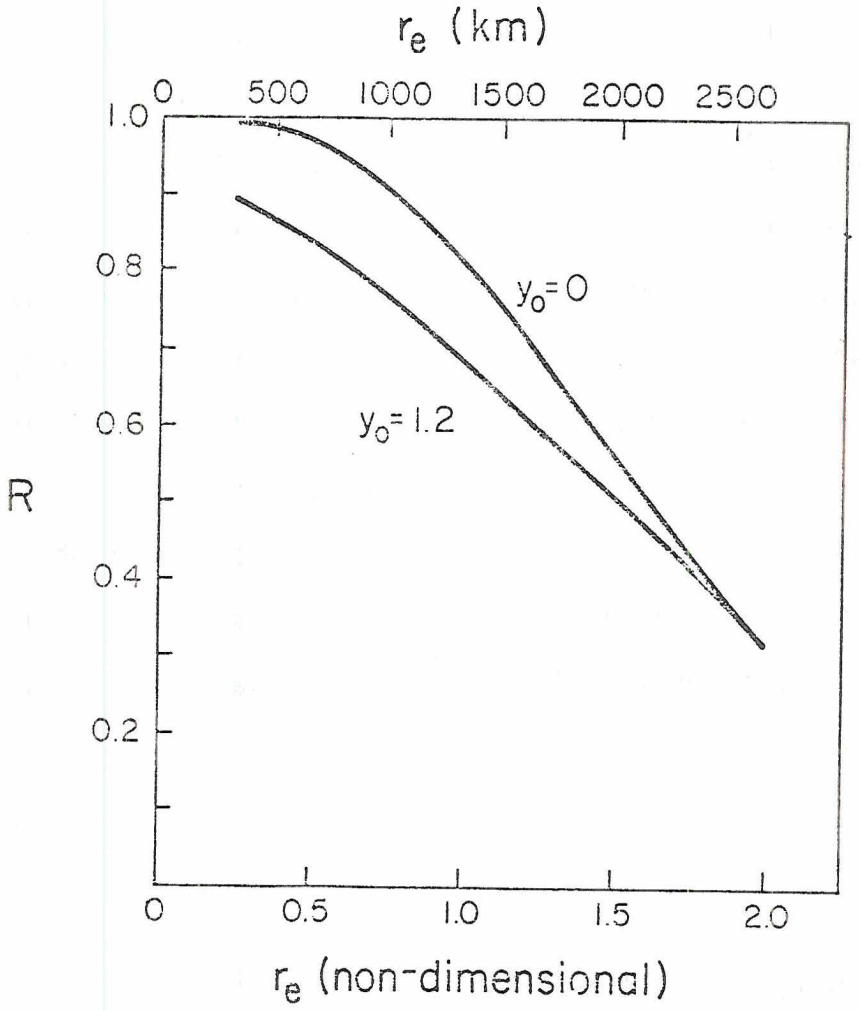

Figure 5.1 Ratio R of the total energy in Rossby modes to the total initial energy as a function of the half-width r_e for the vortex initial condition given by (5.1) centered at the Equator (y_0=0) and at y_0=1.2. The scale at the top is dimensional for ε=500.

scale on top of Figure 5.1 gives r_e in dimensional units assuming ε=500, in which case the disturbances are centered at the Equator and at approximately 14° N.

Figure 5.1 shows that a small vortex of the form (5.1) is projected mostly onto Rossby modes (R>0.95 for a disturbance centered at $y_o = 0$ and r_e<0.5). As the vortex gets bigger and is displaced away from the Equator less energy goes into rotational modes but up to $r_e = 1.5$ the ratio R is larger than 0.5. Thus, contrary to the examples shown in Chapter 4, where the initial condition in the geopotential field was treated, the initial vortex experiment is expected to show small dispersion and to maintain its identity and strength for a longer time.

The partition of energy in the (k,n) space can be studied, through the parameter

$$\overline{c_{k,n}^2} = \sum_{r=0}^{2} c_{k,n,r}^2 \quad , \tag{5.6}$$

where $c_{k,n,r}$ is the projection of $\xi_k(y,o)$ onto the normal modes $\xi_{k,n,r}(y)$. The square of $c_{k,n,r}$ is the energy of the initial condition that is projected onto the mode $\xi_{k,n,r}(y)$. Thus, $\overline{c_{k,n}^2}$ is a measure of energy contained at wavenumber k and meridional mode n including all types of waves.

Figure 5.2 shows the isolines of $\overline{c_{k,n}^2}$ (arbitrary units) for the initial condition (5.1) with $r_e = 0.35$ and $y_o = 0$ i.e., a vortex centered at the Equator. As expected, most of the kinetic energy of the initial vortex is associated with the mixed Rossby gravity wave (n=0) with most energy between wavenumbers 3.0 and 5.0 (non-dimensional). Since the initial condition only excites antisymetric modes the coefficient $\overline{c_{k,n}^2}$ is zero for odd n. As n increases (n even) the energy peak shifts

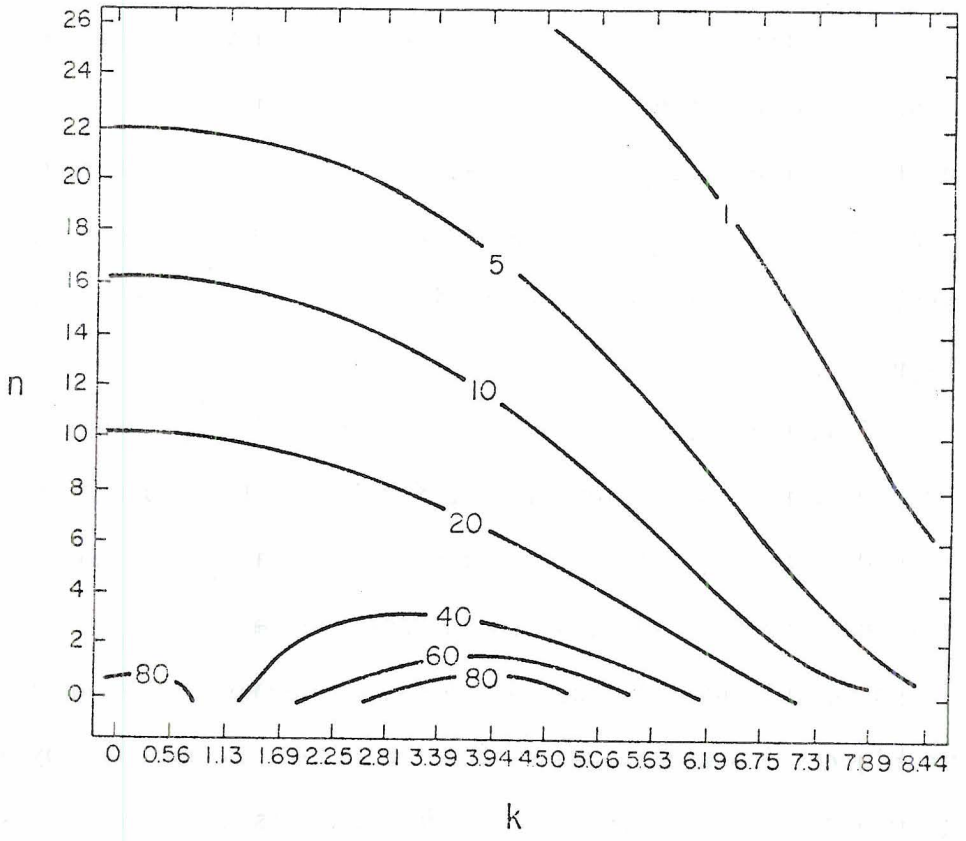

Figure 5.2 Isolines of $\overline{c_{k,n}^2}$ in arbitrary units for the vortex initial condition given by (5.1) with r_e=0.35 and y_0=0 (symmetric modes). $\overline{c_{k,n}^2}$ is defined by (5.6) and is a measure of the energy in all types of waves in wavenumber k and meridional mode n.

towards the origin of the zonal wavenumber axis. This is an effect that can be understood by the energetics of Rossby waves because as n increases, K_v decreases and K_u increases for the same k (Figure 3.9) and therefore we expect high n modes to be a manifestation of the zonal wind component of the initial condition (5.1). The u-component of the Fourier coefficient $\xi_k(y,o)$ in (5.4) is of the form $\exp(-0.25\, r_e^{-2}\, k^2)$ and therefore has a maximum at the origin thus explaining the structure of the isolines of $\bar{c}^2_{k,n}$ for large n in Figure 5.2.

Figure 5.3 and 5.4 show the isolines of $\bar{c}^2_{k,n}$ (arbitrary units) for n odd and even respectively, for the initial condition (5.1) with $r_e = 0.35$ and $y_o = 1.2$. Shifting the initial vortex to higher latitudes has the effect of shifting the highest values of $\bar{c}^2_{k,n}$ to the n=2 mode (even modes) and n=1 mode (odd modes). Comparing the units in Figures 5.3 and 5.4 we notice that there is more energy in odd modes (symmetric modes). In both figures there is a secondary maximum at n=12 (Figure 5.3) and n=7 (Figure 5.4) for any value of k. In Figure 5.4 (odd modes) another energy peak is found at n=21 (about 10% of the maximum value). The general behavior of the distribution of energy in the zonal spectrum is similar to the $y_o = 0$ case i.e., the maximum away from the origin is only found for low n modes. However, in the meridional spectrum (ordinate) we find energy concentrated in definite n-bands when the initial vortex is shifted away from the Equator.

For an initial vortex with parameter $r_e \simeq 1.5$, the initial energy is almost equally partitioned between Rossby and gravity modes according to Figure 5.1. For such an initial condition the energy

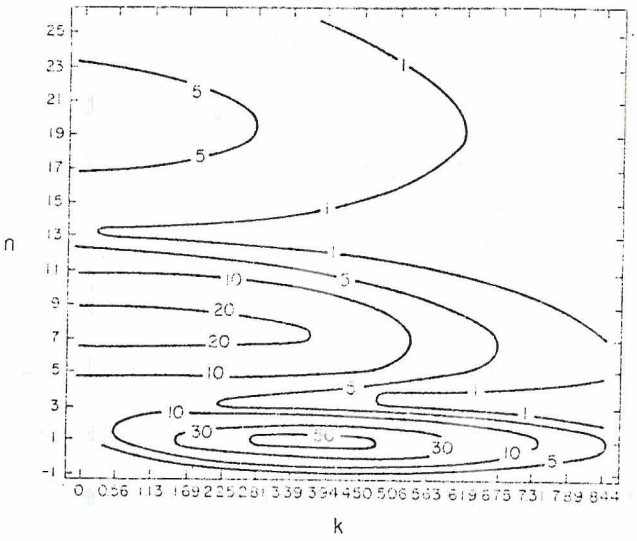

Figure 5.3 Isolines of $\overline{c_{K,n}^2}$ in arbitrary units for the vortex initial condition given by (5.1) with r_e=0.35 and y_o=1.2 (symmetric modes). $\overline{c_{K,n}^2}$ is defined by (5.6) and is a measure of the energy in all types of waves in wavenumber k and meridional mode n.

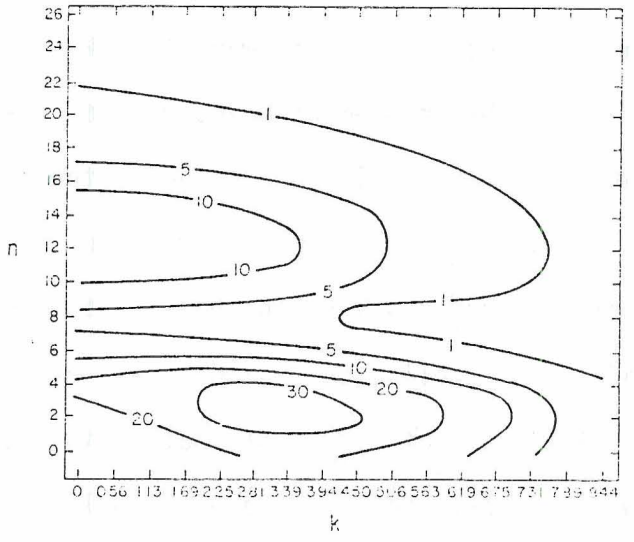

Figure 5.4 Same as Figure 5.3 but for anti-symmetric modes.

is concentrated in a narrow band in the long wave part of the zonal spectrum and according to Figure 3.10 both Rossby and gravity modes have an appreciable amount of energy in both kinetic and potential forms. Thus, a combination of both modes is required to produce the initial condition.

The isolines of $\bar{c}^2_{k,n}$ (arbitrary units) for $r_e = 2$ and $y_o = 0$ are shown in Figure 5.5. The peak in the zonal spectrum is well defined only for n=0 at k = 0.50. However, in this case we know that approximately 70% of the initial energy goes into gravity modes (Figure 5.1) and Figure 5.5 is a combination of Rossby and gravity modes. Figure 5.6 shows the isolines of $c^2_{k,n,o}$ i.e., the energy associated with Rossby modes as a function of k and n. The dashed lines for $k < 2^{-1/2}$ at n=0 is the gravity wave domain of the mixed Rossby gravity wave as discussed in section 2.3.1. Comparing Figure 5.5 with Figure 5.6 we clearly see that the Rossby wave contribution is mostly due to the mixed Rossby gravity wave (for $k > 2^{-1/2}$).

Concerning the problem of adjustment of the mass and wind fields we can anticipate the following, based on the initial energy partition (Figures 5.1 to 5.6). In a small vortex (r_e less than the equatorial Rossby radius of deformation) the bulk of the initial energy is in Rossby modes (shortwaves) and, since these are slowly dispersive (Figure 3.6) and contain more information in the wind field (Figure 3.10), the wind perturbation remains with little dispersion and the pressure adjusts to the wind. Thus, a state of quasi-balance is reached as soon as the energy in gravitational modes leaves the area of the initial disturbance.

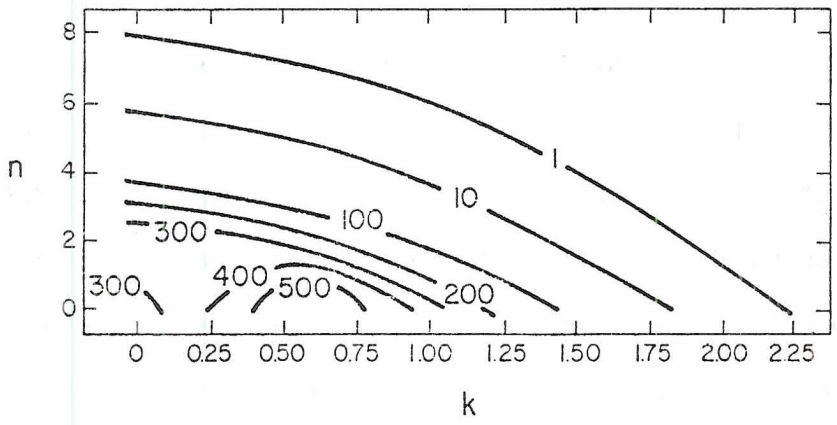

Figure 5.5 Isolines of $\overline{c_{k,n}^2}$ in arbitrary units for the vortex inital condition given by (5.1) with r_e=2.0 and y_o=0 (symmetric modes). $\overline{c_{k,n}^2}$ is a measure of the energy in all types of waves in wavenumber k and meridional mode n.

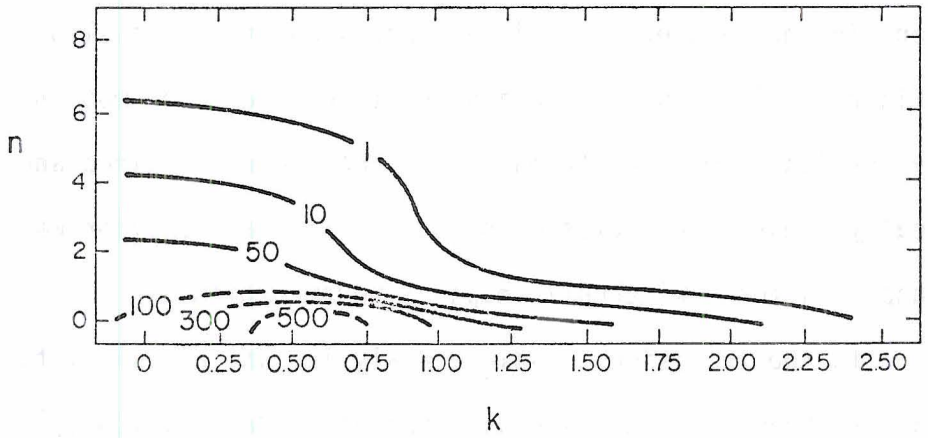

Figure 5.6 Isolines of $c_{k,n,0}^2$ in arbitrary units for the vortex inital condition given by (5.1) with r_e=2.0 and y_o=0 (symmetric modes). $c_{k,n,0}^2$ is a measure of the energy in Rossby waves in wavenumber k and meridional mode n.The dashed line correspond to the mixed Rossby gravity wave.

We should notice that the partition of K_u and K_v in Rossby waves is such that short waves have most of the kinetic energy in the meridional wind component and long waves most of the kinetic energy in the zonal wind component (Figure 3.9). Since $K_u = P$ (3.19) we expect to observe a slow westward dispersion of long Rossby waves appearing as a zonally stretched geopotential and zonal wind perturbation. In the eastward direction the shorter Rossby waves should induce meridional motion and short-wavelength pressure cells in the zonal direction. However, the smaller is the parameter r_e in (5.1) the broader is the spectrum and the time behavior of the solution will not be characterized by a particular zonal wavelength.

On the other hand, a large-scale vortex (compared to the equatorial Rossby radius of deformation) contains more energy in gravitational modes and the energy is concentrated in the long wave part of the zonal spectrum (according to (5.3) and Figure 5.1). The long gravity waves contain the bulk of the initial energy and they are slowly dispersive (Figure 3.6). Thus, the adjusted state, i.e. the motion characterized by the Rossby mode contribution is not clearly defined and we cannot really speak of an adjusted state. A similar behavior was found in Chapter 4 for a wide bell shaped ϕ-perturbation.

In the traditional f-plane analysis, an initial disturbance which is large compared to the Rossby radius of deformation ($\frac{c}{f}$) implies that the wind adjusts to the pressure. Thus, if there is no geopotential perturbation at t=0 there will be no wind in the adjusted state. On the equatorial β-plane (and also on the sphere), the adjusted state is the motion associated with Rossby modes that is left after the

gravity waves are dispersed. Such an adjusted state is observed in our analysis only if the energy in long gravity waves is much less than the energy in Rossby modes. For the bell shaped disturbance considered here, a wide initial perturbation has most of its energy in the longwave part of the spectrum and therefore the concept of adjusted state may be meaningless.

5.3 The vortex initial condition on the equatorial β-plane

Figure 5.7 shows the x-t cross section of the ϕ-field at y = 1.2 up to t = 8.0 ($\simeq$ 3 days for ε=500) for the vortex initial condition with r_e = 0.35 ($\simeq$ 480 km for ε=500) and y_o = 1.2 ($\simeq$14° N for ε=500). The initial disturbance in this experiment is actually a cyclonic vortex and therefore (5.1) has to be multiplied by -1. As mentioned in section 5.1, the maximum wind speed is one non-dimensional unit at t=0 (or 41 ms^{-1} for ε=500). The periodicity in the zonal direction is L_x = 12 for the reasons discussed in section 5.3.

The dynamical response for the initial imbalance is a strong divergence which lowers the ϕ-field to a minimum value of approximately -0.5 non-dimensional units (see (4.2) for conversion to dimensional units assuming ε=500) at t = 0.6 ($\simeq$ 6 hr for ε=500). After reaching the minimum value at t = 0.6 the geopotential increases followed by the formation of a high cell to the east. About 85% of the initial energy goes into Rossby modes and therefore Figure 5.7 is mostly a manifestation of these slow dispersive modes.

Figure 5.8 shows the 2-D structure of the experiment shown in Figure 5.7. The V and ϕ fields are shown in Figures 5.8.a, b, c, and d at t = 0, 2.7, 5.3 and 8.0 (t=0, 1, 2 and 3 days for ε=500) respectively. As time increases the low ϕ-cell generated in response of the

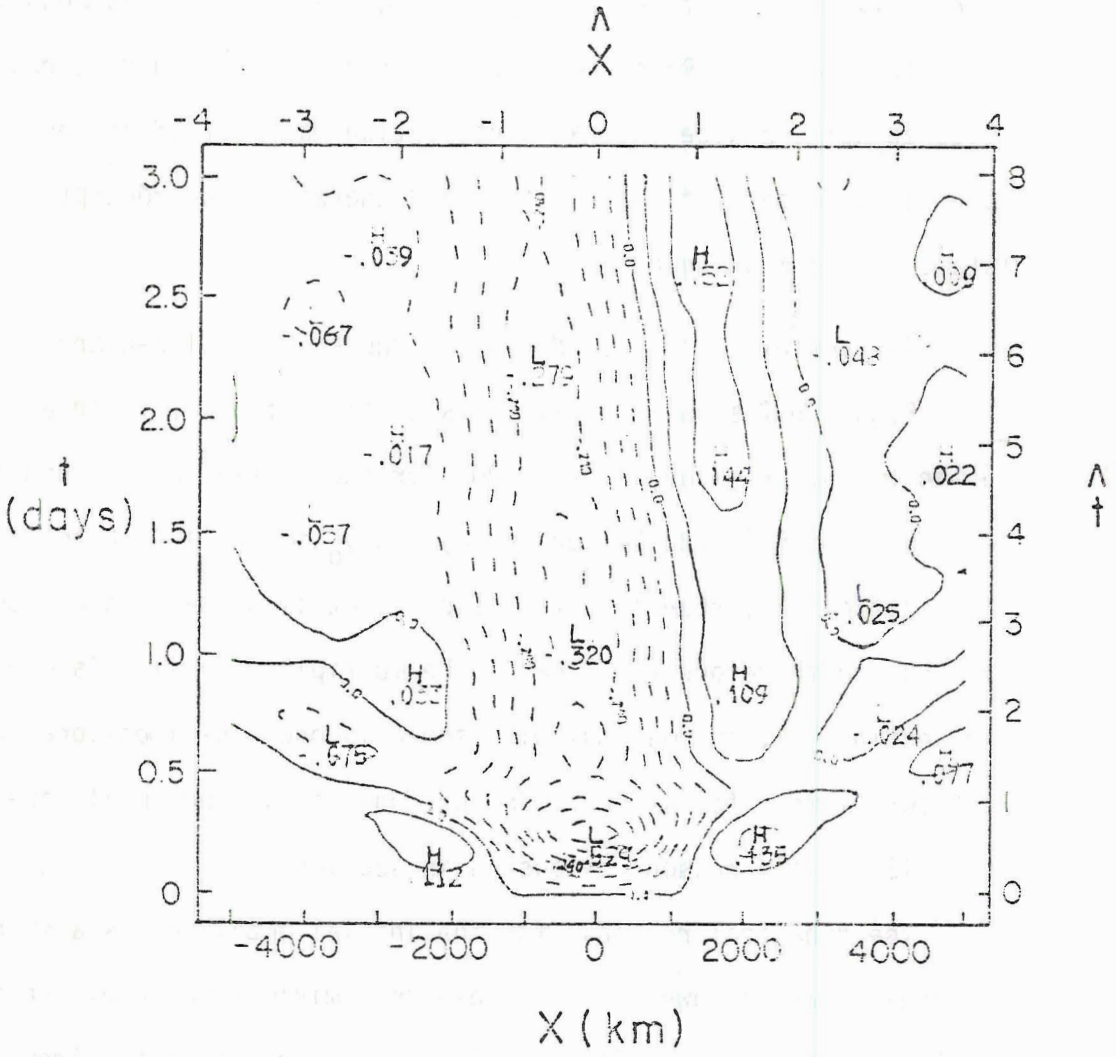

Figure 5.7 x-t cross section of the non-dimensional geopotential field at y=1.2 for the initial condition given by (5.1) with r_e=0.35 and y_0=1.2. The top and right scales are non-dimensional and the bottom and left scales are dimensional for ε=500.

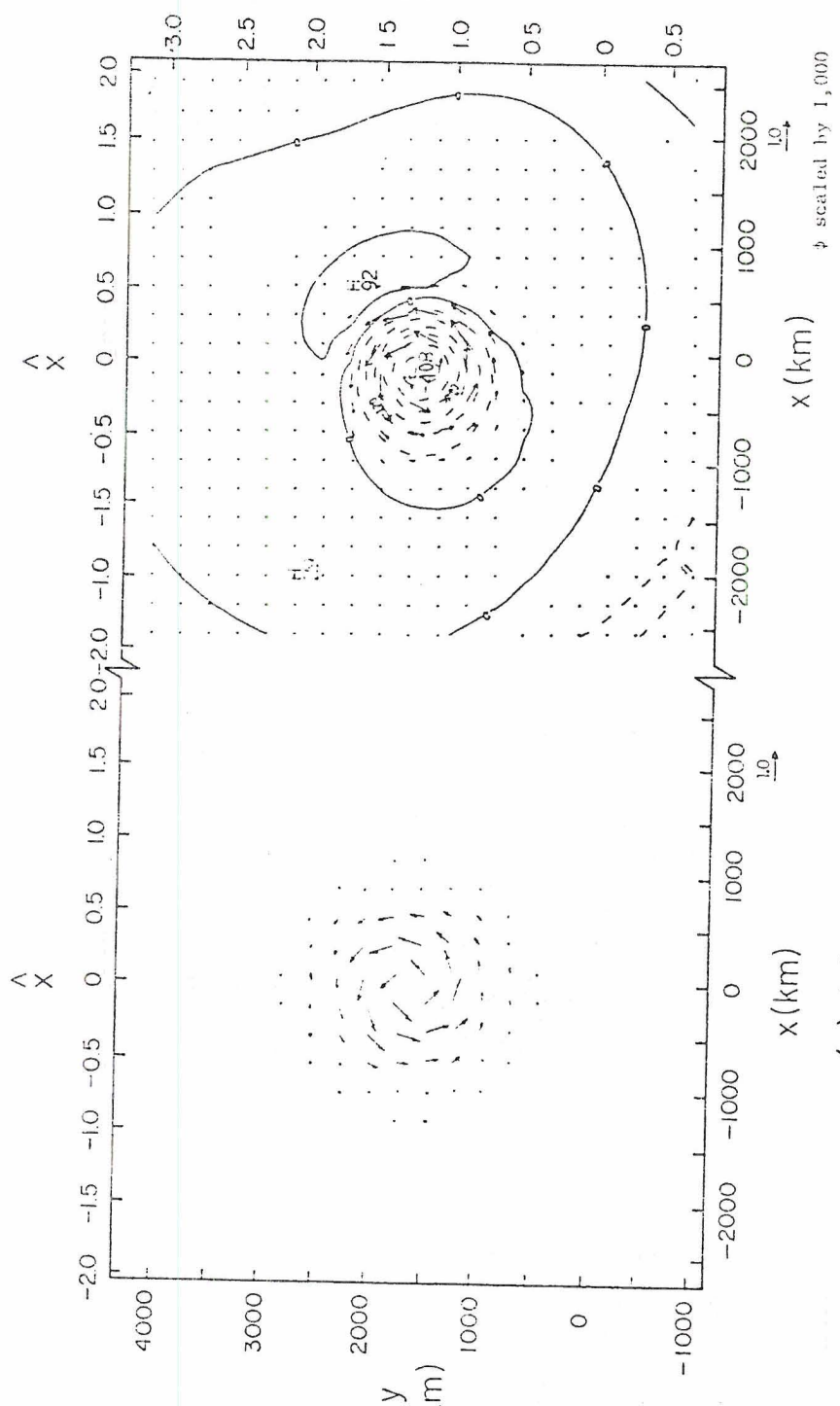

Figure 5.8 Two-dimensional geopotential and wind fields in non-dimensional units for the vortex initial condition given by (5.1) with r_e=0.35 and y_0=1.2. The solution at t=2.7 (t=1 day for ε=500), t=5.3 (t=2 days for ε=500) and t=8.0 (t=3 days for ε=500) is shown in (b), (c) and (d), respectively. The scales on top and right are non-dimensional and the bottom and left scales are dimensional for ε=500.

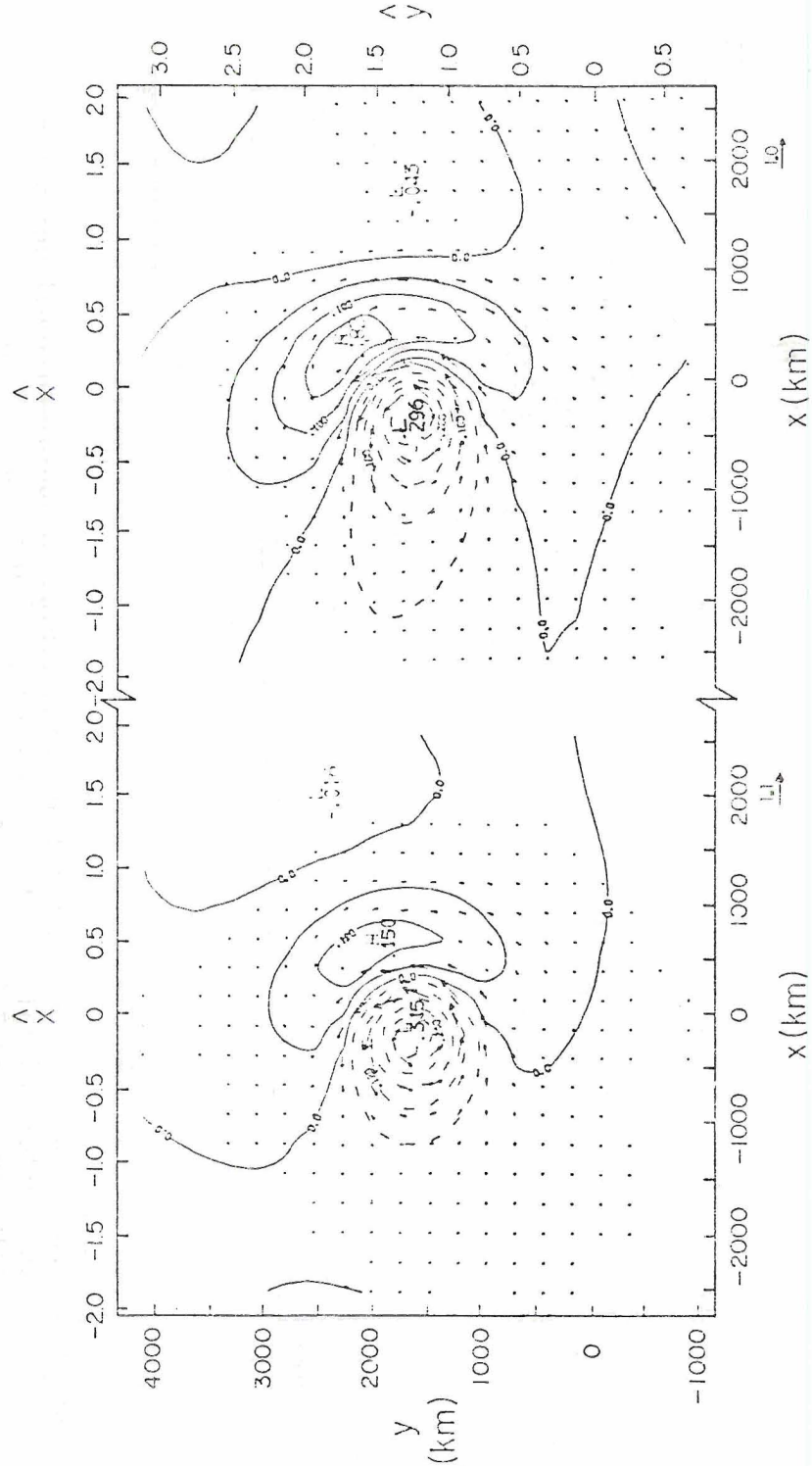

(c) t=5.3 (d) t=8.0

Figure 5.8 (continued)

initial imbalance drifts towards the west and is stretched in the zonal direction. The high ϕ-cell noticed in the x-t cross section is now seen to be more intense in the NE quadrant. As time increases, the low and the high geopotential regions become comparable but the wind field associated to that high cell is primarily meridional. This is in agreement with the qualitative observations made in section 5.2 based solely on the partition of energy and the characteristics of the free modes.

The intensity of the wind field remains practically unchanged up to $t = 8.0$ but the initial symmetrical vortex is intensified between the low and high centers in accordance with the increased pressure gradient.

In the two-level baroclinic model (section 2.1) this experiment can be regarded as an initial condition with cyclonic shear. Thus, the initial response is a cooling in the center of the vortex (thickness decreases) and at the same time a warming occurs in the NE quadrant. In terms of vertical motion, the cyclonic shear induces an upward vertical motion in the center and downward motion in the NE quadrant. Although the vertical shear retains the same intensity, strong east-west asymmetries are observed.

Alternatively, we could look at wind and geopotential fields shown in Figure 5.8 as representing the 750 mb level. In this case the geopotential field at 250 mb would be the negative of the field at 750 mb and the wind would have to be reversed but with the same magnitude. Thus, the initial condition shown in Figure 5.8 can be regarded as a anticyclone overlaying a cyclone. However, in this case

the lowering of the geopotential field at 750 mb and the associated rising at 250 mb implies a thickness increase and, through the thermodynamic equation (2.5.g), sinking motion. The vertical shear in this situation is anticyclonic.

Thus, if the initial condition is an anticyclonic shear with no impression on the temperature field, the dynamic response of the fluid is to set up a sinking motion initially so as to bring the flow to approximate thermal balance. In dimensional units (assuming ε=500), the initial development of the ϕ-field shown in the x-t cross section (Figure 5.7) implies a maximum vertical motion of approximately 40 mb day^{-1} (up or down depending on whether the initial shear is cyclonic or anticyclonic) if the maximum vertical shear ($V_d = V_1 - V_3$) is 1 ms^{-1}.

Figure 5.9 shows the two-dimensional structure at t = 2.7 of the same initial vortex treated so far but centered at the Equator ($y_o = 0$). In both cases ($y_o = 0$ and $y_o = 1.2$) the initial vortex remains almost unchanged up to t = 2.7. The initial condition is such that u is antisymmetric and v is symmetric and therefore only anti-symmetric modes are excited (n is even).

The pressure response is, however, quite different for an initial vortex centered at $y_o = 0$ and $y_o = 1.2$. For the vortex centered at the Equator the intense pressure response occurs to the NE and SE (high and low respectively) though of smaller magnitude than the previous case shown in Figure 5.8.a (notice that the pressure field is scaled by 1000 in Figure 5.8.a and by 10,000 in Figure 5.9). Although the mass readjustment within the initial vortex is small, Figure 5.9 shows

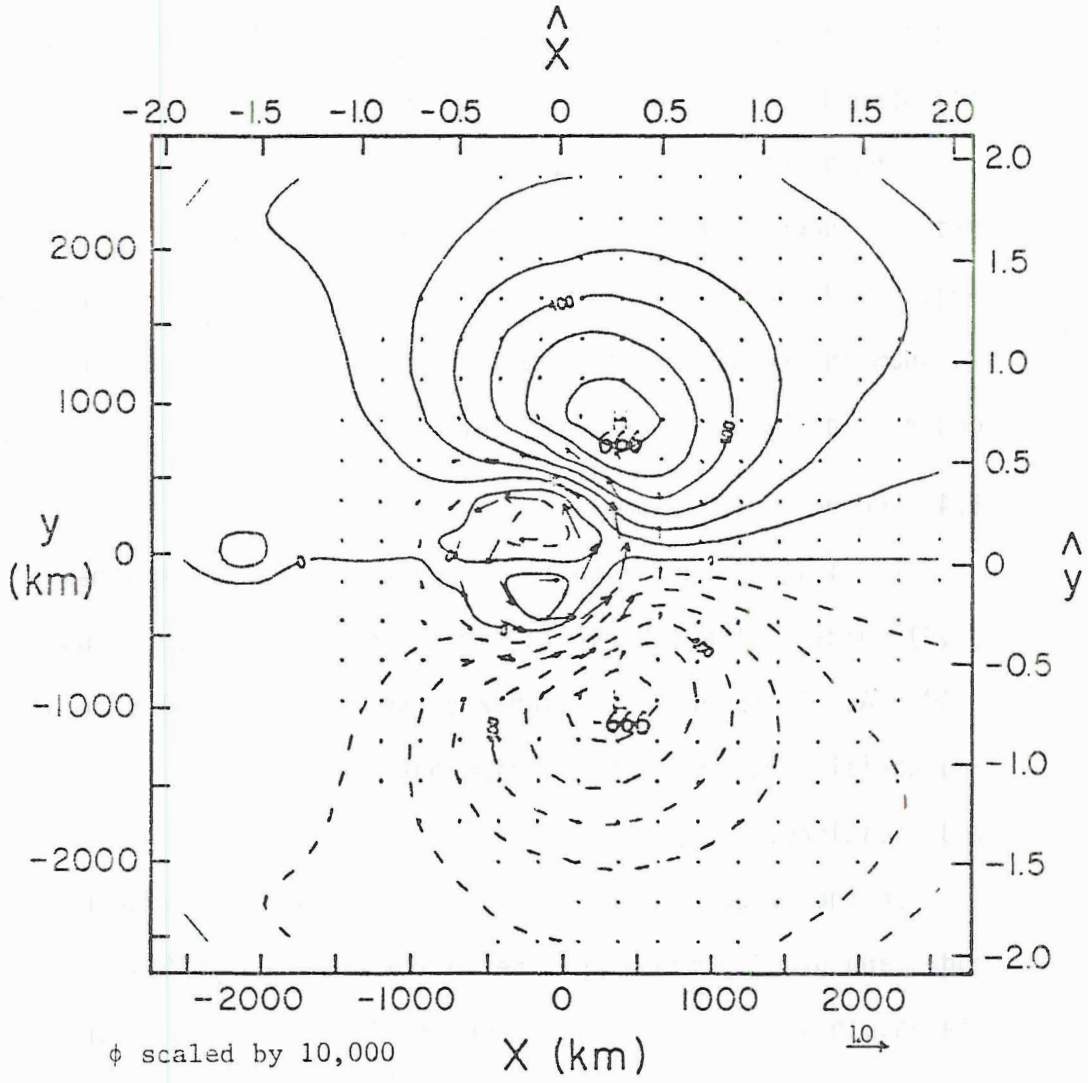

Figure 5.9 Two-dimensional geopotential and wind fields in non-dimensional units for the vortex initial condition given by (5.1) with r_e=0.35 and centered at the Equator (y_0=0) at t=2.7 (t=1 day for ε=500). The scales on top and right are non-dimensional and the bottom and left scales are dimensional for ε=500.

that the ϕ-field lowers in the northern hemisphere in response to the cyclonic flow while the geopotential field goes up in the southern hemisphere in response to the anticyclonic flow.

The barotropic response is similar to the equatorial β-plane results shown in this section provided we appropriately interpret the length and time scales (see Figures 2.2 and 2.3). In the next section we show the results on the sphere for ε=10 over the whole globe in order to emphasize the process of dispersion of energy.

5.4 Sphere (ε=10) example

The initial condition (5.1) can be easily transformed to the (λ,φ) space on the sphere and projected onto the Hough functions for ε=10. As discussed in section 2.5 the method of solution of the equatorial β-plane can be carried out on the sphere with minor modifications.

On the sphere (ε=10) the partition of energy between Rossby modes and gravity modes for the vortex defined by (5.1) is similar to the equatorial β-plane case shown in Figure 5.1 for a vortex centered at the Equator and r_e < 1500 km. For a vortex centered at 40° ($y_o \simeq 1.20$) the equatorial β-plane prediction of the ratio R defined by (4.6) is within 50% for $r_e \leq$ 1500 km.

Figure 5.10 shows the development in time of an initial cyclonic vortex centered at the Equator with r_e = 0.40 ($\simeq$ 1500 km for ε=10). The initial condition is shown in Figure 5.10.a and the geopotential and wind field at t=8 hr, 24 hr., 48 hr., 96 hr., and 144 hr. are displayed in Figures 5.10.b, c, d, e, and f respectively. Only half the globe is shown in Figure 5.10 and the geopotential field is scaled by 10,000; the arrows are proportional to the wind speed as indicated.

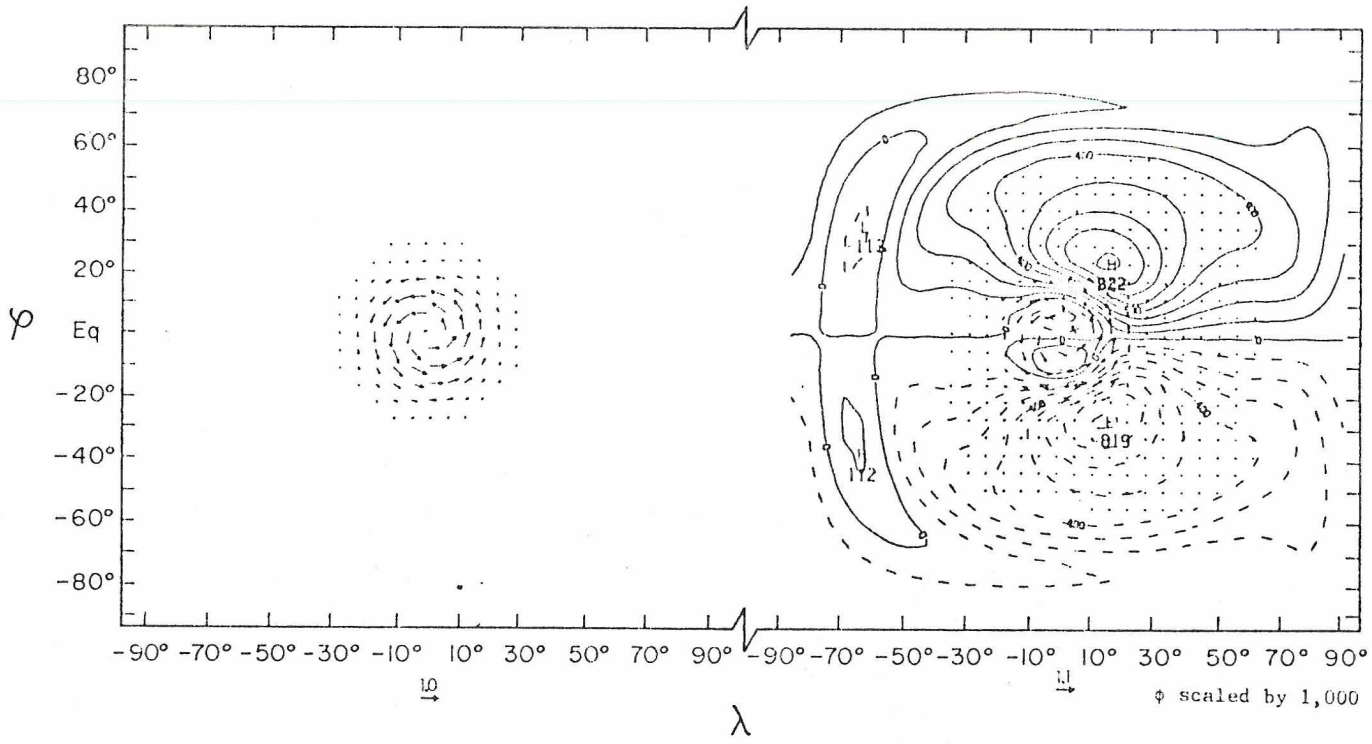

(a) t=0 (b) t=8 hours

Figure 5.10 Two-dimensional geopotential and wind fields (in non-dimensional units) on the sphere (ε=10) for the vortex initial condition (a) given by (5.1) with r_e=1500km and centered at the Equator. The solution at t=8 hours, t=1 day, t=2 days, t=4 days and t=6 days is shown in (b), (c), (d), (e) and (f), respectively.

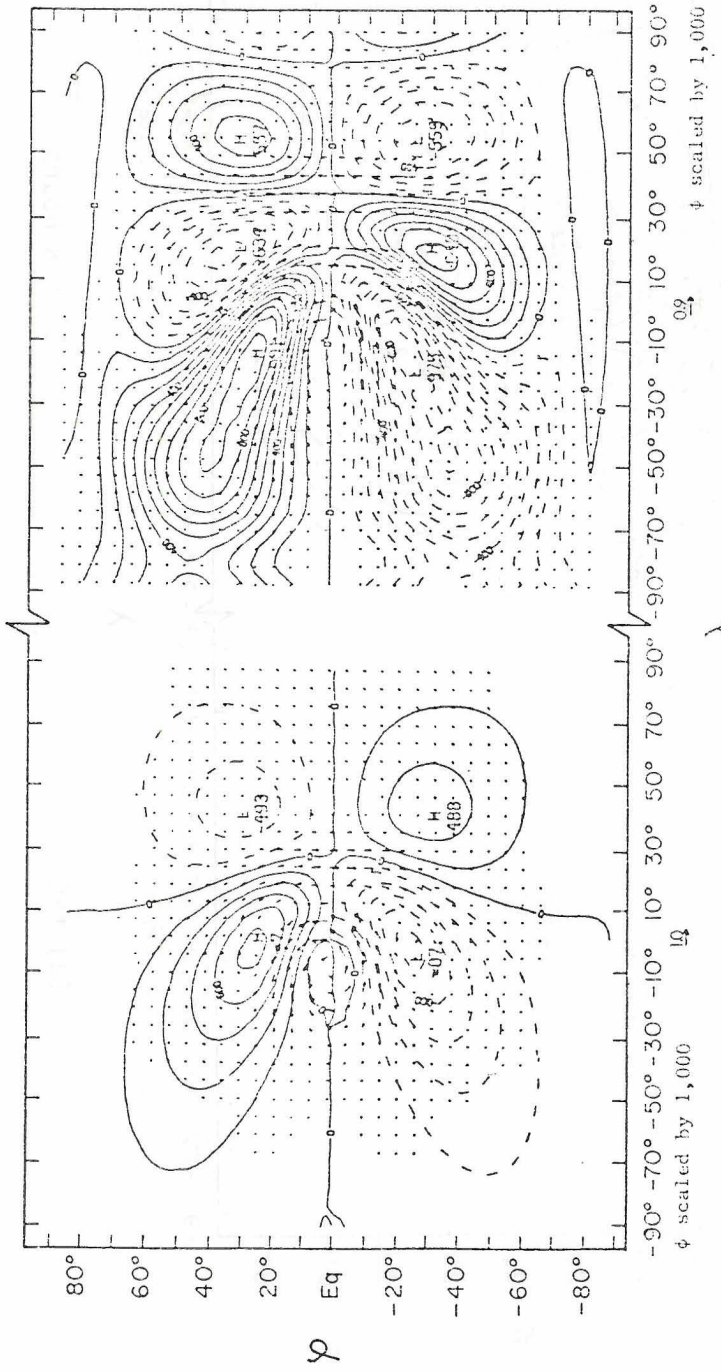

(c) t=1 day (d) t=2 days

Figure 5.10 (continued)

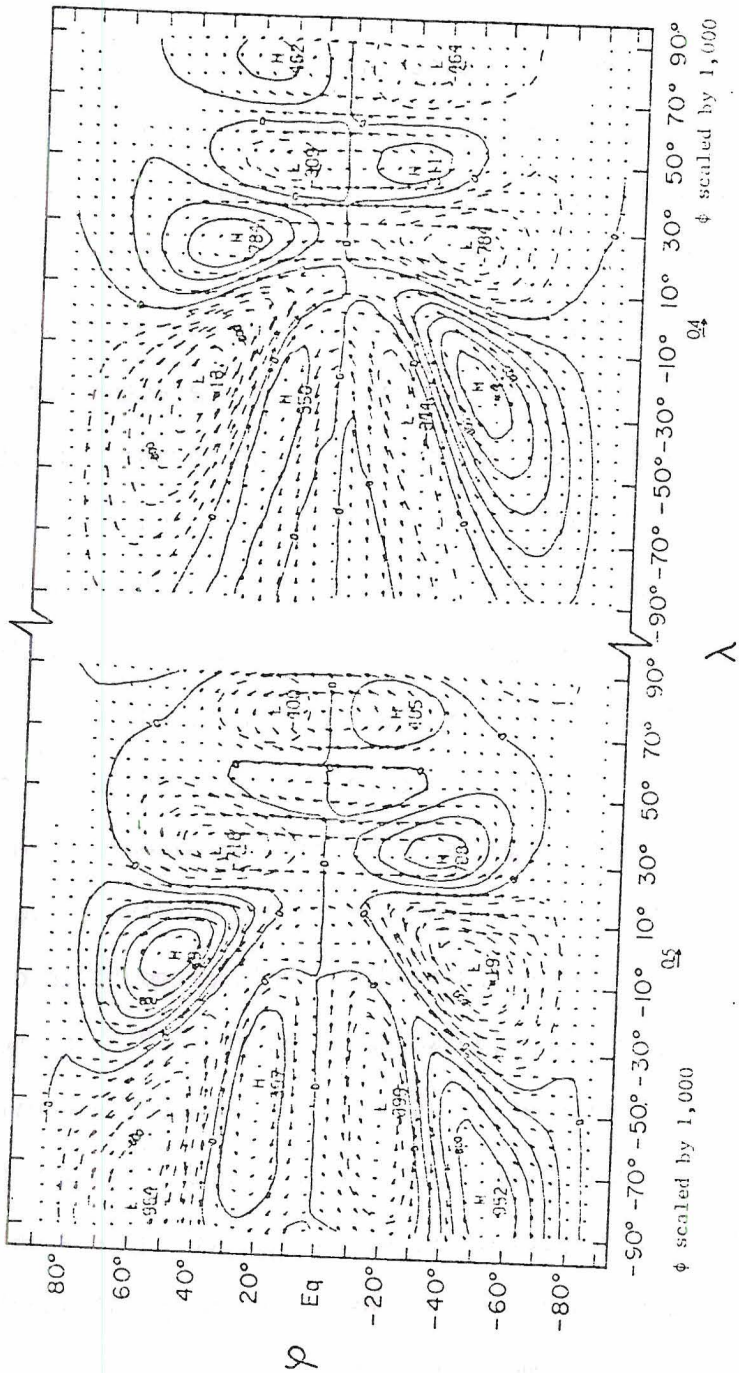

(e) t=4 days

(f) t=6 days

Figure 5.10 (continued)

The solution on the sphere for ε=10 at t=8 hr. (Figure 5.10.b) can be compared to the β-plane solution shown in Figure 5.9 at t = 2.7 ($t \simeq$ 9 hr. for ε=10). We clearly see that the equatorial β-plane result is not only qualitatively but also quantitatively similar to the sphere. At t=24 hr. the β-plane results (not shown) are still qualitatively good when compared to Figure 5.10.c but the positioning and magnitude is not as accurate as at t = 8 hr.

At t = 48 hr. (Figure 5.10.d) we clearly see the eastward dispersion of the mixed Rossby gravity waves characterized by large v-component of the wind at the Equator and approximate geostrophic balance at higher latitudes. The zonally elongated field to the west of the initial vortex is characteristic of the westward dispersion of long Rossby waves with the predominance of zonal over meridional wind (Figure 3.12 and 3.13). The structure of the mixed Rossby-gravity wave observed due east of the initial vortex corresponds to the s=5 wave or k = 2.8 in non-dimensional units. This is approximately the wavelength of maximum energy in the ℓ = 0 mode (or n=0 according to Table 3.2) shown in Figure 5.3. Table 3.3 predicts reinforcement to occur in a time interval of approximately two days and about 27° to the east, implying a group velocity of 14° day^{-1} for a disturbance with peak energy at s = 5. Comparing Figure 5.10.d, e and f (at t = 48 hr., 96 hr., and 144 hr., respectively) we can follow the eastward propagation of the high centers in the northern hemisphere at about the speed predicted by the reinforcement argument.

5.5 Summary and Discussion

In this chapter we have shown the time development of the initial vortex (5.1), which is characterized by the parameter y_0 (latitude of

the center) and r_e (the size of the vortex). The Fourier components of the initial condition are given by (5.4).

The partition of energy between Rossby and gravity modes and the spectral distribution of energy in the zonal wavenumber and meridional index space (k,n) is discussed in section 5.1. For a vortex which is small relative to the equatorial Rossby radius of deformation, the bulk of the initial energy goes into Rossby modes (Figure 3.1). As the vortex size increases or is shifted away from the Equator less energy goes into Rossby modes. In particular, for a vortex characterized by $r_e = 2$ approximately 40% of the energy goes into Rossby modes, and Figure 5.5 shows that it goes primarily to the mixed Rossby gravity wave. Although 40% of the initial energy is in the slow dispersive modes, the rest of the initial energy is concentrated in long gravity waves which are also relatively slowly dispersive (Figure 3.6). Thus, the adjustment time T_a defined by (4.9) is large and we cannot speak of the adjusted state in this case.

A small initial vortex (e.g. $r_e = 0.35$) is characterized by an adjustment of the pressure field to the initial wind configuration. The energy is mostly in Rossby modes and the adjustment is fast as shown in Figure 5.7 which shows an x-t cross section of the ϕ-field at $y = 1.2$ for an initial vortex centered at $y_o = 1.2$.

One might speculate on the implications of the vortex experiment in terms of the maintenance of closed circulations in the atmosphere. If for any reason the intensity of the closed circulation is changed, the mass and wind fields respond in a short time scale in such a way so as to bring the pressure field into approximate geostrophic balance with the perturbed wind which tends to remain unchanged

(Figures 5.8 and 5.9). Thus, the pressure adjusts to the wind and this is true over a wide range of vortex sizes since most of the initial energy goes into Rossby modes (Figure 5.1).

The question that we have to answer now concerns the physical mechanism that might produce such an initial condition, i.e., a sudden intensification of the vortex intensity without changing the pressure field.

In the oceanographic context, an initial condition in the wind field is interpreted as a sudden wind stress applied at the ocean surface (Lighthill, 1969). The wind stress is treated as a body force distributed uniformly in depth over an upper well mixed layer in the ocean. In the atmosphere, cumulus convection may act to redistribute momentum in the vertical and possible generate momentum (Ooyama, 1971; Houze, 1973; Moncrieff and Miller, 1976; and Stevens, 1977). However, the physics of the momentum transport and generation in the atmosphere is not yet fully understood and certainly more complicated than what the simple shallow water equations can describe. Thus, the interpretation of the results shown in this chapter as momentum sources by cumulus convection is speculative but has a diagnostic value as far as the dynamics of the system is concerned.

Numerical studies by Moncrieff and Miller (1976) and Moncrieff (1978) have indicated the possibility of kinetic energy increase at lower and upper levels by deep convection provided the system is embedded in an environment with the wind blowing in opposite directions in upper and lower levels. This is exactly the situation in a tropical storm. It has been recently suggested by McBride (1979) that a favorable condition for the development of a hurricane in a large vorticity

gradient between the 200 mb level and the 900 mb level. Under those circumstances, deep convection might act towards increasing the intensity of the anticyclonic vertical shear and our results indicate a dynamically induced subsidence in the inner part of the vortex. The decrease in the radial circulation traps the energy within the system allowing for local warming and surface pressure fall. Thus, the surface wind increases and the energy input by evaporation further contributes to the enhancement of the disturbance.

We might also speculate on the east-west asymmetry of the resulting adjusted state characterized by the slow dispersive Rossby modes. Anthes (1972) suggests that the asymmetries observed in a hurricane are a result of dynamical (inertial) instability. However, Anthes' argument is based on a model formulated on an f-plane. Our results suggest that asymmetries can also be produced by the variation of the Coriolis parameter.

6. STEADY FORCING

In this chapter we consider the initial value problem governed by the linearized shallow water equations (2.74). In particular, we assume the forcing term is to be independent of time.

In section 6.1 we present an example of a steady bell shaped mass source/sink on the equatorial β-plane. The dynamic response to a switch-on stationary vortex momentum forcing is shown in section 6.2. In the two level baroclinic model this experiment can be interpreted as the momentum forcing induced by clouds in such a way that a cyclonic or anticyclonic shear is continuously applied.

In section 6.3 the latitude dependence and relative position of the mass source/sink are considered. Section 6.4 is a summary of the results to be discussed in this chapter.

6.1 Steady mass source/sink - equatorial β-plane

The initial value problem posed by (2.74) with $\underline{F} \equiv 0$ and $\xi(x,y,o) \neq 0$ can be interpreted as an instantaneous forcing. In this section we consider another particular form of the forcing term $\underline{F}$ such that

$$\underline{F}(x,y,t) = \begin{cases} \begin{bmatrix} 0 \\ 0 \\ f(x,y) \end{bmatrix} & \text{for } t \geq 0 \\ 0 & \text{for } t < 0 \end{cases} \tag{6.1}$$

where

$$f(x,y) = \pm \exp\left\{ - \frac{[x^2 + (y-y_o)^2]}{r_e^2} \right\} \tag{6.2}$$

is time independent. The plus/minus sign in (6.2) represents a mass source/sink in the shallow water equations.

In the stratified atmosphere discussed in section 2.1 the forcing function (6.1) is the projection of the heating forcing onto a particular vertical mode.

In the non-homogeneous case of the two-level baroclinic model we have the relation

$$f(x,y) = c^{-\frac{1}{2}} \beta^{-\frac{1}{2}} R(Q)_2 \tag{6.3}$$

where the subscript (2) in (6.3) refers to the middle level (Figure 2.1), Q is the heating rate in units of ($^{\circ}K\ s^{-1}$) and R is the gas constant for dry air. For c = 41 ms^{-1} (ε=500) equation (6.3) can be written as

$$f(x,y) = (Q)_2\ 6.5 \times 10^{-2}\ deg^{-1}\ day \tag{6.4}$$

The steady forcing considered in this section is expected to give a large response in Rossby modes according to (2.86) since the lower the frequency of the eigenmode the more resonant it is to the stationary forcing. In fact, the geostrophic mode (k=0) is resonant to the forcing (6.1) without the damping term κ and gives a linear growth of the zonal wind and geopotential fields, and therefore no contribution to the divergence field.

Figure 6.1, 6.2 and 6.3 show an x-t cross section at y = 1.2 of the geopotential, vorticity and divergence fields for κ = 0, r_e = 0.35 and y_o = 1.2 ($r_e \approx$ 470 km and $y_o \approx$ 1600 km for ε=500) including Rossby and gravity modes. The Rossby mode contribution to the solution is shown in Figures 6.1b, 6.2b and 6.3b. The initial condition in this experiment is one of no motion and no geopotential perturbation.

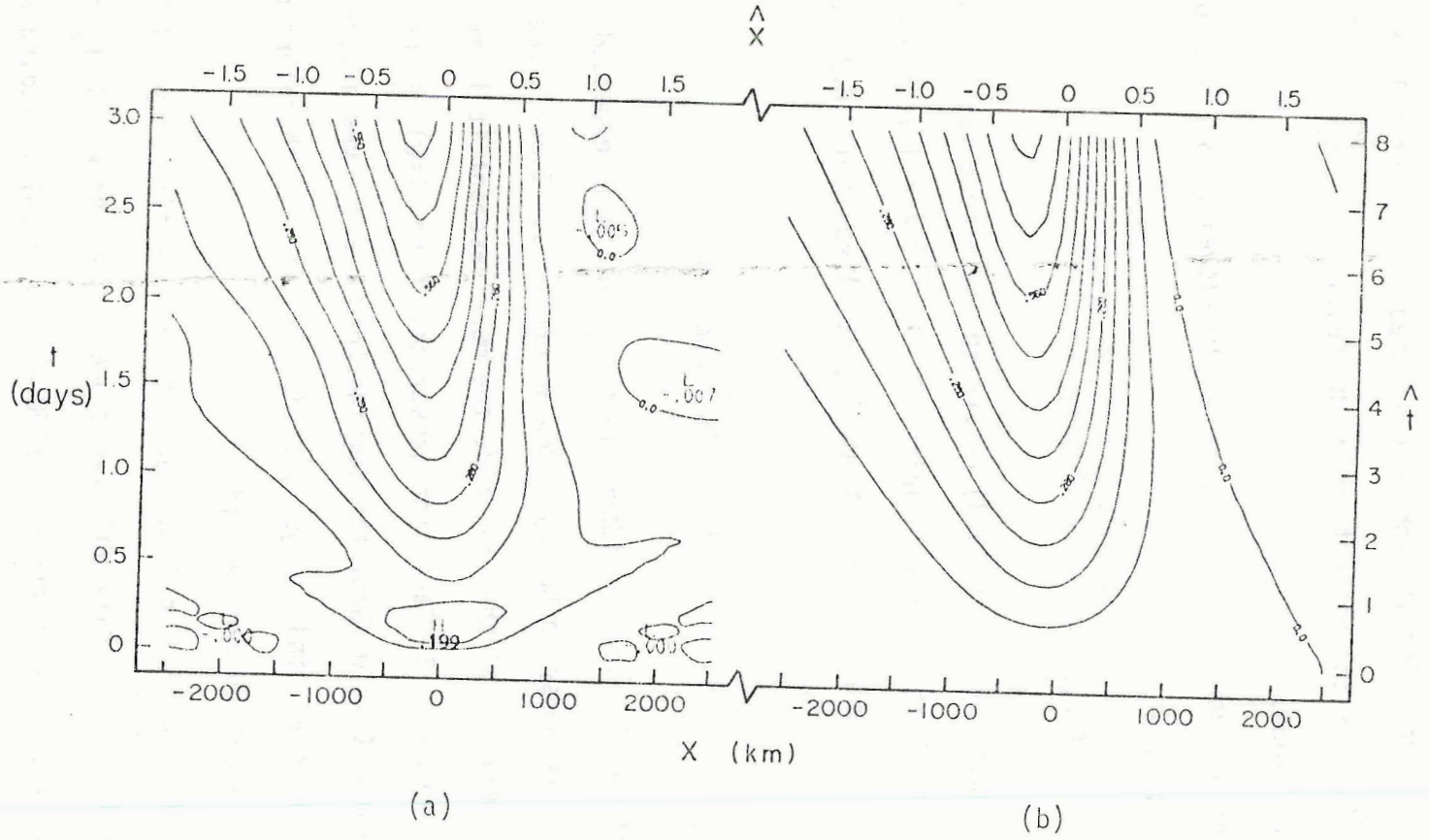

Figure 6.1 x-t cross section of the non-dimensional geopotential field at y=1.2 for the steady mass source given by (6.1) with r_e=0.35 and y_o=1.2. Part (b) is the Rossby mode contribution to the complete solution shown in part (a). The scales on the top and right are non-dimensional and the bottom and left scales are dimensional for ε=500.

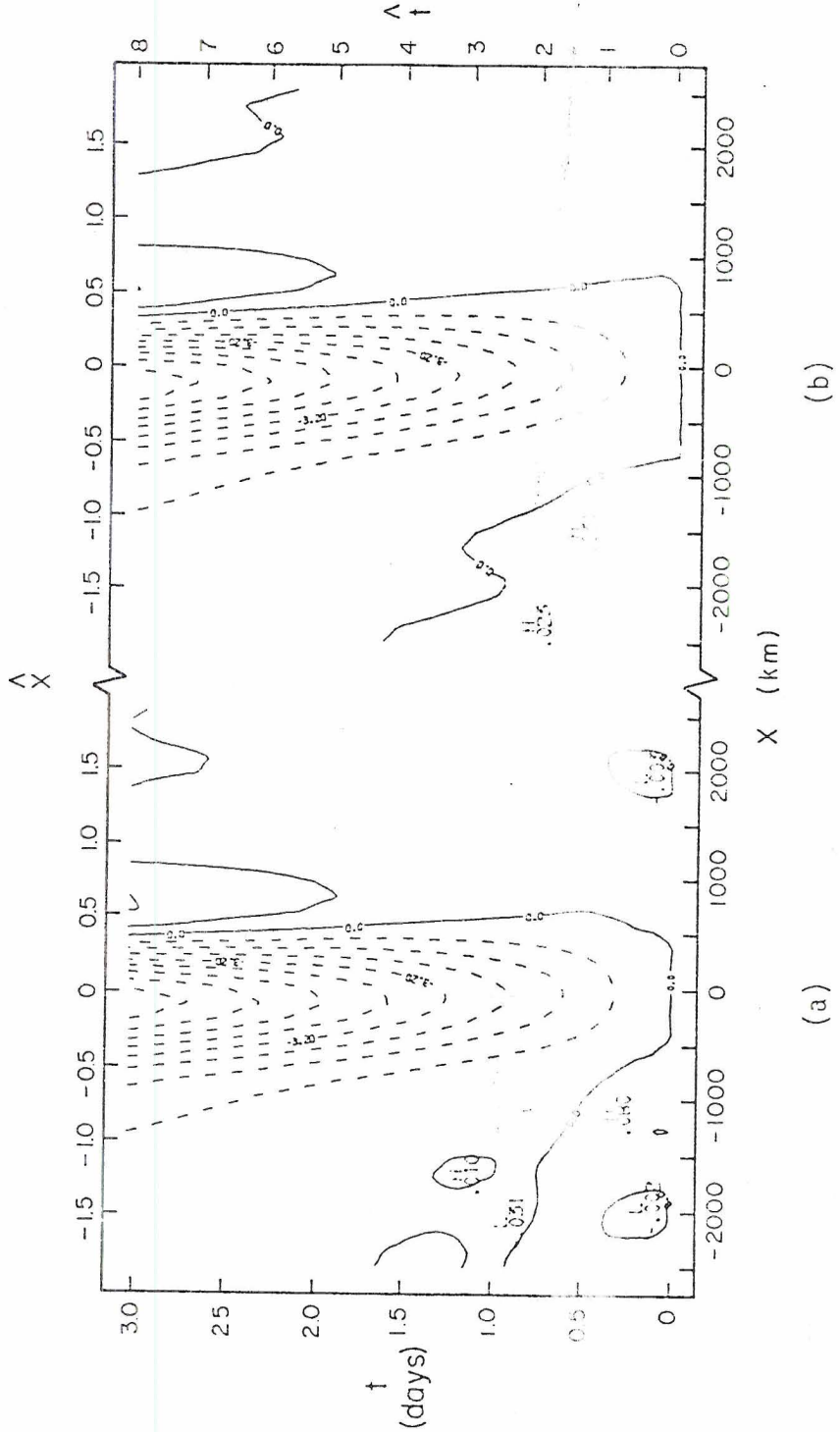

Figure 6.2 Same as Figure 6.1 but for the non-dimensional relative vorticity field.

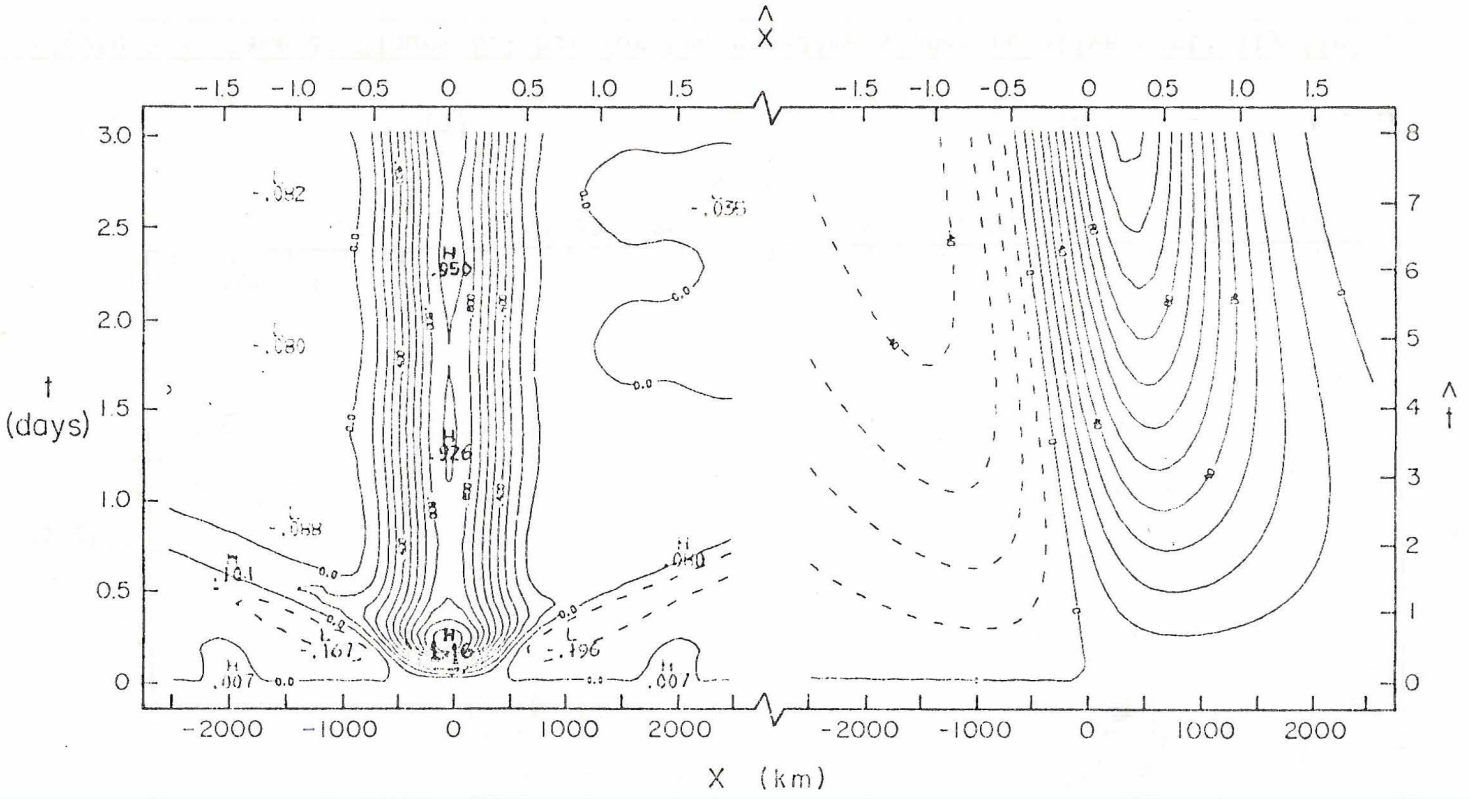

Figure 6.3 Same as Figure 6.1 but for the non-dimensional divergence field. The contours of the Rossby mode solution (b) is scaled by 1,000.

Figure 6.1 shows that the gravity modes have a small contribution to the total solution except for small x and t and along the characteristic line x-t. The vorticity field (Figure 6.2) is practically all due to Rossby modes. Both geopotential and vorticity fields show a westward displacement of the center of maximum intensity although the forcing is fixed in space and time. This behavior has to do with the westward dispersion of long Rossby modes excited by the forcing. An analogous phenomena occurs with the instantaneous forcing as discussed in Chapter 4.

The cross section of the divergence field at y = 1.2 (Figure 6.3) is practically all due to the gravity modes response as can be easily seen by comparing Figure 6.3a with Figure 6.3b (scaled by 1000). The divergence field reaches a quasi-steady state after approximately one non-dimensional time unit (less than 9 hrs. for ε=500). The exact steady state solution implied by Paegle (1978) in a similar problem is a consequence of his f-plane assumption which allows for a steady state solution which is not zonally symmetric.

For the heating rate of 8° C day^{-1}, with maximum in the middle troposphere, the two level baroclinic model (ε=500) would give an almost steady state upper level divergence of approximately 1.4×10^{-5} s^{-1} ($\omega_2 \simeq$ 600 mb day^{-1}) with convergence over a broad region west of the heat source (1.3×10^{-6} s^{-1} implying $\omega_2 \simeq$ 50 mb day^{-1}). The sinking west of the heat source produces a slow warming and consequent increase in thickness as shown in Figure 6.1. To the east of the heat source, the general tendency is for divergence in the upper level and consequently upward vertical motion which induces a cooling and thickness decrease. However, the contribution of the geostrophic

mode (which is non-divergent) is a linear increase of the geopotential field and the zonal component of the wind. The combination of the geostrophic modes with all other modes explains the relative constant value of ϕ east of the heat source as observed in Figure 6.1.

The two dimensional wind and geopotential fields are shown in Figure 6.4 at $t = 2.7$ (1 day for ε=500) for the same experiment shown in Figures 6.1, 6.2, and 6.3. Figure 6.4 can be viewed as representing the upper level of the two level baroclinic model; in this case the lower level flow is reversed and the geopotential field has the opposite sign i.e., we have cyclonic motion at the lower level in agreement with the heat source in the middle of the troposphere.

The heat source is fixed at $x = 0$ and $y_0 = 1.2$ but the maximum geopotential perturbation is displaced to the north about 0.25 non-dimensional units ($\simeq$ 330km for ε=500) and slightly toward the west. The northward displacement is significant since the half width of the heat source is approximately 500 km. At large time the center of the ϕ-perturbation moves towards the west and the whole pressure pattern becomes elongated in the westward direction as suggested in the geopotential x-t cross section at $y = 1.2$ (Figure 6.1).

The wind and geopotential fields associated with the forcing function (6.2) are not symmetrical (Figure 6.4) as an f-plane analysis would indicate. The wind is more intense in the southeastern quadrant where the cross isobaric flow is more prominent. This result seems to be a consequence of the smaller value of f equatorward of the heat source. Figure 6.4 has some resemblance to the observed flow in the upper levels of a hurricane. However, asymmetries in hurricanes may have a variety of causes (Anthes, 1972). Our results simply

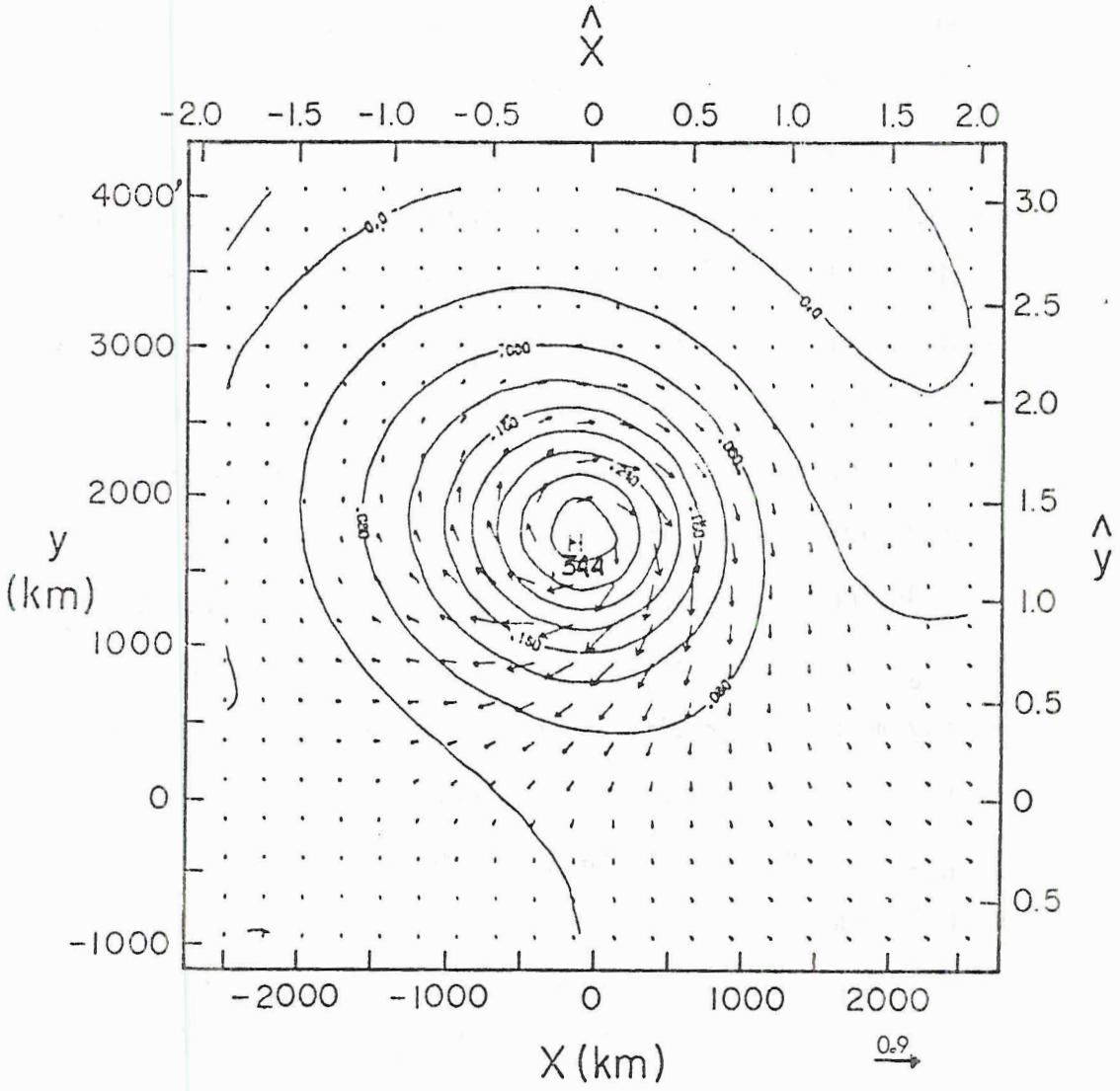

Figure 6.4 Two-dimensional geopotential and wind fields in non-dimensional units for the steady mass source given by (6.1) with r_e=0.35 and centered at y_0=1.2. The scales on the top and right are non-dimensional and the bottom and left scales are dimensional for ε=500.

isolate asymmetries that are attributable only to the dynamical affects of a variable Coriolis parameter.

Another speculative aspect is the displacement of the center of circulation with respect to the center of the forcing function exhibited in Figure 6.4. Results obtained with $r_e = 0.20$ ($r_e \approx 270$ km for ε=500) indicate basically the same features but a more intense divergence field. This could have been anticipated since both cases ($r_e = 0.35$ and $r_e = 0.20$) imply disturbances which are smaller than the equatorial Rossby radius of deformation.

Another way of explaining the similarity between the $r_e = 0.35$ and $r_e < 0.35$ cases is related to the partition of energy between Rossby modes and gravity modes of the forcing function (6.2) From Parseval's theorem and the definition of the expansion coefficient $c_{k,n,r}(t)$ for the stationary forcing (given by 2.90 with $\kappa = 0$) we clearly see that

$$\overline{E}(t) \propto \sum_{\text{all } k,n,r} f^2_{k,n,r} \left(\frac{1 - \cos \omega_{k,n,r} t}{\omega^2_{k,n,r}} \right) \tag{6.5}$$

where $\overline{E}(t)$ is the total energy at time t. The term in parenthesis in (6.5) is bounded for any t provided $\omega_{k,n,r} \neq 0$. However, as $\omega_{k,n,r}$ tends to zero, (6.5) has the asymptotic value

$$\overline{E}(t) \propto f^2_{k,n,r} \frac{t^2}{2} \quad . \tag{6.6}$$

Then, for the geostrophic modes (k = 0, r = 0) the total energy is proportional to t^2 and increases without bound in the inviscid case. As a consequence, as t increases, more and more energy goes into Rossby modes.

Figure 4.1 gives the ratio between the energy in Rossby modes and the total initial energy in the geopotential initial condition. Figure 4.1 can also be interpreted as the ratio of the variance of the forcing (6.2) explained by Rossby modes to the total variance. Thus, although $f_{k,n,r}$ is small for Rossby modes for a bell shaped mass sink/source of small scale, the energy in Rossby modes can be comparable to the energy in all modes because of the asymptotic value of $\overline{E}$ (t) given by (6.6). These results are clearly seen in Figures 6.1-6.3 where the Rossby mode contribution to the solution is shown.

Figure 4.1 shows that the projection of the forcing onto Rossby modes, which are more resonant with the steady forcing, does not show a radical change as it would if we were considering a large-scale forcing (e.g. r_e=2.0). As r_e decreases we expect the divergence field to intensify because there is a progressively larger projection of the forcing onto gravity modes as r_e decreases (Figure 4.1). Gravity waves have more divergence than vorticity as shown in Figure 3.20 and as k increases the gravity waves become primarily divergent. For truly localized forcing functions of the type (6.2) the e-folding width of the Fourier spectrum is large (see 4.4) and therefore we expect a more pronounced divergence field as the size of the forcing decreases, assuming a constant maximum forcing.

The example of a forced problem on the equatorial β-plane shown so far has no damping, i.e. the coefficient κ in (2.86) is zero. For reasonable values of κ such that the e-folding decay time is between 7 and 20 days (for ε=500) the effect is negligible on a time scale of 1 day. In order to illustrate the effect of the damping term κ on the forced stationary motion let us consider the particular form of forcing

$$f(x,y) = \cos kx \quad \exp\left\{-\frac{y^2}{r_e^2}\right\} \tag{6.7}$$

with $r_e = 1.4$. Equation (6.7) represents a sequence of mass sources and sinks alternating along the Equator. This example has been treated by Matsuno with $k = 0.5$ and $\kappa = 0.2$. Figure 6.5a, b, c, and d show the steady state wind and geopotential fields for $\kappa = 0.01$, 0.05, 0.20, and 0.40 respectively. For $\kappa = 0.01$ (Figure 6.5.a) the geopotential and wind field are similar to the $n = 1$ Rossby wave with $k = 0.5$ (Figure 3.12). The maximum pressure deviation is away from the Equator, about $\frac{\pi}{2}$ out of phase with the forcing and maximum at $y \simeq 1.2$. A strong zonal current, directed from mass source towards mass sink, develops along the Equator. It is interesting to note that the maximum pressure response is not centered where the forcing is maximum. As κ increases the maximum pressure response shifts equatorward but is not in phase with the forcing in the zonal direction. Even with $\kappa = 0.40$ (Figure 6.5.d) the highest pressure, although located near the mass source, is slightly shifted eastward so that the outflow region does not exactly correspond to the forcing. This is true for all values of κ and is most apparent for $\kappa = 0.01$ (Figure 6.5.a). Thus, with little damping, the fluid flows along the Equator symmetrically with respect to the mass source or sink and the mass accumulates on both sides of the Equator with little pressure response at the maximum forcing. As κ increases the stationary solution shows a build up of mass at the mass source (removal of mass at the mass sink) but the center of equatorial outflow (inflow) is located eastward (westward) of the maximum mass source (sink).

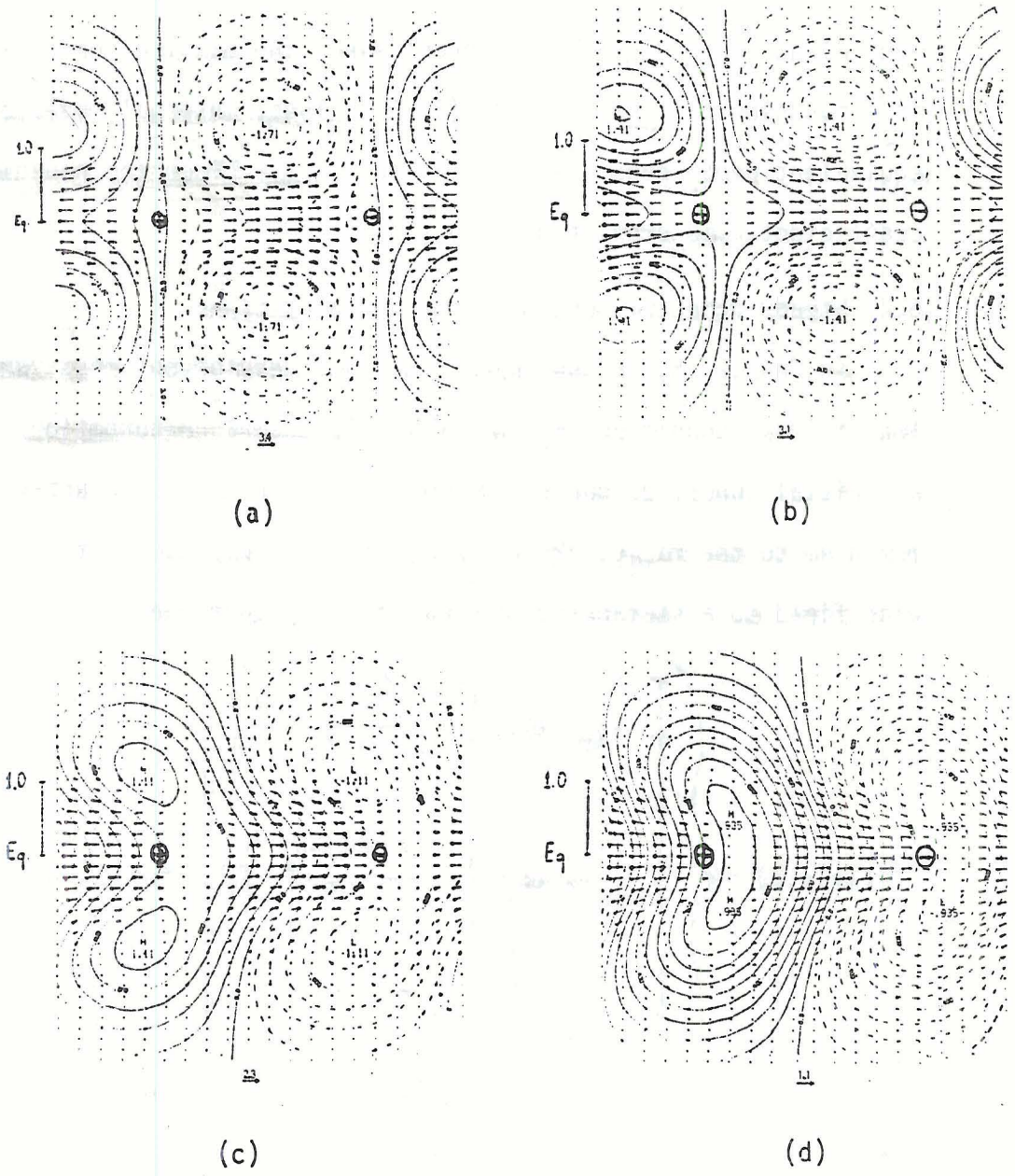

Figure 6.5 The stationary circulation pattern caused by the alternating mass source/sink given by (6.5) with k=0.5 for κ=0.01 (a), κ=0.05 (b), κ=0.20 (c) and κ=0.40 (d). Only one wavelength of the disturbance is shown. The center of the mass source is indicated by $\oplus$ and the center of the mass sink is indicated by $\ominus$.

The sensitivity of the stationary solution to the steady forcing (6.7) reveals that the internal response for different values of the equivalent depth H can be different since the damping coefficient κ is a function of c as shown in (2.76). Thus, internal modes of small equivalent depth behave like the viscous case since the non-dimensional coefficient κ is proportional to [T].

6.2 Steady momentum forcing - equatorial β-plane

In Chapter 5, we considered the time development of a vortex like initial condition with no initial pressure perturbation. Such an initial condition can be interpreted as an impulsive addition of momentum to the fluid. We now consider the response of the mass and wind field to a stationary momentum forcing such that

$$F(x,y,t) = \begin{cases} \begin{bmatrix} (y-y_o) \exp\left\{-\dfrac{[x^2+(y-y_o)]}{r_e^2}\right\} \\ -x \exp\left\{-\dfrac{[x^2+(y-y_o)]}{r_e^2}\right\} \\ 0 \end{bmatrix} & \text{for } t \geq 0 \\ 0 & \text{for } t < 0 \end{cases} \tag{6.8}$$

and

$$\xi(x,y,o) \equiv 0 \tag{6.9}$$

Thus, (6.8) has the same spatial dependence as the impulsive forcing (or initial condition) given by (5.1). The results for $r_e = 0.35$, $y_o = 1.2$ and $\kappa = 0$ are shown in Figure 6.6a, b, c, and d at t = 1.3, 2.7, 5.3 and 8.0 respectively. In dimensional units, this corresponds to t = 0.5, 1, 2 and 3 days respectively assuming the two level

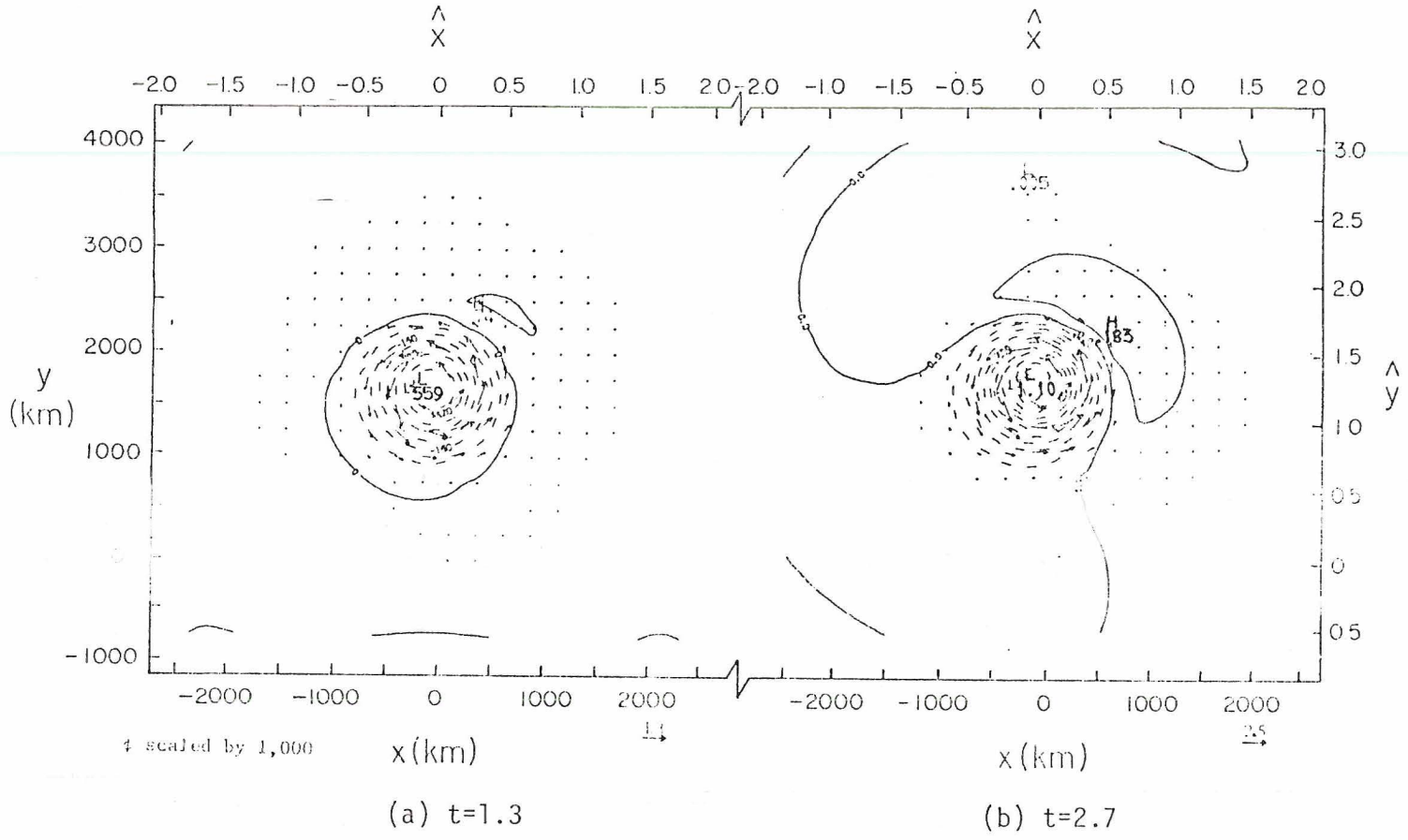

(a) t=1.3 (b) t=2.7

Figure 6.6 Two-dimensional geopotential and wind fields in non-dimensional units for the steady momentum source (cyclonic) given by (6.6) with r_e=0.35 and centered at y_0=1.2. The solution is shown at t=1.3 (a), t=2.7 (b), t=5.3 (c) and t=8.0 (d). The scales on the top and right are non-dimensional and the bottom and left scales are dimensional for ε=500. In dimensional time units (ε=500), the solution is displayed at t=12 hours, t=1 day, t=2 days and t=3 days, respectively.

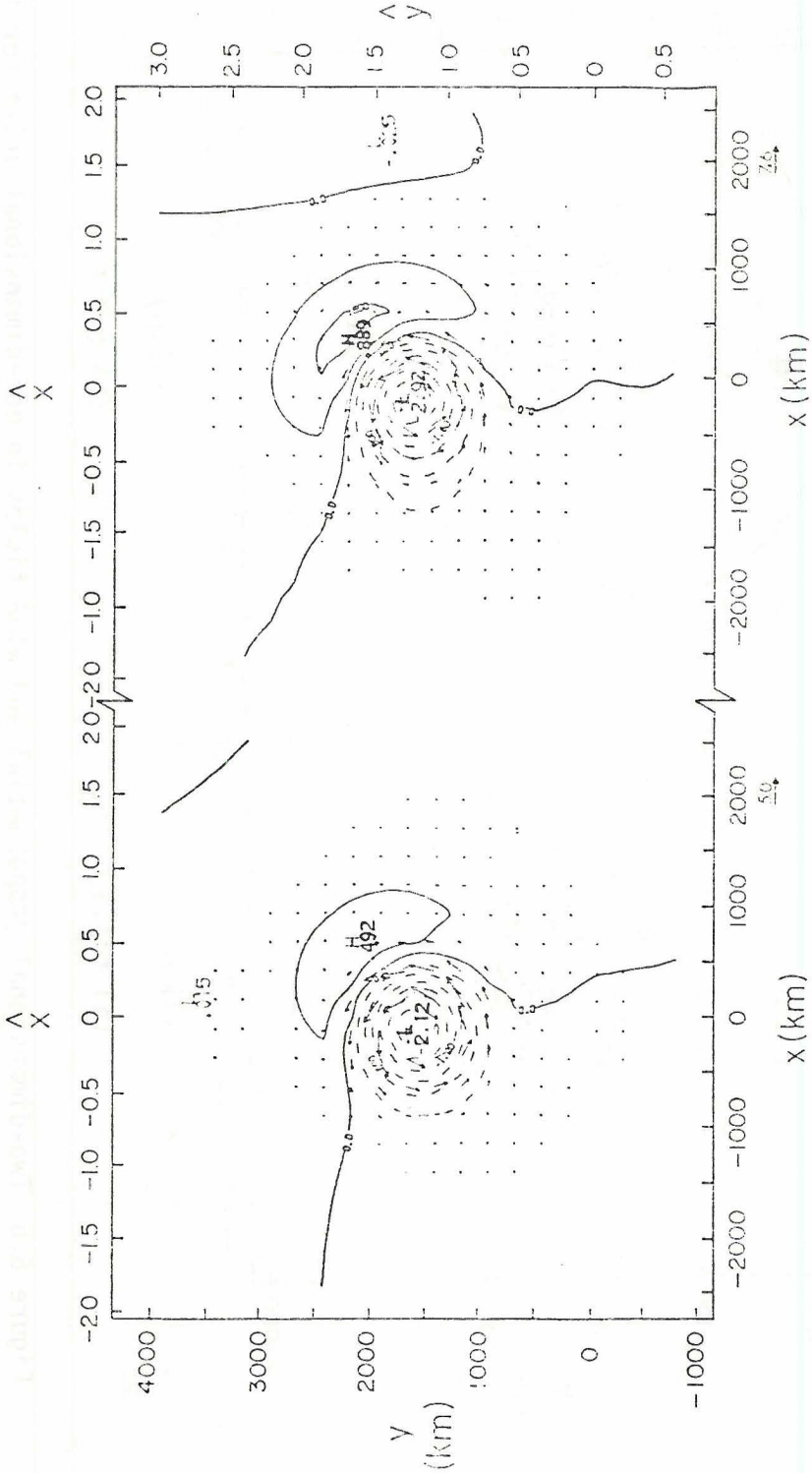
(c) t=5.3
(d) t=8.0
Figure 6.6 (continued)
x (km)
y (km)
H
L

baroclinic model discussed so far (ε=500). The geopotential field in Figure 6.6.a is scaled by 1000 and the arrows are proportional to the wind speed as indicated.

The qualitative characteristics of stationary vortex forcing are similar to the impulsive forcing (Figure 5.8) since the low frequency Rossby modes describe 95% of the initial condition shown in Figure 5.8.a. The build up of the high pressure center in the NE quadrant is also observed. As discussed in Chapter 5, we can interpret the geopotential and wind fields in Figure 6.6 as representative of the 750 mb level of the two-level baroclinic model. In this case the steady momentum forcing can be interpreted as a steady torque applied to the lower layer in the cyclonic direction and an opposite torque in the upper layer. As a result, anticyclonic shear is being steadily forced and subsidence is required in order to satisfy thermal balance.

The difference between the steady forcing and the impulsive forcing is primarily quantitative. In the impulsive case, subsidence occurs initially and as time increases the ϕ-field goes up in the center of the vortex as shown in Figure 5.8. In the steady forcing case the ϕ-field continues to decrease up to t = 8 (3 days for ε=500). In the impulsive case the initial energy is being slowly dispersed by the Rossby modes and in steady forcing cases there is an energy source to replace the energy that is continuously dispersed.

6.3 Steady mass source/sink - sphere (ε=10)

In this section we consider the steady forcing problem on the sphere with ε=10. This section complements some of the results obtained on the equatorial β-plane with an extension to the external mode.

Emphasis is placed on the steady state response of the model assuming that the damping coefficient κ in (2.74) gives an e-folding decay time of 10 days for the external mode.

The forcing function has the functional form given by (6.1) and (6.2) with the appropriate correction for the convergence of meridians. In order to obtain the steady state solution to the stationary forcing with damping terms the expansion coefficient $c_{k,n,r}$ is given by (2.90).

Let us consider now an experiment in which a mass source and mass sink of the same intensity are put at the same latitude but separated in longitude by λ_0 degrees. Figures 6.7 and 6.8 show the steady state solution for the mass source/sink system centered at $\varphi_0 = 20°$ and $\varphi_0 = 60°$ respectively and half width $r_e = 1250$ km. The value of λ_0 is 90° and symmetry about the Equator is imposed by considering only symmetrical modes in the series solution. Also indicated in Figures 6.7 and 6.8 is the location of maximum forcing intensity and the e-folding radius.

In both Figures 6.7 and 6.8 the maximum geopotential response is west-northwest of the maximum forcing, with the low and high centers in the neighborhood of the e-folding range of the forcing function. The tendency for the circulation center and the high or low pressure to be displaced with respect to the forcing was also observed in the transient solution on the equatorial β-plane. Experiments with forcing functions with e-folding width much larger than the local Rossby radius of deformation (not shown) indicate that the forcing and the pressure response tend to coincide in space as the dimension of forcing increases.

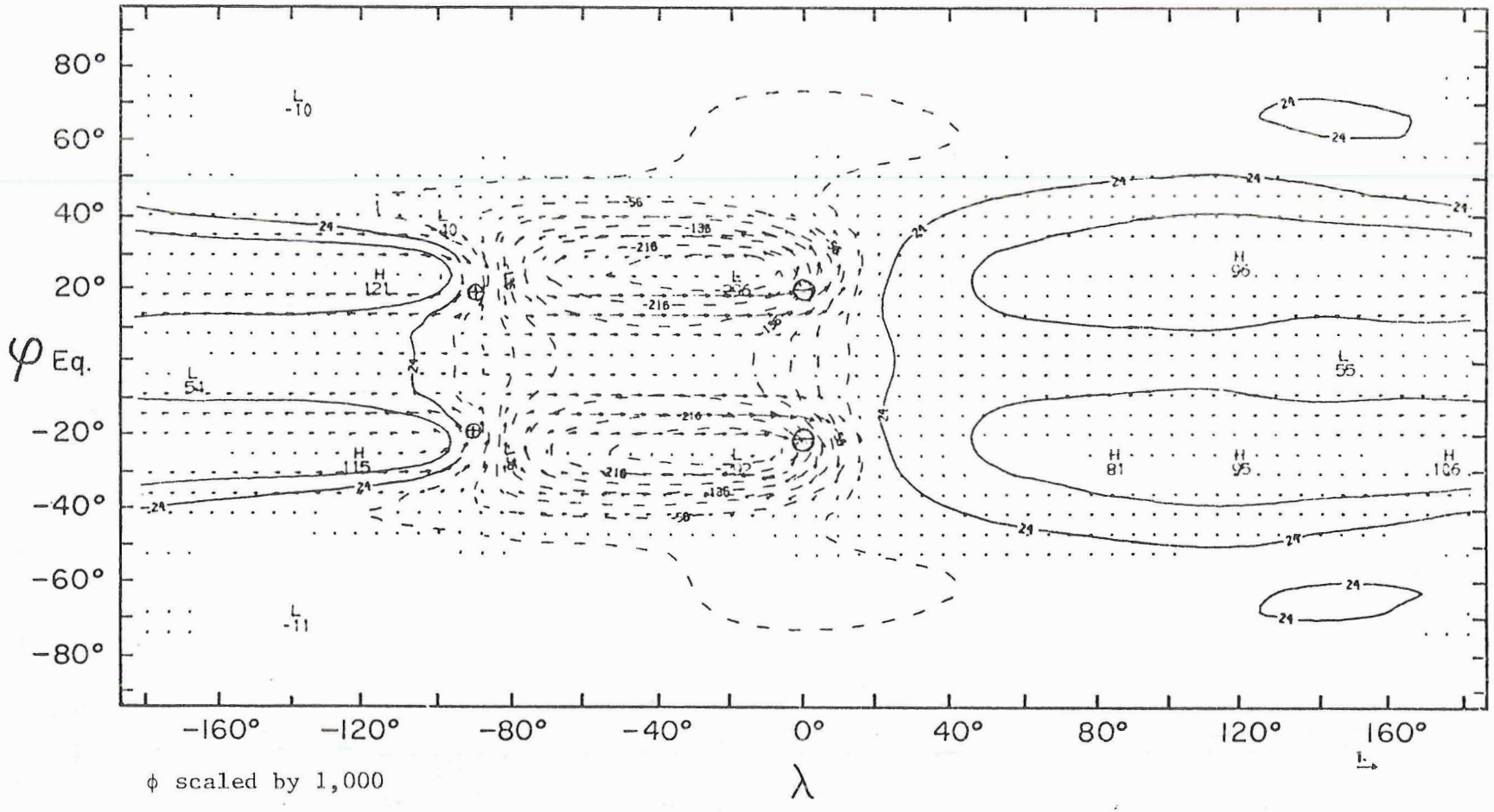

Figure 6.7 Stationary circulation pattern on the sphere (ε=10), caused by the mass source/sink system given by (6.1) separated by 90^0 of longitude with r_e=1250km and centered at $\varphi_o = \pm 20^0$. Latitude and longitude of maximum forcing are indicated by $\oplus$(source) and $\ominus$(sink). The geopotential and wind fields are non-dimensional.

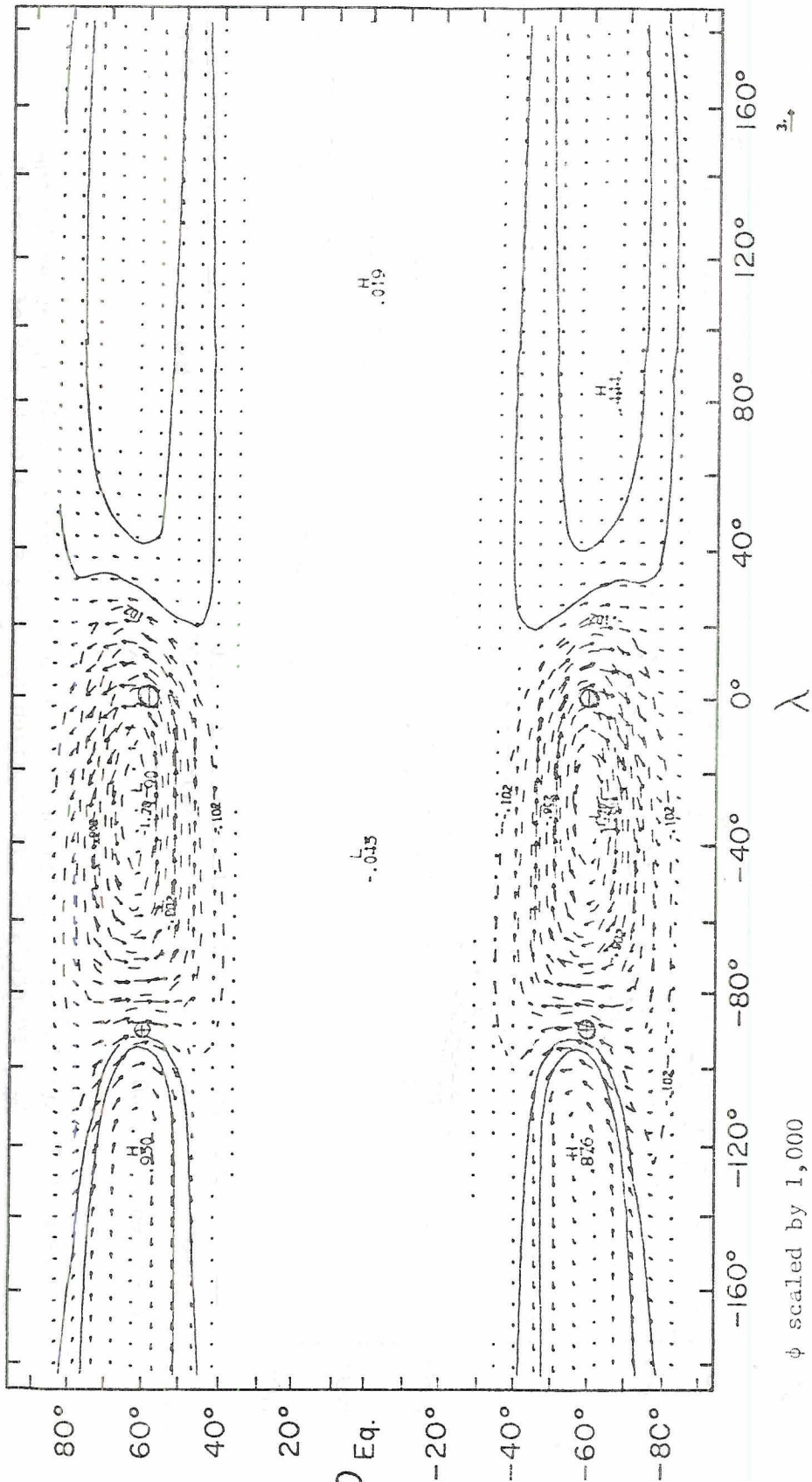

Figure 6.8 Same as Figure 6.7 but for the mass source/sink system centered at $\Psi_o = \pm 60^o$.

Although the mass source/sink system is adding/removing mass at the same rate in the experiments shown in Figures 6.7 and 6.8, the low pressure for the system centered at 60° (Figure 6.8) is approximately six times more intense than the system at 20° (Figure 6.7). However, the steady state maximum wind speed is only twice as intense in the higher latitude system. These results are a consequence of geostrophy since Rossby modes are more resonant to the forcing than gravity modes.

Another interesting feature observed in Figures 6.7 and 6.8 is related to the relative intensity of the high and low pressure centers. Although the only difference between the mass source and sink regions is the sign of the forcing function, the low pressure to the east is more intense than the high pressure. For $\rho_0 = 20°$ (Fig. 6.7) and $\rho_0 = 60°$ (Fig. 6.8) the ratio between the low and the high in absolute value is approximately 2. Thus, low pressure generated in response to the mass sink is approximately twice as intense as the high pressure associated with the mass source.

The high pressure region in Figure 6.7 and 6.8, besides being less intense than the low pressure, is stretched in the zonal direction and covers most of the latitude band, the circulation being well defined only around the low pressure region. Had we reversed the relative position of the mass source and sink regions the results in Figure 6.7 and 6.8 would still be valid (because of linearity) provided we change the sign of the pressure field and reverse the direction of the wind. In this case the circulation about the high pressure area would be well defined and the wind field associated with the low pressure would be stretched in the zonal direction.

Increasing the distance between the mass source and sink makes the pressure systems more symmetrical in the east-west direction. However, decreasing the distance intensifies the relative difference in intensity up to a certain distance where the source and sink areas overlap significantly. For a separation distance of about 40° the east-west asymmetry in the pressure response reaches a maximum and the ratio between the absolute value of the high pressure to the low pressure is approximately 2.6 to 1.

The conclusion is that for a mass source/sink at the same latitude and with the same strength, the system to the east is more intense and the circulation well defined. The east-west mass source/sink problem can be physically interpreted as a highly simplified view of the Walker circulation between the eastern and western oceans. In the western oceans, the high sea temperature favors convection and mass is pumped up in the troposphere. On the eastern side of the ocean, the low sea temperature inhibits deep convection and radiative cooling requires subsidence warming to maintain the energy balance. If we assume that the mass that goes up in the convective region is forced to sink in the eastern region, the hypothetical experiment discussed in this section can be viewed as a gross projection of the Walker circulation forcing onto the barotropic modes. However, in this case the relative position of the mass source/sink areas in Figure 6.7 (ϕ_0=20°) would have to be reversed since the mass sink is associated with the convective region.

We do not claim that the size and latitude of the forcing term in Figure 6.7 quantitatively agrees with the observed regions of active convection and subsidence. The model equations are too simplified to

get more than qualitative agreement with observations. Nevertheless, Figure 6.7 suggests a rather well defined high pressure cell to the NW of the positive forcing; the low pressure area is not so well defined in terms of circulation and intensity. These features of the steady state response have some similarity with the observed features of the east-west circulation in the atmosphere such as the positioning of a strong subtropical high and a not well-defined low pressure area in the western sector of the oceans.

6.4 Summary and discussion

The objective of this chapter is to study the response of the mass and wind fields to steady forcing. In section 2.4 we derived the expression for the expansion coefficient of the solution when the system is subjected to a time independent forcing or alternatively, a zero frequency forcing. Equation (2.86) shows that low frequency modes (Rossby modes) will have large amplitudes while the high frequency modes (gravity modes) are suppressed if the amount of energy projected onto each mode is the same. In particular, the k = 0 geostrophic mode is resonant to the zero frequency forcing if $\kappa = 0$ and linear growth is expected according to (2.91). Thus, if the forcing is such that it is projected mostly onto long waves we expect a large zonal geostrophic component to be observed in the form of a zonally stretched current as time increases.

In section 3.1 we have shown an example of the transient solution on the equatorial β-plane for a bell shaped mass source centered at $y_0 = 1.2$ and half-width $r_e = 0.35$. This experiment can be interpreted as heating in the two-level baroclinic model discussed in section 2.1,

and in this case the perturbation is centered at approximately 14° N and the half-width is approximately 470 km. In Chapter 4 we considered the impulsive forcing case with the same parameters y_o and r_e. As expected, for a steady forcing the Rossby mode contribution to the total solution is much more important than in the case studied in Chapter 4, as can be seen comparing the x-t cross sections shown in Figure 6.1-6.2 with Figures 4.2-4.3. In the forced case however, the divergence field (Figure 6.3) is maintained by the gravity modes since the Rossby modes are primarily rotational (Figure 3.20). The divergence field reaches a quasi-steady state after about 1 non-dimensional unit (9 hours for ε=500). A perfect state divergence cannot be reached on the equatorial β-plane with no damping (κ=0) since energy is trapped within the critical latitudes (Stern, 1963; Bretherton, 1964; Matsuno, 1966). Furthermore, we are considering periodic domains in the x-direction and therefore energy is not allowed to disperse to infinity in any direction.

The two dimensional field of the above experiment is Figure 6.4 at t = 2.7 ($\approx$1 day for ε=500). The asymmetry in the two-dimensional structure of the geopotential and wind fields is due to the β-effect since the forcing is perfectly symmetrical. Of course asymmetries in hurricanes can be due to a variety of causes such as dynamical instability (Anthes, 1972) and the environment in which the storm is embedded (Frank, 1976; McBride, 1979). In Figure 6.4 the β-effect is isolated for a forcing in the mass field. Along this same line we have shown in section 6.2 that a steady momentum forcing such that a vortex is continuously forced also generates asymmetries in the mass and wind fields on a short time scale. The results obtained with the

steady vortex are similar in many regards to the impulsive forcing discussed in Chapter 5, e.g. the subsidence in the center of the vortex and the up motion in the NE quadrant. The dynamically induced up motion is favorable for enhancing convection and this is another example of tropical storm asymmetry induced by the β-effect.

The effect of friction on the forced stationary motion is discussed in section 6.1 for mass sources and sinks alternating along the Equator. This problem was treated by Matsuno (1966) for $\kappa = 0.20$. In the equatorial region the geopotential distribution tends to ignore the mass source when k is small but for high values of k the pressure field tends to be identified with the mass source. At higher latitudes the flow is in approximate geostrophic balance with the pressure field but in the equatorial region the fluid flows from mass source to mass sink forming a strong jet centered at the Equator.

In section 6.3 are some examples of the forced stationary motion on the sphere for the external mode (ε=10). Instead of the single wave structure discussed in section 6.1, we now consider one mass sink and one mass source at the same latitude. The latitude dependence and relative position of the mass source/sink system is considered. For the same mass-source/sink intensity, the higher the latitude the stronger is the pressure response. If a mass source is positioned to the east of a mass sink the high pressure associated with the source is more intense than the low pressure which is the response to the mass sink. For a mass source/sink with e-folding width smaller than the local Rossby radius of deformation the pressure field does not correspond exactly to the impressed source/sink; the high/low is localized to the

west of the source/sink. Since the dynamical response to a steady forcing is more resonant to low frequency modes (Rossby modes), the resulting fields are closer to geostrophic balance.

7.0 SUMMARY AND DISCUSSION

In the standard treatment of the process of geostrophic adjustment the shallow water equations are formulated on an f-plane. Thus, the problem is solved on a flat unbounded earth and the motion indeed tends to perfect geostrophic balance as $t \to \infty$. This is because the gravity waves excited by local sources spread out very rapidly to infinity leaving behind the steady state geostrophic solution.

The real earth, although laterally unbounded, is finite. We have not only the curvature effects of the spherical geometry but also the dynamical effect caused the variation of the Coriolis parameter with latitude. Besides the steady geostrophic solution (zonal current in this case) we also have another type of low frequency motion represented by Rossby waves, which are quasi-geostrophic. Because of the variation of the Coriolis parameter gravity waves are refracted and form envelopes on which the wave amplitude is large (Blandford, 1966; Jacobs, 1967). Another dynamical effect of the variation of f is to allow for waves with appreciable magnitude only in neighborhood of the Equator, a phenomenon called equatorial trapping and discussed by Stern (1963), Bretherton (1964) and Longuet-Higgins (1965).

The existence of a class of waves of low frequency and small group velocity over a wide range of zonal wavenumbers suggests that the concept of geostrophic adjustment can be somewhat generalized; the type of motion characterized by the Rossby modes can be regarded as the adjusted state. Thus, our objective is to follow the development of an initial condition until the slow dispersive motion characterized by the Rossby modes dominates.

The adjustment time on the β-plane, i.e. the time required to observe the Rossby modes contribution to the solution, is determined by the dimensions of the initial perturbation and the group velocity of gravity waves (as in 4.9). Thus, if most of the initial condition is concentrated in long waves, the adjusted state is well-defined only if the energy in Rossby modes is much greater than the energy in gravity modes, since long gravity waves are also slowly dispersive (Figure 3.6). The concept of adjusted state is therefore not only dependent on the partition of energy between quasi-geostrophic modes and gravity modes but also on the spectral distribution of energy.

Let us consider now the motivation for studying the characteristics of the free wave solutions of the shallow water equations on the β-plane. As is usual for differential equations with time independent coefficients, we solve the problem by the method of normal modes or eigenfunction expansion (Butkov, 1968). If the initial condition can be represented as a superposition of normal modes, the solution of the problem is the same superposition where each mode evolves in time at its characteristic frequency. The method of solution for the more general case when friction and external forcing is included is discussed in section 2.4 . The dispersive characteristics of the free waves are displayed in Figure 3.6 where the group velocity as a function of zonal wavenumber and meridional index for the various types of waves is shown.

7.1 Significance of single equivalent depth analysis

In section 2.1 we have shown that the perturbation equation for a basic state of no motion for a stratified atmosphere can be separated

into the horizontal structure equations and the vertical structure equation; the separation constant is the so-called equivalent depth H (Taylor, 1936). The horizontal structure equations are the so-called shallow water equations and H is the depth of the homogeneous ocean.

For simplified mode atmospheres which include some sort of rigid tops ($\omega = 0$ at $p = 0$ is included in this category), the vertical structure equation provides the equivalent depth H as an eigenvalue; furthermore, the boundary value problem posed by the vertical structure equation and the boundary conditions give us a complete set of eigenfunctions. Thus, we can make use of expansion theorems and expand the three-dimensional solution in a series of the eigenfunctions. This is the method used by Bolin (1953) to solve the classical geostrophic-adjustment problem in a stratified fluid. We should also be aware that the completeness of the eigenfunctions in the vertical also allows us to study the transient solution of a forced problem since the vertical structure of the forcing can also be projected onto the eigenfunctions of the vertical structure equation. Lighthill (1969) discusses the ocean case where the external forcing is the wind stress, which can be projected onto the vertical modes.

Models with a discrete number of layers in the vertical and with some sort of rigid top also belong to this category; i.e., we can find the normal modes of the governing equations and expand the solution as a series. The 2-level baroclinic model discussed in section 2.1 is an example. Geisler (1970) discusses the response of a two-layer ocean to a moving hurricane and points out the different time scales of the barotropic and baroclinic responses (see the definition of [T] in section 2.3).

Internal modes (small equivalent depth) are adjusted rather slowly since the maximum group velocity allowed in the system ($c = \sqrt{gH}$) is considerably reduced relative to the barotropic mode (external mode). In the forced problem, where the forcing is time dependent, we clearly see that the transient response is strongly dependent on the frequency of the forcing (see (2.86)) since the closer the forcing frequency is to one of the natural frequencies the larger is the response.

We should notice that in some cases the eigenvalues of the vertical structure equation are part discrete and part continuous as shown by Jacobs (1967). The discrete part in this case is the barotropic divergent mode with Lamb's parameter $\varepsilon \approx 10$ in an isothermal atmosphere. The continuous modes are a consequence of the upper boundary condition; with the radiation condition on the top of the model only the discrete mode is allowed (Lindzen, 1967). Thus, it seems that the existence of a complete set of normal modes in the vertical can be questioned. When the volume of the fluid is infinite it may be possible that energy is radiated to infinity but it is also possible that energy is reflected by particular profiles of the vertical shear of the wind (Eliassen and Palm, 1960). In such cases, the rigid top assumption can be justified and the existence of a complete set of eigenfunctions in the vertical is justifiable.

Eckart (1960) suggests that the eigensolutions in the unbounded case can be identified by a single continuously variable parameter as can the eigenfrequencies. Thus, when the fluid is unbounded the expansion theorems become analogous to the Fourier integral expansion. However, there has been little justification for considering such an expansion in meteorology and application of more elaborate mathematical techniques to initial value problems is lacking.

Our single equivalent depth analysis of the adjustment problem can be justified in a stratified fluid with some sort of rigid top or in terms of the two-level baroclinic model discussed in section 2.1. Interpretation of the results in terms of the external mode also seems justifiable in the case of the unbounded atmosphere. However, we are considering the projection of an initial condition with vertical structure on one particular equivalent depth. Thus, we are implying that our results are significant for initial conditions that are projected mostly onto some particular value of H.

7.2 Significance of the results

In Chapter 4, we considered the problem of the adjustment of an initial condition solely in the geopotential field. The opposite case in which the initial condition is the wind field was treated in Chapter 5. The initial condition in the wind field is assumed to be a vortex with no divergence. The results of the experiments are summarized and discussed in section 4.5 and 5.5, respectively.

For both types of initial condition we have seen that knowledge of the dispersive characteristics of the free modes (section 3.1), the partition of kinetic and potential energy and the two-dimensional structure of the waves (section 3.2) allowed us to explain and predict the characteristics of the solution. This demonstrates the importance of knowing the basis functions in an initial value problem solved by the method of eigenfunction expansion. Although the examples treated in Chapter 4 and 5 are of a particular form, the technique that we used to explain the results is applicable to more general cases such as elongated initial conditions in the zonal or meridional direction; in

such cases we only have to estimate the spectral distribution in the zonal and meridional direction which can be easily evaluated by knowledge of the structure of free modes.

The two examples that we have chosen in Chapter 4 and 5, an initial condition in the mass field and a vortex-like initial condition, respectively, have interesting consequences for tropical dynamics. Let us interpret the initial condition in terms of the two-level baroclinic model with phase speed of internal gravity waves on the order of 40 ms^{-1} ($\varepsilon = 500$). The results in Chapter 4 imply that only about 10% of the input heating is not dispersed by gravity modes, as shown in the example in Figure 4.5. Thus, heating the atmosphere impulsively on a scale less than the equatorial Rossby radius of deformation ($\approx$ 1300 km for $\varepsilon = 500$) does not produce a large local temperature change. The adjustment time (4.9) for a small heating perturbation is certainly fast because the energy is spread over a broad band of zonal wavenumbers and the group velocity of the gravity wave packet is large (Figure 3.6). In section 6.1 we have considered a steady heating case and Figure 6.4 allowed us to estimate a temperature change of about 1° C day^{-1} for a steady heat source of 8° C day^{-1} and of the same shape and size of the impulsive case. Thus, it is clear that any small scale heating in the tropical atmosphere is going to cause a small local temperature tendency. This is certainly a possible explanation for the fact that local temperature changes in the tropics are small and little temperature gradients are observed between convectively active regions and clear regions (Reed and Recker, 1971; Yanai et al., 1973; Gray, 1973).

The situation for an initial condition in the rotational part of the wind field is totally different. Altering the vorticity of the momentum field on a small scale is a very efficient way to maintain the input energy. This is because most of the initial energy goes into Rossby modes which are slowly dispersive. Figure 3.20 shows the ratio of maximum vorticity to maximum divergence for the various types of free waves of the shallow water equations. We clearly see that the maximum vorticity is at least one order of magnitude larger than the divergence for Rossby modes and therefore any initial condition which is rotational will primarily be represented by Rossby modes.

In view of the above, we feel tempted to interpret our results in terms of the efficiency of clouds in altering the geopotential and wind fields. The clouds seem to be inefficient in provoking temperature changes through heating, since most of the input energy is dispersed by gravity waves, provided we are dealing with disturbances less than the equatorial Rossby radius of deformation (Figure 4.1). However, if the clouds do indeed affect the rotational part of the momentum field we have found long lasting effects in the momentum and geopotential fields. In Chapter 5 and 6 we interpreted the vortex experiment in the two-layer baroclinic model as a hypothesized anticyclonic shear induced by the generation of momentum by clouds. The results show that most of the initial energy stays in kinetic form and subsidence is induced in the center of the vortex, thus warming the atmosphere.

In summary, clouds can change the temperature field and the momentum field. The adjustment problem indicates that altering the temperature field is very inefficient since most of the input energy is

dispersed, assuming a small perturbation compared to the equatorial Rossby radius of deformation. On the other hand, if clouds affect the rotational part of the wind on the same scale, the energy is slowly dispersed. However, we do not know the detailed physics of the momentum interaction of clouds with the environment. Thus, we cannot yet ascribe more importance to one mechanism or the other with absolute confidence. The results are therefore speculative, although observations indicate that the cloud effect on the momentum field might be important for hurricane development (McBride, 1979).

Besides the different interpretations of the concept of an adjusted state on the f-plane and β-plane we should point out the important differences found in our results. The adjusted state on the f-plane is symmetrical if the initial condition is symmetrical; on the β-plane this is not true since the dispersive characteristics of the waves are not symmetrical in the east-west direction. Since f increases with latitude, westward propagating Rossby waves are allowed and the absolute value of the group velocities of the westward and eastward gravity waves are not exactly the same. However, more important are the peculiar dispersive characteristics of Rossby waves; long waves disperse the energy towards the west and short waves towards the east. These results can be seen in Chapters 4, 5 and 6. In particular, we notice the elongated patterns to the west and relatively intense pressure centers developing in the eastern sector in both the geopotential and vortex initial condition experiments. This process occurs on a sufficiently short time scale to be of significance since it may interact with convection.

In Chapters 4, 5 and 6 we have also presented results of the initial value problem solved on the sphere for the barotropic mode. However, the results are qualitatively similar to the equatorial β-plane interpreted with the appropriate time and length scales of the external mode ($c \approx 300\ ms^{-1}$). Of course, the qualitative agreement is dependent on the time and length scales of the initial disturbance or forcing and the latitude of the disturbance.

7.3 Recommendations for future work

We have treated the problem of the adjustment of the mass and wind fields based on the dynamics described by the linearized shallow water equations about a basic state of rest. There are two fundamental limitations of such a system of equations as far as the real atmosphere is concerned. The first has to do with the single equivalent depth analysis and the second is related to the assumption of a motionless basic state.

It is clear that stratification and a basic state with horizontal and vertical shear may produce even more interesting results. However, the solution of the problem in such a general situation is only possible in numerical techniques and then we have to deal with the distortion of the process of adjustment by the discretization (Arakawa and Lamb, 1977). Analytical solutions can be obtained in simplified systems such as an atmosphere with simple stratification and no basic state wind as discussed in section 7.1. In the Soviet Russian literature, we can also find some examples of the problem of adjustment in stratified atmospheres (e.g., Kibel, 1963). Dickinson (1969a) also describes the process of adjustment by a point source

in a simplified hydrostatic mode. However, there has been little work doen on the interpretation of theoretical results in light of observations and this can be left as a suggestion for future work.

The introduction of a basic state with meridional shear in the linearized shallow water equations could be expected to cause changes in the results presented here. Blumen and Washington (1969) studied the effect of a basic horizontal shear flow on the linear geostrophic adjustment process in an unbounded barotropic fluid. The motion was assumed to be independent of x and only the adjusted state was considered. The main conclusion is that the process of energy partition between geostrophic and ageostrophic motions is strongly influenced by the presence of the horizontal shear. This effect increases as the horizontal shear increases. Schubert and Hack (1979) consider the partition of energy between geostrophic and ageostrophic motion in an axisymmetric vortex as a function of the Froude number $F = U/c$, where U denotes the characteristic tangential wind speed. Their results indicate that there is an increase in the amount of energy in geostrophic motion for small scale ϕ-perturbations and a decrease for small scale vortex perturbations as the Froude number increases. However, for reasonable values of the Froude number, the partition does not differ qualitatively from that for the motionless basic state.

On the β-plane, the non-linear shallow water equations can be linearized about a basic state with meridional shear. The governing equations can be put in vector form as in section 2.2 with the basic state dependent terms on the right hand side and the method of solution is a Galerkin procedure as in Kasahara (1977). The natural choice for basis functions are the eigenfunctions corresponding to

the free wave solutions of the shallow water equations discussed in section 2.3. The reason for this choice of basis functions is that the partial differential equations of the sheared case are greatly simplified to a set of coupled ordinary differential equations of simple form that can be solved analytically.

As a by-product of the Galerkin method of solution, we get the effects of meridional shear on Kelvin, Rossby, mixed Rossby gravity and gravity waves. Such studies have been already published by Simmons (1978) and Boyd (1978a, 1978b). Dikiy and Katayev (1971) have computed the planetary wave spectrum of the two-dimensional vorticity equation by the Galerkin method. It is shown that if the oscillations are superimposed on a zonal flow different from solid rotation, then of the whole infinite spectrum of Rossby waves there remains only a finite number of discrete modes whose angular phase velocities are less than the minimum velocity in the zonal flow. The rest merge into a continuous spectrum that covers the interval between the minimum and maximum velocities. The discrete modes correspond to the longer Rossby waves deformed by the zonal flow. In fact, for those modes with phase speed between the minimum and maximum velocity of the basic state there are critical latitudes and we might question the validity of the method of solution since there are singularities in the solution (Dickinson, 1969). In order to obtain convergence in the Galerkin method, we have to introduce dissipation and some of the results seem to be particularly sensitive to the singular line effects.

The process of adjustment of the mass and wind fields in the presence of horizontal shear is currently being studied by the author.

And finally, it should be emphasized that there is a need for more work on the interaction of clouds with the large-scale environment, particularly the momentum interaction.

REFERENCES

Arakawa, A., V.R. Lamb, 1977: Methods in Computational Physics, Vol. 17. General Circulation Models of the Atmosphere. Ed. by Julius Chang, Academic Press, 357 pp.

Abramowitz, M. and I.A. Stegun, 1970: Handbook of Mathematical Functions. Dover Publications, Inc., New York.

Anderson, D.L.T. and P. B. Rowlands, 1976: The role of inertial-gravity waves and planetary waves in the response of a tropical ocean to the incidence of an equatorial Kelvin wave on a meridional boundary. J. Mar. Res., 34, 295-312.

Anthes, R.A., 1972: Development of asymmetries in a three-dimensional numerical model of the tropical cyclone. Mon. Wea. Rev., 100, 461-476.

Blandford, R., 1966: Mixed gravity-Rossby waves in the ocean. Deep Sea Research, 13, 941-961.

Blumen, W., 1967: On non-linear geostrophic adjustment. J. Atmos. Sci., 24, 325-332.

Blumen, W., 1972: Geostrophic adjustment. Reviews of Geophysical and Space Physics, 10, 485-528.

Blumen, W. and W.M. Washington, 1969: The effect of horizontal shear flow on geostrophic adjustment in a barotropic fluid. Tellus, 21, 167-176.

Bolin, B., 1953: The adjustment of a non-balanced velocity field towards geostrophic equilibrium in a stratified fluid. Tellus, 5, 373-385.

Bretherton, F.P., 1964: Low frequency oscillations trapped near the Equator. Tellus, 16, 181-185.

Burger, A., 1958: Scale considerations of planetary motions of the atmosphere. Tellus, 10, 195-205.

Burpee, R.W., 1972: The origin and structure of easterly waves in the lower troposphere of North Africa. J. Atmos. Sci., 29, 77-90.

Butkov, E., 1968: Mathematical Physics. Addison-Wesley Publishing Company.

Boyd, P.B., 1978a: The effects of latitudinal shear on equatorial waves. Part I: Theory and methods. J. Atmos. Sci., 12, 2236-2258.

REFERENCES continued

Boyd, P.B., 1978b: The effects of latitudinal shear on equatorial waves. Part II: Applications to the atmosphere. J. Atmos. Sci., 12, 2259-2267.

Cahn, A., 1945: An investigation of the free oscillations of a simple current system. J. Meteor., 2, 113-119.

Cane, M. and E.S. Sarachik, 1976: Forced baroclinic ocean motions: I. The linear equatorial unbounded case. J. Mar. Res., 34, 629-665.

Charney, J.G., 1947: The dynamics of long waves in a baroclinic westerly current. J. Met., 4, 135-163.

Charney, J.G. and A. Eliassen, 1964: On the growth of the hurricane depression. J. Atmos. Sci., 21, 68-75.

Dickinson, R.E., 1969a: Propagators of atmospheric motions, I, Excitation by point impulses. Rev. Geophys. Space Phys., 7, 483-514.

Dickinson, R.E., 1969b: Theory of planetary wave-zonal flow interaction. J. Atmos. Sci., 25, 73-81.

Dikiy, L.A. and V.V. Katayev, 1971: Calculation of the planetary wave spectrum by the Galerkin method. Izv. Atmospheric and Oceanic Physics, 7, 1031-1038.

Dobrischman, E.M., 1964: On Coriolis force variability in the prognostic schemes. Tellus, 16, 18-25.

Eliassen, A. and E. Palm, 1960: On the transfer of energy in stationary mountain waves. Geofys. Publikasjoner, 22, No. 3, 1-23.

Eckart, C., 1960: "Hydrodynamics of Oceans and Atmospheres". Pergamon, New York, 290 pp.

Frank, W.M., 1976: The structure and energetics of the tropical cyclone. Atmos. Sci. Paper No. 258, Depart. Atmos. Sci., Colo. State Univ., CO, 80523.

Geisler, J.E., 1970: Linear theory of the response of two-layer ocean to a moving hurricane. Geophys. Fluid Dyn., 1, 249-272.

Geisler, J.E. and R.E. Dickinson, 1972: The role of variable Coriolis parameter in the propagation of inertia-gravity waves during the process of geostrophic adjustment. J. Phys. Oceanogr., 2, 263-272.

Gray, W.M., 1973: Cumulus convection and larger scale circulations 1. Broadscale and mesoscale considerations. Mon. Wea. Rev., 101, 839-855.

Gray, W.M. and R. Jacobson, Jr., 1977: Diurnal variations of deep cumulus convection. Mon. Wea. Rev., 105, 1171-1188.

Hayashi, Y., 1970: A theory of large-scale equatorial waves generated by condensation heat and accelerating the zonal wind. J. Meteorol. Soc. Japan, 48, 140-160.

Hoskins, B.J., A.J. Simmons, D.G. Andrews, 1977: Energy dispersion in a barotropic atmosphere. Quart. J. R. Met. Soc., 103, 553-567.

Houze, R.A. Jr., 1973: A climatological study of vertical transports by cumulus-scale convection. J. Atmos. Sci., 30, 1112-1123.

Jacobs, S.J., 1967: An asymptotic solution of the tidal equations. J. Fluid Mech., 30, 417-438.

Jacobs, S.J. and A. Winn-Nielsen, 1966: On the stability of a barotropic basic flow in a stratified atmosphere. J. Atmos. Sci., 23, 682-687.

Kasahara, A., 1976: Normal modes of ultralong waves in the atmosphere. Mon. Wea. Rev., 104, 669-690.

Kasahara, A., 1977: Numerical integration of the global barotropic primitive equations with Hough Harmonic expansions. J. Atmos. Sci., 34, 687-701.

Kasahara, A., 1978: Further studies on a spectral model of the global barotropic primitive equations with Hough harmonic expansions. J. Atmos. Sci., 35, 2043-2051.

Kibel, I. A., 1963: An introduction to the hydrodynamical methods of short period weather forecasting. Pergamon Press, 383 pp.

Lamb, H., 1952: Hydrodynamics, 6th ed. Dover Publications, New York, 738 pp.

Lighthill, M.J., 1969: Dynamic response of the Indian Ocean to onset of the southwest monsoon. Philosophical Transactions of the Royal Society of London, A265, 45-92.

Lindzen, R.S., 1967: Planetary waves on beta-planes. Mon. Wea. Rev., 95, 441-451.

Lindzen, R.S., 1974: Wave-CISK in the tropics. J. Atmos. Sci., 31, 156-179.

Longuet-Higgins, M.S., 1964: On group velocity and energy flux in planetary wave motions. Deep-Sea Research, 11, 35-42.

Longuet-Higgins, M.S., 1965: Planetary waves on a rotating sphere II. Proc. Roy. Soc., A284, 40.

REFERENCES continued

Longuet-Higgins, M.S., 1968: The eigenfunctions of Laplace's tidal equations over a sphere. Phil. Trans. Roy. Soc. London, A262, 511-607.

McBride, J.L., 1979: Observational analysis of tropical cyclone formation. Ph.D. Thesis, Dept. of Atmos. Sci., Colo. State Univ., Ft. Collins, CO, 80523.

McBride, J.L., and W.M. Gray, 1978: Mass divergence in tropical weather systems, Paper I: Diurnal variation, Paper II: Large-scale controls on convection. Dept. of Atmos. Sci. Paper No. 299, Colo. State Univ., Ft. Collins, CO, 109 pp.

Mak, M.-K., 1969: Laterally driven stochastic motions in the tropics. J. Atmos. Sci., 26, 41-64.

Manabe, S. and J. Samagorinsky, 1967: Simulated climatology of a general circulation model with a hydrological cycle: II. Analysis of the tropical atmosphere. Mon. Wea. Rev., 95, 155-169.

Matsumoto, S., 1960: A note on Geostrophic Adjustment and gravity wave in the atmosphere. Jour. Met. Soc. of Japan, 39, 18-28.

Matsuno, T., 1966: Quasi-geostrophic motions in the equatorial area. J. Meteor. Soc. Japan, 44, 25-43.

Moncrieff, M.W., 1978: The dynamical structure of two-dimensional steady convection in constant vertical shear. Quart. J. Roy. Met. Soc., 104, 543-567.

Moncrieff, M.W. and M.J. Miller, 1976: The dynamics and simulation of tropical cumulonimbus and squall lines. Quart. J. Roy. Met. Soc., 102, 373-394.

Moore, D.W. and S.G.H. Philander, 1976: Modelling of the equatorial oceanic circulation. The Sea, Vol. 6, Goldberg et. al. eds., New York, Interscience.

Morse, P.M and H. Feshback, 1953: Methods of Theoretical Physics, Part I. New York, McGraw-Hill, 997 pp.

Nitta, T., 1972: Energy budget of wave disturbances over the Marshall Islands during the years of 1956 and 1958. J. Met. Soc. Japan, 50, 71-84.

Nitta, T. and M. Yanai, 1969: A note on the barotropic instability of the tropical easterly current. J. Met. Soc. Japan, 47, 127-130.

REFERENCES continued

Norquist, D.C., E.E. Recker and R.J. Reed, 1977: The energetics of African wave disturbances as observed during Phase III of GATE. Mon. Wea. Rev., 105, 334-342.

Obukhov, A.M., 1949: On the question of the geostrophic wind. Izv. Akad. Novk. USSR Ser Geograf. Geofiz., 13, 4, 281-306.

Ooyama, K., 1964: A dynamical model for the study of tropical cyclone development. Geofis. Intern., 4, 187-198.

Ooyama, K., 1971: A theory on parameterization of cumulus convection. J. Met. Soc. Japan, 49, Special Issue, December 1971, 744-756.

Paegle, J., 1978: The transient mass-flow adjustment of heated atmospheric circulations. J. Atmos. Sci., 35, 1678-1688.

Pedgley, D.E. and T.N. Krishnamurti, 1976: Structure and behavior of a monsoon cyclone over West Africa. Mon. Wea. Rev., 104, 149-167.

Phillips, N.A., 1963: Geostrophic motion. Rev. Geophys., 1, 123-176.

Reed, R.J. and E.E. Recker, 1971: Structure and properties of synoptic-scale wave disturbances in the equatorial western Pacific. J. Atmos. Sci., 28, 117-1133.

Reed, R.J., D.C. Norquist and E.E. Recker, 1977: The structure and properties of African wave disturbances as observed during Phase III of GATE. Mon. Wea. Rev., 105, 317-333.

Rennick, M.A., 1976: The generation of African waves. J. Atmos. Sci., 33, 1955-1969.

Rossby, C.-G., 1938: On the mutual adjustment of pressure and velocity distributions in certain simple current systems. J. Marine Research, 1, 239-263.

Rossby, C.-G., 1945: On the propagation of frequencies and energy in certain types of oceanic and atmospheric waves. J. of Met., 2, 187-204.

Schubert, W.H. and J. Hack, 1979: Geostrophic and gradient adjustment in axisymmetric and asymmetric vorticies. Paper presented at the 12th Technical Conference on Hurricanes and Tropical Meteorology, New Orleans, April 1979.

Simmons, A.J., 1977: A note on the instability of the African jet. J. Atmos. Sci., 34, 1670-1674.

REFERENCES continued

Simmons, A.J., 1978: Some effects of meridional shear and spherical geometry on long stratospheric waves. Quart. J. Roy. Met. Soc., 104, 595-614.

Stern, M.E., 1963: Trapping of low frequency oscillations in an equatorial boundary layer. Tellus, 15, 246-249.

Stevens, D.E., R.S. Lindzen and L.J. Shapiro, 1977: A new model of tropical waves incorporating momentum mixing by cumulus convection. Dyn. Atmos. Oceans, 1, 365-425.

Taylor, G.I., 1936: The oscillations of the atmosphere. Proc. Roy. Soc. London, A156, 318-326.

Tribia, J.J., 1978: Non-linear initialization on an equatorial beta-plane. Submitted to J. Atmos. Sci.

Wiin-Nielsen, A., 1971: On the motion of various vertical modes of transient very long waves. Part I - β-plane approximation. Tellus, 23, 87-98.

Williams, K.T. and W.M. Gray, 1973: A statistical analysis of satellite-observed trade wind cloud clusters in the western north Pacific. Tellus, 21, 313-336.

Yanai, M., S. Esbensen and J.-H. Chu, 1973: Determination of bulk properties of tropical cloud clusters from large-scale heat and moisture budgets. J. Atmos. Sci., 30, 611-627.

Yamasaki, M., 1969: Large-scale disturbances in the conditionally unstable atmosphere in low latitudes. Papers Meteorol. Geophys., 20, 289-336.

Yeh, T., 1949: On energy dispersion in the atmosphere. J. Met., 6, 1-16.

Yashida, K., 1959: A theory of the Cromwell Current (the equatorial undercurrent) and the equatorial upwelling--An interpretation in a similarity of a costal circulation. Journal of the Oceanographic Society of Japan, 15, 1-12.

APPENDIX A

The Hermite polynomials satisfy the usual set of formulas associated with Sturm-Liouville problems (Butkov, 1968) such as the orthogonality over the interval $(-\infty, +\infty)$ with respect to the weight function e^{-y^2},

$$\int_{-\infty}^{+\infty} H_n(y)\, H_m(y)\, e^{-y^2}\, dy = 0 \qquad (n \neq m) \; . \tag{A.1}$$

The normalization constant for Hermite polynomials is

$$\int_{-\infty}^{+\infty} [H_n(y)]^2\, e^{-y^2}\, dy = 2^n\, n!\, \sqrt{\pi} \; . \tag{A.2}$$

The lowest order Hermite polynomial is

$$H_0(y) = 1 \; , \tag{A.3}$$

and the recursion formula is

$$2y\, H_n(y) = 2n\, H_{n-1}(y) + H_{n+1}(y) \; . \tag{A.4}$$

The differentiation formula for Hermite polynomials is

$$\frac{dH_n(y)}{dy} = 2n\, H_{n-1}(y) \quad \text{for} \quad n \geq 1 \; . \tag{A.5}$$

BIBLIOGRAPHIC DATA SHEET	CSU-ATSP-312	

4. Title and Subtitle

The Dynamics of Equatorial Mass-Flow Adjustment

5. Report Date: June 1979

6.

7. Author(s)

Pedro Leité Silva Dias and Wayne H. Schubert

8. Performing Organization Rept. No. 312

9. Performing Organization Name and Address

Department of Atmospheric Science
Colorado State University
Fort Collins, CO 80523

10. Project/Task/Work Unit No.

11. Contract/Grant No.

ATM76-09370
ATM78-08125

12. Sponsoring Organization Name and Address

National Science Foundation

13. Type of Report & Period Covered

14.

15. Supplementary Notes

16. Abstracts

The problem of the adjustment of the mass and wind fields in a divergent barotropic model is solved on the equatorial β-plane. Contrary to the traditional f-plane analysis, the motion does not tend to a perfect geostrophic balance on a short time scale. However, the β-plane approximation allows for the presence of Rossby waves and since these waves are quasi-geostrophic, they may be regarded as the adjusted state. It is also shown that the concept of an adjusted state on the β-plane is dependent on the dispersive properties and energetics of Rossby and gravity waves.

Two basic experiments are shown: the first is a perturbation in the geopotential field, and the second is a perturbation in the rotational part of the wind field. When perturbing the mass field on a small scale compared to the equatorial Rossby radius of deformation, most of the initial energy is dispersed by gravity waves; but altering the vorticity field is a very efficient way to localize the energy input. The adjusted state shows asymmetries that cannot be obtained on an f-plane analysis.

17. Key Words and Document Analysis. 17a. Descriptors

geostrophic adjustment
Rossby waves
gravity waves
equatorial β-plane

17b. Identifiers/Open-Ended Terms

17c. COSATI Field/Group

18. Availability Statement	19. Security Class (This Report) UNCLASSIFIED	21. No. of Pages 203
	20. Security Class (This Page) UNCLASSIFIED	22. Price